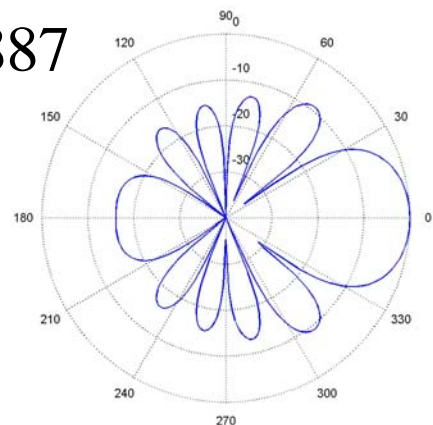


Applied Computational Electromagnetics Society Journal

Special Issue on
ACES 2003 Conference
Part II

Editor-in-Chief
Atef Z. Elsherbeni

March 2004
Vol. 19 No. 1b
ISSN 1054-4887



GENERAL PURPOSE AND SCOPE: The Applied Computational Electromagnetics Society (*ACES*) Journal hereinafter known as the *ACES Journal* is devoted to the exchange of information in computational electromagnetics, to the advancement of the state-of-the art, and the promotion of related technical activities. A primary objective of the information exchange is the elimination of the need to “re-invent the wheel” to solve a previously-solved computational problem in electrical engineering, physics, or related fields of study. The technical activities promoted by this publication include code validation, performance analysis, and input/output standardization; code or technique optimization and error minimization; innovations in solution technique or in data input/output; identification of new applications for electromagnetics modeling codes and techniques; integration of computational electromagnetics techniques with new computer architectures; and correlation of computational parameters with physical mechanisms.

SUBMISSIONS: The *ACES Journal* welcomes original, previously unpublished papers, related to applied computational electromagnetics. Typical papers will represent the computational electromagnetics aspects of research in electrical engineering, physics, or related disciplines. However, papers which represent research in applied computational electromagnetics itself are equally acceptable.

Manuscripts are to be submitted through the upload system of *ACES* web site <http://aces.ee.olemiss.edu> See “Information for Authors” on inside of back cover and at *ACES* web site. For additional information contact the Editor-in-Chief:

Dr. Atef Elsherbeni

Department of Electrical Engineering
The University of Mississippi
University, MS 386377 USA
Phone: 662-915-5382 Fax: 662-915-7231
Email: atef@olemiss.edu

SUBSCRIPTIONS: All members of the Applied Computational Electromagnetics Society who have paid their subscription fees are entitled to receive the *ACES Journal* with a minimum of three issues per calendar year and are entitled to download any published journal article available at <http://aces.ee.olemiss.edu>.

Back issues, when available, are \$15 each. Subscriptions to *ACES* is through the web site. Orders for back issues of the *ACES Journal* and changes of addresses should be sent directly to *ACES* Executive Officer:

Dr. Richard W. Adler

ECE Department, Code ECAB
Naval Postgraduate School
833 Dyer Road, Room 437
Monterey, CA 93943-5121 USA
Fax: 831-649-0300
Email: rwa@attglobal.net

Allow four week’s advance notice for change of address. Claims for missing issues will not be honored because of insufficient notice or address change or loss in mail unless the Executive Officer is notified within 60 days for USA and Canadian subscribers or 90 days for subscribers in other countries, from the last day of the month of publication. For information regarding reprints of individual papers or other materials, see “Information for Authors”.

LIABILITY. Neither *ACES*, nor the *ACES Journal* editors, are responsible for any consequence of misinformation or claims, express or implied, in any published material in an *ACES Journal* issue. This also applies to advertising, for which only camera-ready copies are accepted. Authors are responsible for information contained in their papers. If any material submitted for publication includes material which has already been published elsewhere, it is the author’s responsibility to obtain written permission to reproduce such material.

APPLIED COMPUTATIONAL ELECTROMAGNETICS SOCIETY JOURNAL

Special Issue on
**ACES 2003 Conference
Part II**

Editor-in-Chief
Atef Z. Elsherbeni

March 2004
Vol. 19 No. 1b
ISSN 1054-4887

The ACES Journal is abstracted in INSPEC, in Engineering Index, DTIC, Science Citation Index Expanded, the Research Alert, and to Current Contents/Engineering, Computing & Technology.

The first, fourth, and sixth illustrations on the front cover have been obtained from the Department of Electrical Engineering at the University of Mississippi.

The third and fifth illustrations on the front cover have been obtained from Lawrence Livermore National Laboratory.

The second illustration on the front cover has been obtained from FLUX2D software, CEDRAT S.S. France, MAGSOFT Corporation, New York.

THE APPLIED COMPUTATIONAL ELECTROMAGNETICS SOCIETY

<http://aces.ee.olemiss.edu>

ACES JOURNAL EDITORS

EDITOR-IN-CHIEF/ACES/JOURNAL

Atef Elsherbeni

University of Mississippi, EE Dept.
University, MS 38677, USA

EDITORIAL ASSISTANT

Matthew J. Inman

University of Mississippi, EE Dept.
University, MS 38677, USA

EDITOR-IN-CHIEF, EMERITUS

David E. Stein

USAF Scientific Advisory Board
Washington, DC 20330, USA

ASSOCIATE EDITOR-IN-CHIEF

Alexander Yakovlev

University of Mississippi, EE Dept.
University, MS 38677, USA

EDITOR-IN-CHIEF, EMERITUS

Ducan C. Baker

EE Dept. U. of Pretoria
0002 Pretoria, South Africa

EDITOR-IN-CHIEF, EMERITUS

Allen Glisson

University of Mississippi, EE Dept.
University, MS 38677, USA

MANAGING EDITOR

Richard W. Adler

833 Dyer Rd, Rm 437 EC/AB
NPS, Monterey, CA 93943-5121, USA

EDITOR-IN-CHIEF, EMERITUS

Robert M. Bevensee

Box 812
Alamo, CA 94507-0516, USA

EDITOR-IN-CHIEF, EMERITUS

Ahmed Kishk

University of Mississippi, EE Dept.
University, MS 38677, USA

ACES JOURNAL ASSOCIATE EDITORS

Giandomenico Amendola

Universita' della Calabria
Rende , Italy

John Beggs

NASA Langley Research Center
Hampton, VA, USA

John Brauer

Ansoft Corporation
Milwaukee, WI, USA

Magda El-Shenawee

University of Arkansas
Fayetteville AR, USA

Pat Foster

Microwave & Antenna Systems
Gt. Malvern, Worc. UK

Cynthia M. Furse

Utah State University
Logan UT, USA

Christian Hafner

Swiss Federal Inst. of Technology
Zurich, Switzerland

Michael Hamid

University of South Alabama,
Mobile, AL, USA

Andy Harrison

Radiance
Huntsville, AL

Chun-Wen Paul Huang

Anadigics, Inc.
Warren, NJ, USA

Todd H. Hubing

University of Missouri-Rolla
Rolla, MO, USA

Nathan Ida

The University of Akron
Akron, OH, USA

Yasushi Kanai

Niigata Institute of Technology
Kashiwazaki, Japan

Leo C. Kempel

Michigan State University
East Lansing MI, USA

Andrzej Krawczyk

Institute of Electrical Engineering
Warszawa, Poland

Stanley Kubina

Concordia University
Montreal, Quebec, Canada

Samir F. Mahmoud

Kuwait University
Safat, Kuwait

Ronald Marhefka

Ohio State University
Columbus, OH, USA

Edmund K. Miller

LASL
Santa Fe, NM, USA

Krishna Naishadham

Wright State University
Dayton, OH, USA

Giuseppe Pelosi

University of Florence
Florence, Italy

Vicente Rodriguez

ETS-Lindgren
Cedar Park, TX, USA

Harold A. Sabbagh

Sabbagh Associates
Bloomington, IN, USA

John B. Schneider

Washington State University
Pullman, WA, USA

Abdel Razek Sebak

University of Manitoba
Winnipeg, MB, Canada

Amr M. Sharawee

American University
Cairo, Egypt

Norio Takahashi

Okayama University
Tsushima, Japan

THE APPLIED COMPUTATIONAL ELECTROMAGNETICS SOCIETY

JOURNAL

SPECIAL ISSUE ON ACES 2003 CONFERENCE

Part II

March 2004

TABLE OF CONTENTS

“Use of Model-Based Parameter Estimation for Fast RCS Computation of a Conducting Body of Revolution over a Frequency Band” H. Son, J. R. Mautz, and E. Arvas.....	65
“Triangular Grids: A Review of Resonator and Waveguide Analysis with Classical FIT and Some Reflections of Yee-like FIT- and FEM-Schemes” U. v Rienen.....	73
“Envelope – Finite Element (EVFE) Technique in Electromagnetics with Perfectly Matched Layer (PML)” W. Yao, Y. Wang, and T. Itoh.....	84
“Applications of the Transmission Line Matrix Method to Microwave Scanning Microscopy” R. Ciocan and N. Ida.....	94
“A Novel 3D Pseudo-Spectral Analysis of Photonic Crystal Slabs” K. Varis and A. R. Baghai-Wadji.....	101
“A Hybrid Full MAS and Combined MAS/TSA Algorithm for Electromagnetic Induction Sensing” F. Shubitidze, K. O’Neill, K. Sun, I. Shamatava, and K. D. Paulsen.....	112
“A Novel Dirichlet-Neumann Random-Walk Algorithm for the Solution of Time-Harmonic Helmholtz Equation at Multiple Wavelength Length Scales: 1D and 2D Verification” K. Chatterjee, P. Matos, and Y. L. Le Coz.....	127
“A Novel Numerical Approach for the Analysis of 2D MEMS-Based Variable Capacitors Including the Effect of Arbitrary Motions ” M. Kuroda, N. Miura, and M. M. Tentzeris.....	133
“Coupling Between Highly Conducting and Permeable Metallic Objects in the EMI Frequency Range” F. Shubitidze, K. O’Neill, I. Shamatava, and K. Sun.....	139

“Numerical Study of Coupling between Coagulators and Electrodes of Cardiac Pacemakers
under Consideration of the Human Body”
M. Schick and F. M. Landstorfer.....149

“Correlation Between the Geometrical Characteristics and Dielectric Polarizability of Polyhedra”
A. Sihvola, P. Ylä-Oijala, S. Järvenpää, and J. Avelin.....156

Use of Model-Based Parameter Estimation for Fast RCS Computation of a Conducting Body of Revolution over a Frequency Band

Hyunwung Son, Joseph R. Mautz, and Ercument Arvas
 Department of Electrical Engineering and Computer Science
 Syracuse University, Syracuse, NY 13244
 hson@syr.edu, jrmautz@syr.edu, earvas@syr.edu

Abstract—Frequency-derivative information incorporated with model-based parameter estimation (MBPE) is used to obtain scattering from a perfectly conducting body of revolution (BOR). The electric field integral equation (EFIE) is solved using the method of moments (MoM) to obtain the surface current on the perfectly conducting body. Instead of computing the MoM solution using a pointwise approach, a rational function model is used to approximate the current as a function of frequency. The model coefficients are computed using both frequency and frequency-derivative information at one frequency in the band or alternatively two or more frequencies in the band. With the rotational symmetry of BOR, the computational cost can be significantly reduced compared to that of arbitrary three-dimensional (3-D) objects and more importantly scattering from an electrically large body can be obtained. Numerical results for various perfectly conducting bodies are presented. Results show that the MBPE provides excellent agreement with the pointwise approach over a limited frequency band. In addition, the MBPE performs well for predicting sharp resonances.

I. INTRODUCTION

Most electromagnetic problems are essentially involved in determining the response over a certain bandwidth rather than at one or a few sampling points. Traditionally when the solution over a frequency band is required, a conventional method such as the method of moments (MoM) uses a set of discrete frequency samples with linear or low order polynomial interpolation, which requires a large number of frequency samples to obtain an accurate frequency response curve over the frequency band. In addition, for a response which contains very sharp resonances or is high Q, an excessive number of closely spaced frequency samples are required. As a result, the computational cost would be very high.

In [1]–[2], model-based parameter estimation (MBPE) is introduced to obtain a frequency response curve from both frequency and frequency-derivative data in a procedure where the moment matrix equation is differentiated. As an application, MBPE is used to evaluate the specialized Green's function associated with scatterers inside rectangular guided-wave structures and cavities [3]. Typically, MBPE is applied to predict the radar scattering cross section (RCS) of conducting and dielectric two-dimensional (2-D) bodies over a frequency band [4], [5] and of arbitrarily shaped three-dimensional (3-D) perfectly electric conducting (PEC) objects versus frequency [6], [7].

Specifically, in [4]–[7], the current is approximated by a rational function and its coefficients are determined using frequency and frequency-derivative data. In addition to a one-frequency derivative method, a multi-frequency derivative method has been presented [4], [7]. As a similar approach, Cauchy's technique is utilized to determine the electromagnetic response of a conducting cylinder over a frequency band and the coefficients of the rational function are obtained from the current and its derivatives at a few frequency points [8].

In this work, MBPE is applied to evaluate scattering from a conducting body of revolution (BOR) over a certain frequency range. In fact, the problem of electromagnetic scattering from a BOR has been studied by lots of researchers for many years [9]–[15]. With the rotational symmetry of BOR, the original 3-D problem can be reduced to a series of 2-D problems. As a result, electromagnetic scattering from a BOR can be computed with a significant reduction of computational time and data storage. However, when the frequency response over a frequency band is required, computations involving a BOR can be costly when the pointwise approach is used.

In this work, instead of using a pointwise approach, a rational function model is utilized to approximate the current as a function of frequency and the model coefficients are determined using both frequency information and frequency-derivative information within a frequency band. Consequently, the computational cost can be dramatically reduced.

II. MODEL-BASED PARAMETER ESTIMATION

A. Computing model coefficients using frequency-derivative samples

The fundamental spectral-domain rational function model can be written as

$$F(X) = \frac{N(X)}{D(X)} = \frac{\left[\sum_{i=0}^n N_i X^i \right]}{\left[\sum_{i=0}^d D_i X^i \right]} \quad (1)$$

where X would be the complex frequency ($X = \sigma + j\omega$). Of course, polynomials of any orders can be used in the numerator and denominator of this model. The N_i 's and D_i 's of (1) can be found when frequency-derivative samples at a certain frequency

are available. To find them, we begin by rewriting (1) as

$$F(X)D(X) = N(X). \quad (2)$$

Starting with (2) and differentiating t times with respect to X , the following results occur

$$\begin{aligned} F'D + FD' &= N' \\ F''D + 2F'D' + FD'' &= N'' \\ &\vdots \\ F^{(t)}D + tF^{(t-1)}D' + \dots + \binom{t}{t-m} F^{(m)}D^{(t-m)} \\ &\quad + \dots + FD^{(t)} = N^{(t)} \end{aligned} \quad (3)$$

where $\binom{t}{t-m}$ is the binomial coefficient, and X dependence is implicit. Equations (2) and (3) form a system of $t+1$ equations that can be used to determine the model coefficients.

If the frequency derivatives are known at only a single frequency X_0 , (2) and (3) can be simplified by replacing X by $X - X_0$ where $X - X_0$ represents the frequency deviation from X_0 . Then setting $D_0 = 1$, setting $t = n + d$, and defining $D = t + 1$, we have the following matrix equation for the unknown coefficients

$$[A][B] = [C] \quad (4)$$

where $A =$

$$\begin{bmatrix} 1 & 0 & \dots & \dots & 0 & 0 & 0 & \dots & 0 \\ 0 & 1 & \dots & \dots & 0 & -F_0 & 0 & \dots & 0 \\ 0 & 0 & 1 & \dots & 0 & -F_1 & -F_0 & \dots & 0 \\ \vdots & & & \ddots & \vdots & \vdots & \vdots & \ddots & \vdots \\ 0 & 0 & \dots & \dots & 1 & -F_{n-1} & -F_{n-2} & \dots & -F_{n-d} \\ 0 & 0 & \dots & \dots & 0 & -F_n & -F_{n-1} & \dots & -F_{n-d+1} \\ \vdots & & & \ddots & \vdots & \vdots & \vdots & \ddots & \vdots \\ 0 & 0 & \dots & \dots & 0 & -F_{D-2} & -F_{D-3} & \dots & -F_{D-d-1} \end{bmatrix} \quad (5)$$

$$B = [N_0 \ N_1 \ N_2 \ \dots \ N_n \ D_1 \ \dots \ D_d]^T \quad (6)$$

$$C = [F_0 \ F_1 \ F_2 \ \dots \ F_n \ F_{n+1} \ \dots \ F_{D-1}]^T \quad (7)$$

where $F_m = (1/m!)F^{(m)}(0)$ for $m = 0, 1, \dots, D-1$ and $F_m = 0$ when $m < 0$, F is regarded as a function of $(X - X_0)$, and the superscript T denotes the transpose of a row vector. By solving (4), we obtain the unknown coefficients.

If the frequency-derivative information is available at more than one frequency, then a more general matrix equation needs to be taken instead of (4). Let us consider a two-frequency model and choose sampling points at two frequencies X_1 and X_2 . If we have one frequency sample and n frequency-derivative samples at X_1 and one frequency sample and $d-1$ frequency-derivative samples at X_2 then the system of $n+d+1$ equations can be solved. In detail, (2) can be expanded as the

following equation at the first sampling point X_1

$$\begin{aligned} N_0 + N_1X_1 + N_2X_1^2 + \dots + N_nX_1^n \\ = (1 + D_1X_1 + D_2X_1^2 + \dots + D_dX_1^d)F(X_1) \\ = F(X_1) + D_1F(X_1)X_1 + D_2F(X_1)X_1^2 \\ + \dots + D_dF(X_1)X_1^d \end{aligned} \quad (8)$$

Similarly, (2) can be expanded as the following equation at the second sampling point X_2

$$\begin{aligned} N_0 + N_1X_2 + N_2X_2^2 + \dots + N_nX_2^n \\ = (1 + D_1X_2 + D_2X_2^2 + \dots + D_dX_2^d)F(X_2) \\ = F(X_2) + D_1F(X_2)X_2 + D_2F(X_2)X_2^2 \\ + \dots + D_dF(X_2)X_2^d \end{aligned} \quad (9)$$

Differentiating (8) n times with respect to X_1 and differentiating (9) $d-1$ times with respect to X_2 , we can obtain the following matrix equation to compute the unknown coefficients,

$$\begin{bmatrix} A_{M_1} & B_{M_1} \\ A_{M_2} & B_{M_2} \end{bmatrix} [C_M] = \begin{bmatrix} D_{M_1} \\ D_{M_2} \end{bmatrix} \quad (10)$$

where

$$A_{M_1} = \begin{bmatrix} 1 & X_1 & X_1^2 & \dots & X_1^n \\ 0 & 1 & 2X_1 & \dots & nX_1^{n-1} \\ \vdots & \vdots & \ddots & \vdots & \vdots \\ 0 & 0 & 0 & \dots & \frac{d^n}{dX_1^n} N(X_1) \end{bmatrix} \quad (11)$$

$$A_{M_2} = \begin{bmatrix} 1 & X_2 & X_2^2 & \dots & X_2^d \\ 0 & 1 & 2X_2 & \dots & nX_2^{n-1} \\ \vdots & \vdots & \ddots & \vdots & \vdots \\ 0 & 0 & 0 & \dots & \frac{d^{d-1}}{dX_2^{d-1}} N(X_2) \end{bmatrix} \quad (12)$$

$$B_{M_1} = \begin{bmatrix} -F(X_1)X_1 & \dots & -F(X_1)X_1^d \\ -\frac{d}{dX_1} \{F(X_1)X_1\} & \dots & -\frac{d}{dX_1} \{F(X_1)X_1^d\} \\ \vdots & \vdots & \vdots \\ -\frac{d^n}{dX_1^n} \{F(X_1)X_1\} & \dots & -\frac{d^n}{dX_1^n} \{F(X_1)X_1^d\} \end{bmatrix} \quad (13)$$

$$B_{M_2} = \begin{bmatrix} -F(X_2)X_2 & \dots & -F(X_2)X_2^d \\ -\frac{d}{dX_2} \{F(X_2)X_2\} & \dots & -\frac{d}{dX_2} \{F(X_2)X_2^d\} \\ \vdots & \vdots & \vdots \\ -\frac{d^{d-1}}{dX_2^{d-1}} \{F(X_2)X_2\} & \dots & -\frac{d^{d-1}}{dX_2^{d-1}} \{F(X_2)X_2^d\} \end{bmatrix} \quad (14)$$

$$C_M = [N_0 \ N_1 \ \dots \ N_n \ D_1 \ D_2 \ \dots \ D_d]^T \quad (15)$$

$$D_{M_1} = \left[F(X_1) \ \frac{d}{dX_1} F(X_1) \ \dots \ \frac{d^n}{dX_1^n} F(X_1) \right]^T \quad (16)$$

$$D_{M_2} = \left[F(X_2) \ \frac{d}{dX_2} F(X_2) \ \dots \ \frac{d^{d-1}}{dX_2^{d-1}} F(X_2) \right]^T \quad (17)$$

where the superscript T denotes the transpose of a row vector. By solving (10), we obtain the unknown coefficients.

B. Computing frequency derivatives in a method of moments model

Following the development in [16], one obtains the following moment equation

$$Z \vec{I} = \vec{V} \quad (18)$$

$$Z = \begin{bmatrix} Z_n^{tt} & Z_n^{t\phi} \\ Z_n^{\phi t} & Z_n^{\phi\phi} \end{bmatrix} \quad (19)$$

$$\vec{I} = \begin{bmatrix} I_n^{tq} \\ I_n^{\phi q} \end{bmatrix} \quad (20)$$

$$\vec{V} = \begin{bmatrix} V_n^{tq} \\ V_n^{\phi q} \end{bmatrix} \quad (21)$$

where Z , \vec{I} , and \vec{V} are the $N \times N$ moment matrix and current and voltage, $N \times 1$ column vectors respectively, and they are all functions of frequency through $k = \omega\sqrt{\mu\epsilon}$ where ω is the angular frequency.

In this work, surface currents are modeled by rational functions of frequency. In detail we assume that the i^{th} element of \vec{I} in (18) is $I_i(k)$ modeled by

$$I_i(k) = \frac{N(k)}{D(k)} = \frac{\sum_{j=0}^n N_j k^j}{\sum_{j=0}^d D_j k^j} \quad (22)$$

in which there are $n + d + 1$ coefficients (N_j 's and D_j 's) to be determined (assume that $D_0 = 1$). The N_j 's and D_j 's of (22) can be found when frequency and frequency-derivative samples at a certain frequency are available.

Starting with (18) and differentiating t times with respect to k , there results the following:

$$\begin{aligned} Z \vec{I} &= \vec{V} \\ Z' \vec{I} + Z \vec{I}' &= \vec{V}' \\ Z'' \vec{I} + 2Z' \vec{I}' + Z \vec{I}'' &= \vec{V}'' \\ &\vdots \\ Z^{(t)} \vec{I} + tZ^{(t-1)} \vec{I}' + \dots + \binom{t}{t-m} Z^{(m)} \vec{I}^{(t-m)} \\ &+ \dots + Z \vec{I}^{(t)} = \vec{V}^{(t)} \end{aligned} \quad (23)$$

where $\binom{t}{t-m}$ is the binomial coefficient and the k dependence is implicit. Solving the $(s+1)^{\text{th}}$ of matrix equations (23) for $\vec{I}^{(s)}$ in terms of $\vec{I}, \vec{I}'(1), \dots, \vec{I}^{(s-1)}$, we obtain

$$\begin{aligned} I_i^{(s)} &= \sum_{j=1}^N Y_{ij} \left[V_j^{(s)} - \sum_{m=1}^s \binom{s}{m} \right. \\ &\left. \times \left(\sum_{k=1}^N Z_{jk}^{(m)} I_k^{(s-m)} \right) \right], \quad s = 0, 1, \dots, t \end{aligned} \quad (24)$$

where $I_i^{(s)}$ is the s^{th} derivative with respect to k of the i^{th} element of \vec{I} and Y_{ij} is the ij^{th} element of Z^{-1} . The summation with respect to m in (24) is to be omitted when $s = 0$. The summation index k in (24) is not to be confused with $k = \omega\sqrt{\mu\epsilon}$. Note that the derivatives of the moment matrix and the excitation vector have to be expressed analytically before their numerical computation.

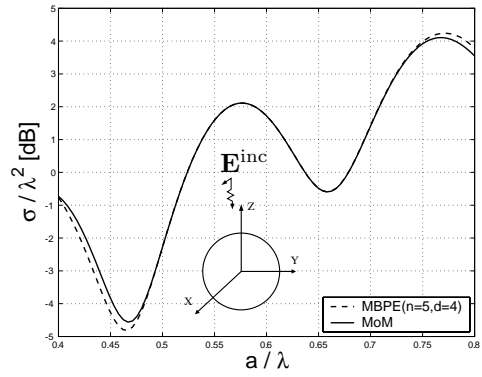


Fig. 1. Normalized RCS of a conducting sphere of radius a using MBPE ($n = 5$ and $d = 4$) and the MoM solution from $a/\lambda = 0.4$ to $a/\lambda = 0.8$. The sampling point of MBPE is at $a/\lambda = 0.6$.

III. NUMERICAL RESULTS

The results of applying MBPE to BOR using MoM are considered below. RCS calculations over frequency bands are done for a conducting sphere, a conducting spherical shell with a 5 degree hole and another with a 30 degree hole, a conducting finite circular cylinder of radius a and height $h (= 2a)$ with flat end faces, a conducting cone-sphere structure, and a conducting cylindrical container. The excitation is a plane wave axially incident. The numerical data obtained using MBPE are compared with the results calculated using the pointwise approach. All the computations reported below were done with a Pentium IV 2.0 Ghz computer.

Triangle and pulse basis functions are put on the generating curve of the conducting sphere in Figures 1 and 2 resulting in 61 unknown current coefficients.

Figure 1 shows two normalized RCS's, MoM and MBPE ($n = 5$ and $d = 4$). The MoM RCS is calculated by MoM at 100 equally spaced points from $a/\lambda = 0.4$ to $a/\lambda = 0.8$. The MBPE RCS is obtained by using information only at $a/\lambda = 0.6$. The MoM solutions for the RCS at the 100 points took 117 seconds of CPU time. On the other hand, the MBPE took 14 seconds of CPU time to obtain the RCS at the same points. The MBPE result agrees with the MoM result to within 1% error between $a/\lambda = 0.49$ and $a/\lambda = 0.73$. MBPE achieves 88% reduction compared to the MoM solution where the % reduction is defined by

$$\% \text{ reduction} = \frac{\text{MoM} - \text{MBPE}}{\text{MoM}} \times 100. \quad (25)$$

In Figure 2 both MBPE's use $n = 5$ and $d = 4$ in (22). The one-frequency MBPE in Figure 2 uses (22) and the first nine derivatives of (22). The two-frequency MBPE in Figure 2 uses (22) at both $a/\lambda = 0.5$ and $a/\lambda = 0.7$, the first four derivatives of (22) at $a/\lambda = 0.5$, and the first four derivatives of (22) at $a/\lambda = 0.7$. The one-frequency MBPE took 14 seconds of CPU time to compute the RCS at 100 equally spaced frequencies whereas the two-frequency MBPE took 27 seconds of CPU time to compute the RCS at the same 100 frequencies. The MoM solution, however, took 117 seconds. The one-frequency MBPE achieves 88% reduction whereas the two-frequency MBPE does 77% reduction. The former agrees with

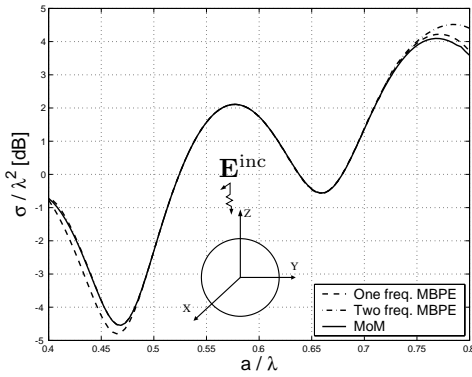


Fig. 2. Normalized RCS of a conducting sphere of radius a using the MoM solution, the one-frequency MBPE, and the two-frequency MBPE from $a/\lambda = 0.4$ to $a/\lambda = 0.8$. The sampling point of the one-frequency MBPE is at $a/\lambda = 0.6$ and the sampling points of the two-frequency MBPE are at $a/\lambda = 0.5$ and $a/\lambda = 0.7$.

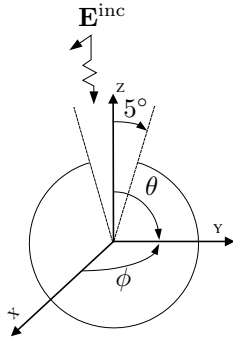


Fig. 3. Geometry of a conducting spherical shell of radius a with a 5 degree hole.

the MoM result to within 1% error between $a/\lambda = 0.49$ to $a/\lambda = 0.73$. On the other hand, the latter agrees with the MoM result to within 1% error between $a/\lambda = 0.43$ to $a/\lambda = 0.72$. In terms of the computational time, the former is less than the latter, but the latter shows better agreement at the low end of the frequency range.

For the demonstration purpose of indicating extremely sharp resonances, a conducting spherical shell of radius a with a 5 degree hole is considered in Figure 3.

In Figure 4, triangle and pulse basis functions are put on the generating curve of the spherical shell resulting in 61 unknown current coefficients. The RCS is calculated at 120 equally spaced points from $a/\lambda = 0.3$ to $a/\lambda = 0.5$. Figure 4 shows the normalized RCS in the vicinity of an extremely sharp resonance and the MBPE sampling point is at $a/\lambda = 0.4$. The MBPE indicates the extremely sharp resonance efficiently whereas MoM does not. MoM took 135 seconds of CPU time to compute the RCS at the 120 points. On the other hand, MBPE took only 15 seconds of CPU time to compute the RCS at the 120 points. As insinuated earlier, the conventional method requires an excessive number of closely spaced samples to obtain the extremely sharp resonance. In this example, although we took 120 equally spaced sampling points, MoM fails to indicate the extremely sharp resonance. An insert in Figure 4 shows MoM clearly indicates the extremely sharp resonance when 201 equally spaced points from $a/\lambda = 0.43$ to $a/\lambda = 0.44$ are

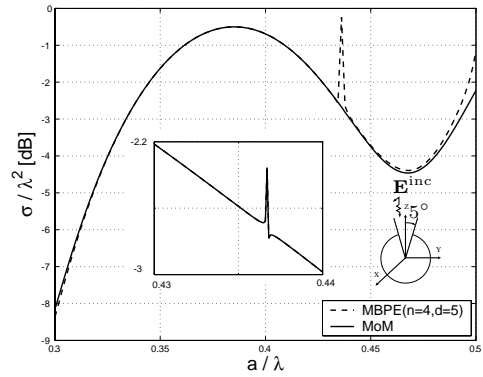


Fig. 4. Normalized RCS of a conducting spherical shell of radius a with a 5 degree hole using MBPE ($n = 4, d = 5$) and the MoM solution from $a/\lambda = 0.3$ to 0.5 . The sampling point is at $a/\lambda = 0.4$.

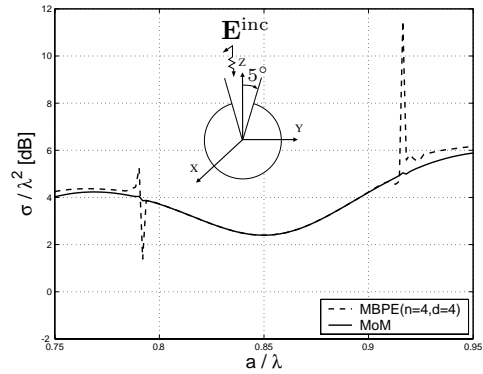


Fig. 5. Normalized RCS of a conducting spherical shell of radius a with a 5 degree hole using MBPE ($n = 4, d = 4$) and the MoM solution from $a/\lambda = 0.75$ to $a/\lambda = 0.95$. The sampling point is at $a/\lambda = 0.85$.

taken.

Figure 5 shows the normalized RCS in the vicinity of two extremely sharp resonances. The MBPE sampling point is at $a/\lambda = 0.85$. Triangle and pulse basis functions are put on the generating curve of the spherical shell resulting in 81 unknown current coefficients. The RCS is calculated at 120 equally spaced points from $a/\lambda = 0.75$ to $a/\lambda = 0.95$. The MBPE indicates two extremely sharp resonances at around $a/\lambda = 0.79$ and $a/\lambda = 0.92$. The MBPE curve adequately indicates the extremely sharp resonances and agrees to within 1% error between the extremely sharp resonances, but elsewhere it deviates from the MoM curve. MBPE took 26 seconds of CPU time to compute the RCS at the 120 points whereas MoM took 242 seconds of CPU time to compute the RCS at the same points, that is, MBPE obtains 89% reduction.

Figure 6 shows the geometry of a spherical shell of radius a with a 30 degree hole.

Figure 7 shows the normalized RCS using the one-frequency MBPE, the two-frequency MBPE, and MoM. Triangle and pulse basis functions are put on the generating curve of the spherical shell resulting in 41 unknown current coefficients. The RCS curves are calculated at 91 equally spaced points from $a/\lambda = 0.1$ to $a/\lambda = 0.4$. Both MBPE's use $n = 5$ and $d = 4$ in (22). The sampling point of the one-frequency MBPE is at $a/\lambda = 0.25$ and the sampling points of the two-frequency

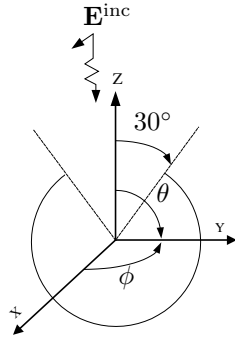


Fig. 6. Geometry of a conducting spherical shell of radius a with a 30 degree hole.

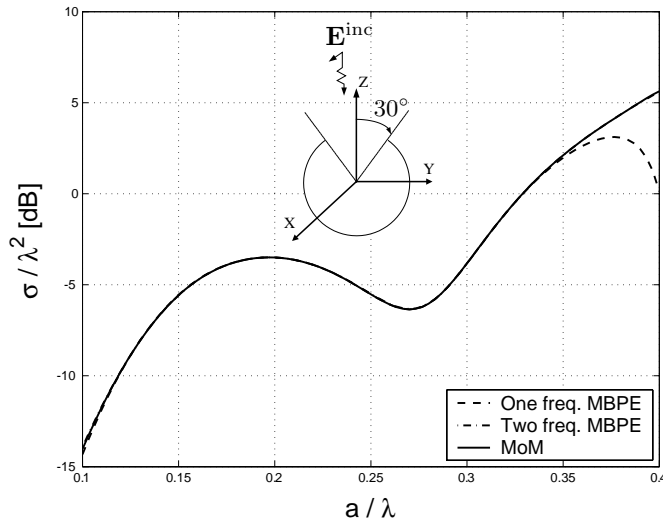


Fig. 7. Normalized RCS of a conducting spherical shell of radius a with a 30 degree hole using the one-frequency MBPE, the two-frequency MBPE, and MoM from $a/\lambda = 0.1$ to $a/\lambda = 0.4$. The sampling point of the one-frequency MBPE is at $a/\lambda = 0.25$ and the sampling points of the two-frequency MBPE are at $a/\lambda = 0.17$ and $a/\lambda = 0.35$.

MBPE are at $a/\lambda = 0.17$ and $a/\lambda = 0.35$. The one-frequency MBPE took 8 seconds of CPU time (83% reduction) and the two-frequency MBPE took 14 seconds of CPU time (70% reduction), whereas MoM took 47 seconds of CPU time. The two-frequency MBPE curve shows better agreement between $a/\lambda = 0.1$ and $a/\lambda = 0.4$ than the one-frequency MBPE curve.

Figure 8 shows the normalized RCS using the one-frequency MBPE, the two-frequency MBPE, and MoM. Triangle and pulse basis functions are put on the generating curve of the spherical shell resulting in 81 unknown current coefficients. The RCS curves are calculated at 121 equally spaced points from $a/\lambda = 0.35$ to $a/\lambda = 0.65$. Both MBPE's use $n = 4$ and $d = 5$ in (22). The sampling point of the one-frequency MBPE is at $a/\lambda = 0.5$ and the sampling points of the two-frequency MBPE are at $a/\lambda = 0.44$ and $a/\lambda = 0.59$. The one-frequency MBPE took 25 seconds of CPU time (89% reduction) and the two-frequency MBPE took 46 seconds of CPU time (80% reduction), whereas MoM took 229 seconds of CPU time. It can be seen that the two-frequency MBPE curve agrees with MoM to within 1% error between $a/\lambda = 0.39$ and $a/\lambda = 0.64$, whereas the one-frequency MBPE curve agrees with MoM to within 1% error only between $a/\lambda = 0.44$ and $a/\lambda = 0.57$.

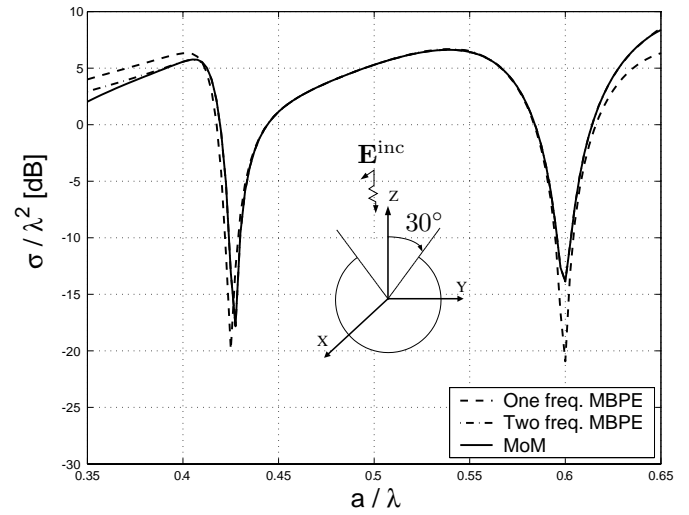


Fig. 8. Normalized RCS of a conducting spherical shell of radius a with a 30 degree hole using the one-frequency MBPE, the two-frequency MBPE, and MoM from $a/\lambda = 0.35$ to $a/\lambda = 0.65$. The sampling point of the one-frequency MBPE is at $a/\lambda = 0.5$ and the sampling points of the two-frequency MBPE are at $a/\lambda = 0.44$ and $a/\lambda = 0.59$.

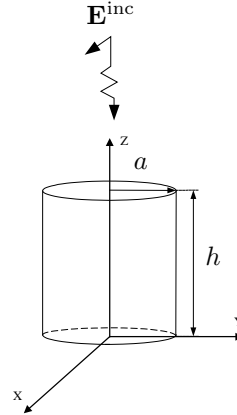


Fig. 9. Geometry of a conducting finite circular cylinder of radius a and height h with flat end faces.

Figure 9 shows the geometry of a conducting finite circular cylinder of radius a and height h .

Figure 10 shows the normalized RCS of a conducting finite circular cylinder of radius a and height $2a$ with flat end faces using the one-frequency MBPE, the two-frequency MBPE, and MoM. Triangle and pulse basis functions are put on the generating curve of the cylinder resulting in 81 unknown current coefficients. The RCS curves are calculated at 100 equally spaced points from $a/\lambda = 0.02$ to $a/\lambda = 0.4$. Both MBPE's use $n = 5$ and $d = 4$ in (22). The sampling point of the one-frequency MBPE is at $a/\lambda = 0.2$ and the sampling points of the two-frequency MBPE are at $a/\lambda = 0.1$ and $a/\lambda = 0.29$. The one-frequency MBPE took 25 seconds of CPU time (87% reduction) and the two-frequency MBPE took 46 seconds of CPU time (76% reduction), whereas MoM took 191 seconds of CPU time. The two-frequency MBPE curve shows slightly better agreement than the one-frequency MBPE curve especially around $a/\lambda = 0.02$.

Figure 11 shows the normalized RCS of the conducting finite circular cylinder of radius a and height $2a$ with flat end faces

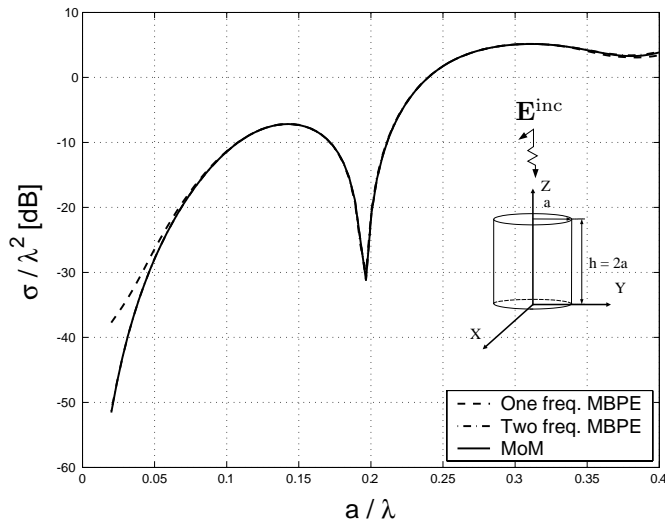


Fig. 10. Normalized RCS of a conducting finite circular cylinder of radius a and height $2a$ with flat end faces from $a/\lambda = 0.02$ to $a/\lambda = 0.4$. The sampling point of the one-frequency MBPE is at $a/\lambda = 0.2$ and the sampling points of the two-frequency MBPE are at $a/\lambda = 0.1$ and $a/\lambda = 0.29$.

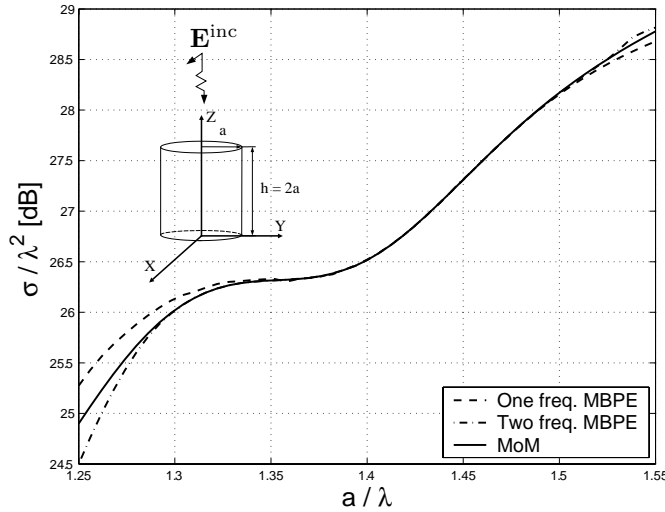


Fig. 11. Normalized RCS of the conducting finite circular cylinder of radius a and height $2a$ with flat end faces from $a/\lambda = 1.25$ to $a/\lambda = 1.55$. The sampling point of the one-frequency MBPE is at $a/\lambda = 1.4$ and the sampling points of the two-frequency MBPE are at $a/\lambda = 1.32$ and $a/\lambda = 1.46$.

in a higher frequency band using the one-frequency MBPE, the two-frequency MBPE, and MoM. Triangle and pulse basis functions are put on the generating curve of the cylinder resulting in 201 unknown current coefficients. The RCS curves are calculated at 100 equally spaced points from $a/\lambda = 1.25$ to $a/\lambda = 1.55$. Both MBPE's use $n = 5$ and $d = 4$ in (22). The sampling point of the one-frequency MBPE is at $a/\lambda = 1.4$ and the sampling points of the two-frequency MBPE are at $a/\lambda = 1.32$ and $a/\lambda = 1.46$. The one-frequency MBPE took 153 seconds of CPU time (88% reduction) and the two-frequency MBPE took 291 seconds of CPU time (77% reduction), whereas MoM took 1289 seconds of CPU time. The two-frequency MBPE curve shows slightly better agreement between $a/\lambda = 1.25$ and $a/\lambda = 1.55$ than the one-frequency MBPE curve.

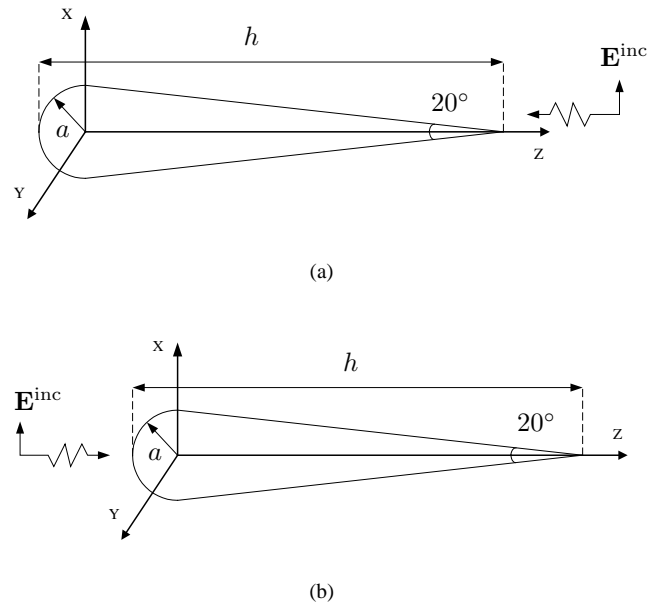


Fig. 12. Geometry of a cone-sphere structure illuminated by a plane wave which is axially incident and propagates either (a) from the cone tip toward the spherical cap or (b) from the spherical cap toward the cone tip.

Figure 12 shows the geometry of a cone-sphere structure illuminated by a plane wave which is axially incident and propagates either from the cone tip toward the spherical cap or from the spherical cap toward the cone tip.

Figure 13 shows the normalized RCS of the cone-sphere in Figure 12(a) using the one-frequency MBPE, the two-frequency MBPE, and MoM. The incident wave propagates from the cone tip toward the spherical cap. Triangle and pulse basis functions are put on the generating curve of the cone-sphere resulting in 61 unknown current coefficients. The RCS curves are calculated at 100 equally spaced points from $a/\lambda = 0.02$ to $a/\lambda = 0.4$. Both MBPE's use $n = 5$ and $d = 4$ in (22). The sampling point of the one-frequency MBPE is at $a/\lambda = 0.2$ and the sampling points of the two-frequency MBPE are at $a/\lambda = 0.14$ and $a/\lambda = 0.26$. The one-frequency MBPE took 14 seconds of CPU time (89% reduction) and the two-frequency MBPE took 26 seconds of CPU time (79% reduction), whereas MoM took 124 seconds of CPU time. The two-frequency MBPE curve agrees with MoM to within 1% error between $a/\lambda = 0.08$ and $a/\lambda = 0.32$, whereas the one-frequency MBPE curve agrees with MoM to within 1% error between $a/\lambda = 0.16$ and $a/\lambda = 0.24$.

Figure 14 shows the normalized RCS of the cone-sphere structure in Figure 12(b) using the one-frequency MBPE, the two-frequency MBPE, and MoM. The incident wave propagates from the spherical cap toward the cone tip. Triangle and pulse basis functions are put on the generating curve of the cone-sphere resulting in 61 unknown current coefficients. The RCS curves are calculated at 100 equally spaced points from $a/\lambda = 0.02$ to $a/\lambda = 0.4$. Both MBPE's use $n = 5$ and $d = 4$ in (22). The sampling point of the one-frequency MBPE is at $a/\lambda = 0.2$ and the sampling points of the two-frequency MBPE are at $a/\lambda = 0.14$ and $a/\lambda = 0.26$. The one-frequency

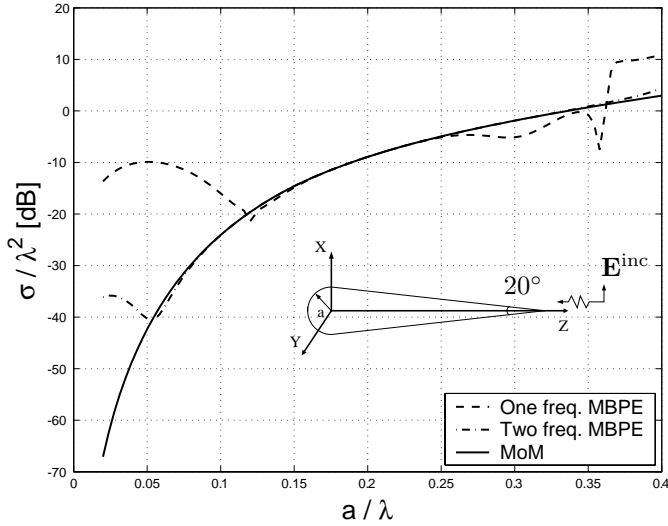


Fig. 13. Normalized RCS of a cone-sphere structure illuminated by a plane wave which is axially incident and propagates from the cone tip toward the spherical cap between $a/\lambda = 0.02$ and $a/\lambda = 0.4$. The sampling point of the one-frequency MBPE is at $a/\lambda = 0.2$ and the sampling points of the two-frequency MBPE are at $a/\lambda = 0.14$ and $a/\lambda = 0.26$.

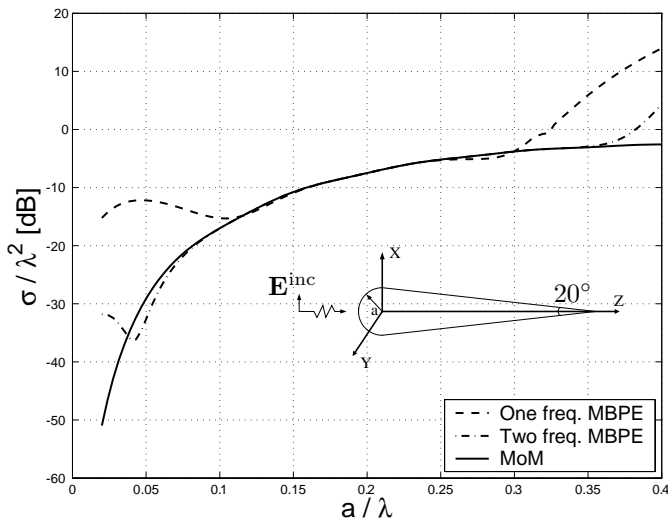


Fig. 14. Normalized RCS of a cone-sphere structure illuminated by a plane wave which is axially incident and propagates from the spherical cap toward the cone tip between $a/\lambda = 0.02$ and $a/\lambda = 0.4$. The sampling point of the one-frequency MBPE is at $a/\lambda = 0.2$ and the sampling points of the two-frequency MBPE are at $a/\lambda = 0.14$ and $a/\lambda = 0.26$.

MBPE took 14 seconds of CPU time (89% reduction) and the two-frequency MBPE took 26 seconds of CPU time (79% reduction), whereas MoM took 124 seconds of CPU time. The two-frequency MBPE curve agrees with MoM to within 1% error between $a/\lambda = 0.08$ and $a/\lambda = 0.34$, whereas the one-frequency MBPE curve agrees with MoM to within 1% error between $a/\lambda = 0.15$ and $a/\lambda = 0.24$.

Figure 15 shows the geometry of a conducting cylindrical container of outside diameter a , inside diameter $\frac{2}{3}a$, height $3a$, and thickness $\frac{1}{3}a$.

Figure 16 shows the normalized RCS of the conducting cylindrical container by using the one-frequency MBPE, the two-frequency MBPE, and MoM. Triangle and pulse basis

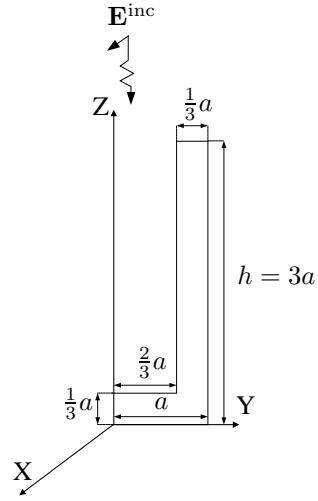


Fig. 15. Geometry of a conducting cylindrical container of outside diameter a , inside diameter $\frac{2}{3}a$, height $3a$, and thickness $\frac{1}{3}a$.

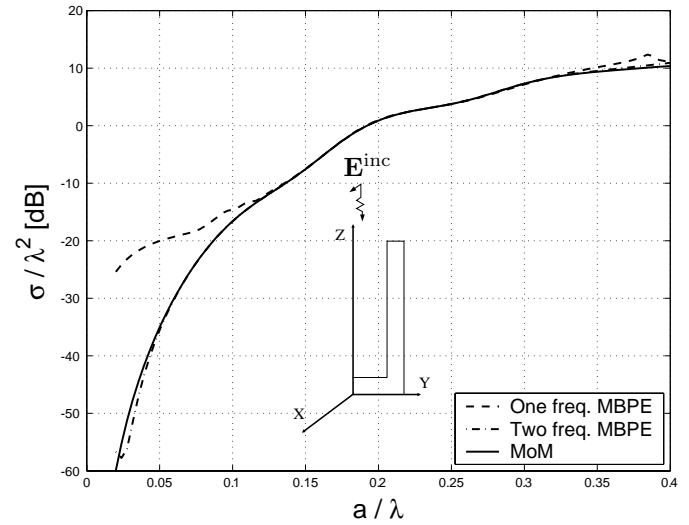


Fig. 16. Normalized RCS of a conducting cylindrical container from $a/\lambda = 0.02$ to $a/\lambda = 0.4$. The sampling point of the one-frequency MBPE is at $a/\lambda = 0.2$ and the sampling points of the two-frequency MBPE are at $a/\lambda = 0.12$ and $a/\lambda = 0.28$.

functions are put on the generating curve of the container resulting in 93 unknown current coefficients. The RCS curves are calculated at 100 equally spaced points from $a/\lambda = 0.02$ to $a/\lambda = 0.4$. Both MBPE's use $n = 5$ and $d = 4$ in (22). The sampling point of the one-frequency MBPE is at $a/\lambda = 0.2$ and the sampling points of the two-frequency MBPE are at $a/\lambda = 0.12$ and $a/\lambda = 0.28$. The one-frequency MBPE took 34 seconds of CPU time (88% reduction) and the two-frequency MBPE took 63 seconds of CPU time (78% reduction), whereas MoM took 289 seconds of CPU time. The two-frequency MBPE curve agrees with MoM to within 1% error between $a/\lambda = 0.05$ and $a/\lambda = 0.35$, whereas the one-frequency MBPE curve agrees with MoM to within 1% error between $a/\lambda = 0.14$ and $a/\lambda = 0.26$.

IV. CONCLUSIONS

An implementation of MBPE for the BOR using MoM in the frequency domain is presented. The RCS for various PEC objects such as a sphere, a spherical shell with a 5 degree hole or with a 30 degree hole, a finite cylinder with flat end faces, a cone-sphere structure, and a conducting cylindrical container are computed and compared with the MoM solutions over frequency bands. Instead of using a pointwise approach, a rational function model is used to approximate the induced surface as a function of frequency. The model coefficients are computed using frequency and frequency-derivative information at one frequency in the band or alternatively at two frequencies in the band. Sample results show the MBPE approach gives excellent results over a limited frequency band, and is much more efficient than the conventional pointwise approach.

As seen in numerical results, the two-frequency MBPE gives better agreement than the one-frequency MBPE in terms of accuracy although a rational function of the same order is used. But the former requires adjustment at two sampling points to obtain the best results, whereas the latter does not.

Even though a higher order model generally gives a better approximation, careful treatment of the model is required. For instance, high order ($n + d \geq 7$) derivatives in the one-frequency MBPE make the sampling matrices ill-conditioned. To avoid this problem, use of the two-frequency MBPE with the same order model is recommended.

Note that the E-field solution fails to provide a unique solution for the current on a conducting body at any resonant frequency of the region enclosed by the conducting surface of the body. Thus, if a sampling point of the MBPE is accidentally at or in the vicinity of a resonant frequency, the results would not be reliable. This problem is more likely to occur when the MBPE is applied to an electrically very large body. Because an electrically large body has resonant frequencies that are close together, wherever a sampling point is chosen it is likely to be in the vicinity of an internal resonant frequency. The problem can be avoided by using the combined field solution instead of the E-field solution. The combined field solution uses a linear combination of the E-field and H-field integral equations. When the combined field solution is used, the MBPE will not incur loss of accuracy caused by proximity to an internal resonant frequency.

REFERENCES

- [1] G. J. Burke and E. K. Miller, "Use of frequency-derivative information to reconstruct an electromagnetic transfer function," *Proceedings of the fourth annual ACES review*, Naval Postgraduate School, Monterey, CA, Mar. 1988.
- [2] G. J. Burke, E. K. Miller, S. Chakrabarti, and K. Demarest, "Using model-based parameter estimation to increase the efficiency of computing electromagnetic transfer functions," *IEEE Trans. Magnetics*, vol. 25, no. 4, pp. 2807–2809, July 1989.
- [3] K. R. Demarest, E. K. Miller, K. Kalbasi, and L. K. Wu, "A computationally efficient method of evaluating Green's functions for 1-, 2-, and 3-D enclosures," *IEEE Trans. Magnetics*, vol. 25, no. 4, pp. 2878–2880, July 1989.
- [4] X. Yang and E. Arvas, "Resonance region scattering," Final technical report, RADC-TR-90-1, Rome Air Development Center, Griffiss Air Force base, NY 13441, USA, Mar. 1990.
- [5] X. Yang and E. Arvas, "Use of frequency-derivative information in two-dimensional electromagnetic scattering problems," *Proc. Inst. Elect. Eng.*, pt. H, vol. 138, no. 4, pp. 269–272, Aug. 1991.

- [6] C. J. Reddy, M. D. Deshpande, C. R. Cockrell, and F. B. Beck, "Fast RCS computation over a frequency band using method of moments in conjunction with asymptotic waveform evaluation technique," *IEEE Trans. Antennas Propagat.*, vol. 46, no. 8, pp. 1229–1233, Aug. 1998.
- [7] C. J. Reddy, "Application of model based parameter estimation for RCS frequency response calculations using method of moments," Contractor Report, NASA/CR-1998-206951, Hampton University, Hampton, VA 23668, Mar. 1998.
- [8] K. Kottapalli, T. K. Sarkar, Y. Hua, E. K. Miller, and G. J. Burke, "Accurate computation of wide-band response of electromagnetic systems utilizing narrow-band information," *IEEE Trans. Microwave Theory Tech.*, vol. 39, no. 4, pp. 682–687, Apr. 1991.
- [9] M. G. Andreasen, "Scattering from bodies of revolution," *IEEE Trans. Antennas Propagat.*, vol. AP-13, pp. 303–310, Mar. 1965.
- [10] J. R. Mautz and R. F. Harrington, "Generalized network parameters for bodies of revolution," Technical Report TR-68-7, Syracuse University, Syracuse, NY 13244, June 1968.
- [11] J. R. Mautz and R. F. Harrington, "Radiation and scattering from bodies of revolution," *Appl. Sci. Res.*, vol. 20, pp. 405–435, June 1969.
- [12] J. R. Mautz and R. F. Harrington, "H-field, E-field, and combined field solutions for bodies of revolution," *AEÜ*, vol. 32, pp. 157–164, Apr. 1978.
- [13] J. R. Mautz and R. F. Harrington, "Computer programs for H-field, E-field, and combined field solutions for bodies of revolution," Technical Report, TR-77-3, Syracuse University, Syracuse, NY 13244, May 1977.
- [14] J. R. Mautz and R. F. Harrington, "A combined-source solution for radiation and scattering from a perfectly conducting body," *IEEE Trans. Antennas Propagat.*, vol. AP-27, pp. 445–454, July 1979.
- [15] A. W. Glisson and D. R. Wilton, "Simple and efficient numerical methods for problems of electromagnetic radiation and scattering from surfaces," *IEEE Trans. Antennas Propagat.*, vol. AP-28, no. 5, pp. 593–603, Sept. 1980.
- [16] J. R. Mautz and R. F. Harrington, "An improved E-field solution for a conducting body of revolution," *AEÜ*, vol. 36, pp. 198–206, May 1982.

Hyunwung Son was born in Busan, Korea, in 1972. He received the B.S. degree in electronics engineering from Kyunghee University, Korea, in 1997 and the M.S. and Ph.D. degrees in electrical engineering from Syracuse University, Syracuse, NY, in 2000 and 2003, respectively.

He is currently a Senior Research Engineer in LG Electronics, Seoul, Korea. His current research interests include numerical electromagnetics, radiation, scattering, antenna design, and microwave circuits and devices.

Joseph. R. Mautz was born in Syracuse, NY, in 1939. He received the B.S., M.S., and Ph.D. degrees in electrical engineering from Syracuse University, Syracuse, NY, in 1961, 1965, and 1969, respectively.

Until July 1993, he was a Research Associate in the Department of Electrical and Computer Engineering of Syracuse University, working on radiation and scattering problems. His primary fields of interest are electromagnetic theory and applied mathematics. He is presently an adjacent professor in the Department of Electrical Engineering and Computer Science, Syracuse University.

Ercument Arvas received the B.S. and M.S. degrees from METU, Ankara, Turkey, in 1976 and 1979, respectively, and the Ph.D. degree from Syracuse University, Syracuse, NY, in 1983, all in electrical engineering.

From 1984 to 1987, he was with the Electrical Engineering Department, Rochester Institute of Technology, Rochester, NY. He joined the Department of Electrical Engineering and Computer Science, Syracuse University, in 1987, where he is currently a Professor. His research interests include numerical electromagnetics, antennas, and microwave circuits and devices.

Triangular Grids: A Review of Resonator and Waveguide Analysis with Classical FIT and Some Reflections on Yee-like FIT- and FEM-Schemes

URSULA VAN RIENEN

Institute of General Electrical Engineering

Rostock University

D-18051 Rostock, Germany

ursula.van-rienen@ettechnik.uni-rostock.de

Abstract—The focus of this paper is on the solution of Maxwell's equations on triangular orthogonal grids for time-harmonic fields in cylindrically symmetric resonators and general time dependant fields in length-homogeneous waveguides, respectively. The method is based on the Finite Integration Technique (FIT) [1], [2]. The 2D simulation on a structured triangular grid combines the advantages of FIT, as e.g. the consistency of the method or the numerical advantage of banded system matrices, with the geometrical flexibility of non-coordinate grids. FIT on triangular grids was first introduced in [3], [4]¹. This paper presents a review describing the underlying theory in FIT operator notation first introduced in [2] and puts this classical approach for FIT on triangular grids in relation to actual research in the field.

I. CLASSICAL FINITE INTEGRATION TECHNIQUE ON A STRUCTURED TRIANGULAR GRID

The Finite Integration Technique solves Maxwell's equations on a pair of dual grids. Actual implementations generally work on a rectangular two- or three-dimensional domain Ω . Sometimes the field-carrying domain Ω_s is only a sub-domain of the domain Ω : $\Omega = \Omega_s \cup \Omega_o$. The solution domain might be composed of several subregions: $\Omega_s = \cup_i \Omega_{s_i}$. Discretization on Ω rather than on Ω_s has the advantage of allowing for higher topological regularity leading to matrices with regular (band) pattern. Usually Ω_o , the overhead, is relatively small.

FIT yields an *exact* representation of Maxwell's equations in integral form on a grid duplet (G, \tilde{G}) , denoted as *Maxwell-Grid-Equations*:

$$\begin{aligned} \mathbf{C}\hat{\mathbf{e}} &= -\frac{\partial}{\partial t}\hat{\mathbf{b}}, & \mathbf{S}\hat{\mathbf{b}} &= \mathbf{0}, \\ \tilde{\mathbf{C}}\hat{\mathbf{h}} &= \frac{\partial}{\partial t}\hat{\mathbf{d}} + \hat{\mathbf{j}}, & \tilde{\mathbf{S}}\hat{\mathbf{d}} &= \mathbf{q}. \end{aligned} \quad (1)$$

The linear operators \mathbf{C} , $\tilde{\mathbf{C}}$, \mathbf{S} and $\tilde{\mathbf{S}}$, the so-called grid voltages $\hat{\mathbf{e}}$ and $\hat{\mathbf{h}}$ as well as the grid fluxes $\hat{\mathbf{b}}$, $\hat{\mathbf{d}}$ and $\hat{\mathbf{j}}$ and the charge vector \mathbf{q} will be introduced below.

Talking of an *exact* representation relates to the discretization error. The topic of errors is treated in more detail in the next subsection.

The FIT grid duplet (G, \tilde{G}) is not necessarily coordinate-bounded, not necessarily orthogonal, not necessarily regular. Often the solution domain Ω_s possesses symmetries or some geometrical invariance such that the 3D problem may be reduced to a 2D problem by appropriate variable separation. For example, this is the case for cylindrically symmetric resonators and longitudinally invariant waveguides as treated in this paper.

The linear operators \mathbf{C} , $\tilde{\mathbf{C}}$, \mathbf{S} and $\tilde{\mathbf{S}}$ in (1) can be interpreted as discrete curl operators \mathbf{C} , $\tilde{\mathbf{C}}$, discrete divergence \mathbf{S} , $\tilde{\mathbf{S}}$ and discrete gradient operators $\mathbf{G} = -\tilde{\mathbf{S}}^T$, $\tilde{\mathbf{G}} = -\mathbf{S}^T$. The discrete operators fulfill the following key properties

$$\begin{aligned} \mathbf{C} &= \tilde{\mathbf{C}}^T, & (2) \\ \mathbf{S}\mathbf{C} = \tilde{\mathbf{S}}\tilde{\mathbf{C}} &= \mathbf{0}, & (3) \end{aligned}$$

as generally shown in [2]. These equations, especially that the transpose $\tilde{\mathbf{C}}^T$ of the dual curl operator equals the primary curl operator \mathbf{C} , represent a topological property resulting from the duality of the grids. For further analytical and algebraic properties resulting from these basic equations the reader is referred e.g. to [2], [5] and [6]. Conservation of energy is just one of the continuous laws for which a proof can be given for the discrete FIT equations, too.

The vectors $\hat{\mathbf{e}}$, $\hat{\mathbf{h}}$, etc. hold scalar state variables defined as field integrals along edges L_i, \tilde{L}_i and across facets A_i, \tilde{A}_i , yielding the so-called *grid voltages* $\hat{\mathbf{e}}$, $\hat{\mathbf{h}}$ and *grid fluxes* $\hat{\mathbf{b}}$, $\hat{\mathbf{d}}$, $\hat{\mathbf{j}}$ on the primary grid G and the dual grid \tilde{G} , respectively:

$$\begin{aligned} \hat{e}_i &= \int_{L_i} \mathbf{E} \cdot d\mathbf{s}, & \hat{b}_i &= \int_{A_i} \mathbf{B} \cdot d\mathbf{A}, \\ \hat{h}_i &= \int_{\tilde{L}_i} \mathbf{H} \cdot d\mathbf{s}, & \hat{d}_i &= \int_{\tilde{A}_i} \mathbf{D} \cdot d\mathbf{A}, \\ & & \hat{j}_i &= \int_{\tilde{A}_i} \mathbf{J} \cdot d\mathbf{A}. \end{aligned} \quad (4)$$

The vector \mathbf{q} holds discrete grid charges q_i which are allocated in the points (nodes) of the primary grid G and are defined as a volume integral over the space charge ρ contained in the surrounding dual grid volume \tilde{V}_i :

$$q_i = \int_{\tilde{V}_i} \rho dV. \quad (5)$$

¹URMEL-T is the resonator and waveguide code based on the classical FIT on triangular grids described here.

With these definitions it is straightforward to derive the discrete form of Maxwell's equations for a given FIT grid duplet (G, \tilde{G}) . It will be shown for a 2D triangular grid G with hexagonal dual grid \tilde{G} in subsection I-A.

The choice of a specific grid is mainly influenced by the following aspects which have to be balanced well:

- 1) a good approximation of the boundary $\partial\Omega_s$ with as few grid points as possible in order to decrease the spatial discretization error while keeping memory requirements as small as possible,
- 2) a most regular grid in order to decrease the condition of the resulting linear or eigenvalue systems yielding a smaller iterative convergence error and/or faster convergence speed,
- 3) a fast and robust grid generation for arbitrary domains Ω_s , especially those with $\Omega_s = \cup_i \Omega_{s_i}$.

There are many more aspects influencing the solution quality which are out of the focus of this paper which concentrates on some basic issues.

Among several types of grids on which FIT has been implemented until today there were first a 2D [1] and later a 3D [2] Cartesian grid allowing for diagonal filling in order to avoid the 'staircase' approximation still usual in FDTD. This grid is easy to implement but good convergence can not always be reached depending on the specific boundary shape of $\partial\Omega_s$. This gave reason to implement FIT on the regular triangular grid [3] described in this paper which achieves good boundary approximations with rather few grid points. Other examples are the non-orthogonal second order convergent quadrangular 3D grid described in [6] and the so-called Conformal FIT (briefly CFIT) [7], on Cartesian grids, also being second order accurate but numerically less expensive. All of these specific grids have their pro's and con's regarding the aspects described above.

A. The Triangular Grid and its Dual Grid

In the following, we describe an application of FIT on a structured 2D triangular grid. The method has been implemented in the URMEL-T code [3]. This may be used for longitudinal and transversal eigenmode computation in cylindrically symmetric resonators and for studies of waves excited in longitudinally invariant waveguides. Often, this 2D code is used in design studies in combination with a 3D code, see e.g. [8]. Also, 2D computations may be used for the simulation of the rf properties of cylindrically symmetric subsections of complex structures when methods using the scattering matrix formulations are applied, see e.g. [9] or [10].

Without loss of generality it is assumed that the electric voltages are allocated on the triangular grid G and the magnetic voltages on the dual grid \tilde{G} (see [4] for special details on the alternative allocation). The mesh generator starts off with a regular triangulation for Ω which is as close as possible to an equilateral triangulation (cf. Fig 3 in subsection III-A). Then, grid points are moved onto the

boundary $\partial\Omega_s$ resp. boundaries $\partial\Omega_{s_i}$ for $\Omega_s = \cup_i \Omega_{s_i}$, i.e. for solution domains which consist out of several subregions Ω_{s_i} . Finally the triangulation of Ω is equilibrated.

For the equilibration all grid points are taken as mass points and all edges as springs. Then, the goal is to find an equilibrium, i.e. to minimize the potential which corresponds to the distance squared. The elastic force of a spring is given by Hooke's law $\mathbf{F} = -k\mathbf{r}$ where \mathbf{r} is the displacement from equilibrium $\mathbf{r} = 0$ and k is the spring constant. The potential energy of motion on a straight line through $\mathbf{r} = 0$ is given by

$$E_{pot}(s) = \frac{1}{2}ks^2 \quad (6)$$

where s corresponds to the distance of two grid points and k is chosen to be $k = 1$ for all points. Points on the boundaries $\partial\Omega$ of the mesh and $\partial\Omega_s$ or $\partial\Omega_{s_i}$, respectively, of the solution domain(s) need a special treatment. The coordinates can be treated one after the other. For each coordinate, a sparse linear system of equations results from (6) and is solved iteratively. Remaining obtuse triangles are searched for. In some typical cases they can be individually transformed into acute triangles, too. Details on this algorithm may be found in [13].

Optimally, the mesh generator can set up the completely orthogonal dual grid \tilde{G}_\perp composed of the perpendicular bisectors of the elementary lines L_i . The intersections of the perpendicular bisectors, the circumcenters, give the dual grid points \tilde{P}_i . Its elementary areas \tilde{A}_i in the grid plane are general hexagons, cf. Fig. 1. In the construction of the material operators also areas normal to the (x, y) -grid plane are needed thus a *virtual* mesh extends for $\pm\Delta z/2$ in the longitudinal z -direction for the waveguide case as displayed in Fig. 2 and for $\pm\Delta\varphi/2$ in the azimuthal φ -direction for the resonator case, respectively.

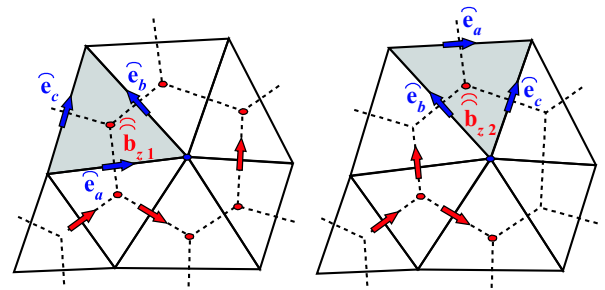


Fig. 1. Classical triangular FIT grid with its dual (hexagonal) grid, and some of the electric and magnetic state variables. The two kinds of primary cells (vertex up and vertex down) associated to each grid point are highlighted each. (This illustration refers to the waveguide case, i.e. (x, y, z) -coordinates. For the resonator case, i.e. (r, φ, z) -coordinates, \hat{b}_{z1} and \hat{b}_{z2} just have to be replaced by $\hat{b}_{\varphi1}$ and $\hat{b}_{\varphi2}$, respectively)

\tilde{G}_\perp is a Delaunay-Voronoi mesh for the complete domain Ω . For this dual-orthogonal FIT grid the continuity of tangential electric field and normal magnetic flux is preserved on all inner boundaries $\partial\Omega_{s_i}$ of different materials within Ω_s .

Only if all triangles of the grid G inside Ω_s are acute or right-angled all grid points \tilde{P}_i of the dual grid \tilde{G}_\perp lie inside

the i -th triangle. It may well happen that obtuse triangles occur near the boundary of Ω_s some of which remain after equilibration of the grid. In that case the circumcenters are chosen for \tilde{P}_i in all acute triangles and barycenters in the (usually very few, cf. subsection III-C) obtuse triangles. Then, the approximation order p is locally reduced to first order, overall p typically still has a value close (but smaller than) two as described below.

B. The Grid Operators on the Triangular Grid

In the previous section the *Maxwell-Grid-Equations* (1) were generally defined. Now we will deal with some of the grid operators on the triangular grid. Special interest is laid on the material operators.

1) *The curl- and divergence operators:* As an example for the derivation of the Maxwell-Grid-Equations on the orthogonal triangular grid we will first regard Faraday's law. With the notations as in Fig. 1 we get:

$$\hat{e}_a + \hat{e}_b - \hat{e}_c = -\frac{\partial}{\partial t} \hat{b}_{z1}, \quad (7)$$

$$-\hat{e}_a - \hat{e}_b + \hat{e}_c = -\frac{\partial}{\partial t} \hat{b}_{z2}. \quad (8)$$

Since there are only grid voltages and fluxes, the time derivative and a linear combination with factors ± 1 this is an *exact* representation of Faraday's law on the primary cell, i.e. the discretization error is zero per definitionem.

Collecting all voltages and fluxes in the vectors $\hat{\mathbf{e}}$ and $\hat{\mathbf{b}}$ and the incidences in the matrix \mathbf{C} yields Faraday's equation on the grid as presented in (1).

Integration of Coulomb's law takes place over the surface of a prism the base of which is indicated by the dotted line in Fig. 1. One of its side faces is depicted in Fig. 2. The flux \hat{d}_z is allocated in the middle of the hexagonal's base while $\hat{d}_{z\text{back}}$ and $\hat{d}_{z\text{front}}$ lie $\pm \Delta z/2$ apart in the virtual grid in z -direction and may be determined from \hat{d}_z via (17). Then, for Coulomb's law we get:

$$\begin{aligned} -\hat{d}_{a\text{left}} + \hat{d}_{a\text{right}} - \hat{d}_{b\text{bottom}} + \hat{d}_{b\text{top}} \\ -\hat{d}_{c\text{bottom}} + \hat{d}_{c\text{top}} - \hat{d}_{z\text{back}} + \hat{d}_{z\text{front}} = q. \end{aligned} \quad (9)$$

The fluxes are collected in the vector $\hat{\mathbf{d}}$, charges in a vector \mathbf{q} and the incidences in the matrix $\tilde{\mathbf{S}}$ yielding Coulomb's law as presented in (1).

The set-up of $\tilde{\mathbf{C}}$ and \mathbf{S} is done analogously just on the other grid, each. The discrete curl operators \mathbf{C} and $\tilde{\mathbf{C}}$ and the discrete divergence operators \mathbf{S} and $\tilde{\mathbf{S}}$ obviously reflect the topology of the triangular (primary) grid, its dual hexagonal grid and the enumeration. See [11] for more details.

2) *The material operators:* In order to derive a discrete equivalent of the constitutive laws we need to find a linear map between grid voltages and fluxes:

$$\hat{\mathbf{d}} = \mathbf{M}_\epsilon \hat{\mathbf{e}}, \quad \hat{\mathbf{b}} = \mathbf{M}_\mu \hat{\mathbf{h}}, \quad \hat{\mathbf{j}} = \mathbf{M}_\sigma \hat{\mathbf{e}}. \quad (10)$$

In Ω_s we assume loss free material, i.e. ϵ, μ and σ are real. Here the conductivity is assumed to be equal to zero (except for the perfect conductor material).

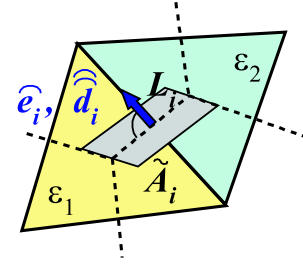


Fig. 2. Classical triangular FIT grid with its dual (hexagonal) grid: Zoom to some dual grid area \tilde{A}_i normal to primary grid plane. The area \tilde{A}_i and the path length L_i are used for material averaging.

In classical FIT, the *material operators* $\mathbf{M}_\epsilon, \mathbf{M}_\mu$ and \mathbf{M}_σ are determined by local averaging of material quantities. This is motivated as follows: Let us regard the dual grid area \tilde{A}_i depicted in Fig. 2. The primary edge L_i perpendicularly intersects \tilde{A}_i . The electric voltage \hat{e}_i along the edge and the electric flux \hat{d}_i through the area are defined as in (4). They are collinear. We may approximate both integrals with help of some *virtual* constant mean value e_i . For \hat{e}_i , we directly get

$$\begin{aligned} \hat{e}_i &= \int_{L_i} \mathbf{E}(\mathbf{r}) \cdot d\mathbf{s} \\ &= (e_i + O(L_i^m)) \int_{L_i} ds \\ &= e_i \cdot L_i + O(L_i^m). \end{aligned} \quad (11)$$

Obviously, this is the moment when the introduction of some discretization error gets unavoidable. The local approximation order m is $m = 2$ if e_i is exactly allocated in the middle point of L_i .

In order to get a similar expression for \hat{d}_i we have to deal with the fact that the dual area \tilde{A}_i intersects several triangles, i.e. primary cells, which all may be filled with different material. For the topological regular grid treated here we have the case shown in Fig. 2 where two cells are intersecting and secondly that one of six intersected triangles indicated by the dotted lines in Fig. 1. So, we introduce an effective permittivity

$$\epsilon_{\text{eff},i} = \frac{1}{\tilde{A}_i} \int_{\tilde{A}_i} \epsilon(\mathbf{r}) dA. \quad (12)$$

Then, we receive the following expression for \hat{d}_i

$$\begin{aligned} \hat{d}_i &= \int_{\tilde{A}_i} \mathbf{D}(\mathbf{r}) \cdot d\mathbf{A} = \int_{\tilde{A}_i} \epsilon(\mathbf{r}) \mathbf{E}(\mathbf{r}) \cdot d\mathbf{A} \\ &= (e_i + O(\tilde{A}_i^n)) \int_{\tilde{A}_i} \epsilon(\mathbf{r}) dA \\ &= \epsilon_{\text{eff},i} \cdot e_i \cdot \tilde{A}_i + O(\tilde{A}_i^n). \end{aligned} \quad (13)$$

For equal ϵ in all intersected primary cells the local approximation order n would be $n = 4$ if \tilde{A}_i would be a square and e_i would be exactly allocated in its middle.

We are searching for the entry $M_{\epsilon,i}$ connecting \widehat{e}_i and \widehat{d}_i in the constitutive law $\widehat{\mathbf{d}} = \mathbf{M}_\epsilon \widehat{\mathbf{e}}$. Since, by orthogonality, we have the one-to-one relation between \widehat{e}_i and \widehat{d}_i they are just connected via multiplication by the diagonal entry $M_{\epsilon,i}$ of the operator \mathbf{M}_ϵ which is purely diagonal. Thus we regard the quotient of \widehat{e}_i and \widehat{d}_i in order to derive an expression for the i -th diagonal entry of the material operator \mathbf{M}_ϵ . From (11) and (13) we get

$$\frac{\widehat{d}_i}{\widehat{e}_i} = \frac{\int_{\tilde{A}_i} \epsilon(\mathbf{r}) \mathbf{E}(\mathbf{r}) \cdot d\mathbf{A}}{\int_{L_i} \mathbf{E}(\mathbf{r}) \cdot d\mathbf{s}} = \frac{\epsilon_{\text{eff},i} \cdot \tilde{A}_i}{L_i} + O(L^p). \quad (14)$$

Thus the local discretization error is linear to quadratic. It depends on the degree of regularity in the mesh: For an equidistant Cartesian mesh the error is quadratic.

We can proceed similarly for the constitutive law connecting the magnetic voltage \widehat{h}_i along a dual edge \tilde{L}_i and the magnetic flux \widehat{b}_i through the corresponding primary area A_i (cf. e.g. [12] for more details). Then, the entries of the permittivity and permeability operator are set to

$$M_{\epsilon,i} = \frac{\epsilon_{\text{eff},i} \cdot \tilde{A}_i}{L_i}, \quad M_{\mu,i} = \frac{\mu_{\text{eff},i}^{-1} \cdot \tilde{L}_i}{A_i}. \quad (15)$$

Thus, the construction of \mathbf{M}_ϵ is based on area-wise averaging (cf. Fig. 2) and the construction of \mathbf{M}_μ is based on lengthwise averaging. The conductivity operator \mathbf{M}_σ is defined in full analogy to \mathbf{M}_ϵ . These operators are diagonal and have only positive entries. This is of special importance for time domain simulations (cf. subsection II-A).

In classical FIT on *orthogonal* grids the transfer of the electromagnetic material equations to the grid space generally results with *diagonal* material operators $\mathbf{M}_\epsilon, \mathbf{M}_\mu, \mathbf{M}_\sigma$.

C. Cylindrically Symmetric Resonators and Length-Homogeneous Waveguides

As described in [3], [4], classical FIT on triangular grids was implemented to solve for eigenmodes in cylindrically symmetric resonant cavities and for fields in translational waveguides. If Ω_s is longitudinally invariant a variable separation is possible for the longitudinal coordinate:

$$\mathbf{E}(x, y, z) = \mathbf{E}_0(x, y) e^{i\beta z} \quad (16)$$

with the propagation constant β . On the discrete level this can be written as

$$\mathbf{E}(x, y, \Delta z) = \mathbf{E}_0(x, y) e^{i\beta \Delta z} \doteq \mathbf{E}_0(x, y) (1 + i\beta \Delta z) \quad (17)$$

with some *virtual* step size Δz in the third dimension of space which is only needed 'on paper' to set up the discrete equations like (9) or (13).

Furthermore, it is assumed that the fields are time-harmonic such that a description by a Fourier series is possible. Finally, the materials are assumed loss free, and non-conducting.

So, additionally *normalizing* with the root of the wave impedance $Z_0 = \sqrt{\mu_0/\epsilon_0}$ and the admittance $Y_0 = \sqrt{\epsilon_0/\mu_0}$,

respectively, where ϵ_0 and μ_0 are the permittivity and permeability of vacuum, we may write

$$\mathbf{E} = \sqrt{Z_0} \sin \omega t \mathbf{E}', \quad \mathbf{H} = \sqrt{Y_0} \cos \omega t \mathbf{H}' \quad (18)$$

with the normalized fields \mathbf{E}' and \mathbf{H}' . Maxwell's equations are then discretized with FIT using the normalized fields as given in (18).

In the resonator case the variable separation is done for the azimuthal coordinate φ and the normalized fields \mathbf{E}' and \mathbf{H}' can then be written as

$$\begin{aligned} \mathbf{E}'(r, \varphi, z) &= \sum_{m=0}^{\infty} [E'_{m,r}(r, z) \cos m\varphi \mathbf{e}_r \\ &\quad + E'_{m,\varphi}(r, z) \sin m\varphi \mathbf{e}_\varphi \\ &\quad + E'_{m,z}(r, z) \cos m\varphi \mathbf{e}_z], \\ \mathbf{H}'(r, \varphi, z) &= \sum_{m=0}^{\infty} [H'_{m,r}(r, z) \sin m\varphi \mathbf{e}_r \\ &\quad + H'_{m,\varphi}(r, z) \cos m\varphi \mathbf{e}_\varphi \\ &\quad + H'_{m,z}(r, z) \sin m\varphi \mathbf{e}_z] \end{aligned} \quad (19)$$

expressing the periodicity with period 2π in the azimuthal variable φ . Then Maxwell's equations are solved for each azimuthal mode number m separately. In case of time harmonic fields the divergence equation is *automatically* fulfilled as was shown in [1]. Therefore it is possible to resolve the equation $\widehat{\mathbf{S}}\widehat{\mathbf{d}} = 0$ for the azimuthal flux density \widehat{d}_φ and substitute \widehat{d}_φ resp. \widehat{e}_φ in the remaining field equations. This formulation reduces the dimension of the system to be solved by the number of grid points N .

Finally, a linear algebraic eigenvalue problem results. In the waveguide case it has the squared propagation constants β^2 for a given frequency ω as eigenvalues, in the resonator case the eigenmodes are just the eigenfrequencies of the resonant monopole ($m = 0$), dipole ($m = 1$) and higher order modes. The propagation constant β may also take complex values, i.e. all waves including complex modes are found for waveguides. More details on these equations and on URMEL-T may be found in [4] and [11] or [13]. Some examples will be given in section III below.

II. CONSIDERATIONS ON FIT AND FEM WITH WHITNEY FORMS, FEM ON ORTHOGONAL GRIDS AND TIME DOMAIN SIMULATIONS

In recent years there have been intensive studies on different approaches more or less related to the classical FIT on triangular grids. In this section, we will try to summarize some of the results and discuss some aspects which are important if triangular grids shall be used for time domain simulations. Of course, this can only touch a few of the wide variety of recent time-domain approaches with FEM, see [14] and references therein.

A. Important Aspects for Time Domain Simulation

The stability of any time domain scheme, either FEM or FIT, is determined by the characteristics of its material operators. In [15] it was shown that positive definiteness of the material matrices is a sufficient condition for energy

conservation and stability in Yee's leap-frog-scheme [16]. Any scheme with *diagonal* material operators, having only positive entries ensures this condition.

The second advantage of diagonal material operators is the possibility to directly invert these matrices and thus to set-up an explicit iteration scheme which is of great advantage with regard to the numerical effort compared to implicit schemes. Thus it is a key point for the construction of a stable explicit time domain simulation to use a discretization scheme with diagonal material operators. Classical FIT on orthogonal grids fulfills these conditions.

Using Yee's leap-frog-scheme with FIT the equations for $\widehat{\mathbf{e}}$ and $\widehat{\mathbf{b}}$ are generally given as (cf. [15] or [12])

$$\widehat{\mathbf{b}}^{k+1} = \widehat{\mathbf{b}}^k - \Delta t \mathbf{C} \widehat{\mathbf{e}}^{k+\frac{1}{2}}, \quad (20)$$

$$\widehat{\mathbf{e}}^{k+\frac{3}{2}} = \widehat{\mathbf{e}}^{k+\frac{1}{2}} + \Delta t \mathbf{M}_\epsilon^{-1} (\widetilde{\mathbf{C}} \mathbf{M}_\mu^{-1} \widehat{\mathbf{b}}^{k+1} - \widehat{\mathbf{j}}^{k+1}). \quad (21)$$

Here $\widehat{\mathbf{b}}^{k+1}$ denotes $\widehat{\mathbf{b}}$ at time $t = t_0 + k\Delta t$ while $\widehat{\mathbf{e}}^{k+\frac{1}{2}}$ is allocated at time $t = t_0 + (k + \frac{1}{2})\Delta t$. The main idea of Yee's scheme is to use a staggered grid in time domain, too. For the time derivatives, central difference approximations are used.

More details about conditions of spatial stability necessary for long-time stable simulations are given in [12]. They are involving eigenvalues of the skew-symmetric matrix which for a lossless structure ($\mathbf{M}_\sigma = 0, \Omega_s = \overline{\Omega}_s$) writes as

$$\mathbf{A} = \begin{pmatrix} \mathbf{0} & -\mathbf{M}_\mu^{-\frac{1}{2}} \mathbf{C} \mathbf{M}_\epsilon^{-\frac{1}{2}} \\ \mathbf{M}_\epsilon^{-\frac{1}{2}} \mathbf{C} \mathbf{M}_\mu^{-\frac{1}{2}} & \mathbf{0} \end{pmatrix} = \begin{pmatrix} \mathbf{0} & \mathbf{A}_{21} \\ -\mathbf{A}_{21}^T & \mathbf{0} \end{pmatrix}. \quad (22)$$

This long-time stability is independent of the time-step. The better known second stability criterion relates to the stable time discretization. It depends on the step size and the material distribution. Thus it implies a caveat for triangular discretizations to take care of avoiding short edges in the grid(s) in order to avoid small time steps. Instead of the locally derived well-known form of the Courant-Friedrich-Levy criterion (CFL-criterion) a generalized form is derived in [12]. This form implies the eigenvalues of the iteration matrix $\mathbf{G}(\Delta t)$

$$\mathbf{G}(\Delta t) = \begin{pmatrix} \mathbf{I} & \Delta t \mathbf{A}_{21} \\ -\Delta t \mathbf{A}_{21}^T & \mathbf{I} + \Delta t^2 \mathbf{A}_{21}^T \mathbf{A}_{21} \end{pmatrix}. \quad (23)$$

A stable update scheme is guaranteed if all eigenvalues $\lambda_{\mathbf{G},i}$ lie within the unit circle of the complex plane while an energy conserving scheme requires that $|\lambda_{\mathbf{G},i}| = 1$ holds for the chosen time step Δt .

In [12], also the relation to the FDTD method is discussed in detail. Both methods are computationally equivalent but, until recently, only FIT allowed by its linear algebraic formulation for an easy but thorough analysis of properties like the energy conservation and for clear and elegant derivations of new developments like local subgridding [17], [18].

B. FEM with Whitney Forms and Mass Lumping

In reference [19] a leap-frog-scheme using the Galerkin approach is presented. The domain Ω_s is covered by a

simplicial mesh consisting of sets of tetrahedra T , facets F , edges E and nodes N . The degree-of-freedom arrays \mathbf{e} and \mathbf{b} on the finite-element mesh represent electromotive forces along the edges and magnetic fluxes over the facets, respectively. They are related to the electric fluxes \mathbf{d} and magnetomotive forces \mathbf{h} in the dual of the FEM mesh in a one-to-one relation. The operators in the discrete constitutive laws

$$\mathbf{d} = \mathbf{M}^{(1)}(\epsilon)\mathbf{e}, \quad \mathbf{h} = \mathbf{M}^{(2)}(\nu)\mathbf{b}. \quad (24)$$

are the mass matrices which result from inner products between the Whitney basis functions (elements): With the edge elements $\mathbf{w}^{(1)}$ and the facet elements $\mathbf{w}^{(2)}$ the entries of $\mathbf{M}_{ij}^{(1)}$ and $\mathbf{M}_{ij}^{(2)}$ are given by

$$\mathbf{M}_{ij}^{(1)}(\epsilon) = \int_{\Omega_s} \epsilon \mathbf{w}_i^{(1)} \cdot \mathbf{w}_j^{(1)}, \quad (25)$$

$$\mathbf{M}_{ij}^{(2)}(\nu) = \int_{\Omega_s} \nu \mathbf{w}_i^{(2)} \cdot \mathbf{w}_j^{(2)}. \quad (26)$$

These matrices are non-diagonal but positive-definite, symmetric and sparse.

The leap-frog-scheme for FEM with Whitney forms can then be formulated in full analogy to (20), (21):

$$\mathbf{b}^{k+1} = \mathbf{b}^k - \Delta t \mathbf{C} \mathbf{e}^{k+1/2}, \quad (27)$$

$$\mathbf{e}^{k+1/2} = \mathbf{e}^{k-1/2} + \Delta t \left[\mathbf{M}^{(1)}(\epsilon)^{-1} \mathbf{C}^T \mathbf{M}^{(2)}(\nu) \mathbf{b}^k \right]. \quad (28)$$

As in [19] it was assumed here that the current \mathbf{J} vanishes in Ω_s . The main differences between (21) and (28) lie in the following:

- 1) With $\widetilde{\mathbf{C}} = \mathbf{C}^T$ FIT explicitly defines a curl operator on its dual grid which is applied there to $\widehat{\mathbf{h}}$ while the transpose of the curl operator \mathbf{C} on the FEM grid is applied there to $\mathbf{M}^{(2)}(\nu)\mathbf{b}$.
- 2) The material operator related to the magnetic state variables is \mathbf{M}_μ in FIT and $\mathbf{M}^{(2)}(\nu)$ in the FEM formulation with the reluctivity $\nu = 1/\mu$.

From the physical meaning both procedures are, of course, equivalent.

As shown in [20] the first mass matrix $\mathbf{M}^{(1)}(\epsilon)$, which needs to be inverted in each time step according to (28), can be replaced by some diagonal matrix $\mathbf{H}^{(1)}(\epsilon)$ under the constraint that its entries are positive in order to provide positive-definiteness as necessary condition for the stability:

$$\mathbf{H}^{(1)}(\epsilon) = - \int_{\Omega_s} \epsilon \text{grad } w_i^{(0)} \cdot \text{grad } w_j^{(0)}. \quad (29)$$

This mass lumping gathers entries of $\mathbf{M}^{(1)}(\epsilon)$ related to edges and thus differs from summing up entries of a row as used in scalar case.

The authors of [19] state that the mass lumping procedure should be less stringent than the condition of all angles to be acute as e.g. in the classical FIT on a structured Delaunay-Voronoi grid as described above. Yet, they found out that the positiveness of the entries is not easily met in practice. Since, on the other hand, they observed that a mesh with only 5-10%

non-positive entries in $\mathbf{H}^{(1)}(\epsilon)$ is rather easily to be achieved they suggest to replace the mass matrix $\mathbf{M}^{(1)}(\epsilon)$ by a *partially* diagonalized matrix $\mathbf{H}_M^{(1)}(\epsilon)$ with as many positive entries of $\mathbf{H}^{(1)}(\epsilon)$ as possible. These percentages have to be compared with the practically found percentages of obtuse triangles in the classical FIT with structured Delaunay-Voronoi grid given e.g. in subsection III-C.

Of course, the partial mass lumping implies that no fully explicit scheme results.

The procedure for the partial diagonalization is described in detail in [19]. It is stated there that, in practice, the success of the partial diagonalization is highly dependent on the mesh generator. For the scheme without mass lumping the additional numerical effort for the iterative solution of the mass matrix equation in each time step is estimated as about 400-fold compared to a fully explicit scheme using a direct inversion of its diagonal operator. For the scheme with the partially diagonalized operator the computational load is about 400p-fold compared to the fully explicit scheme, with $0 \leq p \leq 1$ [19].

Also, one drawback of non-diagonal mass matrices compared to the classical Yee scheme (underlying the classical FIT) is pointed out in [19]: More care has to be taken in order to properly impose boundary conditions.

Allowing for some non-orthogonal regions in an orthogonal Delaunay-Voronoi grid used with classical FIT usually leads to only a small percentage of non-orthogonal cells (cf. subsection III-C). In consequence, also only a few off-diagonal entries are introduced in the corresponding material matrix. Without anticipating a systematic study of this question it seems that the effort for FIT with non-orthogonal cells and the partial mass lumping in FEM as described above is more or less comparable.

C. FEM with Orthogonal Vector Basis Functions

Several authors avoid the mass lumping because instability can not be excluded a priori, see e.g. [21], [22]. Both schemes start with the second order vector wave equation. In these two papers, a diagonal mass matrix is constructed using 2D and 3D orthogonal vector basis functions, respectively. With these basis functions a stable explicit scheme is set up. The 2D orthogonal basis presented in [21] ensures diagonality or positive-definiteness of the employed mass matrices and thus allows for a stable explicit scheme. The price for this is a blow up of the factor three in the new set of basis functions, i.e. in the degrees of freedom, but in numerical experiments the cpu time nevertheless dropped down by a factor of three for the same number of cells compared. In some numerical experiments the 3D orthogonal basis presented in [22] proved to be nearly about an order of magnitude more efficient in terms of cpu time than the traditional zeroth- and first-order vector basis [22].

D. FIT with Whitney Forms

As already noted above, in classical FIT interpolation gets necessary in the construction of the material operators on non-orthogonal grids. This destroys the one-to-one relation between the allocation of the state variables leading to off-diagonal entries in the material operators.

In search for a stable FIT scheme for non-orthogonal, non-coordinate grids an approach is studied in [23] to construct a discrete constitutive relation compatible with the integral definition of voltages and fluxes in FIT but using Whitney forms as interpolating functions.

At arbitrary points inside the cell field values are interpolated from the electric voltages \hat{e}_i using Whitney forms:

$$\mathbf{E}(\mathbf{r}) = \sum_i \hat{e}_i \mathbf{w}_i^{(1)}(\mathbf{r}). \quad (30)$$

This is in correspondence to the FE approach with the electric grid voltage \hat{e}_i corresponding to the degree of freedom e_i .

Next, the electric flux components \hat{d}_i are computed according to (4) now using the interpolated field values from (30):

$$\begin{aligned} \hat{d}_i &= \int_{\tilde{A}_i} \mathbf{D}(\mathbf{r}) \cdot d\mathbf{A} = \int_{\tilde{A}_i} \epsilon(\mathbf{r}) \mathbf{E}(\mathbf{r}) \cdot d\mathbf{A} \\ &= \sum_j \hat{e}_j \int_{\tilde{A}_i} \epsilon(\mathbf{r}) \mathbf{w}_j^{(1)}(\mathbf{r}) \cdot d\mathbf{A}. \end{aligned} \quad (31)$$

Obviously the new material operator is not diagonal but it has also off-diagonal entries:

$$M_{\epsilon,ij} = \int_{\tilde{A}_i} \epsilon(\mathbf{r}) \mathbf{w}_j^{(1)}(\mathbf{r}) \cdot d\mathbf{A} \quad (32)$$

which generally do not vanish - even for orthogonal grid duplets (G, \tilde{G}) .

Next, the authors of [23] investigate a single triangular cell with the barycenter as dual grid point and the dual edges intersecting the primary ones at their midpoints, i.e. the dual edges not being one straight line, but a kinked line. The resulting non-diagonal material matrix is different from the FE mass matrices. Unfortunately it is not symmetric in general.

After all, a 2D grid set up could be presented in [23] with *symmetric* material operator. This grid allows for obtuse triangles with angles up to 120° using the so-called symmetry points as dual grid points. Using these points as dual grid points the symmetry of the material operator is enforced. The symmetry point is located on the connecting line of barycenter and circumcenter of the triangle and divides this line in a 1:4 ratio. Again, this material operator is different from the one obtained by classical FIT and from the FE material operator. Thus, one important result is that "the classical FIT scheme on triangular grids ... cannot be interpreted in terms of Whitney-type basis functions." A straightforward extension of this scheme to 3D tetrahedral grids could not be found.

The new 2D algorithm was implemented and results are presented in [23]. The numerically determined convergence

rate for eigenmode computations was found to be typically between 1.3 and 2.5 depending on the grid quality and its refinement strategy.

E. Classical FIT on Triangular Grids

As described in subsection I-A, the angular limit to obtain an Delaunay-Voronoi grid and thus a *diagonal* material operator is 90° . Often the given geometry implies some unavoidable obtuse angles near the boundary of the meshed 2D cut of the problem domain Ω_s . If a local non-orthogonal grid is chosen in and neighbouring this triangle interpolation and projection of components becomes necessary introducing off-diagonal elements in the material operators.

Regarding the fact that these entries will only occur in a very small percentage of the matrix (cf. subsection III-C) this approach seems to be comparable to the FEM approach with mass lumping described above. Another approach could in principal follow a methodology presented in [24]. Yet, this approach based on the use of the longest-edge bisection technique introduces new points and thus destroys the topological regularity of the grid. Nevertheless both attempts or other new ideas, e.g. for FIT on an unstructured Delaunay-Voronoi diagram, to treat the problem of obtuse triangles seem to be worth some studies.

III. EXAMPLES

Several examples of simulations with URMEL-T which is based on the Finite Integration Technique on triangular grids as described above may be found in earlier publications as e.g. [3], [4], [11], [25], [8], [26], [27] or [28].

We present three typical specimen for cylindrically symmetric resonators and one waveguide example. All simulations in subsections III-A - III-C have been performed on a SUN Enterprise 450 with 300 MHz, 4 processors and 4 GB RAM.

A. Cylindrical Resonator

A cylindrical resonator, also denoted as 'pillbox' cavity, is suited well for convergence studies since the analytical solution is available. We chose a pillbox with the dimensions of 16.5 cm height and 22 cm width as studied in [19], see Fig. 3.

The authors of [19] computed the resonant frequencies up to 2.5 GHz with their 3D FEM code on a mesh with 7,038 tetrahedra and compared those with results from the 3D FIT code [15] with 7,293 cells using a rectangular grid with possibility of diagonal filling. Here, the eigenmodes are computed in frequency domain with the resonator option in URMEL-T for different grids. Exploiting all symmetries it is sufficient to discretize a quarter of the cavity's cross-section, an example grid with $N = 925$ points is displayed in Fig. 3. As Ω equals Ω_s , the grid is nearly perfectly equilateral.

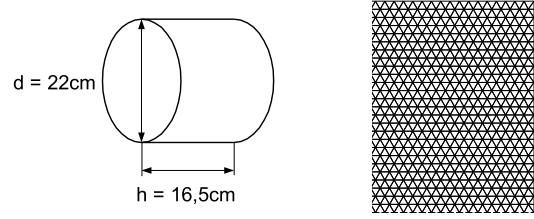


Fig. 3. Left: Cylindrical cavity, also denoted as 'pillbox' cavity. Right: Triangular grid with $N = 925$ grid points, i.e. 1850 triangles, for the right upper quarter of the pillbox cross-section in (r, z) -plane which only needs to be computed. In this simple case the final mesh is identical with the start mesh of the mesh generator since $\Omega = \Omega_s$ holds here.

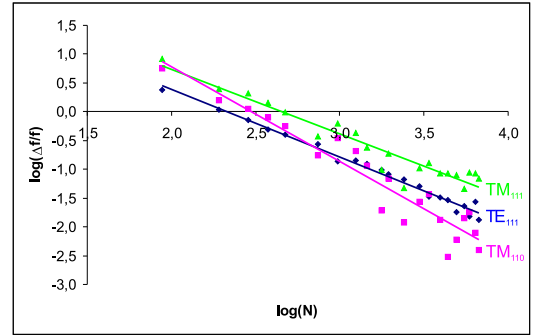


Fig. 4. Relative frequency error $\Delta f/f$ as function of number N of grid points for the TE_{111} -, TM_{110} - and TM_{111} -mode of the pillbox cavity; logarithmic scale. The convergence goes with $N^{-1.18}$ for the TE_{111} -mode, with $N^{-1.65}$ for the TM_{110} -mode and with $N^{-1.12}$ for the TM_{111} -mode.

In Fig. 4, a convergence study is presented for three selected modes. The convergence order for these modes ranges between first and second order. Best convergence is achieved for the TM_{110} -mode with $O(N^{-1.65})$. Also, the CPU time as function of the number of grid points is presented in Fig. 5. It scales with $O(N^{1.28})$. Note that three unknowns (\hat{e}_a , \hat{e}_b , \hat{e}_c) are related to each of the N grid points.

B. Resonator with Nose-Cone

As another cylindrically symmetric geometry where its cross-section is neither rectangular like for the pillbox described in subsection III-A nor having a smooth and simple to approximate boundary shape like that one shown below in subsection III-C, we chose also some resonator cavity with a so-called 'nose-cone' which comes rather close to a re-entrant corner.

For comparison, an unstructured Delaunay triangulation obtained by the open source code Triangle [29] is shown in Fig. 6 together with a FIT grid of comparable number of triangles. The code Triangle generates constrained conforming Delaunay triangulations while most other codes only generate conforming, but *unconstrained* triangulations. In addition to the Delaunay triangulations, Triangle also offers the related Voronoi diagram.

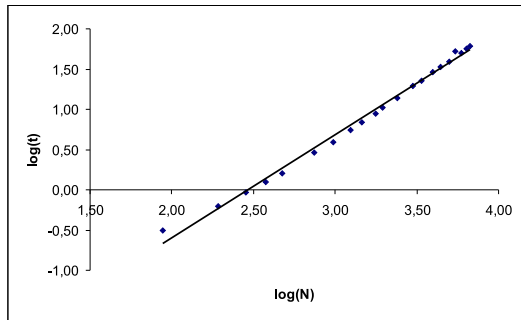


Fig. 5. CPU time t /sec as function of number N of grid points for the pillbox cavity. The cpu time depends as $t = 0.0007 \cdot N^{1.2812}$.

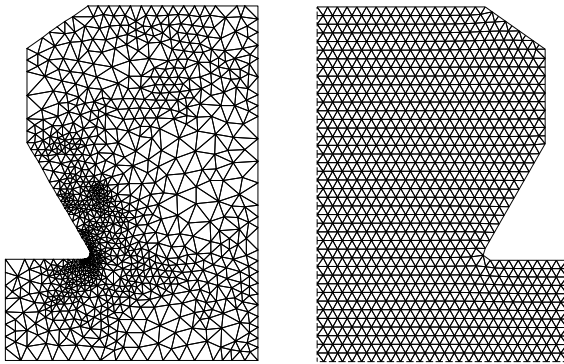


Fig. 6. Left: Delaunay triangulation with 1,860 triangles for Ω_s generated by the code Triangle [29]. Right: FIT mesh as generated for the right half of the PETRA cavity by URMEL-T with 1,015 grid points, i.e. 2,030 triangles for Ω ($\Omega \setminus \Omega_s$ is modelled as perfect conductor and thus fields are only to be computed in Ω_s). Again, for symmetry reasons only the upper left or right quarter of the cross-section in (r, z) -plane needs only to be computed.

The Triangle program informs about important grid characteristics and its construction. In the example shown in Fig. 6 the divide-and-conquer method [30] was used. In the mesh quality statistics smallest and largest area and edge are given, each. If we denote their ratio as *total* aspect ratio, the total area ratio in this example results to $2.5 \cdot 10^2$ and the total edge ratio amounts to $1.9 \cdot 10^1$. Also, the aspect ratio which relates the longest edge to the shortest altitude is given; it is 2.9374 in our example. The smallest angle is 34.004° , the largest angle is 111.5° in the grid displayed in Fig. 6. In total there are 209 obtuse triangles (11%), of those 145 (8%) have an angle between 90° and 100° , 61 (3%) an angle between 100° and 110° and 3 (0.02%) have an angle of 110° to 120° . Much more information like a list of bad and so on is available, too.

Obviously the structured FIT grid has much smaller total aspect ratios and much less obtuse triangles (cf. Table I) thanks to the equilibration algorithm imbedded in the automatic grid generation. So, the FIT grid is most regular which leads to a better condition of the matrix of the resulting linear algebraic eigenvalue problem. Also, this greater regularity has a positive impact on the maximal time step if this mesh should be used for time domain simulations. It would be interesting to compare the numerical effort necessary to reach

the same error for a simulation with both type of grids, the structured Delaunay grid used in URMEL-T and the unstructured Delaunay grid. This will be the subject of a future research project.

C. Multicell Resonators

In the design studies for the future linear collider project TESLA [31] different multicell superconducting resonator structures have been investigated. One of them is the 4x7-cell so-called superstructure [32]. Without the attached couplers the structure is again a cylindrically symmetric one so that it can be simulated with the 2D code URMEL-T.

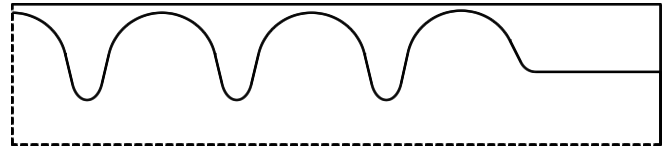


Fig. 7. Geometry of the TESLA 7-cell cavity. For symmetry reasons only the upper right quarter of the (r, z) -cross-section needs to be computed.

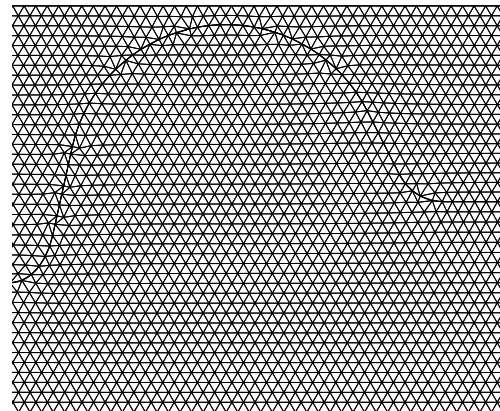


Fig. 8. Triangular grid in the right end-cell of the TESLA 7-cell cavity.

Here we chose this structure as an example to study the percentage of obtuse triangles. Fig. 7 shows the part of the cross-section used for simulation. Fig. 8 displays a zoom to the grid of the end-cell. The total number of triangles amounts to 13,366 triangles. Among them, there are 35 (0.26%) triangles with an angle larger than 90° , none of those has an angle larger than 100° .

Table I also shows the results for coarser grids used for the full 7-cell structure and a full 9-cell structure (only around 1,500 triangles per cell; 'full' refers to the complete upper half of the cross-section, 'half' to its right half as shown in Fig. 8). The percentage of obtuse triangles only amounts to 0.26% - 0.37%. Triangles with an angle larger than 100° do not always occur - if so, then they only amount to less than 0.05%. As to be expected, there seems to be a tendency that finer grids have a smaller percentage of obtuse triangles.

These far less than 1% of obtuse triangles automatically obtained in the mesh generator of URMEL-T have to be

	# triangles	angle > 90°	angle > 100°
9-cell, full	12,150	45 (0.37%)	4-5 (0.04%)
7-cell, full	12,320	43 (0.37%)	4-5 (0.04%)
7-cell, half	13,366	35 (0.26%)	0

TABLE I

PERCENTAGE OF OBTUSE TRIANGLES IN THE MESH OF THE TESLA
7-CELL- AND 9-CELL-RESONATOR.

compared with the 5-10% non-positive entries achieved in the partial mass lumping, e.g.. This small percentage of obtuse triangles is achieved by an equilibration procedure with low computational cost. Of course, more statistics and careful comparison of the numerical results are necessary before coming to final statements.

Fig. 9 shows some field plots for the accelerating mode in one 7-cell cavity of the 4x7-cell superstructure. The TM_{01} -mode used for the "acceleration" of electrons or positrons, respectively, passing the cavity on axis with nearly speed of light has its field maximum of the longitudinal electric field on axis such that a maximum of energy can be transferred to the particles while their passage of the structure. The plots also show that a good field flatness is achieved with the chosen cavity geometry.

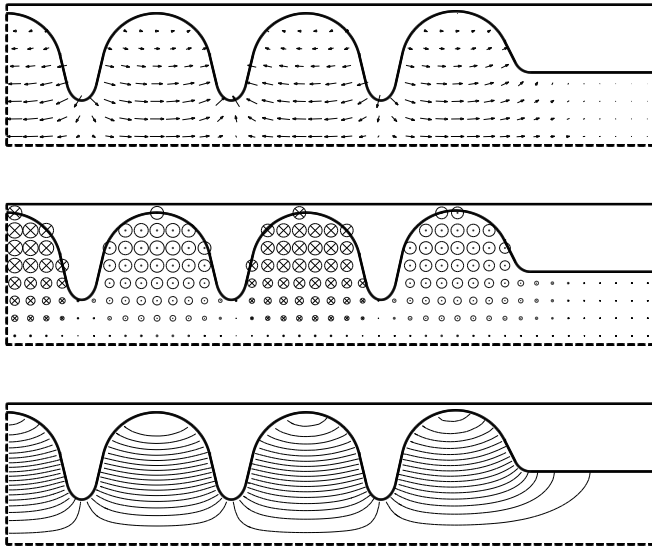


Fig. 9. Snap shots of the electric and magnetic field of the TM_{01} -mode with frequency 1.3 GHz used to accelerate electrons passing the structure on axis from left to right. The middle plot shows the azimuthal magnetic field. The size of the arrows and circles corresponds to the local magnitude of the field. Their midpoint *always* lies within Ω_s but for large magnitudes the circles or arrows might partly extend to the outside Ω_s .

D. Dielectrically Filled Rectangular Waveguide

We will show one waveguide example here, others may be found in earlier publications (see e.g. [11]). We regard the dispersion relation for a dielectric loaded waveguide. A rectangular waveguide filled with some dielectrics [4] is shown in Fig. 10.

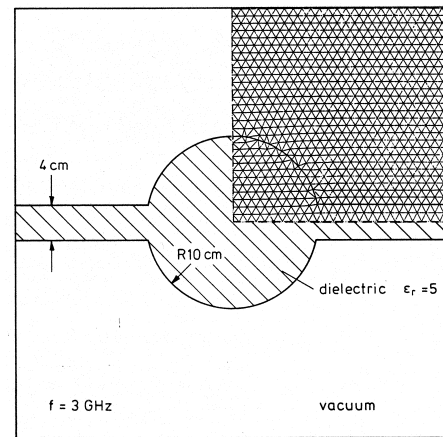


Fig. 10. Dielectric waveguide. Mesh for the computational domain.

Its fundamental mode has the frequency 3 GHz. The dispersion relation between frequency ω and propagation constant β has been computed. For different frequencies the highest β 's are displayed in a fit through a few dozen distinct values in Fig. 11. Note that for each wavenumber $k_0 = \omega/c$ one URMEL-T run has to be performed.

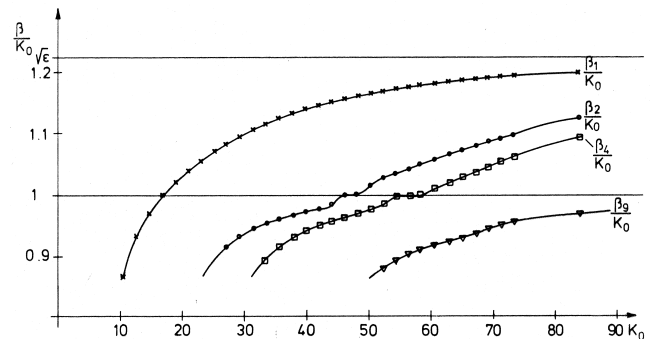


Fig. 11. Dielectric waveguide. Dispersion relation.

IV. SUMMARY

This paper revisited the application of the Finite Integration Technique on triangular grids. The corresponding code URMEL-T is successfully applied in many different locations, mainly universities and accelerator laboratories. The underlying method has been reviewed and some example resonator- and waveguide computations have been shown. Regarding the question of time domain simulations, some recent FEM approaches seeking for diagonal or partially diagonal mass matrices have been cited as well as an approach for FIT with a Whitney-based material operator.

Starting point was the following: Diagonal material operators with positive entries ensure energy conservation and stability in Yee's leap-frog-scheme for time domain simulations

(and allow for an explicit scheme). FEM with mass lumping and classical FIT on a structured Delaunay-Voronoi grid with acute angles both achieve a diagonal matrix with positive entries. Yet, both are not easily met in practice. Next best are positive definite symmetric material operators with only few off-diagonal entries. For FEM, a partially diagonalized mass matrix with about 5-10% non-positive entries has been suggested in literature. This has to be compared with the maximally 0.5-1% off-diagonal entries in the material matrix caused by remaining obtuse triangles in classical FIT on a structured, equilibrated Delaunay-Voronoi grid, as it was found for the examples presented here. The numerical effort to achieve a small percentage of obtuse triangles is very low - probably smaller than that one needed for the partial diagonalization of the mass matrix. Yet, this question could not be studied here but still needs more detailed studies in future.

These first studies let it seem to be worthwhile to invest some further research on a Yee-like scheme with classical FIT on structured, equilibrated Delaunay-Voronoi grids.

V. ACKNOWLEDGEMENT

The author wishes to thank R. Schuhmann and M. Dohlus for valuable hints and fruitful discussions. Also, she would like to thank H.R. Arndt for performing the simulations in subsections III-A - III-C and for his study on different open source codes for Delaunay triangulations.

REFERENCES

- [1] T. Weiland, "Eine Methode zur Lösung der Maxwell'schen Gleichungen für sechskomponentige Felder auf diskreter Basis," *AEÜ*, vol. 31, pp. 116-120, 1977.
- [2] T. Weiland, "On the Unique Numerical Solution of Maxwellian Eigenvalue Problems in Three Dimensions," *Part.Acc.*, vol. 17, pp. 227-242, 1985.
- [3] U. van Rienen and T. Weiland, "Triangular Discretization Method for the Evaluation of RF-Fields in Cylindrically Symmetric Cavities," *IEEE Transactions on Magnetics*, vol. 21, pp. 2317-2320, November 1985.
- [4] U. van Rienen and T. Weiland, "Triangular Discretization Method for the Evaluation of RF-Fields in Waveguides and Cylindrically Symmetric Cavities," *Part.Acc.*, vol. 20, pp. 239-267, 1986/87.
- [5] M. Clemens, R. Schuhmann, U. van Rienen, and T. Weiland, "Modern Krylov Subspace Methods in Electromagnetic Field Computation Using the Finite Integration Theory," *ACES Journal, Special Issue on Applied Mathematics: Meeting the challenges presented by Computational Electromagnetics*, vol. 11, pp. 70-84, March 1996.
- [6] R. Schuhmann and T. Weiland, "Stability of FDTD Algorithm on Nonorthogonal Grids Related to the Spatial Interpolation Scheme," *IEEE-MTT*, vol. 34, pp. 2751-2754, Sept. 1998.
- [7] B. Krietenstein, R. Schuhmann, P. Thoma, and T. Weiland, "The Perfect Boundary Approximation Technique Facing the Big Challenge of High Precision Field Computation," in *LINAC 98*, (Chicago, USA), pp. 695-697, 1998. <http://accelconf.web.cern.ch/AccelConf/198/PAPERS/TH4041.PDF>.
- [8] P. McIntosh, "RF Cavity Computer Design Codes," in *1995 Particle Accelerator Conf. (PAC'95)*, pp. 2353 - 2355, 1995. <http://accelconf.web.cern.ch/AccelConf/p95/ARTICLES/MPC/MPC19-.PDF>.
- [9] H. Glock, K. Rothemund, and U. van Rienen, "CSC - A Procedure for Coupled S-Parameter Calculations," *IEEE Trans. on Magn.*, vol. 38, pp. 1173-1176, 2002.
- [10] J.-Y. Raguin, "Network Representation of Multi-Cell Accelerating Structures," in *2001 Particle Accelerator Conf. (PAC'01)*, pp. 3027 - 3029, 2001. <http://accelconf.web.cern.ch/AccelConf/p01/PAPERS/RPAH080.PDF>.
- [11] U. van Rienen, "Finite Integration Technique on Triangular Grids Revisited," *Int. Journal of Numerical Modelling: Electronic Networks, Devices and Fields, Special Issue "Finite Difference Time and Frequency Domain Methods"*, vol. 12, pp. 107-128, 1999. (invited paper).
- [12] T. Weiland, *Computational Electromagnetics*, vol. 28 of *Lecture Notes in Computational Science and Engineering*, ch. Finite Integration Method and Discrete Electromagnetism, pp. 183-198. Springer Verlag, 2003.
- [13] U. van Rienen, *Zur numerischen Berechnung zeitharmonischer elektromagnetischer Felder in offenen, zylindersymmetrischen Strukturen unter Verwendung von Mehrgitterverfahren*. PhD thesis, Darmstadt University of Technology, 1989.
- [14] J. Lee, R. Lee, and A. Cangellaris, "Time-domain finite element methods," *IEEE Trans. Antennas Propagat.*, vol. 45, no. 3, pp. 430-442, 1997. (invited review paper).
- [15] T. Weiland, "Time Domain Electromagnetic Field Computation with Finite Difference Methods," *Int. Journal of Numerical Modelling: Electronic Networks, Devices and Fields*, vol. 9, no. 4, pp. 295-319, 1996.
- [16] K. Yee, "Numerical Solution of Initial Boundary Value Problems Involving Maxwell's Equations in Isotropic Media," *IEEE-AP*, vol. 14, pp. 302-307, 1966.
- [17] P. Thoma and T. Weiland, "A Subgridding Method in Combination with the Finite Integration Technique," in *25th European Microwave Conference*, vol. 2, pp. 770 - 774, 1995.
- [18] O. Podebrad, M. Clemens, and T. Weiland, "New Flexible Subgridding for the Finite Integration Technique," *IEEE Trans. Magn.*, vol. 39, pp. 1662-1665, May 2003.
- [19] A. Keränen, J. Kangas, A. Ahola, and L. Kettunen, "Implicit Yee-Like Scheme on Tetrahedral Mesh," *IEEE Trans. Magn.*, vol. 38, pp. 717-720, March 2002.
- [20] A. Bossavit and L. Kettunen, "Yee-like Schemes on a Tetrahedral Mesh with Diagonal Lumping," *Int. J. Numer. Modelling, Special Issue "Finite Difference Time and Frequency Domain Methods"*, vol. 12, no. 1/2, pp. 129-142, 1999.
- [21] D. White, "Orthogonal basis functions for the time domain finite element solution of the vector wave equation," *IEEE Trans. Magn.*, vol. 35, no. 3, pp. 1458-1461, 1999.
- [22] D. Jiao, J.-M. Jin, and E. Michielssen, "Three-Dimensional Orthogonal Vector Basis Functions for Time-Domain Finite Element Solution of Vector Wave Equation," in *Antennas and Propagation Society, 2001 IEEE Intern. Symp.*, pp. 201-207 vol.3, 2001.
- [23] R. Schuhmann, P. Schmidt, and T. Weiland, "A New Whitney-Based Material Operator for the Finite-Integration Technique on Triangular Grids," *IEEE Trans. Magn.*, vol. 38, pp. 409-412, 2002.
- [24] N. Hitschfeld and M. Rivara, "Non-Obtuse Boundary Delaunay Triangulations," in *6th Int. Meshing Roundtable*, (Sandia Natl. Lab., USA), p. 391, October 1997.
- [25] J. Corlett and J. Byrd, "Measurement and Computation of the Higher Order Modes of the ALS 500 MHz Accelerating Cavities," in *Particle Accelerator Conf. (PAC'93)*, pp. 3408 - 3410, 1993. <http://accelconf.web.cern.ch/AccelConf/p93/PDF/PAC19933408.PDF>.
- [26] C. Dawson, D. Dykes, and P. McIntosh, "The Tuning of the Cavity Options for DIAMOND," in *Particle Accelerator Conf. (PAC'97)*, pp. 2956 - 2958, 1997. <http://accelconf.web.cern.ch/accelconf/pac97/papers/pdf/2P037.PDF>.
- [27] Z. Zhao, W. Pan, D. J. Sun, Y. Z. Li, H. Qu, Z. Liu, L. Feng, and K. Jin, "Design of a Copper Cavity for HLS," in *2001 Particle Accelerator Conf. (PAC'01)*, pp. 1201 - 1203, 2001. <http://accelconf.web.cern.ch/AccelConf/p01/PAPERS/MPPH308.PDF>.
- [28] Y. Pei, W. He, K. Jin, C. Wu, and S. Dong, "The Simulation and Analysis of Secondary Emission Microwave Electron Gun," in *2nd Asian Particle Accelerator Conf. (APAC'01)*, pp. 562 - 564, 2001. <http://accelconf.web.cern.ch/AccelConf/a01/PDF/WEDM02.pdf>.
- [29] J. R. Shewchuk, "Triangle: Engineering a 2D Quality Mesh Generator and Delaunay Triangulator," in *Applied Computational Geometry: Towards Geometric Engineering* (M. C. Lin and D. Manocha, eds.), vol. 1148 of *Lecture Notes in Computer Science*, pp. 203-222, Springer-Verlag, May 1996. From the First ACM Workshop on Applied Computational Geometry.
- [30] J. Shewchuk, "Lecture Notes on Delaunay Mesh Generation," tech. rep., Departm. of Electr. Eng. and Comp. Science, University of California at Berkeley, Berkeley, CA 94720, USA, May 1999.
- [31] R. Brinkmann, K. Flöttmann, J. Rossbach, P. Schmüser, N. Walker, and H. Weise, "TESLA - Technical Design Report, Part II," DESY 2001-011, Deutsches Elektronen-Synchrotron DESY, D-22607 Hamburg, Germany, March 2001. available: <http://tesla.desy.de>.

- [32] J. Sekutowicz, M. Ferrario, and C. Tang, "Superconducting superstructure for the TESLA collider: A concept," *Phys. Rev. ST Accel. Beams*, vol. 2, no. 6, pp. 062001-1 – 062001-7, 1999. <http://prstab.aps.org/pdf/PRSTAB/v2/i6/e062001>.



Ursula van Rienen received the Diplom degree in mathematics from the Rheinische Friedrich-Wilhelms-Universität, Bonn, Germany, in 1983 and the Doctorate degree in mathematics from the Darmstadt University of Technology, Germany, in

1989. She received the *habilitation* in theoretical electrical engineering and in scientific computing in 1997.

Currently, she is a full professor at the Faculty of Engineering of Rostock University, Germany, where she was appointed to the chair of theoretical electrical engineering in 1997. She is head of a study group in computational electrodynamics. From 1983 to 1990, she was a Research Assistant at the Deutsches Elektronen Synchrotron (DESY), Hamburg, Germany. She spent several extended research stays at Los Alamos, USA, in the Accelerator Technology Division. From 1990 to 1997, she was a Research Assistant at the Darmstadt University of Technology, Germany. From 1995 to 1997 she was a Scholar of the Deutsche Forschungsgemeinschaft. The actual research covers different topics in computational electrodynamics and numerical linear algebra with practical backgrounds in accelerator physics, high voltage engineering, electromagnetic radiation, biophysics, bio- and medical technology.

Envelope - Finite Element (EVFE) Technique in Electromagnetics with Perfectly Matched Layer (PML)

WeiJun Yao, Yuanxun Wang, and Tatsuo Itoh

Abstract — *In this paper, the perfectly matched layer (PML) has been implemented into the Envelope Finite Element (EVFE) technique. The PML performance tests show that it can provide sufficient absorption of the incident waves both in 2D and 3D cases. The 3D guided wave structures are efficiently analyzed by the EVFE technique with the PML boundary condition. Furthermore, a new plane wave excitation scheme inside the PML boundary with EVFE technique is also presented here for the analysis of scattering problems, and the numerical examples validate the formulations.*

I. INTRODUCTION

In modern optical and wireless communication systems, the digital modulated signals are usually further modulated with a very high frequency carrier, such that the signal bandwidth to carrier frequency ratio is very small. To analyze the transient response of the components and devices in this kind of system, the traditional time domain techniques are not efficient and precise enough. The reasons are: first, although we can develop implicit method to make the time domain algorithms unconditionally stable, such as implicit finite element time domain (FETD) method [1], the time step size is still governed by Nyquist sampling criterion, which requires that the sampling rate is at least twice of the simulation bandwidth. As the simulation bandwidth in FETD ranges from DC to the highest frequency of the narrowband modulated signal, the required time step should be very small in order to follow the variance of high frequency carrier. Second, as FETD is low pass type of algorithm, the time dispersion error is smallest at DC, and continually increases as frequency increases. This characteristic made traditional FETD unsuitable to simulate narrow band systems because its time dispersion will be very large at the carrier frequency [2].

Recently, a new numerical technique called envelope finite element was proposed in [2]-[5]. In this method, the carrier information is de-embedded from the narrowband signal thus only the complex signal envelopes are sampled. Its simulation bandwidth is much smaller compared with finite element time domain (FETD) method. Numerical

tests in [2] shows, with same time step size, EVFE has a much lower time dispersion error than FETD. This is accomplished while, keeping the same time dispersion error, suggesting that EVFE can use much larger time step size than FETD. It can be asserted that EVFE is a powerful tool to simulate the transient response of components and devices in the narrowband system. The concept of envelope simulation itself is not new, which has been employed into the circuit simulator, such as ADS's Circuit Envelope Simulator [6]. It has been proven to be much more efficient than the regular transient simulator. EVFE technique makes it possible to do the efficient EM and circuit co-simulation combining with Circuit Envelope Simulator.

Previous researchers have already applied EVFE technique to 2-D guided wave problems [3] and 3-D microwave passive structures [4] with the first order absorbing boundary condition (ABC); however, an alternative and better choice to ABC is perfectly matched layer (PML) boundary condition, which has wider bandwidth and can provide more absorption of the incident waves. Perfectly matched layer was first introduced into finite difference time domain (FDTD) method by Berenger [7], however, it has several limitations such as the governing equation inside the PML region is non-Maxwellian. Sacks [8] has suggested a new PML based on a lossy uniaxial medium and successfully implemented into frequency domain finite element method. Gendey [9] further developed the formulation for the FDTD method with anisotropic perfectly matched layer and applied it in the analysis of microwave circuits and antennas. Recently, PML has been successfully implemented into finite element time domain technique (FETD) in the analysis of scattering problems [10], and active nonlinear microwave circuit modeling [11]. Based on the anisotropic PML concept, we derived the PML formulations for EVFE technique. Several numerical tests and examples will be shown to validate our formulations.

This paper is organized as follows. Section II presents the EVFE formulations for implementing the anisotropic perfectly matched layer and two examples are presented to test the PML's performance both in 2-D and 3-D. Section III presents 3-D examples for the analysis of guided wave structures with EVFE and PML technique. In section IV a

new plane wave excitation scheme inside the PML boundary is proposed and scattering problems are analyzed with this method. Finally, conclusions are made in section V.

II. PML FOR EVFE FORMULATIONS

In this section, the PML formulation will be derived for EVFE technique. To make the discussion more general, we present 3-D formulations here, which can be easily reduced to 2-D formulations. We would like to start from the general time-harmonic form of Maxwell equations in PML regions:

$$\begin{aligned}\nabla \times \vec{H} &= j\omega \epsilon_0 \epsilon_r \vec{E} + \vec{J}_i, \\ \nabla \times \vec{E} &= -j\omega \mu_0 \mu_r \vec{H},\end{aligned}\quad (1)$$

where

$$\vec{\epsilon} = \vec{\mu} = \begin{bmatrix} \frac{s_y s_z}{s_x} & 0 & 0 \\ 0 & \frac{s_x s_z}{s_y} & 0 \\ 0 & 0 & \frac{s_x s_y}{s_z} \end{bmatrix}\quad (2)$$

$$\text{and } s_i = 1 + \frac{\sigma_i}{j\omega \epsilon_0}, \quad i = x, y, z. \quad (3)$$

Here we assume there is no source in PML region, and the second-order wave equation from (1), (2), and (3) is:

$$\nabla \times ([\vec{\mu}]^{-1} \cdot \nabla \times \vec{E}) - \omega^2 \epsilon [\vec{\epsilon}] \vec{E} = -j\omega \frac{1}{\mu} \vec{J}. \quad (4)$$

Based on the vector finite element method, we can recast (4) into the following form

$$\begin{aligned}-\omega^2 e_j Q_x \frac{s_y s_z}{s_x} + e_j P_x \frac{s_x}{s_y s_z} - \omega^2 e_j Q_y \frac{s_x s_z}{s_y} + e_j P_y \frac{s_y}{s_x s_z} \\ -\omega^2 e_j Q_z \frac{s_y s_x}{s_z} + e_j P_z \frac{s_z}{s_y s_x} = -j\omega \int_v \frac{1}{\mu} \vec{N}_i \cdot \vec{J} dv,\end{aligned}\quad (5)$$

where

$$\begin{aligned}Q_x &= \int_v \epsilon N_x^j N_x^i dv, \\ Q_y &= \int_v \epsilon N_y^j N_y^i dv, \\ Q_z &= \int_v \epsilon N_z^j N_z^i dv,\end{aligned}$$

$$P_x = \int_v \frac{1}{\mu} (\nabla \times \vec{N}^j)_x (\nabla \times \vec{N}^i)_x dv,$$

$$P_y = \int_v \frac{1}{\mu} (\nabla \times \vec{N}^j)_y (\nabla \times \vec{N}^i)_y dv,$$

$$P_z = \int_v \frac{1}{\mu} (\nabla \times \vec{N}^j)_z (\nabla \times \vec{N}^i)_z dv, \quad (6)$$

while \vec{N}^i, \vec{N}^j are the vector basis functions.

To solve equation (5), we need to define another three variables:

$$\Phi_x = \frac{s_x}{s_y s_z} e_j, \quad \Phi_y = \frac{s_y}{s_x s_z} e_j, \quad \Phi_z = \frac{s_z}{s_x s_y} e_j. \quad (7)$$

Equations (3)-(5) are reduced to

$$\begin{aligned}-\omega^2 \Phi_x Q_x s_y^2 + P_x \Phi_x - \omega^2 \Phi_x Q_y s_z^2 + P_y \Phi_y \\ -\omega^2 \Phi_z Q_z s_x^2 + P_z \Phi_z = -j\omega \int_v \frac{1}{\mu} \vec{N} \cdot \vec{J} dv\end{aligned}\quad (8)$$

and defining the signal envelope as

$$\begin{aligned}e_j(t) &= u_j(t) e^{j\omega_c t}, \\ \Phi_j(t) &= \psi_j(t) e^{j\omega_c t}, \\ J_z(t) &= j_z(t) e^{j\omega_c t}.\end{aligned}\quad (9)$$

Substituting (9) into (8) we can obtain the differential equation about the signal envelope

$$\begin{aligned}Q_x \frac{d^2 \psi_z}{dt^2} + [S_1] \frac{d \psi_z}{dt} + [S_2] \psi_z + Q_y \frac{d^2 \psi_x}{dt^2} + \\ [S_3] \frac{d \psi_x}{dt} + [S_4] \psi_x + Q_z \frac{d^2 \psi_y}{dt^2} + [S_5] \frac{d \psi_y}{dt} + \\ [S_6] \psi_y = -\left(\frac{\partial f_i}{\partial t} + j\omega_c f_i\right)\end{aligned}\quad (10)$$

where

$$\begin{aligned}S_1 &= 2(j\omega_c + \frac{\sigma_y}{\epsilon_0}) Q_x, & S_2 &= (j\omega_c + \frac{\sigma_y}{\epsilon_0})^2 Q_x + P_x, \\ S_3 &= 2(j\omega_c + \frac{\sigma_z}{\epsilon_0}) Q_y, & S_4 &= (j\omega_c + \frac{\sigma_z}{\epsilon_0})^2 Q_y + P_y, \\ S_5 &= (j\omega_c + \frac{\sigma_x}{\epsilon_0})^2 Q_z + P_z, & S_6 &= 2(j\omega_c + \frac{\sigma_x}{\epsilon_0}) Q_z, \\ f_i &= \int_v \frac{1}{\mu} \vec{N}_i \cdot \vec{J} dv.\end{aligned}\quad (11)$$

Using Newmark-Beta formulation to discretize (10), we can obtain the time recursive formulation

$$R_1\psi_z^{n+1} + R_2\psi_z^n + R_3\psi_z^{n-1} + R_4\psi_x^{n+1} + R_5\psi_x^n + R_6\psi_x^{n-1} + R_7\psi_y^{n+1} + R_8\psi_y^n + R_9\psi_y^{n-1} = -\left(\frac{f_i^{n+1} - f_i^{n-1}}{2\Delta t} + j\omega_c \frac{f_i^{n+1} + 2f_i^n + f_i^{n-1}}{4}\right) \quad (12)$$

where R_i are the coefficient matrixes. According to (7), we can obtain the relationship between the ψ_{ξ} ($\xi=x,y,z$) and u with Newmark-Beta formulation

$$\psi_{\xi}^{n+1} = a_{\xi 5}\psi_{\xi}^n + a_{\xi 6}\psi_{\xi}^{n-1} + a_{\xi 7}u^{n+1} + a_{\xi 8}u^n + a_{\xi 9}u^{n-1}, \quad (13)$$

where $\xi=x,y,z$ and $a_{\xi i}$ are the complex coefficients. Combining equations (12) and (13), and solving them, the complex signal envelope vectors $u=[u_1, u_2, \dots, u_N]$ and $\Psi_{\xi}=[\Psi_{\xi 1}, \Psi_{\xi 2}, \dots, \Psi_{\xi N}]$ can be solved in time domain.

In order to reduce the discretization error, we use spatially variant conductivity along the normal axis [7]

$$\sigma_z(z) = \frac{\sigma_{\max} |z - z_0|^m}{\sqrt{\epsilon_r} d^m} \quad (14)$$

where z_0 is the interface between the PML region and non-PML region, d is the depth of the PML and m is the order the polynomial variation. The order $m=2$ is chosen for better absorption.

Two examples will be presented here to validate our EVFE formulations with PML boundary conditions. The first one is a 2-D example with the PML set at the end of a parallel waveguide. The incident modulated Gaussian pulse's carrier frequency is 2.91 GHz and the excitation bandwidth is 0.8 GHz. The second example is a 3-D rectangle waveguide terminated with PML absorber. The crossection of the waveguide is 10.16 mm and 22.86 mm. The excitation's carrier frequency is about 10 GHz and the bandwidth is about 4 GHz.

Figs 1 and 2 show the results of PML tests. Both in 2-D and 3-D cases, PML can provide about -40dB absorption when four layers of PML are set. As the layers of PML increase, the absorption to the incident increases quickly.

III. WAVEGUIDE PROBLEM SOLUTION WITH THE 3-D EVFE AND PML

Two numerical examples will be shown here to verify the precision and efficiency of EVFE technique with PML. The first simulation structure is a rectangular waveguide with a dielectric post discontinuity shown in Fig. 3. The same geometry was analyzed by J-S Wang using FEM [12]. The waveguide has a width $a = 22.86$ mm (y-direction) and height $b = 10.16$ mm (x-direction). The dielectric slab has a height equal to that of the guide, width

$c = 12$ mm, and length $d = 6$ mm. The relative dielectric constant of the slab is 8.2. In order to avoid the influence of the higher order modes, we set the observation point far enough from the discontinuity. TE₁₀ mode is excited inside the waveguide with the center frequency 10 GHz and bandwidth 4 GHz. The excitation of EVFE in equation is represented as

$$J(t) = j(t) e^{j\omega_c t} = \exp\left[-\frac{(t-t_0)^2}{T^2}\right] e^{j\omega_c t} \quad (15)$$

where $T = 4dt$, $t_0 = 12dt$ and $dt = 25$ ps.

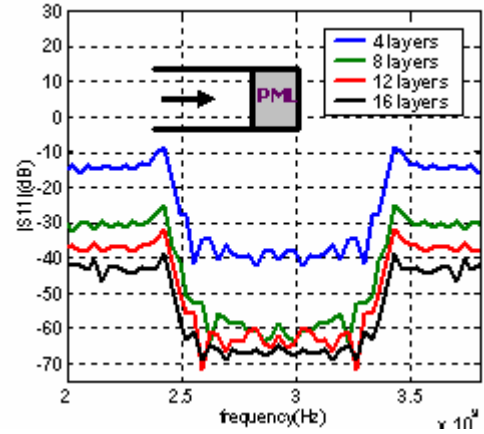


Fig. 1. Performance of PML for 2-D.

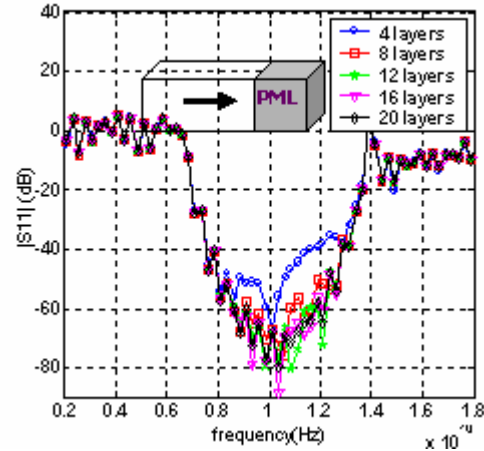


Fig. 2. Performance of PML for 3-D.

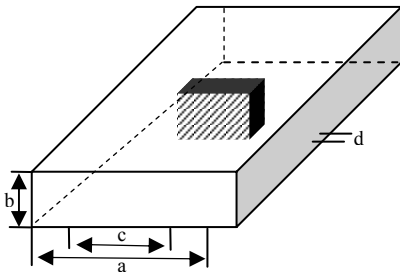


Fig. 3. Dielectric post discontinuity in a rectangular waveguide.

In FETD or FDTD case, CFL condition requires the time step to be less than 2ps. The total steps are about 12.5 times as many as what EVFE requires. In this example, 10 layers of PML are set at the each end of the waveguide.

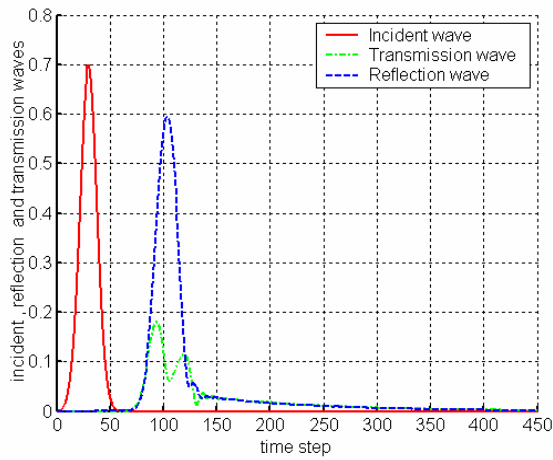


Fig. 4. Incident, reflection and transmission waves.

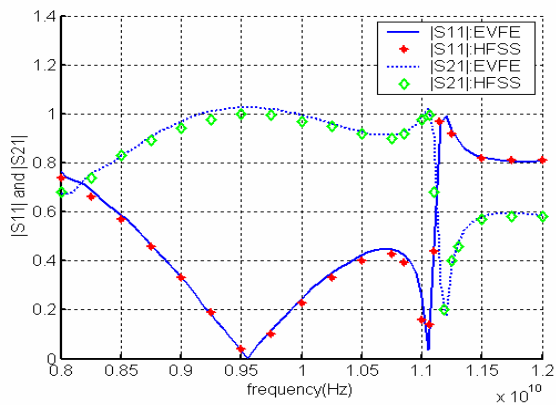


Fig. 5. Magnitudes of S_{11} and S_{21} .

Numerical Results for the time domain fields and magnitudes of S_{11} and S_{21} are shown in Fig. 4 and Fig. 5 respectively. The magnitudes of S_{11} and S_{21} are compared with the results calculated using HFSS, and they agree with each other very well.

The second example is a waveguide with a rectangle corner bend, filled with air, shown in Fig. 6. The waveguide has a width $a = 20$ mm and height $b = 4$ mm, with 10 layers PML set in two ends. In order to avoid the influence of the high order modes, we set the observation point far enough from the discontinuity. TE_{10} mode is excited inside the waveguide with a center frequency, $f_c = 13$ GHz and bandwidth $\Delta f = 4$ GHz. Numerical results of magnitudes of S_{11} and S_{21} are shown in Fig. 7. S_{11} and S_{21} are compared with the results calculated using HFSS, and they agree very well.

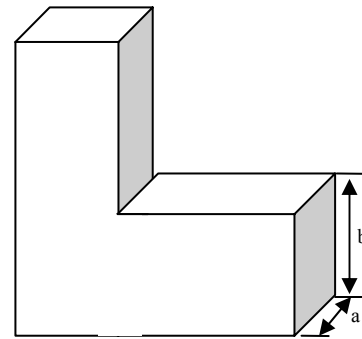


Fig. 6. Waveguide with right-angle corner band. $a = 20$ mm, $b = 4$ mm.

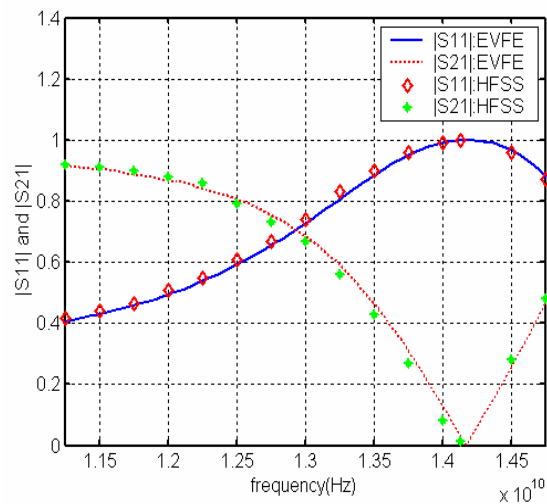


Fig. 7. Magnitudes of S_{11} and S_{21} .

IV. ANALYSIS OF 2-D SCATTERING PROBLEMS WITH EVFE & PML

Finite element methods have been extensively applied for scattering problem analysis with absorbing boundary conditions (ABCs). The plane wave excitation is straightforward for traditional Mur's ABCs. However, how to excite a plane wave in finite element analysis coupled with Perfect Matching Layer (PML) efficiently has not been thoroughly studied. In [13], a scattered field formulation is used for the entire computational domain. Therefore the applicability is limited for conductor only cases. In [10] and [14] the first effective approach addressing the excitation problem is proposed. The wave equation for the total field is used for the computational region while in PML region the incident field is switched to that in free space. To solve the unknown scattered field, however, it involves the updating of incident fields over the entire computational domain. Here, a simple and physically clear way to excite the plane wave is proposed based on the equivalence principle. The essential idea is to use both equivalent electric and magnetic currents on the virtual surface between these two regions. Though this concept has been well accepted for finite difference time domain (FDTD) simulations with PML [15], the implementation to the finite element approach has not been reported in literature yet. The main reason is that FEM is based on the single field (E-field) formulation, while both equivalent electric and magnetic currents need to be used to satisfy equivalence principle. In this paper, we shall present the implementation of the equivalence principle for plane wave incidence. With the proposed approach, this technique is applied to solve the scattering problems using finite element time domain (FETD) or envelope-finite element (EVFE) techniques, as the final performance of these techniques are strongly dependent on the perfect implementation of the PML boundary condition.

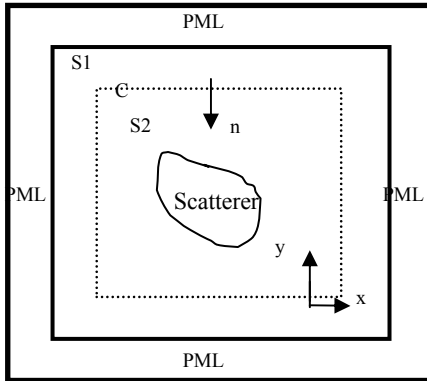


Fig. 8. Geometry of the 2-D scattering problem.

To derive the EVFE_PML formulations for the 2-D scattering problems, we start from the general wave equation in PML region

$$\nabla \times ((\mu[\Lambda])^{-1} \cdot \nabla \times \vec{E}) - \omega^2 \epsilon[\Lambda] \vec{E} = 0. \quad (16)$$

This formulation can be extended to the whole computational area by defining $s_x=s_y=s_z=1$ in the non-PML region. Use testing function T to test the wave equation (16), we can obtain

$$\int_S \frac{\omega^2}{c^2} \epsilon_r[\Lambda] \vec{E} T ds = \int_S T \nabla \times [(\mu_r[\Lambda])^{-1} \nabla \times \vec{E}] ds \quad (17)$$

where S is the surface of the whole 2-D computational domain. Defining an inner boundary C , S is separated into the inner region S_2 and outer region S_1 , as shown in Fig. 8. It should be noted that the equivalent sources are placed on C and the inner boundary should be selected in the free space area enclosed by PML. Therefore, we represent the field in S_1 and S_2 by \vec{E}^+ , \vec{E}^- and \vec{H}^+ , \vec{H}^- . Rewriting (17) in the region S_1 and S_2 yields,

$$\int_{S_1} \frac{\omega^2}{c^2} \epsilon_r[\Lambda] \vec{E}^+ T ds + \int_{S_1} \nabla T \times [(\mu_r[\Lambda])^{-1} \nabla \times \vec{E}^+] ds - \oint_C T [\Lambda]^{-1} \nabla \times \vec{E}^+ \cdot d\vec{l} = 0. \quad (18)$$

$$\int_{S_2} \frac{\omega^2}{c^2} \epsilon_r[\Lambda] \vec{E}^- T ds + \int_{S_2} \nabla T \times [(\mu_r[\Lambda])^{-1} \nabla \times \vec{E}^-] ds - \oint_{-C} T [\Lambda]^{-1} \nabla \times \vec{E}^- \cdot d\vec{l} = 0. \quad (19)$$

Furthermore, the field can be expanded using finite element basis functions by letting

$$T = N_i, \quad \vec{E}^\pm = \sum_{j=1}^N \hat{z} N_j e_j^\pm. \quad (20)$$

Substituting (1), (2), (20) into (18) and (19), for 2-D TM wave incidence, it yields

$$\sum_{j=1}^N \int_{S_1} \frac{\omega^2}{c^2} \epsilon_r S_x S_y N_i N_j e_j^+ ds - \sum_{j=1}^N e_j^+ \int_{S_1} \frac{1}{\mu_r} \left[\frac{s_y}{s_x} \frac{\partial N_j}{\partial x} \frac{\partial N_i}{\partial x} + \frac{s_x}{s_y} \frac{\partial N_j}{\partial y} \frac{\partial N_i}{\partial y} \right] ds - \oint_C N_i (-j\omega \mu_r \mu_0 \vec{H}^+) \cdot d\vec{l} = 0, \quad (21)$$

$$\sum_{j=1}^N \int_{s_2} \frac{\omega^2}{c^2} \epsilon_r S_x S_y N_i N_j e_j^- ds - \sum_{j=1}^N e_j^- \int_{s_2} \frac{1}{\mu_r} \left[\frac{s_y}{s_x} \frac{\partial N_j}{\partial x} \frac{\partial N_i}{\partial x} + \frac{s_x}{s_y} \frac{\partial N_j}{\partial y} \frac{\partial N_i}{\partial y} \right] ds - \oint_C N_i (-j\omega \mu_r \mu_0 \vec{H}^-) \cdot d\vec{l} = 0. \quad (22)$$

Adding (21) and (22) together, we can obtain

$$\sum_{j=1}^N \int_{s_1+s_2} \frac{\omega^2}{c^2} \epsilon_r S_x S_y N_i N_j e_j ds - \sum_{j=1}^N e_j \int_{s_1+s_2} \frac{1}{\mu_r} \left[\frac{s_y}{s_x} \frac{\partial N_j}{\partial x} \frac{\partial N_i}{\partial x} + \frac{s_x}{s_y} \frac{\partial N_j}{\partial y} \frac{\partial N_i}{\partial y} \right] ds - \oint_C N_i [-j\omega \mu_r \mu_0 (\vec{H}^+ - \vec{H}^-)] \cdot d\vec{l} = 0. \quad (23)$$

In (23), e represents e^+ inside region S_1 and e^- inside S_2 . The loop integral in (23) shows the contribution of the equivalent electric current on C. The relation between the fields in region 1 and region 2 can be expressed as

$$\vec{E}^+ - \vec{E}^- = \vec{E}^{inc}, \quad (24)$$

$$\vec{H}^+ - \vec{H}^- = \vec{H}^{inc}. \quad (25)$$

Because the electric field on the boundary C is not continuous due to the magnetic current excitation, it needs to be defined. Here we assume $e=e^-$ on C, thus e^+ unknowns on the excitation boundary can be eliminated by using (24). Substituting (24) and (25) into (23) yields a general equation for E fields

$$\sum_{j=1}^N e_j \int_s \frac{\omega^2}{c^2} \epsilon_r S_x S_y N_i N_j ds - \sum_{j=1}^N e_j \int_s \frac{1}{\mu_r} \left[\frac{s_y}{s_x} \frac{\partial N_j}{\partial x} \frac{\partial N_i}{\partial x} + \frac{s_x}{s_y} \frac{\partial N_j}{\partial y} \frac{\partial N_i}{\partial y} \right] ds = \oint_C N_i [-j\omega \mu_r \mu_0 (H^{inc})] \cdot d\vec{l} - \sum_{j=1}^{N_1} \int_s \frac{\omega^2}{c^2} \epsilon_r S_x S_y N_i N_j E_j^{inc} ds + \sum_{j=1}^{N_1} E_j^{inc} \int_s \frac{1}{\mu_r} \left[\frac{s_y}{s_x} \frac{\partial N_j}{\partial x} \frac{\partial N_i}{\partial x} + \frac{s_x}{s_y} \frac{\partial N_j}{\partial y} \frac{\partial N_i}{\partial y} \right] ds. \quad (26)$$

In (26), both electric and magnetic currents are included in the right hand side. N_1 denotes the element numbering which are related with the excitation boundary C.

Thus we can obtain the matrix equation

$$-\frac{\omega^2}{c^2} s_x s_y e_j [A] + e_j \frac{s_x}{s_y} [B] + e_j \frac{s_y}{s_x} [C] = j\omega \mu_0 f + \frac{\omega^2}{c^2} s_x s_y E_j^{inc} [A] - E_j^{inc} \frac{s_x}{s_y} [B] - E_j^{inc} \frac{s_y}{s_x} [C] \quad (27)$$

where

$$[A]_{ij} = \int_s \epsilon_r N_i N_j ds,$$

$$[B]_{ij} = \int_s \frac{1}{\mu_r} \frac{\partial N_j}{\partial y} \frac{\partial N_i}{\partial y} ds,$$

$$[C]_{ij} = \int_s \frac{1}{\mu_r} \frac{\partial N_j}{\partial x} \frac{\partial N_i}{\partial x} ds,$$

$$[f]_i = \oint_C H^{inc} N_i \mu_r \cdot d\vec{l}.$$

Notice that E^{inc} is zero except on the excitation boundary C. The internal boundary integral terms inside PML vanish because of the continuity of tangential H field. If we define another variable Φ and Φ^{inc}

$$\Phi_j = e_j / (-\omega^2 s_x s_y)$$

$$\text{and} \quad \Phi_j^{inc} = E_j^{inc} / (-\omega^2 s_x s_y) \quad (28)$$

and substitute (28) into (27), we get

$$-\frac{\omega^2}{c^2} s_x s_y e_j [A] - \Phi_j \omega^2 s_x^2 [B] - \Phi_j \omega^2 s_y^2 [C] = \frac{\omega^2}{c^2} s_x s_y E_j^{inc} [A] + \Phi_j^{inc} \omega^2 s_x^2 [B] + \Phi_j^{inc} \omega^2 s_y^2 [C] + j\omega \mu_0 f. \quad (29)$$

So far, (29) is the derived frequency domain wave equation in PML medium. A transformation is needed in order to change (29) to time/envelope domain. First we define the complex signal envelope of the fields as

$$\begin{aligned} e_j(t) &= u_j(t) e^{j\omega_c t}, & \Phi_j(t) &= \psi_j(t) e^{j\omega_c t}, \\ e_j^{inc}(t) &= u_j^{inc}(t) e^{j\omega_c t}, & J_z(t) &= j_z(t) e^{j\omega_c t}, \\ \Phi_j^{inc}(t) &= \psi_j^{inc}(t) e^{j\omega_c t}, \end{aligned} \quad (30)$$

where ω_c is the carrier frequency and u, ψ, j_z are the complex envelopes. Further incorporating the Fourier transform relationship between frequency domain and time domain, the transform between the frequency domain operators and envelope domain operators are:

$$j\omega \rightarrow \frac{\partial}{\partial t} e^{j\omega_c t} + j\omega_c e^{j\omega_c t}, \quad (31)$$

$$-\omega^2 \rightarrow \frac{\partial^2}{\partial t^2} e^{j\omega_c t} + 2j\omega_c \frac{\partial}{\partial t} e^{j\omega_c t} - \omega_c^2 e^{j\omega_c t}.$$

It is evident that setting ω_c as zero in the above formulas leads to the conventional Fourier transform. Therefore, (29) is converted into envelope domain:

$$\begin{aligned}
& [T_1] \frac{d^2 u_j}{dt^2} + [T_2] \frac{du_j}{dt} + [T_3] u_j + [T_4] \frac{d^2 \psi_j}{dt^2} + [T_5] \frac{d\psi_j}{dt} \\
& + [T_6] \psi_j = \frac{\partial f}{\partial t} + [T_1] \frac{d^2 u_j^{inc}}{dt^2} + [T_2] \frac{du_j^{inc}}{dt} + [T_3] u_j^{inc} \\
& + [T_4] \frac{d^2 \psi_j^{inc}}{dt^2} + [T_5] \frac{d\psi_j^{inc}}{dt} + [T_6] \psi_j^{inc},
\end{aligned} \tag{32}$$

where

$$\begin{aligned}
[T_1]_{ij} &= \frac{[A]_{ij}}{c^2}, \\
[T_2]_{ij} &= \frac{[A]_{ij}}{c^2} \left(2j\omega_c + \frac{\sigma_x + \sigma_y}{\epsilon_0} \right), \\
[T_3]_{ij} &= \frac{[A]_{ij}}{c^2} \left(-\omega_c^2 + j\omega_c \frac{\sigma_x + \sigma_y}{\epsilon_0} + \frac{\sigma_x \sigma_y}{\epsilon_0^2} \right), \\
[T_4]_{ij} &= [B]_{ij} + [C]_{ij}, \\
[T_5]_{ij} &= 2 \left(j\omega_c + \frac{\sigma_x}{\epsilon_0} \right) [B]_{ij} + 2 \left(j\omega_c + \frac{\sigma_y}{\epsilon_0} \right) [C]_{ij}, \\
[T_6]_{ij} &= \left(j\omega_c + \frac{\sigma_x}{\epsilon_0} \right)^2 [B]_{ij} + \left(j\omega_c + \frac{\sigma_y}{\epsilon_0} \right)^2 [C]_{ij}.
\end{aligned} \tag{33}$$

For the same reason, equation (28) results in,

$$\begin{aligned}
u_j^{inc} &= \frac{\partial^2 \psi_j^{inc}}{\partial t^2} + \left(2j\omega_c + \frac{\sigma_x + \sigma_y}{\epsilon_0} \right) \frac{\partial \psi_j^{inc}}{\partial t} \\
& + \left(-\omega_c^2 + j\omega_c \frac{\sigma_x + \sigma_y}{\epsilon_0} + \frac{\sigma_x \sigma_y}{\epsilon_0^2} \right) \psi_j^{inc}. \\
u_j &= \frac{\partial^2 \psi_j}{\partial t^2} + \left(2j\omega_c + \frac{\sigma_x + \sigma_y}{\epsilon_0} \right) \frac{\partial \psi_j}{\partial t} + \left(-\omega_c^2 + j\omega_c \frac{\sigma_x + \sigma_y}{\epsilon_0} + \frac{\sigma_x \sigma_y}{\epsilon_0^2} \right) \psi_j.
\end{aligned} \tag{34}$$

Using Newmark-Beta formulations [3] to discretize (32) and (34) in time domain yields two difference equations. The ‘‘Mutual Difference’’ scheme [5] can then be used to solve these two equations jointly to update the complex signal envelope vector $u = [u_1, u_2, \dots, u_N]$ and $\Psi = [\Psi_1, \Psi_2, \dots, \Psi_N]$ in time.

Two numerical examples are presented to validate the proposed scheme. The scattering problem about the cylindrical perfect electric conductor (PEC) is first solved using EVFE technique. Here we define the incident plane wave in the form of modulated Gaussian pulse. For simplicity, we assume the incident wave impinges in x direction, and the carrier frequency is ω_c , the envelopes of the incident fields thus become

$$\vec{E}^{inc} = \hat{z} \exp \left(- \left[\frac{t - t_2 - x/v}{t_1} \right]^2 - j\omega_c x/v \right)$$

$$\begin{aligned}
\vec{H}^{inc} &= -\hat{y} \frac{1}{\mu} \\
& \int \left(2 \left[\frac{t - t_2 - x/v}{vt_1^2} \right] - \frac{j\omega_c}{v} \right) \exp \left(- \left[\frac{t - t_2 - x/v}{t_1} \right]^2 - j\omega_c x/v \right) dt.
\end{aligned} \tag{35}$$

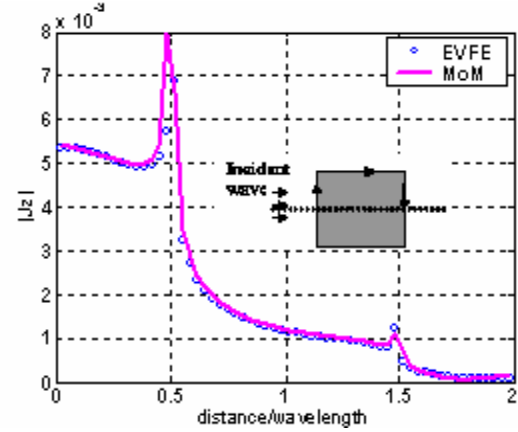


Fig.9. Magnitude of surface current on upper half cylinder at $f=2$ GHz.

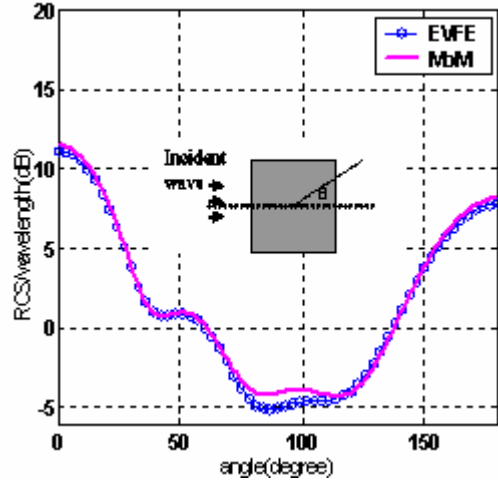


Fig.10. Normalized RCS of the cylinder in Fig. 9 at different observation angles at $f=2$ GHz.

Consider a perfectly conducting square cylinder with the side length 0.15 m. Six PML layers are set 2.5 cm away from the PEC cylinder’s surface. The incidence wave is a modulated Gaussian pulse (35) with a center frequency 2 GHz and a bandwidth of 1 GHz. The polarization is TM. The excitation boundary C is only 1.5 cm away from the

PEC object and 1 cm away from the PML region. The result for the surface current on the upper half of the cylinder is plotted in Fig. 9, where the frequency is 2 GHz. The result of the normalized RCS is presented in Fig. 10. The results agree well with those obtained using Method of Moments (MoM).

Another example is a square two-dimensional homogeneous anisotropic dielectric scatterer. The scatterer to be simulated is a square anisotropic cylinder with $\epsilon_{zz}=1.5$, $\mu_{xx}=1.5$, $\mu_{yy}=3$ and $k_0s=10$, where k_0 is set according to the center frequency of the Gaussian incident plane wave, and s is the side length of the square cylinder. In this case, the excitation boundary C is only $0.1\lambda_0$ away from the scatterer and $0.1\lambda_0$ away from the ten layers PML region, where λ_0 is according to the center frequency. The result about the magnitude of the magnetic current on center frequency is plotted in Fig. 11 which agrees well with the result of FDTD [16].

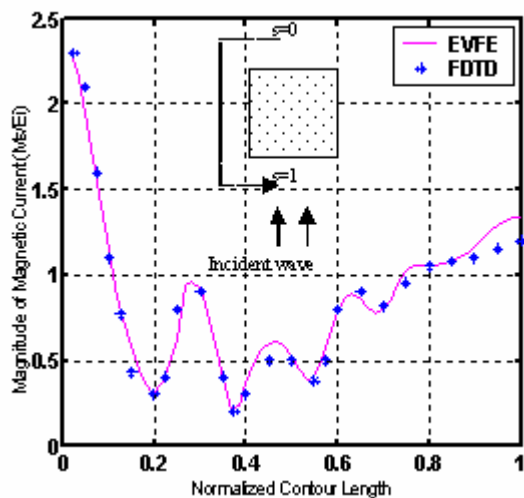


Fig. 11. Surface magnetic current distribution of square anisotropic cylinder with $\epsilon_{zz}=1.5$, $\mu_{xx}=1.5$, $\mu_{yy}=3$ and $k_0s=10$.

V. CONCLUSION

In this paper, anisotropic PML has been implemented into the 2-D and 3-D EVFE formulations. Numerical examples have been presented to evaluate the PML's performance and about 40dB absorption is achieved when a 4-layer absorber is used in both 2-D and 3-D cases. The EVFE technique with PML is validated through the simulation of the guided wave structures. The new method for exciting a plane wave inside the PML boundary has been proposed

and the numerical examples of scattering problems are also presented to show the validity of the formulations.

REFERENCE

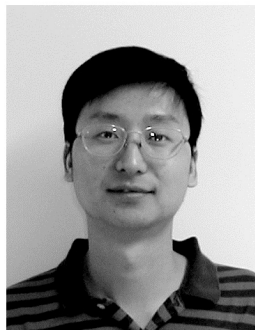
- [1] S. D. Gedney and U. Navsariwala, "An unconditionally stable finite element time-domain solution of the vector wave equation", *Microwave and Guided Wave Letters, IEEE [see also IEEE Microwave and Wireless Components Letters]*, pp. 332-334, Vol. 5, Issue: 10, Oct. 1995.
- [2] W. Yao and Y. Wang, "Numeric Dispersion Analysis of 3D Envelope-Finite Element (EVFE) Method", *IEEE-Antenna and Propagation Symposium 2003, Columbus, Ohio*.
- [3] Y. Wang and T. Itoh, "Envelope-finite element (EVFE) Technique – A more efficient time domain scheme", *IEEE Trans. Microwave Theory Tech.* Vol. 49, pp 2241 -2247, Dec. 2001.
- [4] H. P. Tsai, Y. Wang and T. Itoh, "Efficient analysis of microwave passive structures using 3-D envelope-finite element (EVFE)", *IEEE Trans. Microwave Theory Tech.* Vol. 50, Issue: 12, pp. 2721 –2727, Dec. 2002.
- [5] W. Yao and Y. Wang, "An Equivalence Principle Based Plane Wave Excitation in Time/Envelope Domain Finite Element Analysis", submitted to *IEEE - Antennas and Wireless Propagation Letters*.
- [6] H. S. Yap, "Designing to digital wireless specifications using circuit envelope simulation," in *Asia-Pacific Microwave Conf.*, pp. 173–176, 1997.
- [7] J. P. Berenger, "A perfectly matched layer for the absorption of electromagnetic waves," *J. Comput. Phys.*, Vol. 114, pp. 185–200, Oct. 1994.
- [8] Z. S. Sacks, D. M. Kingsland, R. Lee, and J.-F. Lee, "A perfectly matched anisotropic absorber for use as an absorbing boundary condition," *IEEE Trans. Antennas Propagat.*, Vol. 43, pp. 1460–1463, Dec. 1995.
- [9] S.D. Gedney, "An Anisotropic Perfectly Matched Layer Absorbing Medium for the Truncation of FDTD Lattices," *IEEE Trans. Antennas Propagat.*, Vol. 44, no. 12, pp. 1630-1639, Dec. 1993.
- [10] D. Jiao, J. M. Jin, E. Michielssen and D. J. Riley "Time-Domain Finite-Element Simulation of Three-Dimensional Scattering and Radiation Problems Using Perfectly Matched Layers", *Trans. Antennas Propagat.*, Vol. 51, (no. 2), pp. 296-305, Feb. 2003.
- [11] H. P. Tsai, Y. Wang and T. Itoh, "An Unconditionally Stable Extended (USE) Finite Element Time Domain Solution of Active Nonlinear Microwave Circuits Using Perfectly Matched

- Layers”, *IEEE Trans. Microwave Theory Tech.*, pp 2226–2232, Oct. 2002.
- [12] J-S Wang and R. Mittra, “Finite Element Analysis of MMIC Structures and Electronic Packages Using Absorbing Boundary Conditions,” *IEEE Trans. Microwave Theory and Tech.*, Vol. 42, No. 3, pp. 441-449, Mar. 1994.
- [13] D.M. Kingsland, J. Gong, J. L. Volakis and J.-F. Lee, “Performance of an anisotropic artificial absorber for truncating finite-element meshes”, *IEEE Transactions on Antennas and Propagation*, Vol. 44, pp. 979–981, July 1996.
- [14] J. Jin, “The finite element method in electromagnetics”, second edition, John Wiley & Sons, Inc, 2002.
- [15] A. Taflove, “Computational electrodynamics– the finite-difference time-domain Method”, Artech House, Inc, 1995.
- [16] B. Beker, K. R. Umashankar and A. Taflove, “Numerical analysis and validation of the combined field surface integral equations for electromagnetic scattering by arbitrary shaped two-dimensional anisotropic objects”, *IEEE Trans. Antenna and Propagation*. Vol. 37, pp 1573-1581, Dec. 1989.



Weijun Yao received the B.S. degree in electrical engineering from University of Science and Technology of China (USTC), China in 2001 and M.S degree in electrical engineering department from University of California, Los Angeles in 2003. He is currently a Ph.D

student in the department of electrical engineering in University of California, Los Angeles. His research interest includes smart antenna system design, UWB system design, and numeric modeling of microwave circuits and antenna.



Yuanxun Wang received the B.S. degree in electrical engineering from University of Science and Technology of China (USTC), Hefei, in 1993, the M.S. and the Ph.D. degrees in electrical engineering from University of Texas at Austin, in 1996 and 1999. From 1995 to

1999, he worked as a Research Assistant in the Department of Electrical and Computer Engineering, University of Texas at Austin.

From 1999 to 2002, he worked as a research engineer and lecturer, in the Department of Electrical Engineering, University of California at Los Angeles (UCLA), prior to joining the faculty. He is an assistant professor in Electrical Engineering Department since 2002. His work is focused on high performance antenna array and microwave amplifier systems for wireless communication and radar, as well as numerical modeling techniques. His current research interests feature the fusion of signal processing and circuit techniques in microwave system design. He is a member of IEEE and SPIE. He has authored and coauthored over 60 refereed journal and conference papers.



Tatsuo Itoh received the Ph.D. Degree in Electrical Engineering from the University of Illinois, Urbana in 1969.

From September 1966 to April 1976, he was with the Electrical Engineering Department, University of Illinois. From April 1976 to August 1977, he was a Senior Research Engineer in the Radio Physics Laboratory, SRI International, Menlo Park, CA.

From August 1977 to June 1978, he was an Associate Professor at the University of Kentucky, Lexington. In July 1978, he joined the faculty at The University of Texas at Austin, where he became a Professor of Electrical Engineering in 1981 and Director of the Electrical Engineering Research Laboratory in 1984. During the summer of 1979, he was a guest researcher at AEG-Telefunken, Ulm, West Germany. In September 1983, he was selected to hold the Hayden Head Centennial Professorship of Engineering at The University of Texas. In September 1984, he was appointed Associate Chairman for Research and Planning of the Electrical and Computer Engineering Department at The University of Texas. In January 1991, he joined the University of California, Los Angeles as Professor of Electrical Engineering and holder of the TRW Endowed Chair in Microwave and Millimeter Wave Electronics. He was an Honorary Visiting Professor at Nanjing Institute of Technology, China and at Japan Defense Academy. In April 1994, he was appointed as Adjunct Research Officer for Communications Research Laboratory, Ministry of Post and Telecommunication, Japan. He currently holds Visiting Professorship at University of Leeds, United Kingdom. He received a number of awards including Shida Award from Japanese

Ministry of Post and Telecommunications in 1998, Japan Microwave Prize in 1998, IEEE Third Millennium Medal in 2000, and IEEE MTT Distinguished Educator Award in 2000. He was elected to a member of National Academy of Engineering in 2003. Dr. Itoh is a Fellow of the IEEE, a member of the Institute of Electronics and Communication Engineers of Japan, and Commissions B and D of USNC/URSI. He served as the Editor of IEEE Transactions on Microwave Theory and Techniques for 1983-1985. He serves on the Administrative Committee of IEEE Microwave Theory and Techniques Society. He was Vice President of the Microwave Theory and Techniques Society in 1989 and President in 1990. He was the Editor-in-Chief of IEEE Microwave and Guided Wave Letters from 1991 through 1994. He was elected as an Honorary Life Member of MTT Society in 1994. He was the Chairman of USNC/URSI Commission D from 1988 to 1990, and Chairman of Commission D of the International URSI for 1993-1996. He is Chair of Long Range Planning Committee of URSI. He serves on advisory boards and committees of a number of organizations.

He has 310 journal publications, 640 refereed conference presentations and has written 30 books/book chapters in the area of microwaves, millimeter-waves, antennas and numerical electromagnetics. He generated 60 Ph.D. students.

Applications of the Transmission Line Matrix Method to Microwave Scanning Microscopy

Razvan Ciocan

Physics and Astronomy Department,
Clemson University, SC 29634-0978, USA
ciocan@clemson.edu

Nathan Ida

Electrical Engineering Department,
The University of Akron, OH 44325-3904, USA
ida@uakron.edu

Eugenia Ciocan

412 Old Central Rd # 4 SC 29631, USA
eugeniac1@yahoo.com

Huabei Jiang

Physics and Astronomy Department,
Clemson University, SC 29634-0978, USA
hjiang@clemson.edu

Abstract - A three-dimensional transmission-line matrix (TLM) model was developed to simulate microwave-scanning microscopy. A TLM algorithm that allows the simulation of the scanning was developed. Numerical modeling was carried out for frequencies that are commonly used in microwave nondestructive testing (1GHz – 20GHz). Structures with local discontinuities in the electric permittivity are modeled numerically. The excitation parameters used in numerical modeling of scanning microwave microscopy were determined based on an initial frequency experimental response obtained from a plate with known permittivity. The numerical model developed in this paper is based on the symmetric condensed node. The description of the TLM algorithm is given in a Hilbert space using a three-index notation.

I. INTRODUCTION

Microwave scanning microscopy is now one of the fastest growing areas among nondestructive methods. This method is applied in very different areas: aircraft industry, biological investigation, semiconductor industry and civil engineering. All these applications are based on the fact that microwave propagation is affected by a large number of material properties: composition, structure, moisture, delamination and presence of discontinuities. To make the microwave inspection a powerful tool in quantitative characterization of materials it is necessary to have a well-defined mathematical model of the testing problem. Because of the complexity of the problems, numerical methods were proven to give more appropriate models than analytical methods [1]. Microwave probes are robust enough to be placed in a hand-held configuration, which is the main advantage of microwave microscopy. Very high resolution

can be achieved with probes that can work in-situ and on line. By comparison with other methods, currently used in nondestructive evaluation of materials, the advantages of the microwave microscopy are:

- Possibility to detect subsurface discontinuities.
- There are no problems related to material contamination caused by coupling.
- No physical contact is required between the probe and the material to be investigated; therefore the surface can be surveyed rapidly.
- No changes are caused in the material; the measurement is entirely nondestructive.
- In the microwave frequency region, variation of dielectric permittivity for dielectric materials is significantly larger than the contrast due to density.

The Transmission Line Matrix (TLM) as a time domain technique that can deal with complex geometries is one of the most suitable numerical methods to model microwave testing. Unlike some other numerical techniques, the TLM algorithm does not involve any convergence criteria, a property that makes it an inherently stable method. This stability is reflected in the flexibility of the TLM method when dealing with various types of input signals and boundaries. These advantages can be exploited for nondestructive investigation in several ways:

- A configuration can be numerically modeled in order to improve the experiment design and for a better understanding of the results obtained.

- The TLM method offers a versatile tool to reconstruct the initial signal based on the actual digitized signal, for homogeneous media.
- The TLM method can easily generate a time or frequency domain signal for known configurations. Based on this, a multi-layer structure can be fully characterized using an iterative process. The material parameters, of the multi-layer structure under investigation can be changed in the TLM model, so that the numerically generated signal fits the experimental signal.

The first published account of TLM method dates back to 1971 [2]. This and following publications demonstrated that TLM could be used in a wide range of applications. Almost 30 years after the first article was published, the method is considered to be “a modeling process rather than a numerical method for solving differential equations” [3]. The advantage of TLM is that it provides a direct simulation of the phenomenon and not of the equation governing it [4].

II. ALGORITHM DESCRIPTION

The TLM algorithm developed in this paper is based on Symmetrical Condensed Node (SCN) [5]. A description of the algorithm is given in a Hilbert space and it is based on a previous work [6]. This description was adapted to the three-index notation used consistently in numerical implementation. The use of this notation has two immediate advantages:

- A physical interpretation for the scattering matrix written in symmetrical notation is revealed [7].
- The equivalence between the classical notation and the three-index notation is obtained directly.

In Table 1 the first two rows and the last two columns were added in order to show the correspondence between the voltages used in the three-index notation (first row, last column) and the classical notation (second row, 13th column). The scattering matrix in symmetrical notation is obtained by changing the positions of rows and columns respectively in such a way that the initial scattering matrix is rewritten as a system of three four by four matrices [8]. The first two rows and last two columns in Table 1 show how the permutations between lines and columns, respectively, took place. The three-index notation shows that these permutations group together the voltages corresponding to each polarization (Figure 1).

Table 1. Elements of scattering matrix in symmetrical notation.

V_{xny}	V_{xpy}	V_{xnz}	V_{xpz}	V_{ynz}	V_{ypz}	V_{ynx}	V_{ypx}	V_{znx}	V_{zpx}	V_{zny}	V_{zpy}		
3	11	6	10	5	7	1	12	2	9	4	8		
0	0	0	0	0	0	1	-1	0	0	1	1	3	V_{xny}
0	0	0	0	0	0	-1	1	0	0	1	1	11	V_{xpy}
0	0	0	0	1	1	0	0	1	-1	0	0	6	V_{xnz}
0	0	0	0	1	1	0	0	-1	1	0	0	10	V_{xpz}
0	0	1	1	0	0	0	0	0	0	1	-1	5	V_{ynz}
0	0	1	1	0	0	0	0	0	0	-1	1	7	V_{ypz}
1	-1	0	0	0	0	0	0	1	1	0	0	1	V_{ynx}
-1	1	0	0	0	0	0	0	1	1	0	0	12	V_{ypx}
0	0	1	-1	0	0	1	1	0	0	0	0	2	V_{znx}
0	0	-1	1	0	0	1	1	0	0	0	0	9	V_{zpx}
1	1	0	0	1	-1	0	0	0	0	0	0	4	V_{zny}
1	1	0	0	-1	1	0	0	0	0	0	0	8	V_{zpy}

Having this formulation for the scattering matrix, TLM can be represented by a numerable set of real quantities. A Hilbert space representation of the field state and evolution was introduced in [9]. Using this representation, the scattering matrix can be expressed by an operator as shown below. Considering the scattering matrix in symmetrical notation as given by Table 1, the scattering matrix operator, \bar{S} , is a real, symmetric and hermitian operator and it is written as

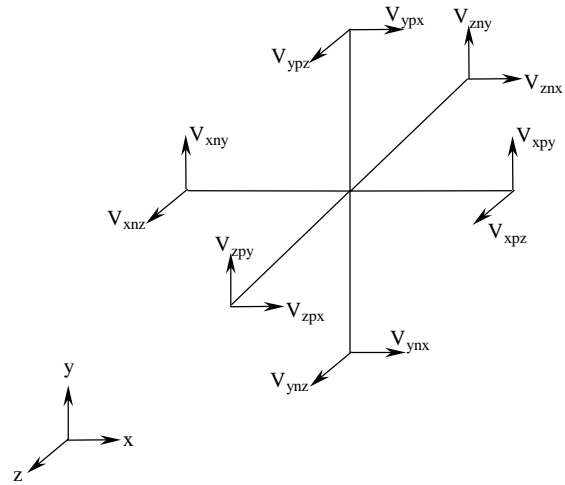


Figure 1. A schematic of SCN node.

$$\bar{S} = \begin{bmatrix} 0 & \bar{S}_0 & \bar{S}_0^{-T} \\ \bar{S}_0^{-T} & 0 & \bar{S}_0 \\ \bar{S}_0 & \bar{S}_0 & 0 \end{bmatrix} \quad (1)$$

with the matrix \bar{S}_0 given by

$$\bar{S}_0 = \frac{1}{2} \begin{bmatrix} 0 & 0 & 1 & -1 \\ 0 & 0 & -1 & 1 \\ 1 & 1 & 0 & 0 \\ 1 & 1 & 0 & 0 \end{bmatrix}. \quad (2)$$

Consider the node with the discrete space coordinates (l, m, n) . This corresponds to the space point of coordinates (x, y, z) , with: $x=l\Delta x$, $y=m\Delta y$ and $z=n\Delta z$. At the discrete time coordinate k , corresponding to the time $t=k\Delta t$, all the incident and scattered wave amplitudes can be described using the 12-dimensional complex vectors of space C^{12} , \bar{V}_{lmn}^i and \bar{V}_{lmn}^r respectively. These vectors belong to a twelve dimensional complex vector space C^{12} , and are related, using the indices l, m, n and k respectively, to the node with the discrete spatial coordinates (l, m, n) and to the temporal coordinate k . A Hilbert space, H_m , is introduced [8], having a system of orthonormal space domain vectors $|l, m, n\rangle$ assigned to each node positioned at (l, m, n) . In a similar way a Hilbert space, H_t , is introduced by associating the time coordinate k with the base vector $|k\rangle$. The Hilbert space where the TLM algorithm can be described is the Cartesian product of the previously introduced Hilbert spaces

$$H_w = C^{12} \otimes H_m \otimes H_t. \quad (3)$$

In this space the incident and reflected amplitudes are written as

$$|V^i\rangle = \sum_{k,l,m,n=-\infty}^{\infty} \bar{V}_{lmn}^i |k; l, m, n\rangle, \quad (4)$$

$$|V^r\rangle = \sum_{k,l,m,n=-\infty}^{\infty} \bar{V}_{lmn}^r |k; l, m, n\rangle. \quad (5)$$

In the H_w space the following operators are defined:

- Time shift operator \bar{T} ,

$$\bar{T}|k; l, m, n\rangle = |k+1; l, m, n\rangle. \quad (6)$$

- X-shift operator (\bar{X}) and its Hermitian conjugate (\bar{X}^*),

$$\bar{X}|k; l, m, n\rangle = |k; l+1, m, n\rangle, \quad (7)$$

$$\bar{X}^*|k; l, m, n\rangle = |k; l-1, m, n\rangle. \quad (8)$$

- Y-shift operator (\bar{Y}) and its Hermitian conjugate (\bar{Y}^*),

$$\bar{Y}|k; l, m, n\rangle = |k; l, m+1, n\rangle, \quad (9)$$

$$\bar{Y}^*|k; l, m, n\rangle = |k; l, m-1, n\rangle. \quad (10)$$

- Z-shift operator (\bar{Z}) and its Hermitian conjugate (\bar{Z}^*),

$$\bar{Z}|k; l, m, n\rangle = |k; l, m, n+1\rangle, \quad (11)$$

$$\bar{Z}^*|k; l, m, n\rangle = |k; l, m, n-1\rangle. \quad (12)$$

- Connection operator (\bar{F}),

$$|V^i\rangle = \bar{F}|V^r\rangle. \quad (13)$$

The connection operator shows that the reflected amplitudes are incident into the neighboring nodes and it is defined as

$$\begin{aligned} \bar{F} = & \bar{X} (\bar{\Delta}_{xny, xpy} + \bar{\Delta}_{xnz, xpz}) + \bar{X}^* (\bar{\Delta}_{xpy, xny} + \bar{\Delta}_{xpz, xnz}) + \\ & + \bar{Y} (\bar{\Delta}_{ynz, ypz} + \bar{\Delta}_{ynx, ypx}) + \bar{Y}^* (\bar{\Delta}_{ypz, ynz} + \bar{\Delta}_{ypx, ynx}) + \\ & + \bar{Z} (\bar{\Delta}_{znx, zpx} + \bar{\Delta}_{zny, zpy}) + \bar{Z}^* (\bar{\Delta}_{zpx, znx} + \bar{\Delta}_{zpy, zny}). \end{aligned} \quad (14)$$

In Eq. (14) the matrices $\bar{\Delta}_{o,p}$ (o, p are each three- index notations defined in row 1 of Table 1) are 12 by 12 matrices and each element of these matrices $(\bar{\Delta}_{i,j})_{o,p}$ is defined as

$$(\bar{\Delta}_{i,j})_{o,p} = \delta_{i,o} \delta_{j,p}. \quad (15)$$

The connection operator (\bar{F}) is a hermitian and unitary operator and therefore

$$\bar{F} = \bar{F}^{-1} = \bar{F}^*. \quad (16)$$

The simultaneous scattering matrix at all TLM mesh nodes is described as

$$|V^r\rangle = \bar{T}\bar{S}|V^i\rangle. \quad (17)$$

Eq. (17) shows that scattering by a TLM node causes a unit time delay Δt . The voltages defined in Figure 1 can be related to the tangential field components at the TLM node boundary by introducing the following vectors for each of the six faces of the TLM node:

- Reflected wave vectors,

$$\vec{V}_f^r = -\frac{1}{2} \left[\vec{n}_f \times (\vec{n}_f \times \vec{E}) + Z \vec{n}_f \times \vec{H} \right], \quad f = 1, 6. \quad (18)$$

- Incident wave vectors,

$$\vec{V}_f^i = -\frac{1}{2} \left[-\vec{n}_f \times (\vec{n}_f \times \vec{E}) + Z \vec{n}_f \times \vec{H} \right], \quad f = \overline{1, 6}. \quad (19)$$

The correspondence between the node cube faces denoted by f in Eqs. (18) and (19), and the three-index notation is given in Table 2:

Table 2. The correspondence between the TLM node face notation (f index) and the three-index notation.

f index	1	2	3	4	5	6
Corresponding plane in three index notation	xn	xp	yn	yp	zn	zp

As an example, the plane xp (corresponding to $f=2$) from Table 2 is that located on the positive half of the x axis. This plane contains the voltages V_{xpy} and V_{xpz} . The normal to this plane is given by,

$$\vec{n}_2 = [1 \ 0 \ 0]^T. \quad (20)$$

The field components in this plane are given by [6],

$$\vec{E} = \begin{bmatrix} k \begin{bmatrix} E_x \\ E_y \\ E_z \end{bmatrix}_{l+1/2, m, n} \end{bmatrix}, \quad (21)$$

$$\vec{H} = \begin{bmatrix} k \begin{bmatrix} H_x \\ H_y \\ H_z \end{bmatrix}_{l+1/2, m, n} \end{bmatrix}. \quad (22)$$

Substituting Eqs. (20) - (22) into Eqs. (18) and (19) the local reflected and incident wave vectors for a node located at (l, m, n) at moment k are given by [10]

$$\vec{V}_{2(l, m, n)}^r = [0 \ V_{xpy}^r \ V_{xpz}^r]^T, \quad (23)$$

$$\vec{V}_{2(l, m, n)}^i = [0 \ V_{xpy}^i \ V_{xpz}^i]^T. \quad (24)$$

The field quantities can be written in a more intuitive fashion in the three-index notation. For example, considering the notations in Figure 1, the components of the electric and magnetic fields are given by

$$E_x = -\frac{1}{2\Delta l} (V_{ynx}^i + V_{ypx}^i + V_{zpx}^i + V_{znx}^i), \quad (25)$$

$$E_y = -\frac{1}{2\Delta l} (V_{xny}^i + V_{xpy}^i + V_{zpy}^i + V_{zny}^i), \quad (26)$$

$$E_z = -\frac{1}{2\Delta l} (V_{xnz}^i + V_{xpz}^i + V_{ypz}^i + V_{ynz}^i), \quad (27)$$

$$H_x = \frac{V_{zpy}^i - V_{ynz}^i + V_{zpx}^i - V_{zpy}^i}{2Z_o \Delta l}, \quad (28)$$

$$H_y = \frac{V_{xnz}^i + V_{zpx}^i - V_{xpz}^i - V_{znx}^i}{2Z_o \Delta l}, \quad (29)$$

$$H_z = \frac{V_{xpy}^i - V_{ypx}^i - V_{xpy}^i + V_{ynx}^i}{2Z_o \Delta l}. \quad (30)$$

The numerical implementation of a desired model is performed in three steps: pre-processing, computation and post-processing.

The pre-processing step includes determining the excitation signal parameters and generating the boundary coordinates of complex geometries. The excitation parameters in the TLM model are changed until a good fit is obtained between the experimental and numerical generated curves for a simple geometry. For instance, one experimental response was obtained from a bakelite plate. An appropriate numerical excitation that can give the same response as that obtained from this reflector was a Gaussian pulse with central frequency 1.6 GHz.

The processing step is made mainly of the TLM algorithm. The main steps of this algorithm are [11]: initialization, scattering and connection. An additional step called scanning was added to these components. This step involves changing the position of excitation according to the experimental scanning pattern whereby the TLM algorithm is repeated for each new position. The time response for each position is saved in an output file for further processing.

The programs developed for the post-processing part perform the following tasks:

- Reading the data input files generated by the processing program.
- Data visualization in two or three dimensions for each iteration considered.
- Signal processing of the numerically generated signal in time and frequency domain.

III. ALGORITHM IMPLEMENTATION

The scattering matrix implementation of the SCN used for this application is based on an algorithm that explores the symmetry of the scattering matrix [12]. The voltages in the port model for SCN can be assigned using a three-character name [13]. A representation for this node is given in Figure 1. In Figure 1 the first index denotes polarization (x , y or z), the second is related to position on the link line, positive or negative (p or n) and the last index is related to link line (x ,

y or z). The voltages at all ports can be obtained considering all circular permutations of indices (x,y,z) denoted in general form as (i,j,k) . These voltages are obtained according to the scattering matrix. To minimize the number of operations the reflected voltages at any port are obtained using the following scheme [14]

$$V_{inj}^r = V_{temp} - V_{dif}, \quad (31)$$

$$V_{ipj}^r = V_{temp}. \quad (32)$$

In Eqs. (31) and (32) the following notations were used

$$V_{temp} = \frac{1}{2}(V_{kni} + V_{kpi} + V_{dif}), \quad (33)$$

$$V_{dif} = V_{ipj} - V_{inj}. \quad (34)$$

The parameter used to obtain a microwave image is S_{11} . This parameter cannot be obtained directly from the TLM algorithm because an incident field cannot be separated. To solve this problem, two successive runs of the program are needed. The first run is performed with excitation without a reflecting object. This run will provide data for the reference port. A second run of the program will be performed considering boundary conditions for objects to be investigated. The S_{11} parameter is given by

$$S_{11} = \frac{F_i - F_0}{F_i + F_0}. \quad (35)$$

In relation (35) F_0 and F_i are the frequency response obtained for the same position of excitation source without reflecting object and with reflector respectively.

IV. RESULTS

To validate the numerical model, the experimental set-up for microwave microscopy depicted schematically in Figure 2 was used. It consisted of a microwave resonator (open-ended coaxial line sensor) connected to a network analyzer. The probe was mounted horizontally over an x - y table. During the scanning process, the probe was held at a constant height over the sample (typically $10 \mu\text{m}$) Stepper motors controlled via a serial interface by computer assured the positioning of the sample (the minimum step size was $1 \mu\text{m}$).

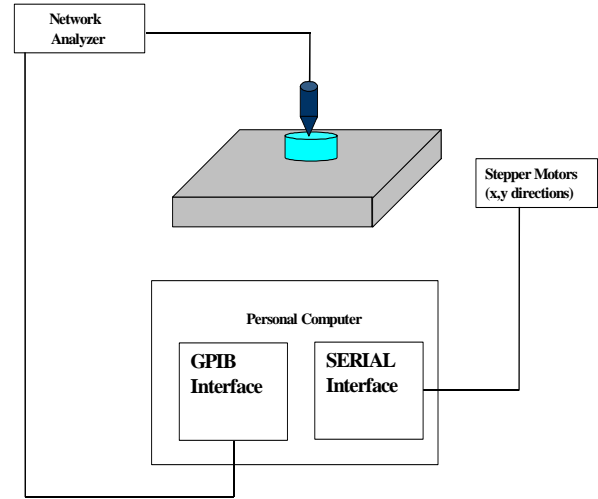


Figure 2. The experimental set-up used in microwave microscopy experiments.

Figure 3 shows the plot of the S_{11} parameter for three different materials: metal, bakelite ($\epsilon_r = 5$) and teflon ($\epsilon_r = 2$). The plot demonstrates the capability of the proposed TLM model to differentiate between materials with different electric permittivities. The frequency response was obtained after two intermediary signal - processing steps: filtering and windowing. The same signal processing process was applied to the reference and to the reflected signals.

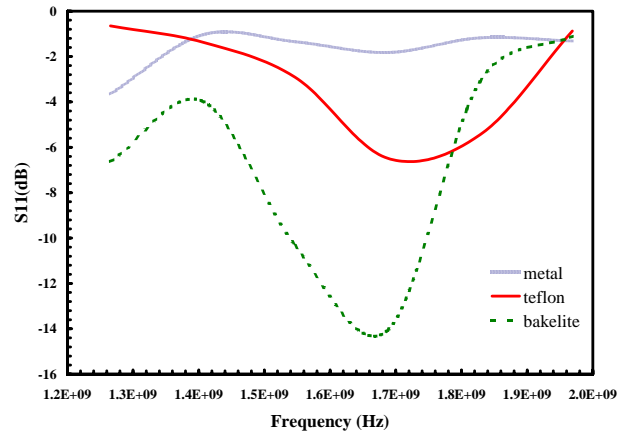


Figure 3. S_{11} parameter extracted from the TLM generated signals for different materials.

Figure 4 shows the numerical results for simulation of scanning over two small pieces of bakelite and teflon respectively. The length of the dielectric pieces was 1.6 mm and the step size in scanning was 0.033 mm . The dielectric profiles were obtained by selecting the corresponding computed S_{11} parameter for 1.72 GHz . This procedure is

identical to that used in experimental microwave microscopy [15].

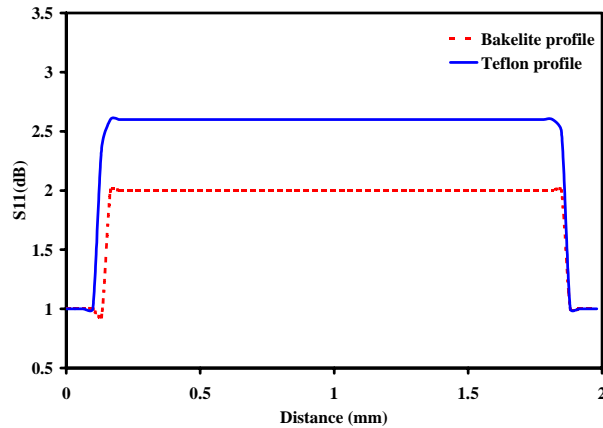


Figure 4. Results of numerical scanning for two pieces of dielectric.

The results obtained prove that the TLM algorithm can be used to model detection of local variation in permittivity. Furthermore, the TLM algorithm presented in this paper can be implemented as the forward solution subroutine for the reconstruction of the permittivity profile. A reconstruction process of inhomogenities in permittivity based on a Newton's iterative scheme for microwave imaging was proposed before [16]. This reconstruction code will involve the following steps:

1. Computing the electric fields using the TLM algorithm described here for each of the different excitations, initially assuming a homogeneous sample.
2. Obtaining the difference between the measured and computed fields (determined in step 1) at a finite number of locations for a finite number of incident fields.
3. Constructing the Jacobian matrix required in the Newton's method [17].
4. Computing a perturbation of complex valued wave number squared, Δk^2 .
5. Modifying the values of k^2 based on the computed Δk^2 and repeating steps 1-4 until a convergence criteria is satisfied.

V. ACKNOWLEDGEMENT

The assistance of Professor Milton Kult in collecting data for microwave measurements is appreciated.

VI. CONCLUSIONS

A numerical model for scanning microwave microscopy was implemented. The model is based on the TLM algorithm. The results shown in this paper demonstrate that the models can be applied to the dimensional

characterization of structures with different electric permittivities. The scanning process was also implemented in the numerical model. The results obtained show that the numerical model can be run in parallel with the experimental scanning. This allows a better characterization of reflectors detected by microwave microscopy. Using TLM algorithm in reconstruction of permittivity profiles based on microwave measurements is proposed in this article.

REFERENCES

- [1] Ida N. "Microwave NDT" Kluwer Press, 1992
- [2] Johns, P. B. Beurle, R. L. "Numerical solution of Two-Dimensional Scattering Problems Using a Transmission-Line Matrix" *Proc. IEEE*, vol 118, pp. 1203-1209, 1971.
- [3] Sadiku, M.N.O.; Obiozor, C.N. "A comparison of finite difference time-domain (FDTD) and transmission-line modeling (TLM) methods", Southeastcon 2000. Proceedings of the IEEE pp: 19 –22, 2000.
- [4] Porti, J.A Morente "TLM method and acoustics" *International Journal of numerical modeling*, Vol 14, pp.171-183 2001.
- [5] Johns P. B. "A symmetrical condensed node for the TLM method", *IEEE transaction on Microwave theory and techniques* vol. MTT_35 No.4 pp370-377, 1987.
- [6] Krumpholz, M., Russer, P. "A field theoretical derivation of the transmission line method" *IEEE transaction on Microwave theory and techniques* Vol.42 No. 9. pp. 1660-1668, 1994.
- [7] Krumpholz, M., Russer, P. "Discrete time-domain Green's function for three dimensional TLM modeling of the radiating boundary conditions "Applied Computation Electromagnetic Society, Monterey, CA, pp. 458-466, 1993.
- [8] So, P.M., Woefel, W.J.R."A new look at the 3D condensed node TLM scattering" *Microwave Symposium Digest, IEEE MTT-S International* vol.3 pp.1443-1446, 1993.
- [9] Russer, P., Krumpholz, M. "The Hilbert space formulation of the TLM method" *International journal of numerical modelling: Electronic Networks, Devices and Fields*, Vol.6, No.1, pp.29-45, 1993.
- [10] Ciocan, R. "Numerical models for elastic and electromagnetic waves propagation with applications to nondestructive characterization of materials", Ph.D. thesis, The University of Akron, May 2003.
- [11] Hofer W.J.R., So P.M., *The electromagnetic wave simulator*, John Wiley & Sons, 1993.
- [12] Tong C. E., Fujino, Y. "An efficient algorithm for transmission line matrix analysis for electromagnetic problems using the symmetrical condensed node", *IEEE Trans. Microwave Theory Tech*, Vol. MTT-39, No.8 pp. 1421-1424, 1991.
- [13] Trenkic, V., Christopoulos, C., Benson T.M. "Theory of the symmetrical Super-condensed node for the TLM method" *IEEE Trans. Microwave Theory Tech*, Vol. MTT-43, No. 6, pp. 1342-1348, 1995.
- [14] Herring J. L. "Developments in the transmission-Line modelling method for electromagnetic compatibility studies" Ph.D thesis University of Nottingham, May 1993.
- [15] Ciocan, R. Tabib-Azar, M. "Transient thermography of semiconductors using Microwave Microscope", *Microscale Thermophysical Engineering* Vol. 3 (4), pp.321-327, 1999.
- [16] Meaney P.M., Paulsen K. D., Ryan, T.P. "Two dimensional hybrid element image reconstruction for TM illumination" *IEEE transaction on antennas and propagation* Vol. 43, No. 3, March, pp.239-247, 1995.
- [17] Jiang, H., Keith D., Osterberg, U. "Optical image reconstruction using frequency domain data: simulation and experiments", *J. Opt. Soc. Am. A*. Vol. 13 No. 2 pp. 253-266, 1996.



Razvan Ciocan is currently a postdoctoral fellow in the Physics and Astronomy Department at Clemson University, Clemson, SC, USA. He got his PhD in Electrical Engineering at the University of Akron, OH, USA. He received the MS in Electrical Engineering from Case Western Reserve University, Cleveland, OH, USA and the BS in Applied Physics from University of Bucharest, Romania. His research focuses on microwave and ultrasonic imaging.



Nathan Ida is currently Professor of electrical engineering at The University of Akron, Akron, Ohio, USA, where he has been since 1985. His current research interests are in the areas of numerical modeling of electromagnetic fields, electromagnetic wave propagation, nondestructive testing of materials at low and microwave frequencies and in computer algorithms. Dr. Ida received his B.Sc. in 1977 and M.S.E.E. in 1979 from the Ben-Gurion University in Israel and his Ph.D. from Colorado State University in 1983.



Eugenia Ciocan received her Ph.D. degree at the "Al. I. Cuza" University, Iasi, Romania in 1998. She worked in numerical modeling of heat and mass transport phenomena at the Institute for Nuclear Research, Pitesti and in optical characterization of materials at Case Western Reserve University, Cleveland, Ohio, USA. Her current research interests include the application of the numerical methods in electromagnetics and elastic wave propagation



Huabei Jiang is a Professor of physics at Clemson University, Clemson, SC, USA. His research interests include biomedical applications of model-based optical, microwave and ultrasonic imaging. Dr. Jiang received his first PhD in 1988 from the University of Electronic Science and Technology of China, Chengdu, China, and his second PhD in 1995 from Dartmouth College, Hanover, NH, USA

A Novel 3D Pseudo-spectral Analysis of Photonic Crystal Slabs

K. Varis^(a), and A. R. Baghai-Wadji^(b)

^(a)Helsinki University of Technology, Optoelectronics Laboratory,
P.O. Box 3500, FIN-02015 HUT, Finland, EU
karri.varis@hut.fi

^(b)Vienna University of Technology, E351,
Gusshausstrasse 27-29, A-1040 Vienna, Austria, EU
alireza.baghai-wadji@tuwien.ac.at

Abstract—We consider a double-periodic slab which is characterized by two lattice vectors \mathbf{a}_1 and \mathbf{a}_2 on the (x, y) -plane, the thickness h_z and a three-dimensional scalar function $\varepsilon(x, y, z)$ specifying the dielectric constitution of the slab. Above and below the slab is free space. These assumptions imply that the z -direction is special in this problem. Therefore, following a general scheme we diagonalize the Maxwell's equations with respect to this direction. The periodicity in two directions suggests the use of spatially harmonic functions as a basis. We exploit this property; however, contrary to the traditional schemes, we propose an expansion of the fields in the form $\Psi(\mathbf{r}, z) = \sum_n f_n(z) \exp(j\mathbf{k}_n \cdot \mathbf{r})$ allowing $f_n(z)$ to be a fairly general function of the z -coordinate, rather than an exponential function. In this expression \mathbf{r} is the position vector in the (x, y) -transversal plane. To guarantee maximum flexibility we discretize f in terms of finite differences. We demonstrate the superiority of our method by discussing the following properties: *i*) Diagonalization only involves the transversal field components, *ii*) Diagonalization allows us easily to construct and implement various boundary conditions at the bounding surfaces $z = 0$ and $z = h_z$, *iii*) The resulting discretized system is extraordinarily stable and robust, and facilitates fast computations; from the computational performance point of view it compares well with existing methods, while it by far applies to larger class of problems, *iv*) It allows to use both the radian frequency ω and the wavevector \mathbf{K} as input parameters. Therefore, the resulting discrete system can be solved at individual (ω, \mathbf{K}) -points of interest, *v*) Finally, the method is applicable to both the eigenstate and the excitation problems.

I. INTRODUCTION

We consider a doubly-periodic slab which is characterized by a dielectric function $\varepsilon(x, y, z)$ satisfying the condition $\varepsilon(\mathbf{r} + m\mathbf{a}_1 + n\mathbf{a}_2, z) = \varepsilon(\mathbf{r}, z)$ for arbitrary negative or positive whole numbers m and n . Here \mathbf{r} is the position vector and \mathbf{a}_1 and \mathbf{a}_2 are lattice vectors in the (x, y) -plane. Above and below the slab, which is bounded by the planes $z = 0$ and $z = h_z$, various boundary conditions can be accommodated, e.g. electrically or magnetically conducting,

or, dielectrically or magnetically open, or, a combination of both. In the case of open boundaries we require that the cladding media satisfy the following conditions: a) the dielectric media are independent of the z -coordinate; i.e. $\partial\varepsilon(x, y, z)/\partial z \equiv 0$, and b) the media possess the same periodicity properties as in the slab along the lattice vector directions.

The periodicity property in two directions suggests the use of spatially harmonic basis functions in the transversal (x, y) -plane. Obviously the z -direction in our slab problem, suggests the diagonalization of the Maxwell's equations with respect to this "normal" direction. We exploit these properties and expand the fields in terms of a sum of products of separable functions in the form $\Psi = \sum_n f_n(z) \exp(j\mathbf{k}_n \cdot \mathbf{r})$. In order to determine various functions $f_n(z)$, we discretize them in terms of finite differences (FD) which leads to a simple yet powerful implementation. Standard FD techniques involve all the three components of the electric field \mathbf{E} and the magnetic field \mathbf{H} . On contrary, in the proposed diagonalized form only an optimized subset of field components are involved: It turns out that only those field components which enter the interface- and boundary conditions on $z = \text{const}$ planes have to be included in our formalism. In the next section it is shown that, once the transversal field components $\mathbf{e} = (e_1, e_2)$ and $\mathbf{h} = (h_1, h_2)$ are known on a $z = \text{const}$ plane, the remaining components in the normal (diagonalization) direction can be derived easily, straightforwardly and inexpensively.

II. PLANEWAVE FD IN 3D

A. Constructing the diagonalized operator

The curl operator can be written in the form

$$\nabla \times = \partial_x \mathbf{N}_1 + \partial_y \mathbf{N}_2 + \partial_z \mathbf{N}_3, \quad (1)$$

where

$$\mathbf{N}_1 = \begin{bmatrix} 0 & 0 & 0 \\ 0 & 0 & -1 \\ 0 & 1 & 0 \end{bmatrix}, \quad (2a)$$

$$\mathbf{N}_2 = \begin{bmatrix} 0 & 0 & 1 \\ 0 & 0 & 0 \\ -1 & 0 & 0 \end{bmatrix}, \quad (2b)$$

$$\mathbf{N}_3 = \begin{bmatrix} 0 & -1 & 0 \\ 1 & 0 & 0 \\ 0 & 0 & 0 \end{bmatrix}. \quad (2c)$$

Adopting this notation the Maxwell's equations are

$$(\partial_x \mathbf{N}_1 + \partial_y \mathbf{N}_2 + \partial_z \mathbf{N}_3) \mathbf{E} = j\omega\mu \mathbf{H}, \quad (3a)$$

$$(\partial_x \mathbf{N}_1 + \partial_y \mathbf{N}_2 + \partial_z \mathbf{N}_3) \mathbf{H} = -j\omega\varepsilon \mathbf{E}. \quad (3b)$$

In what follows we describe a simple recipe for the diagonalization of Maxwell's equations as written in (3). Thereby, we arbitrarily choose any of the directions x , y , or z . However, we reference to our discussion in the introduction and select the z -direction as our diagonalization direction. To this end, we consider the decomposition of the 3×3 identity matrix \mathbf{I} in the following form

$$\mathbf{I} = \begin{bmatrix} 1 & 0 & 0 \\ 0 & 1 & 0 \\ 0 & 0 & 0 \end{bmatrix} + \begin{bmatrix} 0 & 0 & 0 \\ 0 & 0 & 0 \\ 0 & 0 & 1 \end{bmatrix} \quad (4a)$$

$$= \begin{bmatrix} 0 & 1 & 0 \\ -1 & 0 & 0 \\ 0 & 0 & 0 \end{bmatrix} \begin{bmatrix} 0 & -1 & 0 \\ 1 & 0 & 0 \\ 0 & 0 & 0 \end{bmatrix}$$

$$+ \underbrace{\begin{bmatrix} 0 & 0 & 0 \\ 0 & 0 & 0 \\ 0 & 0 & 1 \end{bmatrix}}_{\mathbf{U}_3} \quad (4b)$$

$$= \mathbf{N}_3^T \mathbf{N}_3 + \mathbf{U}_3, \quad (4c)$$

where the matrix \mathbf{U}_3 in (4b) has been introduced in the obvious manner. The superscript T denotes transposition.

Recognizing the form of $\mathbf{N}_3^T \mathbf{N}_3$ (Eqs. (4)) and the orthogonality property of \mathbf{N}_3 and \mathbf{U}_3 , and thus \mathbf{N}_3^T and \mathbf{U}_3 , the diagonalization procedure amounts to the following steps: (i) Multiply (3a), from the left, successively by \mathbf{N}_3^T and \mathbf{U}_3 , (ii) multiply (3b), from the left, successively by \mathbf{N}_3^T and \mathbf{U}_3 . (iii) It is immediately seen that the equations obtained from the \mathbf{U}_3 -multiplication allow us to express the transversal field components e_1 , e_2 , h_1 and h_2 in terms of the normal field components e_3 , h_3 . Furthermore, it can be seen that these equations do not involve any z -derivatives at all. Substituting the resulting matrix equation in the combined systems of equations, obtained from the multiplication of \mathbf{N}_3^T , results in the desired diagonalized form. In the following we provide examples by discussing several special cases.

In the present case, considering isotropic media only, the equations (3) are extraordinarily simple: Once the equations are written out explicitly the reader can easily recognize all

the aforementioned relationships just simply by inspection. We have

$$\begin{aligned} & \partial_x \begin{bmatrix} 0 \\ -e_3 \\ e_2 \end{bmatrix} + \partial_y \begin{bmatrix} e_3 \\ 0 \\ -e_1 \end{bmatrix} - j\omega\mu \begin{bmatrix} h_1 \\ h_2 \\ h_3 \end{bmatrix} \\ &= -\partial_z \begin{bmatrix} -e_2 \\ e_1 \\ 0 \end{bmatrix}, \end{aligned} \quad (5a)$$

$$\begin{aligned} & \partial_x \begin{bmatrix} 0 \\ -h_3 \\ h_2 \end{bmatrix} + \partial_y \begin{bmatrix} h_3 \\ 0 \\ -h_1 \end{bmatrix} + j\omega\varepsilon \begin{bmatrix} e_1 \\ e_2 \\ e_3 \end{bmatrix} \\ &= -\partial_z \begin{bmatrix} -h_2 \\ h_1 \\ 0 \end{bmatrix}. \end{aligned} \quad (5b)$$

Due to the properties of the Maxwell's equations, (5b) can be obtained from (5a) simply by the replacements $h_i \leftrightarrow e_i$ ($i = 1, 2, 3$) and $\varepsilon \leftrightarrow -\mu$. Therefore, it is sufficient to restrict our manipulations only to one set of these equations. We consider (5a). Obviously these equations split into the equations

$$\partial_x \begin{bmatrix} e_3 \\ 0 \end{bmatrix} + \partial_y \begin{bmatrix} 0 \\ e_3 \end{bmatrix} + j\omega\mu \begin{bmatrix} h_2 \\ -h_1 \end{bmatrix} = \partial_z \begin{bmatrix} e_1 \\ e_2 \end{bmatrix}, \quad (6)$$

and

$$h_3 = \frac{1}{j\omega\mu} \partial_x e_2 - \frac{1}{j\omega\mu} \partial_y e_1. \quad (7)$$

The counterpart of (7) is

$$e_3 = -\frac{1}{j\omega\varepsilon} \partial_x h_2 + \frac{1}{j\omega\varepsilon} \partial_y h_1. \quad (8)$$

Substituting e_3 from (8) into (6) we obtain

$$\mathcal{A} \begin{bmatrix} h_1 \\ h_2 \end{bmatrix} = \partial_z \begin{bmatrix} e_1 \\ e_2 \end{bmatrix}, \quad (9)$$

where

$$\mathcal{A} = \begin{bmatrix} \partial_x \frac{1}{j\omega\varepsilon} \partial_y & -\partial_x \frac{1}{j\omega\varepsilon} \partial_x + j\omega\mu \\ \partial_y \frac{1}{j\omega\varepsilon} \partial_y - j\omega\mu & -\partial_y \frac{1}{j\omega\varepsilon} \partial_x \end{bmatrix}. \quad (10)$$

Performing the aforementioned replacements we obtain the corresponding counterpart

$$\mathcal{B} \begin{bmatrix} e_1 \\ e_2 \end{bmatrix} = \partial_z \begin{bmatrix} h_1 \\ h_2 \end{bmatrix}, \quad (11)$$

where

$$\mathcal{B} = \begin{bmatrix} -\partial_x \frac{1}{j\omega\mu} \partial_y & \partial_x \frac{1}{j\omega\mu} \partial_x - j\omega\varepsilon \\ -\partial_y \frac{1}{j\omega\mu} \partial_y + j\omega\varepsilon & \partial_y \frac{1}{j\omega\mu} \partial_x \end{bmatrix}. \quad (12)$$

Therefore, we have transformed the Maxwell's curl equations into the following two sets of equations

$$\begin{bmatrix} 0 & \mathcal{A} \\ \mathcal{B} & 0 \end{bmatrix} \begin{bmatrix} e_1 \\ e_2 \\ h_1 \\ h_2 \end{bmatrix} = \partial_z \begin{bmatrix} e_1 \\ e_2 \\ h_1 \\ h_2 \end{bmatrix}, \quad (13)$$

and

$$\begin{bmatrix} 0 & 0 & \frac{1}{j\omega\epsilon} \partial_y & -\frac{1}{j\omega\epsilon} \partial_x \\ -\frac{1}{j\omega\mu} \partial_y & \frac{1}{j\omega\mu} \partial_x & 0 & 0 \end{bmatrix} \begin{bmatrix} e_1 \\ e_2 \\ h_1 \\ h_2 \end{bmatrix} = \begin{bmatrix} e_3 \\ h_3 \end{bmatrix}. \quad (14)$$

Equation (13) is the desired diagonalized form with the aforementioned properties: This equation only involves variables which enter into the *interface conditions* if we cross a $z = z_i = \text{const}$ plane at a point (x_i, y_i, z_i) in the z -direction. This property implies that if we are given the field distribution on the z_i -plane, we obtain the rate of change of the field distribution in the z -direction by applying the matrix operator at the LHS of (13). Consequently, by having the information about the field distribution on the z_i -plane, and its rate of change we can approximate the field distribution on a neighboring plane $z = z_0 \pm \Delta$. We would like to point out that by repeated application of the matrix operator at the LHS of (13) to this equation, and using (13), we obtain higher-order derivatives of the field vector in (13). Having computed higher-order derivatives, and using Taylor series expansions we can construct approximations to the fields to any order of accuracy desired.

We wish to conclude this section with the following comment: The *Normal components* e_3 and h_3 can be computed from the transversal field distribution by using operators and material parameters which only depend on the x and y transversal coordinates as seen in (14).

B. Discretization

1) *Field expansions*: The periodicity in two dimensions suggests the following expansion for the fields

$$\Psi(x, y, z) = \sum_{m,n} f_{m,n}(z) e^{j\mathbf{k}_{m,n} \cdot \mathbf{r}}, \quad (15)$$

where Ψ represents any of the transversal field components and \mathbf{r} is the position vector on a $z = \text{const}$ plane. The reciprocal vector $\mathbf{k}_{m,n}$ denotes a certain lattice vector superimposed by a Bloch phasing vector $\mathbf{K} = K_1 \mathbf{k}_1 + K_2 \mathbf{k}_2$ which can be conveniently written in the following form

$$\mathbf{k}_{m,n} = (m + K_1) \mathbf{k}_1 + (n + K_2) \mathbf{k}_2, \quad (16)$$

for a discrete $M \times N$ set of reciprocal lattice. The expansion coefficients $f_{m,n}(z)$ are generally functions of z -coordinate. The next section is devoted to the discretization of the fields in the z -direction, followed by a thorough discussion of the specifics of the numerical implementation.

The choice of the harmonic dependence in the (x, y) -plane has been inspired by two reasons: (i) operators \mathcal{A} and \mathcal{B} only involve derivatives with respect to x and y which can be evaluated efficiently and (ii) the implementation of the Bloch periodic boundaries is straightforward.

2) *Discretization in the orthogonalization direction*: According to our diagonalization formula, the application of the matrix operator, as defined in (10), to the transversal magnetic \mathbf{h} -field on a certain plane $z = z_0 = \text{const}$, results in the normal derivative of the transversal electric \mathbf{e} -field on the same plane. This property can be utilized in establishing a relationship between fields which are defined on consecutive $z = \text{const}$ layers. In this section we develop the general idea and briefly address issues concerning the accuracy of the numerical results. In the next section we will focus on procedural details.

To communicate the basic idea, we start with probably the simplest assumption: Assume that $e_2 \equiv 0$ and $h_1 \equiv 0$ and that h_2 is given on the plane $z = 0$. Our goal is to establish a relationship between e_1 on planes $z = -\Delta/2$ and $z = \Delta/2$ to h_2 on the plane $z = 0$. Using Taylor's series expansion we can write

$$e_1 \left(\frac{\Delta}{2} \right) = e_1(0) + \frac{\Delta}{2} \left\{ \left(\frac{\partial e_1}{\partial z} \right) (0^+) \right\} + \frac{\Delta^2}{8} \left\{ \left(\frac{\partial^2 e_1}{\partial z^2} \right) (0^+) \right\} + \mathcal{O}^3(\Delta), \quad (17a)$$

$$e_1 \left(-\frac{\Delta}{2} \right) = e_1(0) - \frac{\Delta}{2} \left\{ \left(\frac{\partial e_1}{\partial z} \right) (0^-) \right\} + \frac{\Delta^2}{8} \left\{ \left(\frac{\partial^2 e_1}{\partial z^2} \right) (0^-) \right\} + \mathcal{O}^3(\Delta), \quad (17b)$$

where the symbols $+$ and $-$, respectively, indicate that the z -derivatives have to be computed at $0 + \epsilon$ and $0 - \epsilon$ for arbitrarily small but positive ϵ . The derivatives can be calculated using (9) and the information about the function h_2 on the $z = 0$ plane. Subtracting (17b) from (17a), and keeping the first order terms only, we obtain

$$e_1 \left(\frac{\Delta}{2} \right) - e_1 \left(-\frac{\Delta}{2} \right) = \frac{\Delta}{2} \left\{ \left(\frac{\partial e_1}{\partial z} \right) (0^+) + \left(\frac{\partial e_1}{\partial z} \right) (0^-) \right\}. \quad (18)$$

In view of the operator \mathcal{A} in (10) we recognize that if the material parameters on the two sides of the $(z = 0)$ -plane are the same, the involved derivatives are equal to an arbitrary order. In present case the second order derivatives cancel out and the error term in this expression is an O^3 -term in Δ . If the material parameters on the two sides of the $(z = 0)$ -plane are different, then they have to be averaged, leading to an accuracy of only order O^2 in Δ . Similar results can be obtained for the remaining three transversal field components.

3) *Construction of the system matrix:* In our formulation we have adopted the following notation: Assume a basis consisting of $M \times N$ plane waves. Let \mathbf{e}_o and \mathbf{h}_o , respectively, be $2 \times M \times N$ coefficient vectors representing the electric and magnetic fields, which are defined on the $z = o\Delta$ -plane. (Note that $M \times N$ coefficients are required for each of the x - and y -directions.) Let the $2 \times M \times N$ by $2 \times M \times N$ sub-matrix $\hat{\mathbf{A}}_o$, be the discrete version of \mathcal{A} , multiplied by Δ , and evaluated on the plane $z = o\Delta$. Similarly, let $\hat{\mathbf{B}}_o$ represent \mathcal{B} . Using this notation we can establish relationships between the electric fields on the planes $o - 1/2$ and $o + 1/2$, and the magnetic field on the interleaved plane o . Likewise we can establish relationships between the magnetic fields on the planes o and $o + 1$, and the electric field on the interleaved plane $o + 1/2$. Keeping first order expansion terms only, we obtain the result given in (19),

$$\mathbf{e}_{o-\frac{1}{2}} - \mathbf{e}_{o+\frac{1}{2}} + \hat{\mathbf{A}}_o \mathbf{h}_o = \mathbf{0}, \quad (19a)$$

$$\mathbf{h}_o - \mathbf{h}_{o+1} + \hat{\mathbf{B}}_{o+\frac{1}{2}} \mathbf{e}_{o+\frac{1}{2}} = \mathbf{0}. \quad (19b)$$

We recognize that the equation in (19) comprise a finite difference implementation. However, in contrast to the standard formulations, the present formulation is based on a finite difference discretization of the Fourier coefficients, rather than of the fields in the spatial domain [1].

The dielectric function characterizing the slab is defined between layers $[0, O\Delta]$, where O is the index of the last layer. Furthermore, in order to incorporate the boundary condition equations in our system of equations, we need to define the electric fields on two layers, -0.5Δ and $(O + 0.5)\Delta$, outside the slab

$$\Phi_l \mathbf{e}_{0.5} - \mathbf{h}_0 = \mathbf{0}, \quad (20a)$$

$$\mathbf{h}_O + \Phi_u \mathbf{e}_{O+0.5} = \mathbf{0}. \quad (20b)$$

The following section is devoted to the construction of these equations.

The general system equation can be created by formulating equations (19) for each of the z -layer in the slab and incorporating the boundary conditions (20). Collecting all

unknowns into one vector \mathbf{f} and all multipliers into one matrix \mathbf{M} leads to

$$\mathbf{M}\mathbf{f} = \mathbf{0}. \quad (21)$$

The efficient solution of this homogeneous equation will be discussed below.

C. Boundary conditions

Our goal is to interrelate the electric- and magnetic fields on the lowest- and most upper bounding planes.

Various boundary conditions can arise in the applications: In the case of electrically- or magnetically conducting boundaries, e.g. we merely need to require that the electric or the magnetic field, respectively, vanishes. In this paper we address a slightly more complex problem with mixed-type boundary conditions by assuming free space above ($z > h_z$) and beneath ($z < 0$) our slab. Generally speaking our formulation is valid whenever the following conditions are met: (i) $\partial \varepsilon(x, y, z) / \partial z \equiv 0$ for $z < 0$ and $z > h_z$. (Material is homogeneous in the z -direction). (ii) The materials above and below the slab share the lattice periodicity with the slab.

These conditions suggest slightly different field expansions for the fields in regions outside the slab:

$$\Psi(x, y, z) = \sum_{m,n,o} \alpha_o f_{m,n,o} e^{\lambda_o z} e^{j\mathbf{k}_{m,n} \cdot \mathbf{r}}. \quad (22)$$

Here λ_o represents the complex-valued propagation constant in z -direction associated with one of the $4 \times M \times N$ eigenvectors, and $f_{m,n,o}$ is the corresponding coefficient. Substituting (22) into (13) and utilizing the orthogonal property of the basis functions involved results in the eigenvalue equation in (23),

$$\begin{bmatrix} 0 & \mathcal{A} \\ \mathcal{B} & 0 \end{bmatrix} \begin{bmatrix} \mathbf{e} \\ \mathbf{h} \end{bmatrix} = \lambda \begin{bmatrix} \mathbf{e} \\ \mathbf{h} \end{bmatrix}. \quad (23)$$

For ε varying in the (x, y) -plane, we need to solve the system numerically for $4 \times M \times N$ eigenpairs. Restricting ourselves to constant ε , the general $4 \times M \times N$ eigenvalue system decouples into $M \times N$ (analytically solvable) eigenvalue systems of dimension 4. For constant ε , the system has two doubly degenerate eigenvalues for each $[m, n]$ pair

$$\lambda_{m,n} = \pm w_{m,n} = \pm \sqrt{d_x^2(m,n) + d_y^2(m,n) - \omega^2 \varepsilon \mu}, \quad (24)$$

where w is the magnitude of the eigenvalue. The symbol $d_x(m, n)$ is related to the numerical value of the basis function derivative as defined in (25).

$$\frac{\partial}{\partial x} e^{j\mathbf{k}_{n,m} \cdot \mathbf{r}} = j d_x(m, n) e^{j\mathbf{k}_{n,m} \cdot \mathbf{r}} \quad (25)$$

A similar definition holds for $d_y(m, n)$. These values depend on the reciprocal lattice geometry and will be considered in more detail later.

The corresponding eigenvectors can also be solved analytically, which are summarized below

$$\Psi_{-w}^1 = \begin{bmatrix} -j \frac{d_x d_y}{w \omega \varepsilon} \\ -j \frac{d_y^2 - \omega^2 \varepsilon \mu}{w \omega \varepsilon} \\ 1 \\ 0 \end{bmatrix}, \quad \Psi_{-w}^2 = \begin{bmatrix} j \frac{d_x^2 - \omega^2 \varepsilon \mu}{w \omega \varepsilon} \\ j \frac{d_x d_y}{w \omega \varepsilon} \\ 0 \\ 1 \end{bmatrix}, \quad (26a)$$

$$\Psi_w^1 = \begin{bmatrix} -j \frac{d_x d_y}{w \omega \varepsilon} \\ -j \frac{d_y^2 - \omega^2 \varepsilon \mu}{w \omega \varepsilon} \\ -1 \\ 0 \end{bmatrix}, \quad \Psi_w^2 = \begin{bmatrix} j \frac{d_x^2 - \omega^2 \varepsilon \mu}{w \omega \varepsilon} \\ j \frac{d_x d_y}{w \omega \varepsilon} \\ 0 \\ -1 \end{bmatrix}. \quad (26b)$$

Since eigenvectors are known up to a constant multiplier the normalization of the eigenvectors is arbitrary. Here we have chosen a multiplier which produces a h -field with unity length as depicted in (20).

A few remarks are in place: *i*) If w becomes complex-valued for any m, n pair, then the corresponding eigenmode radiates energy away from the slab into infinity, preventing the formation of bounded modes. *ii*) For $z > h_z$ we have to discard half of the eigenvectors which correspond to positive eigenvalues in order to satisfy the Sommerfeld's radiation condition (Inclusion of the fields with finite energy.). Similarly we have to discard eigenvectors corresponding to $\lambda < 0$ in the $z < 0$ region.

Finally, it should be pointed out that in our finite difference implementation we have defined the e -fields at discrete $z = (o + 0.5)\Delta$ -layers, while the h -fields have been defined at $z = o\Delta$ -layers. We should be aware of this fact whenever a shift of the fields by a distance 0.5Δ becomes necessary, e.g. in establishing a relationship between the field components. In present case this relationship can be established fairly easily since we know the z -directional propagation constant of the eigenvectors.

Taking into account these details we obtain the matrices

which describe the boundary conditions

$$\Phi_{l,u}(m, n) = \frac{e^{0.5\Delta w_{l,u}(m,n)}}{j w_{l,u}(m, n) \omega \varepsilon_{l,u}} \quad (27)$$

$$\times \begin{bmatrix} d_x(m, n) d_y(m, n) & -d_x^2(m, n) + \omega^2 \varepsilon_{l,u} \mu \\ d_y^2(m, n) - \omega^2 \varepsilon_{l,u} \mu & -d_x(m, n) d_y(m, n) \end{bmatrix}$$

Here the subindices l and u , respectively, indicate the lower and the upper semispaces. We can obtain discretized versions of this equation by replacing the matrix entries by diagonal submatrices, whose elements individually correspond to different (m, n) -pairs. For semispaces with non-constant ε , these submatrices will become dense since the eigenvectors of (23) will in general have $4 \times M \times N$ non-zero elements.

D. Solving the equation system

Ordinarily system matrices for three dimensional problems can be prohibitively large. Therefore, we recommend the use of iterative solvers. Most solvers operate only on matrix vector products which frees us from constructing the matrix; only a routine constructing vector products is needed. Our choice for iterative solver has been the transpose free quasi minimal residual method (TFQMR) [2], which is efficient, handles non-symmetric and non-Hermitian matrices well, and even manages to solve nearly singular matrices.

1) *Numerical evaluation of operators:* The operators in our problem generally involve derivatives and spatial functions appearing in multiplicative form. We discretize the equations by treating the derivatives in Fourier domain and the spatial functions in real domain. To perform the calculations we Fourier transform the trial vectors back and forth from spatial domain to spectral domain and vice versa. This is justified because derivation in Fourier domain, and multiplication by a function, i.e., ε , in real domain are both $O(N)$ operations for a trial vector with N elements. The prohibitive factor is the FFT, which is an $O(N \ln(N))$ operation. Alternatively, we could operate exclusively in Fourier domain, by treating multiplications by ε by means of discrete convolution, which is a costly $O(N^3)$ operation.

We illustrate the aforementioned ideas by an example: The application of the operation $\partial_x \{1 / (j \omega \varepsilon(x, y))\} \partial_y$ to a trial vector \mathbf{f} consists of the following steps:

- multiply \mathbf{f} by a y -derivative matrix, to be defined below,
- inverse Fourier transform the result,

- multiply the result by a sampled version of $1/(j\omega\epsilon(x,y))$,
- Fourier transform, and, finally,
- perform the x -derivative.

The computation of derivatives is fairly straightforward. Once the reciprocal lattice vectors k_1 and k_2 have been chosen, differentiation with respect to x -coordinates yields multiplication by a diagonal matrix with elements being

$$j[(\widehat{m} + K_1)k_1^x + (\widehat{n} + K_2)k_2^x], \quad (28)$$

$$m \in [0, M-1], n \in [0, N-1],$$

where K_1 and K_2 are Bloch phasing factors and k_1^x and k_2^x are projections of reciprocal lattice vectors on the x -axis. The whole number \widehat{m} is defined as follows

$$\widehat{m} = \begin{cases} m & 0 \leq m \leq \frac{M}{2} \\ m - M & \frac{M}{2} < m \leq M - 1 \end{cases}. \quad (29)$$

A similar definition holds for \widehat{n} . The rationale behind this definition is that we need to include negative harmonics into the set of basis functions in order to make it complete. The ordering of harmonics is irrelevant, however, this choice is implemented in most FFT algorithms. The matrix for the y -derivative can be obtained from (28) by replacing the projections on x -axis with projections on y -axis.

2) *Solving excitation problems:* The interface condition for the magnetic field can be written as follows

$$\lim_{\delta \rightarrow 0} h_x \left(z^0 + \frac{\delta}{2} \right) - h_x \left(z^0 - \frac{\delta}{2} \right) = \rho_y(z^0), \quad (30)$$

where $h_x(z)$ is the x -directional magnetic field component and ρ_y is a y -directional current element. Consider (19b) and insert a new layer, designated by h'_{o+1} , at the location $z = (o+1)\Delta - \delta$ where δ represents an infinitesimally small distance.

Assume that there is a horizontal current filament ρ positioned at plane $z = (o+1)\Delta - \frac{\delta}{2}$. Using the above information and (30) we can rewrite (19b) in order to include the assumed excitation,

$$\mathbf{h}_o - \mathbf{h}_{o+1} + \mathbf{B}'_{o+\frac{1}{2}} \mathbf{e}_{o+\frac{1}{2}} = -\rho_{o+\frac{1}{2}}. \quad (31)$$

We specify the excitation by $o + \frac{1}{2}$ since it is inserted between the layers o and $o+1$. The incorporation of this condition into the system equation (21) can be achieved by simply replacing the RHS zero vector by the Fourier transform of the assumed excitation current function

$$\mathbf{M}_{\mathbf{K}}(\omega) \mathbf{f}_{\mathbf{K}}(\omega) = \rho_{\mathbf{K}}(\omega). \quad (32)$$

The Bloch vector \mathbf{K} and angular frequency ω are written explicitly in (32) to emphasize their role as input parameters.

It should be pointed out that using the Bloch-wave basis not only we can solve phased-periodic excitation problems, but also we can tackle elementary excitation problems: The latter are defined as elementary non-periodic excitations of geometrically periodic structures.

3) *Solving eigenproblems:* Equation (21) is a homogeneous system and has non trivial solutions if and only if \mathbf{M} is singular. Therefore, the eigenmodes of the system for a given \mathbf{K} can be found by defining a suitable measure for the detection of the singularity of \mathbf{M} as a function of ω . A possible measure for singularity is, e.g. the magnitude of the determinant. However, solving determinants iteratively is computationally costly and complicated. Instead, we propose a method which is more physics-based: We assume a current distribution to excite the system under consideration, and compute the square norm of the resulting field coefficients. For \mathbf{M} near the singularity, the norm grows - ideally - without bounds. Furthermore, the solution approaches the eigenvector corresponding to the eigenvalue 0. The formal justification for this approach is given in [3] but we review the important steps here:

Consider the following system of equations

$$\mathbf{A} \mathbf{y} = \mathbf{b}. \quad (33)$$

Both sides of this equation can be expanded in terms of the eigenvectors \mathbf{v}_j of \mathbf{A} as

$$\sum_j \alpha_j \lambda_j \mathbf{v}_j = \sum_j \beta_j \mathbf{v}_j. \quad (34)$$

Here α_j is the coefficient set for \mathbf{y} and λ_j is the eigenvalue of \mathbf{A} corresponding to eigenvector \mathbf{v}_j . Due to the linear independence of the eigenvectors, we can write

$$\mathbf{y} = \sum_j \frac{\beta_j}{\lambda_j} \mathbf{v}_j. \quad (35)$$

From this form it is easy to see that if one of the eigenvalues λ_j is close to zero, the only significant contribution to the solution comes from the corresponding eigenvector \mathbf{v}_j . Furthermore, as λ_j approaches zero, the norm of the solution vector approaches infinity.

This behaviour can be understood from physical reasoning as well: If the system is in resonance with the excitation, the energy in the system grows indefinitely as time elapses rendering the eigensolution an infinite energy.

Instead of seeking the maximum of the solution norm, we alternatively, seek the minimum of its inverse

$$G_{\mathbf{K}}(\omega) = \frac{1}{\sqrt{\|\mathbf{f}_{\mathbf{K}}(\omega)\|_2}}, \quad (36)$$

where \mathbf{f}_K is the solution to (32). The introduction of the square root is to smoothen out the curve. We have a great flexibility in choosing the current distribution for eigenmode computations but practise has shown that with a few randomly placed and oriented dipoles the functional G behaves smoothly between the singular points. One should be aware of the fact if $\langle \mathbf{v}_j, \mathbf{b} \rangle = 0$ in (33), then $\beta_j = 0$ and the solution norm does not grow even if $\lambda_j = 0$. As an example, this happens if the system is excited with a single y -directional dipole positioned exactly at a node of h_x for the corresponding eigenmode. Numerically this means that G does not necessarily possess a minimum even if \mathbf{M} is singular for a given ω .

4) *Preconditioning*: Typically, iterative solvers converge poorly for non-preconditioned systems, and very often they even completely fail to converge. Therefore, the implementation of a good preconditioner is a prerequisite for performance enhancement. Instead of solving (32), we suggest solving the modified system in (37)

$$\mathbf{P}_1^{-1} \mathbf{M} \mathbf{P}_2^{-1} (\mathbf{P}_2 \mathbf{f}) = \mathbf{P}_1^{-1} \rho, \quad (37)$$

for the new unknown vector $\mathbf{y} = \mathbf{P}_2 \mathbf{f}$. The problem is to find suitable preconditioner matrices \mathbf{P}_1 and \mathbf{P}_2 such that the solver converges faster for the new matrix $\mathbf{B} = \mathbf{P}_1^{-1} \mathbf{M} \mathbf{P}_2^{-1}$. It can be shown that the convergence is quicker if \mathbf{B} is near diagonal.

We construct \mathbf{P}_1 out of submatrices which we encounter in the main block diagonal of the matrix \mathbf{M} . More precisely, we discretize the matrix operator elements $\mathcal{A}_{\infty, \infty}$, $\mathcal{A}_{\infty, \infty}$, $\mathcal{B}_{\infty, \infty}$ and $\mathcal{B}_{\infty, \infty}$ defined in (10) and (12) for all z -layers in the system, from which we can construct a block diagonal matrix. In place of boundary condition matrices in \mathbf{M} , we use diagonal unity matrices in \mathbf{P}_1 . Due to the block diagonal property, \mathbf{P}_1 is fairly easy to invert, as each block can be inverted individually. However, it should be noted that in practice \mathbf{P}_1 is never actually constructed nor inverted: Instead we first invert the operators analytically in a sense that $\mathcal{L}^{-1}(\mathcal{L}f) = f$ for a suitably chosen test function f , and then carry out their discretized versions as outlined earlier. As an example, the inverse of $\partial_x \{1/(j\omega \epsilon_0(x,y))\} \partial_y$ is $\mathbf{I}_y (j\omega \epsilon_0(x,y)) \mathbf{I}_x$ where \mathbf{I}_ξ denotes integration with respect to ξ . In Fourier domain, integrals can be computed by the application of the inverse of the derivative matrix (28).

It should be noted that (28) may contain zero elements and, therefore, prevent inversion. However, there is a simple remedy to circumvent this problem: *select a suitable orientation for the lattice vector relative to the coordinate system*. We illustrate this idea with an example. However, before doing so, we summarize a few facts from the theory of Fourier analysis which will be of help to our discussion.

Comments:

- **Invariance and symmetry properties of the Fourier transform:** A significant part of the utility of the Fourier transform is due to the fact that it has natural invariance properties under the actions of rotations, dilations, and translations. In particular, a rotation is an orthogonal matrix with determinant 1 (a special orthogonal matrix).

- **Proposition:** Let ρ be a rotation of \mathbf{R}^N . We define $\rho f(x) = f(\rho(x))$. Then we have the formula: $\widehat{\rho f} = \rho \widehat{f}$

Proof: Remember that ρ is orthogonal and has determinant 1. We then have

$$\widehat{\rho f}(\xi) = \int dt (\rho f)(t) e^{-jt\xi} \quad (38a)$$

$$= \int dt f(\rho(t)) e^{-jt\xi} \quad (38b)$$

$$= \int ds f(s) e^{-j\rho^{-1}(s)\xi} \quad (38c)$$

$$= \int ds f(s) e^{-js\rho(\xi)} \quad (38d)$$

$$= \widehat{f}(\rho\xi) \quad (38e)$$

$$= \rho \widehat{f}(\xi). \quad (38f)$$

In the above we have used the variable substitution $s = \rho(t)$, and the fact that $\rho^{-1} = \rho^T$ for an orthogonal matrix, with the superscript T denoting the transposition.

We now are in a position to continue with our example. Consider a rectangular lattice with reciprocal lattice vectors $\mathbf{k}_1 = k_1 \mathbf{u}_x$ and $\mathbf{k}_2 = k_2 \mathbf{u}_y$. The projections of \mathbf{k}_1 and \mathbf{k}_2 , respectively, onto the x -axis are $k_{1,x} = k_1$ and $k_{2,x} = 0$. Assuming for the components of the Bloch phasing factor $K_1 = 0$ and $K_2 \neq 0$ results in a zero element in (28) for $\widehat{m} = 0$. A simple yet very effective solution to this problem can be obtained by rotating the original (x, y) -coordinate system around the z -axis about an angle θ . Denote the new coordinate system by $(\tilde{x}, \tilde{y}, \tilde{z})$. Projections of \mathbf{k}_1 and \mathbf{k}_2 , respectively, onto the \tilde{x} -axis are $k_{1,\tilde{x}} = k_1 \cos(-\theta)$ and $k_{2,\tilde{x}} = k_2 \cos(\pi/2 - \theta) \neq 0$. The angle θ can easily be selected in such a manner that there are no zero elements in either of the derivative matrices. The solution to the problem remains unaltered as the choice of the coordinate system is arbitrary.

It should be noted that there is still the point $[K_1, K_2] = [0, 0]$ at which the singularity cannot be removed by changing the coordinate system. (The point $\mathbf{K} = \mathbf{0}$ corresponds to strictly periodic field distributions without any phase change

in two consecutive cells. The field is static and no wave propagation takes place.) Therefore, $\mathbf{K} = \mathbf{0}$ does not cause a serious problem: All bounded fields in the slab have $\omega = 0$ at this point.

Additional improvements can be achieved by appropriately choosing the matrix \mathbf{P}_2 . Our approach is to use the system matrix for a simpler auxiliary problem for which $\partial_x \varepsilon(x, y, z) = \partial_y \varepsilon(x, y, z) \equiv 0$, and, $\bar{\varepsilon}_k = \text{ave}(\varepsilon_k(x, y))$ where ave means averaging in the (x, y) -plane over one unit cell. Since $\bar{\varepsilon}_k$ is constant in our auxiliary problem, the resulting system matrix $\hat{\mathbf{M}}$ will have nonzero elements only on five diagonals. This matrix can be constructed explicitly. Our goal is that \mathbf{P}_2^{-1} diagonalizes $\mathbf{P}_1^{-1}\mathbf{M}$ as closely as possible. Therefore, we set

$$\mathbf{P}_2 = \text{diag}(\mathbf{P}_1^{-1})\hat{\mathbf{M}}, \quad (39)$$

where ‘‘diag(A)’’ means the main diagonal of \mathbf{A} . Instead of explicitly inverting \mathbf{P}_2 we perform an LU-decomposition and use the resulting coefficients to solve $\mathbf{x} = \mathbf{P}_2\mathbf{f}$. In our implementation of the LU-decomposition we omit pivoting. This omission enables us to store the coefficients in locations of nonzero elements of the original matrix, instead of occupying a general banded matrix. Fortunately, it appears as if pivoting is not necessary in first place: In our systematic and comprehensive testings we never encountered a vanishingly small pivot element.

In summary, the application of $\mathbf{P}_1^{-1}\mathbf{M}\mathbf{P}_2^{-1}$ to a certain test vector $\tilde{\mathbf{f}}$ consists of the following steps: *i)* Compute $\mathbf{z} = \mathbf{P}_2^{-1}\tilde{\mathbf{f}}$ by solving $\tilde{\mathbf{f}} = \mathbf{P}_2\mathbf{z}$ using the LU-coefficients, *ii)* compute $\mathbf{x} = \mathbf{M}\mathbf{z}$, and, finally, *iii)* apply \mathbf{P}_1^{-1} to \mathbf{x} . Once the iterative solver reports convergence, the non-preconditioned solution can be obtained from $\mathbf{f} = \mathbf{P}_2^{-1}\tilde{\mathbf{f}}$.

We conclude this section with the following remarks: *i)* Setting $\mathbf{P}_1 = \mathbf{I}$ and $\mathbf{P}_2 = \hat{\mathbf{M}}$ is sufficient to solve the system. However, defining \mathbf{P}_1 as described above seems to improve the iterative procedure by a significant factor in most problems and not worsen it in any problems we have solved so far. *ii)* We also experimented with a diagonal preconditioner in which $\mathbf{P}_1 = \mathbf{I}$ and $\mathbf{P}_2 = \text{diag}(\mathbf{M})$. However, the results were not satisfying. For most problems the system did not converge at all, and even if it did, thousands of iterations were required. *iii)* Typically, convergence requires 10 – 300 iterations, depending on the specific values of \mathbf{K} and ω , and the function $\varepsilon(x, y, z)$, and the singularity of \mathbf{M} .

III. NUMERICAL RESULTS

We have computed a variety of test examples with our method and compared them, whenever possible, to the corresponding results obtained by the planewave method [4].

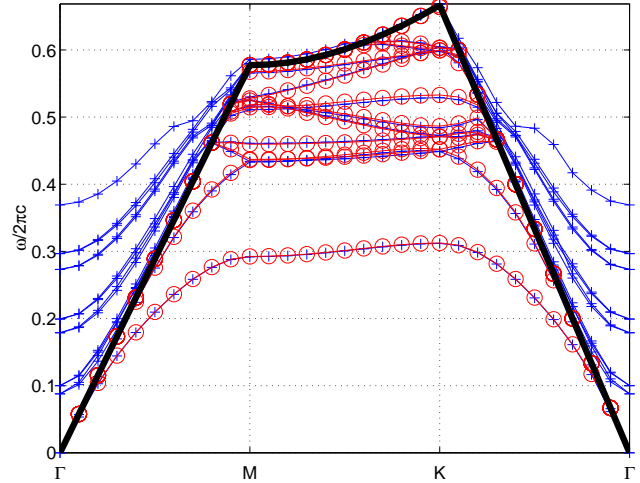


Fig. 1. Shows the dispersion diagram for a triangular lattice of cylindrical holes (voids) in a dielectric slab. Curves marked with ‘o’ have been computed with our method, and those marked with ‘+’ have been computed with the planewave method. The thick black line represents the light-line along which the modes become guided in free space. Modes located above this line are not guided by the slab, and are artifacts due to artificial periodization of the structure required by the planewave method.

Planewave method is not fully adapted to slab problems, because it assumes the structure to be periodic in all spatial directions. It can be used though, by introducing a long lattice vector in z -direction. This extended unit cell, a supercell, is first filled with the background material and the slab is then inserted into it. This approach is justified as long as the modes of interest are well confined around the slab in z -direction, and thus the interaction between neighbouring supercells can be assumed to be negligibly small. If the modes are not well localized, the solutions will interfere, and we can expect a significant deterioration of the results. Furthermore, modes that are not guided by the slab, will appear guided due to this artificial periodization. Results can be verified by increasing the z -directional lattice vector until convergence is reached.

A. Dispersion diagram of equilateral triangular lattices

Our first test case is an equilateral triangular lattice of cylindrical air holes (voids) in a dielectric slab. The thickness of the slab is $h_z = 0.4$, and the dielectric constant is $\varepsilon = 12$. The radius of the air holes is $r = 0.38$, and the lattice constant $a = 1.0$. The cladding material above and below the slab is free space.

Dispersion diagram computed with our method and with the planewave method is shown in Fig. (1).

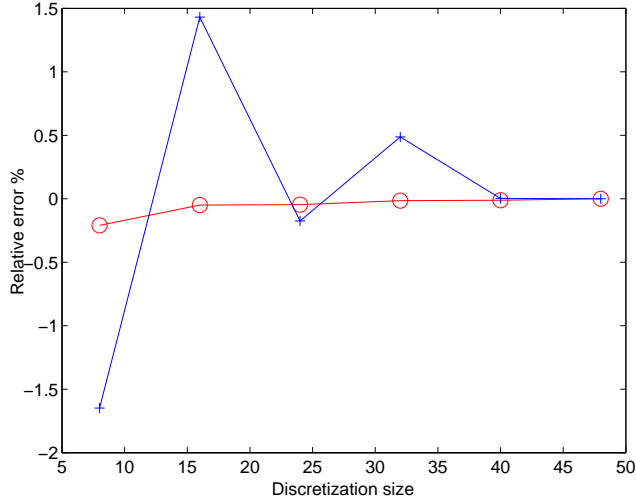


Fig. 2. Convergence as a function of grid size for the lowest order mode at $\mathbf{K} = [0, 0.5]$. Relative error compared to the result obtained with 48 grid points in all directions. The curve with marker '+' is computed with the planewave method, while the curve with marker 'o' with our method. It can be seen that our method provides accurate results with comparatively few grid points. The difference between the two methods at finest discretization is 0.0205%

In both methods we used 32 planewaves in both lattice vector directions. In our method, we used 25 electric field layers and 24 magnetic field layers in z -direction. In the planewave method we used a super-cell with the periodicity length in z -direction being $10a$, with a denoting the lattice constant. Thereby, we employed 384 planewaves. This results in 15.36 planewaves for a slab with the thickness $h_z = 0.4$.

Quite often the lowest bands are the most significant ones; therefore, we conducted a convergence analysis for the first mode at the M -point ($\mathbf{K} = [0, 0.5]$) (see Fig. (1)). We solved the problem utilizing both methods with several discretizations and compared the results as shown in Fig. (2). Problem parameters were as above except that we used the same number of grid points in all directions. In the planewave method this means using $10/0.4 = 25$ times more planewaves in z -direction in order to compensate for the larger super-cell size.

B. Fields in an array of dielectric spheres

Our second test case consists of a rectangular lattice of dielectric spheres positioned on a dielectric substrate. The structure is shown in Fig. (3).

The fields shown in Figs. (4) and (5) are solved for the lowest order eigenmode, at the frequency $\omega = 0.298(2\pi c)$

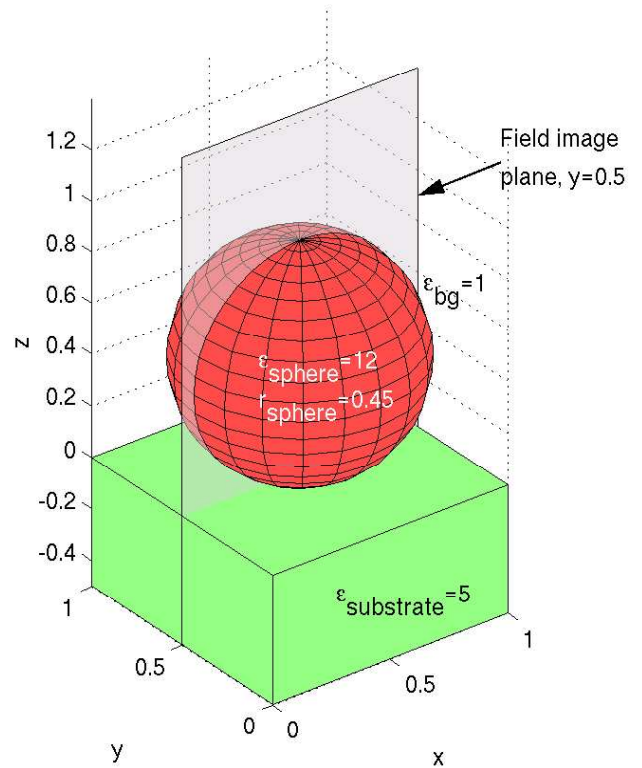


Fig. 3. Geometry of test case 2. Spheres with $r = 0.45$ are positioned on a dielectric substrate with a rectangular lattice specified by $a = 1$. The spheres, having the dielectric constant $\epsilon_{\text{sphere}} = 12$, are immersed in free space. The dielectric constant of the substrate is $\epsilon_{\text{substrate}} = 5$. Fields are plotted on the plane marked with $y = 0.5$.

and the point $[K_1, K_2] = [0.5, 0.5]$. The eigenfrequency has been determined iteratively using the technique described in Section 3); when the result converged, we Fourier transformed the solution to get the real space fields.

In the solution we used 48 planewaves in x -direction, and 48 planewaves in y -direction. In z -direction we used 48 and 47 layers for the electric and magnetic fields, respectively. The electromagnetic field outside the slab ($z < 0$ and $z > 0.9$) has been computed using the eigenpairs for Maxwell's equations in free space. Note that we already have constructed these eigenpairs for the implementation of boundary conditions. Note also that having imposed the interface- and boundary conditions the unknowns in our problem, and, therefore, field distributions in the slab as well as in free space are uniquely determined. Finally, note that while the transversal fields e_1 , e_2 , h_1 and h_2 have been obtained from the solution of (37), the orthogonal field components e_3 and h_3 are computed as a postprocessing step using (14).

IV. ACKNOWLEDGEMENTS

One of the authors (K. Varis) thanks the Finnish Graduate School of Modern Optics and Photonics, and the Ausseninstitut at Vienna University of Technology for providing research scholarships which made possible a visit to Vienna, Austria for finalizing the current project.

This work was partially done while the second author (A. R. Baghai-Wadji) was visiting the Institute for Mathematical Sciences, National University of Singapore and Institute for High Performance Computing (IHPC) in 2003. This visit was supported by the Institute and IHPC.

REFERENCES

- [1] K. Varis, and A. R. Baghai-Wadji, "A Novel 2D Pseudo-spectral Analysis of Photonic Crystals," submitted for publication (ACES Journal 2004).
- [2] R. W. Freund, N. M. Nachtigal, "A Transpose-Free Quasi-Minimal Residual Algorithm for Non-Hermitian Linear Systems," SIAM Journal on Scientific Computing. 14 (1993) pp. 470-482
- [3] W. H. Press, S. A. Teukolsky, W. T. Wetterling, and B. P. Flannery, "Numerical Recipes in C: the Art of Scientific Computing," Cambridge University Press, Cambridge, pp. 493-495, 2nd edition, 2002.
- [4] S. G. Johnson, and J. D. Joannopoulos, "Block-Iterative Frequency-domain Methods for Maxwell's Equations in a Planewave Basis," Optics Express 8, no., 173-190, 2001.

Karri Varis was born in Espoo, Finland, in 1974. He received a M.Sc. degree in Electrical Engineering from Helsinki University of Technology in 1999. Since then, he has been a doctoral student in the Finnish Graduate School of Modern Optics and Photonics

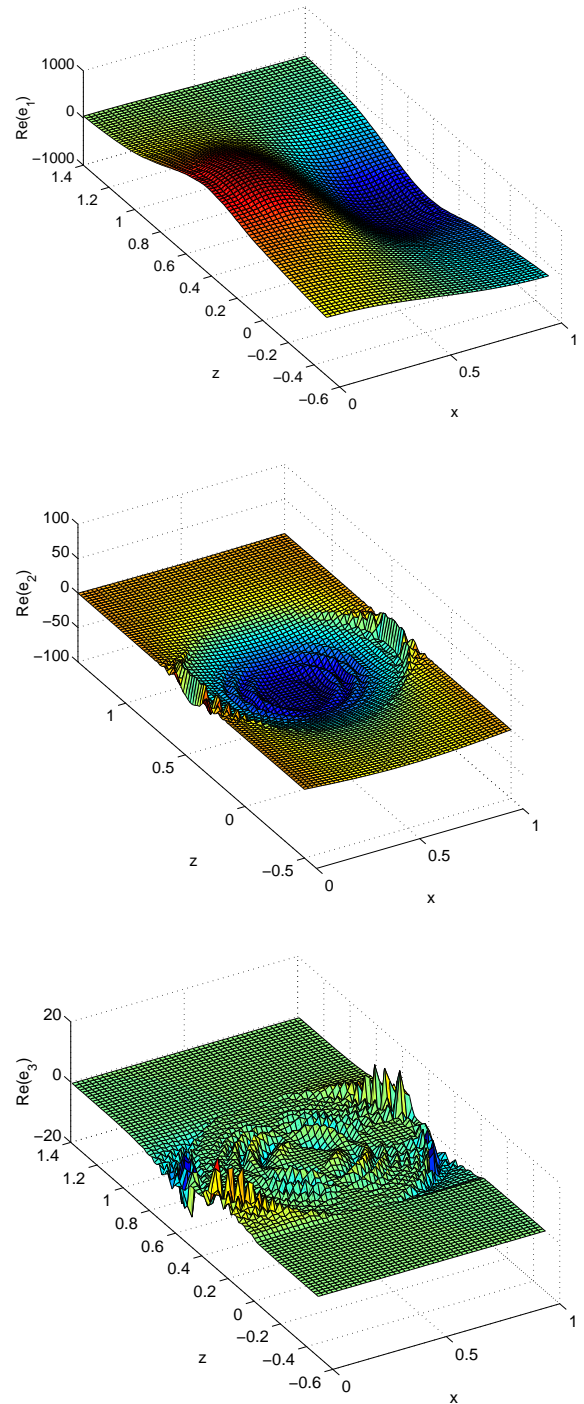


Fig. 4. Electrical field distributions for test case 2, which consists of dielectric spheres on a dielectric surface. Spheres are centered at $[x, y, z] = [0.5, 0.5, 0.45]$ and for $z < 0$ the dielectric constant is $\epsilon_{subst} = 5$. The spheres are immersed in free space. Ripples on e_3 are most likely due the properties of Fourier transform. However, the amplitude of this field component is negligibly small.

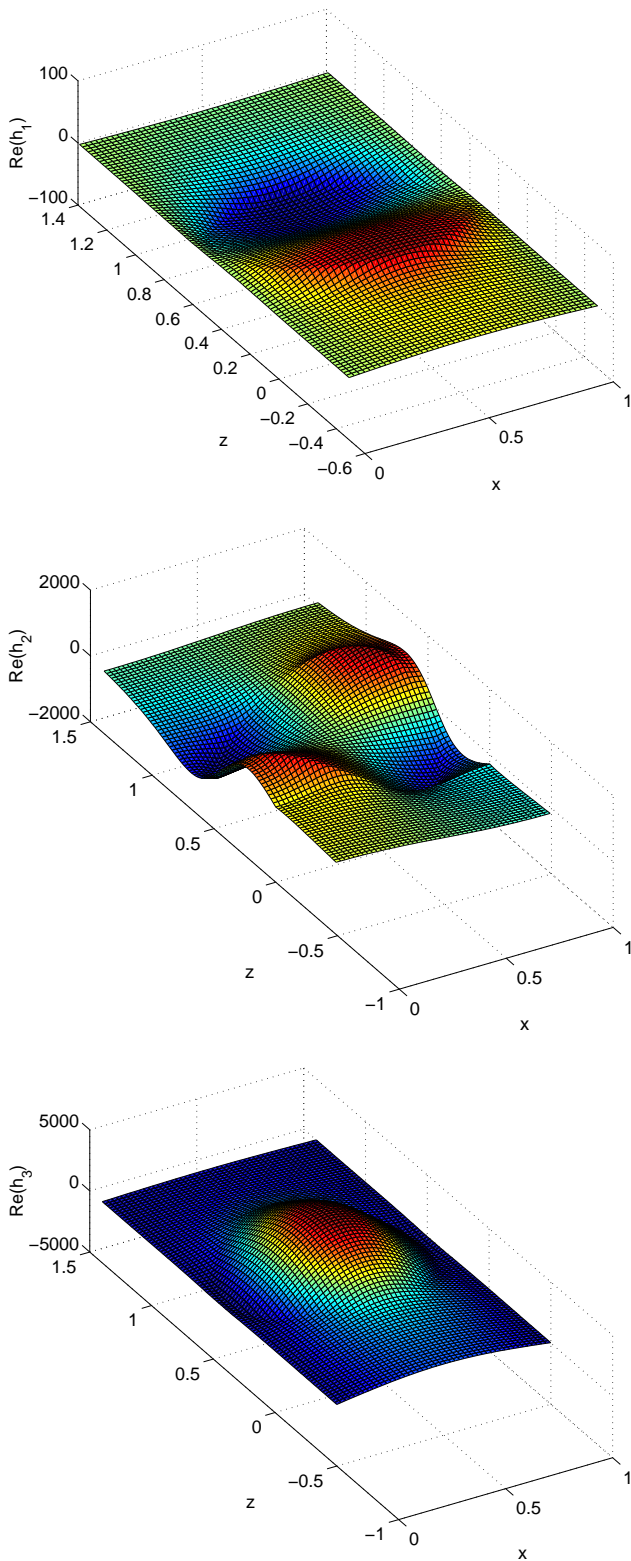


Fig. 5. Magnetic fields for testcase 2.

and working in the Optoelectronics Laboratory, Helsinki University of Technology. His current research interest includes the enhancement and development of computational techniques for the analysis of periodic and non-periodic systems, with an emphasis on photonic crystals and optical devices.

Ali R. Baghai-Wadji was born in Marand, Iran, on May 6, 1953. He has been with the Electrical Engineering and Information Technology Department at Vienna University of Technology (VUT), Vienna, Austria, since 1979. From 1979 to 1984 he was an associate researcher in Physical Electronics and Applied Electronics Groups, where he developed computer models for microelectronic and microacoustic devices. He earned his M.Sc. and Ph.D. in electrical engineering in 1984 and 1987, respectively, and obtained his *venia docendi* in physical electronics in 1994, all from VUT. Since 1997 he has been an associate professor at VUT. Currently he is heading the Accelerated Computational Technology (ACT) Group at the Institute for Fundamental and Theory of Electrical Engineering at VUT. Three times he was awarded the Kurt Gödel research scholarship from Austria, allowing him to spend a total of 10 months at UCI, University of California, Irvine, during the years 1990, 1991, and 1992. From 1994 to 1999 he was, on leave of absence from VUT, a principal engineer consultant in the United States serving more than four years for Motorola, Government System and Technology Group, Scottsdale, Arizona, and nearly one year for CTS-Wireless components in Albuquerque, New Mexico. In 1999 and 2000 he was (15 months) a visiting professor at Materials Science Laboratory, Helsinki University of Technology (HUT). That professorship was awarded by Nokia Research Foundation, and TEKES, a national science foundation in Finland. In addition, in the Fall 2000 he was awarded a Nokia Visiting Fellowship. In 2003 he was awarded a *venia docendi* for modeling and simulation of classical and quantum electronic devices and materials at HUT for an initial period of 6 six years. In 2003 he was four months an invited senior member of the Institute for Mathematical Sciences, and a visiting professor at the Institute for High Performance Computing, in Singapore. Since 1995 he has also been affiliated with Arizona State University as an adjunct professor at the Department for Mathematics and Statistics. In 2002 he was elected an honorary member of the Electromagnetics Academy, Massachusetts, USA. He has supervised five PhD dissertations, and eleven Masters' theses. He has lectured 12 short courses at various IEEE conferences internationally. He has authored more than 120 publications in reviewed journals and conference proceedings, and has one patent. His current research interest includes the development of accelerated computational modeling techniques, quantum mechanics, photonic crystals, and molecular electronics. Since 1995 he has been a senior member of the IEEE, an IEEE-UFFC associate editor, and an IEEE-UFFC technical program committee member. He was the guest editor for a special issue on *Modeling, Optimization, and Design of Surface and Bulk Acoustic Wave Devices* in IEEE Transactions on Ultrasonics, Ferroelectrics, and Frequency Control (Sept. 2001, Vol. 48, Num. 5). He will serve as the general chairman of the PIERS'05 conference.

A hybrid full MAS and Combined MAS/TSA Algorithm for Electromagnetic Induction Sensing

F. Shubitidze⁽¹⁾, K. O'Neill^(1,2), K. Sun⁽¹⁾, I. Shamatava⁽¹⁾, and K. D. Paulsen⁽¹⁾

⁽¹⁾ Thayer School of Engineering, Dartmouth College,
Cummings Hall, HB 8000, Hanover NH, 03755, USA

⁽²⁾ USA ERDC Cold Regions Research and Engineering Laboratory,
72, Lyme Road, Hanover NH, 03755, USA

Abstract –Electromagnetic induction (EMI) sensing, in both frequency and time domains, is emerging as one of the most promising remote sensing technologies for detection and discrimination of buried metallic objects, particularly unexploded ordnance (UXO). UXO sites are highly contaminated with metallic clutter so that the major problem is discrimination not detection. This requires high fidelity forward modeling for successful inversion and classification. Recently, the method of auxiliary sources (MAS) has been applied for solving a large range of ultra-wideband (1 Hz- 300 kHz) electromagnetic induction problems [1] - [6]. For a highly conducting and permeable metallic object, when the skin depth becomes small (at high frequency, i.e. induction number >100) the efficiency of the MAS is reduced significantly [6]. Other methods are stressed in this region as well. At the same time the Thin Skin Approximation (TSA) [7] - [9], which is based on the divergence free Maxwell's equation in a thin layer, infinitely close to the boundary interior, has shown very accurate results at high frequency/induction number. In this paper a hybrid algorithm, with standard MAS and also the MAS with TSA, is introduced and applied for solving the electromagnetic induction forward problem. Once the broadband frequency domain (FD) electromagnetic response is found it is translated into time domain (TD) using an inverse Fourier transform specialized for the characteristic TD input form. Numerical experiments are performed for highly conducting and permeable canonical objects, illuminated by a magnetic dipole or a loop antenna. These tests indicate that an algorithm using either the full MAS or MAS-TSA formulation, where appropriate, should provide a simulator that is applicable and efficient enough for fast 3-D solutions on a PC, under all conditions across the EMI band in both frequency and time domains.

Keywords: Hybrid, method of auxiliary sources, electromagnetic induction, skin-depth, time domain, frequency domain.

I. Introduction

Efficient and accurate numerical modeling of electromagnetic induction (EMI) responses by metallic objects finds application in many fields and has been a subject of research for some time [10 and references therein]. Recently, interest has been driven in part by the necessity for cleaning up buried unexploded ordnance (UXO). This is a potential problem in perhaps 10,000,000 to 15,000,000 acres within the United States, and is an even more severe problem in other parts of the world where military conflicts have taken place. Even rather distant history, e.g. World War I, has left a large legacy of dangerous and possibly polluting UXO in populated areas [11]. Use of remote sensing for UXO clearance is greatly limited by the fact that it is not possible to detect remotely the

explosive contained within a more or less intact metal casing. Therefore, we are left having to interpret signals produced by the metal body itself. These bodies can be quite complex in both geometry and composition. Furthermore, widespread metallic clutter at UXO sites and possibly multiple UXO near one another enormously complicate signal interpretation. For effective target inversion or classification algorithms, one requires very high fidelity, efficient forward models to apply in data processing schemes.

Ultra-wideband (~ 20 Hz to 100's of kHz) electromagnetic induction (EMI) sensors are among the most promising tools for the detection and discrimination of buried UXO [1] - [9], [11] - [30]. Most metallic objects produce broadband responses; different metals also produce different responses in the EMI band; and clutter is prominent. Therefore, one must resort to processing broadband data from many different looks at an unseen object, to achieve sufficient information diversity to classify targets successfully. This places a great burden on processing and the associated modeling, which has driven the development of new analyses and analytical tools for studying EMI scattering problems. The only well established analytical solutions to date for broadband EMI scattering are for the case of the sphere in both frequency and time domain [31], [32] and cylinder of infinite length oriented transverse to the primary field [33]. Recently progress has been reported for analytical solution of EMI scattering from spheroids [34], [35], including specialization to treat high frequency conditions, when penetration of the object is slight [35] using the small penetration approximation (SPA). Remaining evaluation problems for the spheroidal shapes in the mid-induction number region of the EMI band have recently been solved using asymptotic methods [36], so that a relatively complete analytical solutions for spheroids are now available. Particularly for arbitrary 3-D geometries, one must usually resort to numerical models to obtain results most relevant to the variety of target types that must be considered. Targets of arbitrary shape have been attacked using the Method of Moments (MoM) with an impedance boundary condition (IBC) [19]. More recently, bodies of revolution (BOR) have been modeled using the MoM with full, rigorous boundary conditions, requiring substantial computation times [14]. Hybrid finite element method (FEM) –boundary element method (BEM) approaches not reliant on the IBC have also been developed [23] – [24]. In the FD, a compact numerical formulation has been produced for arbitrary shapes using the Thin Skin Approximation (TSA) [7] - [9], which only applies the divergence equation for magnetic field inside the target.

This performs very well for the difficult realm of high frequency conditions, and for high permeability cases has remarkably broadband applicability. The decision whether to apply a full numerical treatment of the problem or one of the small penetration formulations (TSA, SPA) is most easily made in FD approaches, where skin depth is fixed for a given material and frequency. However a parallel system has also succeeded in direct TD formulations [37]. In what follows, we will pursue only the FD-TSA, converting to TD by inverse Fourier transform (FT).

Most recently, the authors have developed the Method of Auxiliary Sources (MAS [1] - [6]) for numerical solution of the full EMI problem for penetrable, highly conducting and permeable metallic targets. The MAS was originally designed for solving various electromagnetic radiations and scattering problems [38 and references therein]. Later, it was successfully combined with the SPA [6] and TSA [39] for analysis of EMI scattering phenomena. In the standard MAS for EMI [1], boundary value problems are solved numerically by representing the electromagnetic fields in each domain of the structure under investigation by a finite linear combination of analytical solutions of the relevant field equations, corresponding to sources situated at some distance away from the boundaries of each domain. The "auxiliary sources" producing these analytical solutions are chosen to be elementary currents/charges located on fictitious auxiliary surface(s), usually conforming to the actual surface(s) of the structure. In practice, at least as the method is realized here, we only require points on the auxiliary and actual surfaces, without resorting to the detailed mesh structures as required by other methods (FEM, BEM, etc).

EMI scattering responses are often expressed relative to the induction number $\chi \equiv \sqrt{\sigma\omega\mu} a$, where a (m) is a characteristic dimension of the object (usually the smallest one), ν = frequency (Hz), $\mu = \mu_0\mu_r$ is magnetic permeability [H/m] and σ (S/m) is the scatterer's electrical conductivity. (The time dependence expression $e^{j\omega t}$ is assumed and its expression suppressed in all FD equations that follow, where j is the square root of minus one, t is time (s), and ω is 2π times frequency in Hz). The quantity χ is proportional to a/δ , where δ is the skin depth, and serves as a dimensionless, scaled frequency.

While we have shown various advantages of the MAS for the EMI scattering problem, its main limitation is reduced accuracy and efficiency at the high frequency end of the EMI band [9]. This is because the influence of source entities sought in the solution decays over a distance of a few δ , which becomes very small at high frequencies (induction numbers). That distance becomes much smaller than the mesh spacing, when the numerical resolution is only fine enough to represent the object shape accurately. This means that without intolerably fine meshing the source quantities sought cannot interact; many matrix elements become almost zero (within the accuracy of the computer); the matrix becomes ill-conditioned and the solution unstable. The same problem arises whether one places the unknown sources

mathematically on auxiliary surfaces, or on the physical surfaces, as in popular integral equation techniques.

To avoid this kind of difficulty, several types of approximations were developed recently, including the TSA and SPA, which are related to impedance boundary conditions. The accuracy and validity of the TSA in conjunction with the BEM have been studied previously [9], in application to highly conducting and permeable (e.g. steel) metallic objects with regular geometries, such as the sphere, ellipsoid, prolate, and oblate spheroid, subject to a uniform primary magnetic field. Under these constraints it has been shown that, for a wide class of EMI scattering problems, the TSA is very accurate and efficient over the entire broadband EMI frequency range [9]. It is easy to implement for an arbitrary geometry. At the same time, the BEM-TSA cannot treat low induction number cases reliably, particularly for non-permeable materials. Recently, a hybrid MAS-SPA algorithm was developed in [6]. It has been shown that MAS-SPA is very efficient for analyzing EMI responses at high induction numbers for spheroidal objects. The algorithm employs a factor f (see eq. 56 in [35]) that can readily be obtained for spheroidal shapes. However, it is very difficult to extend this algorithm for arbitrary geometries. Later the combined MAS/TSA algorithm was introduced and tested for highly permeable and conducting regular shapes under highly variable primary (transmitted) fields as well non-regular geometries [39]. Here we introduce a hybrid MAS – MAS/TSA system, in which the algorithm switches between the full MAS and the MAS/TSA as needed.

Many EMI sensors operate in the time domain (TD), with transmitted signals that are approximately step functions. They are designed to record only during the time immediately after the steady transmitted field has been shut off (the "turn off" case). Here an inverse Fourier transform is used to obtain transient TD response from the FD MAS – MAS/TSA solution for a highly conducting and permeable metallic object, for both turn-on and turn-off cases. A fast and reliable algorithm for the inverse transform has been developed, specialized for the step function input. It treats a singularity in the integrand effectively, even for relatively sparse data points. Because the MAS – MAS/TSA algorithm can operate stably, accurately, and efficiently from the lowest (~static) to the highest (~PEC) EMI frequencies, sufficient bandwidth is achieved in the numerical solutions so that FD results can be inverted into TD without perturbations, even in the most extreme time ranges.

The full MAS formulation applied at low frequencies only requires modest numerical resolution, on the order of that to define the geometry. In the combined MAS/TSA algorithm applied at higher frequencies, only about the same order of resolution is required, while the number of unknowns is reduced by a factor of 3 in 3-D problems. Single frequency computations are approximately four times faster. For multi-frequency cases, the matrices expressing magnetic fields produced by auxiliary magnetic charges do not depend on frequency and can be stored for use, without recalculation, over an extended band. Most important, the thorough investigation of numerical experiments clearly shows superior stability, computational speed, and robustness of the hybrid

MAS – MAS/TSA algorithm relative to the standard MAS method at high induction number.

II. Governing equations

2.1 The magneto-quasistatic assumption

All solutions in this study are based in part on two reasonable assumptions. The first is that, throughout the entire UWB EMI frequency band, electromagnetic phenomena are magneto-quasistatic. While this may be taken as something of a foregone conclusion in low frequency EMI, we examine the assumption explicitly here because recent developments have raised the upper frequency limits for EMI practice to about 300 kHz. This makes the magneto-quasistatic assumption more suspects. The second assumption, also examined here, is that electrical currents induced in surrounding soil have a negligible effect compared to those in the (substantial) metal target.

Consider a highly conducting and permeable metallic scattering object, with permeability $\mu = \mu_r \mu_0$ and conductivity σ [S/m] embedded in a uniform background. The time dependence expression of $e^{j\omega t}$ is suppressed subsequently. The governing equations that form the basis for any pertinent analysis of EMI scattering physics are Maxwell's equations. In both static and transient fields, Maxwell's magnetic field divergence equation must be satisfied

$$\nabla \cdot \mathbf{H} = 0. \quad (1)$$

This form of the equation assumes spatially uniform μ . In practice here we will assume that μ may vary between different portions of an object of interest, but that it is constant within any given section or sub-region. Thus (1) applies within every (sub)region, except on boundaries, where we apply a boundary condition instead.

The particular equations in Maxwell's complete set that pertain most directly to induction are Faraday's and Ampere's Laws,

$$\nabla \times \mathbf{E} = -j\omega\mu\mathbf{H}, \quad (2)$$

$$\nabla \times \mathbf{H} = \sigma\mathbf{E} + j\omega\epsilon\mathbf{E}. \quad (3)$$

Here \mathbf{E} is the electric field (V/m) and \mathbf{H} is magnetic field (A/m). The quantity $j\omega\epsilon\mathbf{E}$ is called the displacement current, where ϵ is the permittivity of the medium (farad/m). Note that, even in the frequency domain, ϵ as used here does *not* include any portion resulting from the electrical conductivity of the medium, σ , the effects of which will always be expressed separately. The term $\sigma\mathbf{E}$ represents conduction electric currents in the medium. We wish to examine the magnitudes of these terms, relative to each other and also relative to the various derivatives on the left side of the equation. We will do this by tracing the influence of each of the terms on the right hand side within an equation entirely in \mathbf{H} , obtained by

combining (3) with other of Maxwell's equations. Taking the curl of (3) and performing manipulations yields

$$\nabla^2 \mathbf{H} = j\omega\sigma\mu\mathbf{H} - \omega^2\epsilon\mu\mathbf{H}. \quad (4)$$

The first and second terms on the right in (4) descend from the first and second terms on the right in (3), respectively. Specifically, the relative magnitude of the first (second) term on the right hand side of (3) corresponds to the relative magnitude of the first (second) term on the right hand side of (4) and we will analyze them latter. The three parameter regions where this equation will be examined are those for air (free space), the soil, and the metallic scatterers.

The situation is different in each of the three parameter regions. In the air we assume that σ is approximately zero, so that the second term in (4) drops out. This leaves a classical wave equation with wavenumber k defined as

$$k = \frac{2\pi}{\lambda} = \omega\sqrt{\epsilon\mu} \quad (5)$$

where λ is the wavelength.

At the top of the MF-EMI band (300 kHz), this expression indicates that the electromagnetic wavelength is one kilometer. Typical distances over which we are concerned about electromagnetic interactions are on the order of 1 m. Thus there is negligible phase difference between different points within the domain of consideration in the air. Fields change essentially in unison throughout, with the structure of static fields, gaining time dependence only through the action of sources and boundary conditions. This results in the uniform time factor $e^{j\omega t}$, and a quasi-static phenomenology. The ultimate significance of this in connection with the equations above is that *both* terms on the right hand side of (4) are negligible, as both are FD expressions for time derivatives. Thus the corresponding terms in (3) are also negligible, and the H field is irrotational ($\nabla \times \mathbf{H} = 0$). An irrotational field may be represented as the gradient of a scalar potential, ψ (A)

$$\mathbf{H} = -\nabla\psi. \quad (6)$$

Substituting (6) in (1) produces the governing equation for the air region

$$\nabla^2\psi = 0. \quad (7)$$

Within the soil, σ is nonzero and the ratio of the magnitude of the third to the second term in (4) is $\omega\epsilon/\sigma$. As a "worst" case, i.e. the one that most threatens the MQS assumption, we assume $\omega \sim 10^6$ rad/s, $\sigma \sim 10^{-2}$ S/m, and $\epsilon \sim 10^{-10}$ F/m. This combination of parameters means that we would be operating at the extreme upper limit of the MF-EMI band and presupposes a particularly unlucky set of soil properties, with low conductivity but rather high dielectric constant. Even this combination of parameters implies that the third (displacement

current) term is not larger than the second (electric current) term. To estimate the significance of the electric currents in the soil, compare their magnitude to those induced in the metallic target. By general continuity conditions, the electric field \mathbf{E} will be on the same order in the soil immediately surrounding the target and in the parts of the metal where the most significant currents are flowing. As the currents are equal to $\sigma\mathbf{E}$, the ratio of currents in metal and soil will be approximately equal to the ratio of their conductivities. A reasonable upper bound on soil conductivity is $\sigma \sim 10^{-2}$ S/m. A typical metal of interest has $\sigma \sim 10^7$ S/m. Thus the currents in the metal are about nine orders of magnitude stronger than those in the soil. Unless the metal scatterer is extremely small and simultaneously the sensor samples an enormously larger volume of soil (not the case here), the fields in the soil will be dominated by those produced by currents in the metal. That is, the electric currents in the soil will not be a significant factor in determining the fields in the soil. Thus we conclude that the term containing the soil currents may be dropped (first term on the right in (4)). We have already concluded that the second term is not more significant than the first; therefore the entire right hand side of (4) is again negligible. Thus, in the soil as in the air, we conclude that the magnetic fields are irrotational and can be represented using a scalar potential, i.e with the governing equation (7). Representing of the magnetic field by the scalar potential ψ , instead of a vector potential, has two main advantages: first the calculation of Greens function related to the Laplace equation (7) is very simple and fast, and second the scattered magnetic field can be represented as summation of the fields produced by a set of magnetic charges. This reduces number of unknowns at least a factor of 2 relative to the vector potential representation.

Within the metal, we again examine the quantity $\omega\epsilon/\sigma$. Using the typical values cited above we immediately conclude that the displacement current term is negligible compared to the electric current term. However, the electric currents within the metal are by no means negligible; rather, they are a fundamental source of the scattered signals. Thus two terms remain in (4), which may be constructed as a Helmholtz equation

$$\nabla^2 \mathbf{H} + k^2 \mathbf{H} = 0, \quad k = \sqrt{-j\omega\sigma\mu}. \quad (8)$$

Here k is sometimes referred to as a wavenumber, by analogy with higher frequency solutions to the equation. However, note that (8) is *not* a wave equation, as the second term $-j\omega\sigma\mu\mathbf{H}$ is the frequency domain equivalent of $\sigma\mu$ times the *first* derivative of \mathbf{H} with respect to time, not the second derivative. We can generate traveling undulations within the metal by imposing sinusoidal behavior on its surface. However these are not true waves, e.g. they do not reflect. As in the wave case, fundamental solutions of (8) can be expressed as

$$\mathbf{H} \sim \frac{e^{jkR}}{\mu_r R}, k = \gamma + i\gamma, \gamma = \frac{\sqrt{\omega\sigma\mu}}{\sqrt{2}}, \mathbf{R} = \mathbf{r} - \mathbf{r}'. \quad (9)$$

Because the real and imaginary parts of k are equal, the spatially oscillating factor e^{jkR} decays by $1/e$ in less than one sixth of its spatial period.

2.2 The method of auxiliary sources

In the EMI frequency regime the EM fields penetrate the scatterer, at least to some degree. Internal and external fields at the surface of the object must satisfy the continuity of tangential components of \mathbf{H} and normal component of \mathbf{B}

$$\hat{\mathbf{n}} \times (\mathbf{H}_1^{\text{sc}} + \mathbf{H}^{\text{pr}}) = \hat{\mathbf{n}} \times \mathbf{H}_2, \quad (10)$$

$$\hat{\mathbf{n}} \cdot (\mathbf{H}_1^{\text{sc}} + \mathbf{H}^{\text{pr}}) = \hat{\mathbf{n}} \cdot \mu_r \mathbf{H}_2. \quad (11)$$

Here $\hat{\mathbf{n}}$ is a unit normal vector on the real surface, \mathbf{H}^{pr} is the primary (transmitted) magnetic field, \mathbf{H}_1^{sc} is the scattered magnetic field which we consider to be radiated by the auxiliary magnetic charges, which are distributed over the inner auxiliary surface [1]; \mathbf{H}_2 is the total magnetic field inside the object, produced mathematically by the auxiliary magnetic sources placed on the outer auxiliary surface. Using conventional MAS [1] the boundary conditions (10) and (11) can be written in the following compact matrix form:

$$\begin{bmatrix} G_n^Q & \mu_r G_n^{P_u} & \mu_r G_n^{P_v} \\ G_u^Q & G_u^{P_u} & G_u^{P_v} \\ G_v^Q & G_v^{P_u} & G_v^{P_v} \end{bmatrix} \begin{bmatrix} Q \\ P_u \\ P_v \end{bmatrix} = - \begin{bmatrix} H_n^{\text{pr}} \\ H_u^{\text{pr}} \\ H_v^{\text{pr}} \end{bmatrix}. \quad (12)$$

Here Q is a vector containing the amplitude of auxiliary magnetic charges, P_k , $k=u,v$ is a vector containing the amplitudes of auxiliary magnetic dipoles oriented along u and v , which are orthogonal directions on an auxiliary surface, G_ξ^Q is exterior field expressed with Green's function $1/(4\pi R)$ where $R = |\mathbf{r} - \mathbf{r}'|$ and $G_\xi^{P_\gamma}$ is the interior solution expressed ultimately in terms of dipole sources distributed over an exterior auxiliary surface, together with a Green function of the form $e^{jkR}/4\pi R$. More explicit forms of the G_ξ^Q , and $G_\xi^{P_\gamma}$ matrices, where $\hat{\xi} = \hat{\mathbf{n}}, \hat{\mathbf{u}}, \hat{\mathbf{v}}; \gamma = u, v$, are presented in [1]. When the skin depth becomes small so that both real and imaginary parts of k become high, the $G_\xi^{P_k}$ matrix's elements become very small compared to G_ξ^Q matrix elements. At relatively high frequency (more than 10 kHz for common steel, copper, aluminum, brass etc), the $G_\xi^{P_k}$ matrix elements decay very rapidly in space and the system (12) becomes unstable.

2.3 Combination of MAS with TSA

To avoid this problem it is desirable to establish an alternative formulation that would be applicable for high frequencies. It is well known that at high induction numbers the fields in the interior of the scatterer are non-zero only in a thin layer close the surface (Fig. 1). Under this condition, we exploit the divergence free Maxwell's equation applied in that near surface region. That equation and the thinness of the surface layer provide a boundary condition on the external field, obviating the necessity for complete solution of the internal field. We will proceed in a manner analogous to that in [8], [9]. In those references linear interpolation of unknowns is used over piecewise flat surface elements, in a Galerkin integral treatment of the governing relation. Here consider a general curvilinear surface, with completely continuous tangents and normals, and a subdomain integration of the governing equation. Gauss's Law (the magnetic field divergence equation) is integrated over a thin finite volume just below the object's surface, to produce the relation

$$\nabla \cdot \mathbf{H}_2 = 0 \Rightarrow \oint_A \mathbf{H}_2 \cdot d\mathbf{A} = 0, \quad (13)$$

or

$$\begin{aligned} H_{2,n_2} A_{n_2} - H_{2,n_1} A_{n_1} + H_{2,u_2} A_{u_2} - H_{2,u_1} A_{u_1} \\ + H_{2,v_2} A_{v_2} - H_{2,v_1} A_{v_1} = 0 \end{aligned} \quad (14)$$

where $A = A_{n_2} + A_{n_1} + A_{u_2} + A_{u_1} + A_{v_2} + A_{v_1}$ is a total area of the thin volume. Dividing (14) equation by the layer thickness d and take limit as $d \rightarrow 0$ yields

$$\begin{aligned} A_n \frac{\partial H_{2,n}}{\partial n} + H_{2,n} \frac{\partial A_n}{\partial n} + H_{2,u_2} L_{u_2} - H_{2,u_1} L_{u_1} \\ + H_{2,v_2} L_{v_2} - H_{2,v_1} L_{v_1} = 0. \end{aligned} \quad (15)$$

Here $\partial n = \partial d$. The basic tenet of the TSA is that fields just

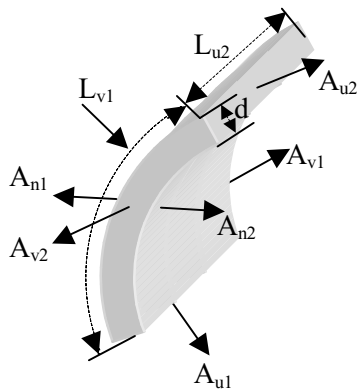


Fig. 1. Geometry of volume just below the real surface A.

below the surface within the thin layer vary approximately one-dimensionally, normal to the surface. Thus, as $d \rightarrow 0$ the normal component of the magnetic field $H_{2,n}$ and its derivative $\frac{\partial H_{2,n}}{\partial n}$ along normal $\hat{\mathbf{n}}$ are related to each other through [9]:

$$\frac{\partial H_{2,n}}{\partial n} = jkH_{2,n}(0, \mathbf{u}, \mathbf{v}) \quad (16)$$

where $H_{2,n}(0, \mathbf{u}, \mathbf{v})$ is the value as $n \rightarrow 0$ on the interior of the surface. Based on the boundary conditions (10) and (11) together with the TSA condition (16), equation (15) can be rewritten for external magnetic field on boundary in a form involving only quantities on the surface:

$$\begin{aligned} \left[H_{1,n}^{sc} \frac{1}{\mu_r} \left(jkA_n + \frac{\partial A_n}{\partial n} \right) \right] + \\ \left[H_{1,u_2}^{sc} L_{u_2} - H_{1,u_1}^{sc} L_{u_1} + H_{1,v_2}^{sc} L_{v_2} - H_{1,v_1}^{sc} L_{v_1} \right] = -[Y], \end{aligned} \quad (17)$$

or, in matrix form:

$$[Z][Q] = -[Y]. \quad (18)$$

Here

$$\begin{aligned} [Z] = \left[G_n^Q \frac{1}{\mu_r} \left(jkA_n + \frac{\partial A_n}{\partial n} \right) + G_{u_2}^Q L_{u_2} - G_{u_1}^Q L_{u_1} \right] + \\ \left[G_{v_2}^Q L_{v_2} - G_{v_1}^Q L_{v_1} \right], \end{aligned} \quad (19)$$

and

$$\begin{aligned} [Y] = \left[H_n^{pr} \frac{1}{\mu_r} \left(jkA_n + \frac{\partial A_n}{\partial n} \right) \right] + \\ \left[H_{u_2}^{pr} L_{u_2} - H_{u_1}^{pr} L_{u_1} + H_{v_2}^{pr} L_{v_2} - H_{v_1}^{pr} L_{v_1} \right]. \end{aligned} \quad (20)$$

When the near-surface layer of electromagnetic activity is sufficiently thin relative to object dimensions ($a/d \sim 0.1$ or less), the equations above are completely sufficient to include the interior response of the target and to connect it to the exterior fields. To apply MAS to the exterior region, a set of magnetic charges is placed mathematically inside the physical surface, on the auxiliary surface S_1^{aux} shown in Fig. 2. The secondary magnetic field due to the target is expressed as a superposition of the fields generated from a finite number (N) of point charges, $\{Q_i\}$, $i = 1, 2, 3, \dots, N$ placed on the surface S_1^{aux} . The total secondary magnetic field at the position \vec{r}_n due to the auxiliary charges is expressed as Eq.

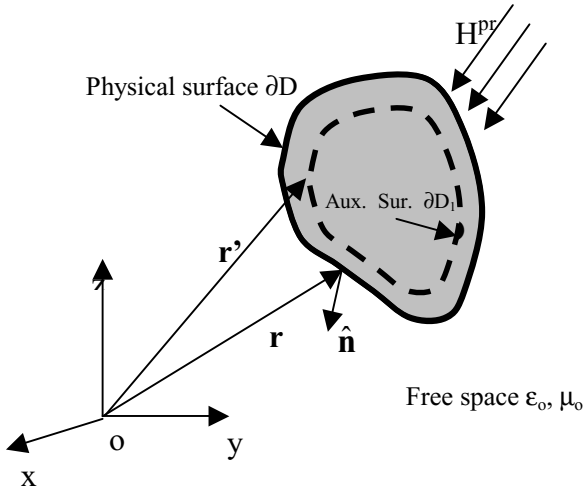


Fig. 2. Combined MAS-TSA.

(21) in [1]. By applying equation (17) at M collocation point on S and expressing \vec{H}_1^{sc} using the $\{Q_i\}$, we cast into an $N \times M$ linear system of equations, where normally we set $M=N$.

The significance of all this is that TSA together with standard boundary conditions across the boundary allows us to write the entire problem strictly in terms of *exterior* field quantities (17). These in turn can be solved for in terms of a simple set of *scalar* auxiliary source strengths, distributed relatively sparsely over an auxiliary surface. We term this formulation the combined MAS-TSA algorithm, because it retains an MAS formulation for the exterior field, but treats the interior field only through the TSA. The "full MAS" designates an MAS formulation applied to both interior and exterior regions. One can also mix MAS and TSA in another sense, namely applying the full MAS under conditions where it is appropriate, and easily switching to the combined MAS/TSA where it is appropriate, e.g. at higher frequencies. This provides a full EMI band simulator, essentially from the magneto-static lower limit to the upper PEC limit at some 100's of kHz.

2.4 Transient response of a highly conducting and permeable object

TD EMI instruments have been very prominent in localized subsurface surveying, particularly for detection and discrimination of UXO [40 and references therein]. The transient response can be obtained from the MAS –MAS/TSA FD solutions by an inverse Fourier transform

$$H(t) = \frac{1}{2\pi} \int_{-\infty}^{\infty} H(\omega) H^{pr}(\omega) e^{j\omega t} d(\omega). \quad (21)$$

Here ω is angular frequency and $H(\omega)$ is the FD solution. In measurement practice, the primary magnetic field is typically a downward step function

$$H^{pr}(t) = H_0^{pr} u(t) \quad (22)$$

where

$$u(t) = \begin{cases} 1, & t < 0 \\ 0, & t \geq 0 \end{cases}$$

which corresponds to the "turn off" case. In the FD

$$H^{pr}(\omega) = H_0^{pr} \sqrt{\frac{\pi}{2}} \left(\frac{1}{j\pi\omega} + \delta(\omega) \right). \quad (23)$$

III. Numerical Results

In this section the hybrid standard MAS and combined MAS/TSA method are applied to the analysis of broadband electromagnetic scattering by highly conducting and permeable metallic objects. The validity and sensitivity of TSA in conjunction with the BEM method has been widely tested for canonical geometries under time varying uniform field [9]. While we expect the underlying approximation to produce an accurate system at sufficiently high induction numbers, past BEM/TSA experience suggests that applicability may be wider than that, depending on the scatterer's permeability. Therefore, we will perform numerical tests of the new method across the entire EMI band. The results are compared with a solution obtained by full (conventional) MAS and experimental data obtained using the

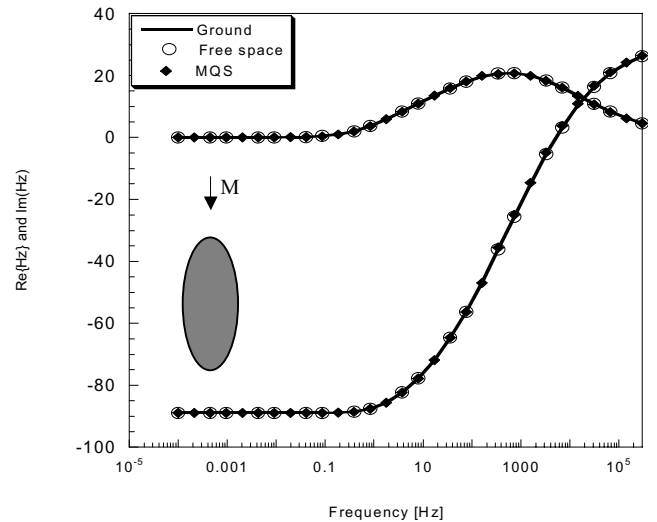


Fig. 3. Scattered magnetic field versus frequency, for a spheroid.

GEM-3 sensor [41]. All MAS calculations described below were done with the simplest point matching, point source code [1]. Finally, transient TD EMI responses are simulated and analyzed for highly conducting, permeable and non-permeable spheroidal objects.

Validity of MQS assumption

First we perform calculations to check the validity of the MQS assumption over the entire EMI band. A prolate spheroid, with minor axis $a=10$ cm, major axis $b=50$ cm, and conductivity $\sigma = 10^7$ S/m and relative permeability $\mu_r = 100$, is excited by a magnetic dipole placed above it. The distance between the center of the spheroid and dipole is 60 cm. Fig. 3 shows the scattered magnetic fields versus frequency for three

permeable and non-permeable spheres, illuminated by an oscillating magnetic field from a loop antenna. The radius of the sphere is $a = 10$ cm, with electromagnetic parameters $\sigma=4 \times 10^6$ [S/m] and $\mu_r = 1$ or 150. The field produced by the multi-loop antenna is described in detail elsewhere [41], [5]. The distance between the antenna's center and top part of the sphere is 5cm. The observation point is at the center of the antenna. The co-planar, concentric inner and outer loop radii are 10 cm and 20 cm, respectively. The current amplitudes and

TABLE I: MAS and hybrid MAS-TSA complexity for the generation of the results in Fig.4 Computation was done on Pentium IV, 2 GHz speed.

Induction number range	Standard MAS $\mu_r = 1$		Standard MAS $\mu_r = 150$		Combined MAS-TSA any μ_r	
	Number of unknowns	CPU Time (secs)	Number of unknowns	CPU Time (secs)	Number of unknowns	CPU Time (secs)
$0 < ka < 10$	40	0.15	60	0.25	14	0.015
$11 < ka < 100$	60	0.25	120	1.12	14	0.015
$101 < ka < 1000$	80	0.52	280	5.8	14	0.015

cases. In the first case, the spheroid is placed in a uniform ground with conductivity $\sigma = 10^{-2}$ S/m and simulation is done including a displacement and electric currents, both within the object and outside it (no MQS assumption, solid line in the figure). The second case assumes that the spheroid is placed in free space and again simulation is done without MQS assumption (circles). Finally, a third case employs the MQS assumption throughout (no electric currents in surrounding space, no displacement currents throughout: diamonds). In all

their directions on the loops are chosen in such way that at the centers of the loops the primary field is zero. Fig. 4 shows comparisons of scattered magnetic field calculated by standard MAS [1] with number of sources N and by the combined MAS-TSA [39], both with formulations assuming a body-of-revolution (BOR). The figure shows the “full” range of induction numbers in that the problem ranges from lowest values of interest, in which the primary field penetrates the object completely (\sim magnetostatic case), up to asymptotic

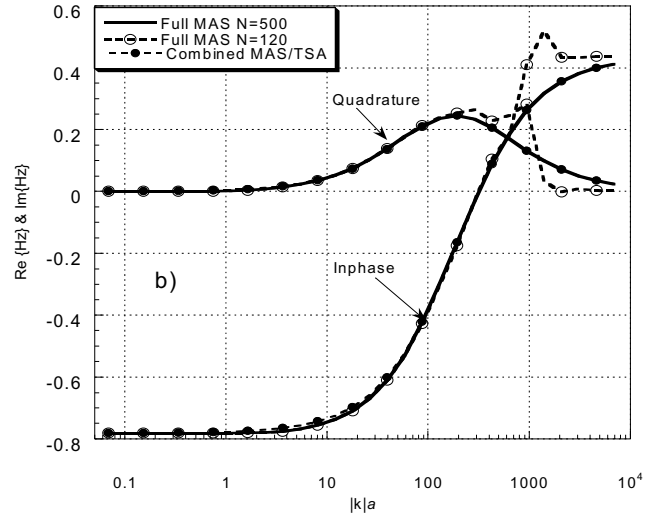
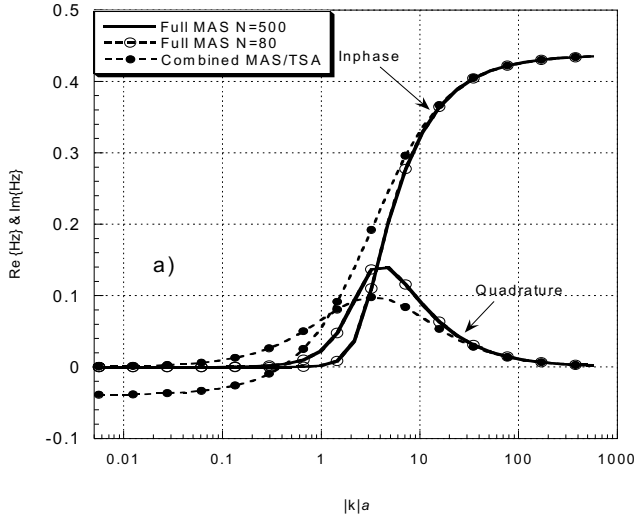


Fig. 4. The scattered magnetic field versus induction number for sphere subject to a realistic sensor: a) non-permeable, b) permeable case.

three cases the scattered magnetic fields for the spheroid are the virtually the same, i.e the MQS assumption is very accurate across the entire EMI frequency range.

1. Accuracy and Complexity of combined MAS-TSA algorithm for non-uniform excitation

Next we examine the performance of the two formulations for simulating EMI scattering from highly conducting,

high frequency limits, with arbitrarily small skin depth (\sim PEC case). At low induction numbers the full MAS gives high accuracy results compared to the combined MAS/TSA method for the non-permeable sphere. As induction number increases, this difference becomes insignificant (in these cases, as in the BEM-TSA [7] – [9] in cases with uniform fields, when the induction number is more than about 20). For the highly permeable sphere the full MAS with relatively dense distribution of sources and combined MAS/TSA algorithm are

in very good agreement over the entire band. However, the standard MAS with small number of sources becomes unstable (Fig. 4 b) after induction number 100, which is not the case for non-permeable sphere (Fig. 4 a). This means that, at any particular resolution, the stability of the full MAS is determined by two factors: induction number and permeability. Both these parameters affect the matrix elements G_{ζ}^R in equation (12) in approximately the same way. Thus,

8000 with no apparent difficulties associated with change in skin depth and associated resolution requirements.

Comparisons between CPU time and source density for two standard MAS and combined MAS/TSA solutions are given in table I. For full MAS solution of the same problem at high induction number (single frequency) approximately from 6 to 12 times more unknowns were required. However, depending on the object geometry, a much higher number of unknowns may be necessary to achieve convergence of the solutions

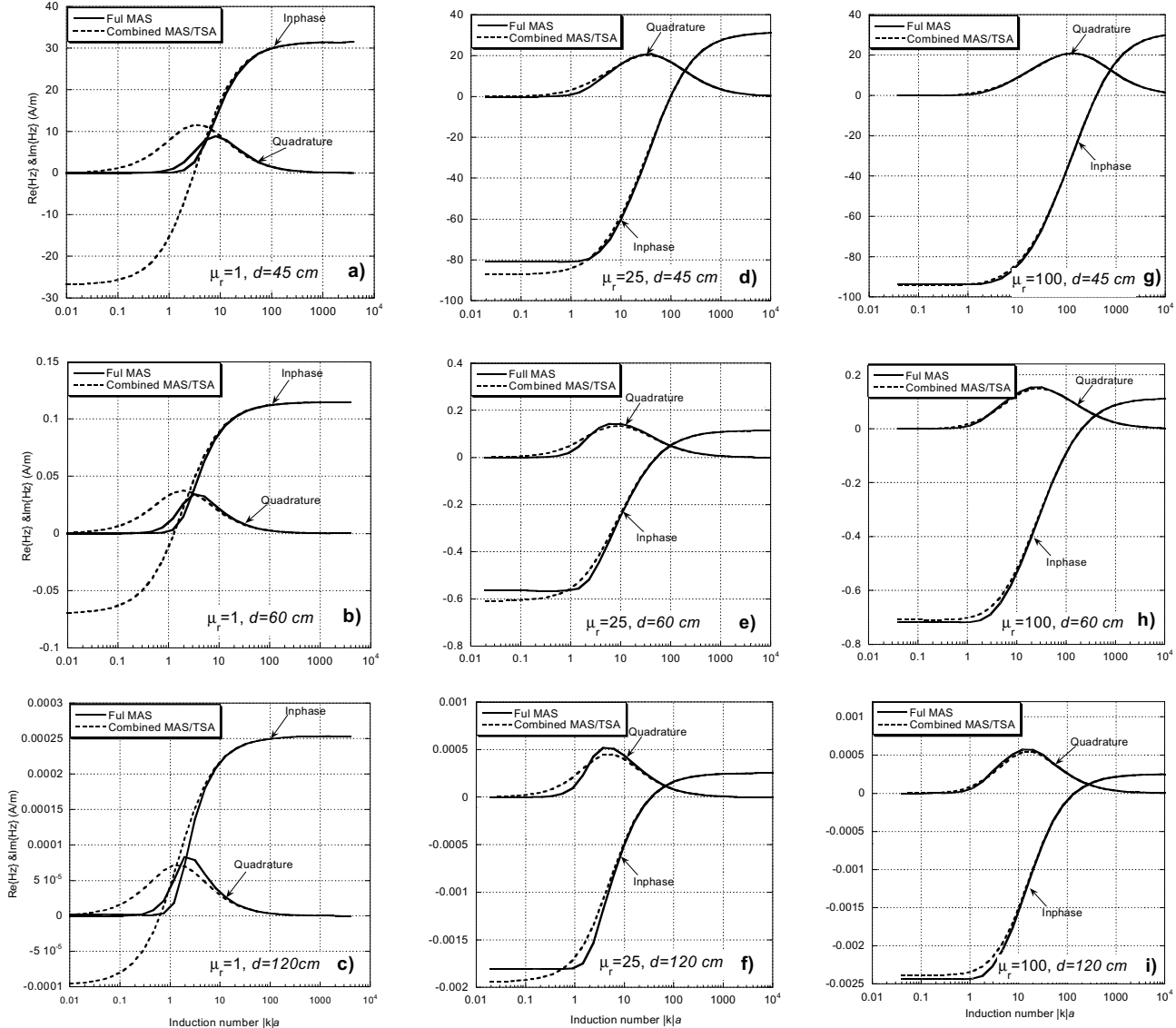


Fig. 5. The scattered magnetic field versus induction number for a prolate spheroid.

when these parameters increase, the total magnetic field H_2 inside the object decays steeply, interaction between the discretized quantities degenerates, and the system (12) becomes unstable. At the same time, the accuracy of combined MAS/TSA algorithm significantly increases at low induction numbers for high permeability (Fig. 4 b), as in the BEM-TSA [7] – [9] in cases with uniform fields. For the highly permeable case, the MAS/TSA covers the whole band from induction number 0.01 up through induction number

from the standard MAS. In the comparisons between CPU time shown, it is obvious that the reduction in complexity resulting from use of MAS/TSA for this problem is dramatic and becomes more significant as: 1) the induction number increases, and 2) the permeability of the object increases. Note here that results in Table I show two very significant facts, applicable at least to spherical scatterers:

1. For the high permeability objects the accuracy of the MAS/TSA method is reasonably good over entire broadband electromagnetic induction range.
2. To obtain highly accurate results for high permeability objects, the full MAS method requires a very dense distribution of unknowns, which dramatically increases computational time and computer resource requirements.

Compared to conventional MAS, the MAS/TSA algorithm has several features that make it attractive to a wide range of EMI problems. The number of unknowns in MAS/TSA is reduced by a factor of 3 in general 3D EMI problems (see equations (12) and (18)). In the MQS regime, the scattered field is very smooth. This allows the MAS/TSA method, with very low computational cost requirement, to get highly accurate results with a point source/point matching technique, with only the mesh density that is required to represent the geometry accurately. The matrix that produces the scattered field associated with magnetic charges in (17) does not depend on the frequency. Within its realm of validity, MAS/TSA should be much more attractive compared to other numerical techniques such as MoM [14] and FEM, e.g. [23], [24]). The greatest advantages of combining the MAS and MAS/TSA is accuracy over all EMI frequencies for all electromagnetic parameters, with quite simple programming, especially relative to sophisticated MoM type techniques such as the Fast

in b), e), h); and 120 cm in c), f), i) The solid line corresponds to full MAS with $N=500$ number of sources and dashed line to MAS/TSA algorithm. These figures demonstrate in cases that, when the induction number is more than about 20, both techniques produce virtually the same results. However, at low frequency for non-permeable cases, the MAS/TSA algorithm produces significantly different results (Fig. 5 a-c). These errors are reduced as the dipole moves from the object. Again, as permeability increases the differences between standard MAS and MAS/TSA algorithm become insignificant over the entire EMI frequency range, particularly for $\mu_r=100$, e.g. Fig. 5 g. As the dipole moves from the object with permeability 100, the error between MAS and MAS/TSA become slightly worse, but not significantly. These results also show that depending on the distance between the target and sources of excitation the frequency spectrum of the scatterer is different. This contrasts with the observation in [8], where frequency response is independent of observation point, but under a uniform primary field. For example, for the highest permeability spheroid the peak of the quadrature or imaginary part, associated with volume currents, moves from induction number 100 to 10. It is obvious, that when dipole is close to the object it excites strong eddy currents within the closest part, and in turn these currents will dominate the received signal. When the source is close to the end of the spheroid, its response is reminiscent of that from a sphere, both in terms of performance of the MAS/TSA and in

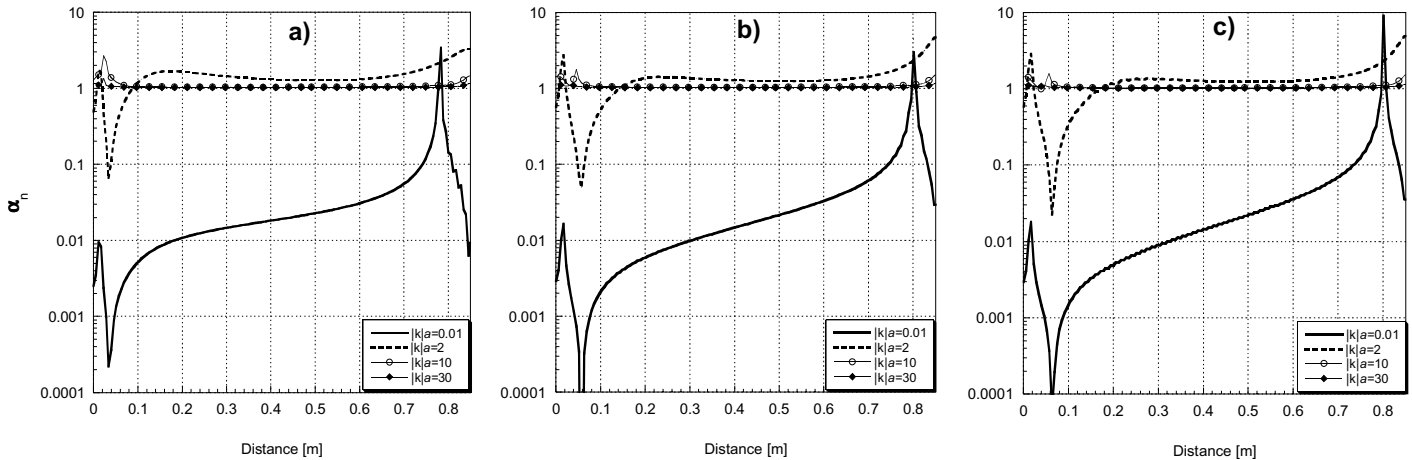


Fig. 6. Error criteria α_n versus distance along surface of the spheroid for permeability a) $\mu_r=1$, b) $\mu_r=25$, and c) $\mu_r=100$.

Multi-pole Method [42].

To check the accuracy of the MAS/TSA algorithm in non-spherical cases, we examine EMI scattering from both non-permeable and permeable prolate spheroids. The spheroid's major to minor axis aspect ratio is four ($b/a = 4$) and minor axis is $a = 10$ cm. It is excited by an axially oriented magnetic dipole placed outside the spheroid on its axis of the symmetry. EM parameters are $\mu_r = 1, 25, 100$. Results are shown relative to induction number $|k|a$, so that $\sigma = 4 \times 10^6$ S/m does not appear explicitly.

Fig. 5 shows results for $\mu_r=1$ (a-c); $\mu_r=25$ (d-f); and $\mu_r=100$ (g-i). The dipole sources are placed at three different distances from the spheroid's center: 45cm in a) d), g); 60 cm

location of peak response. As the source moves away, the geometrical heterogeneity of the object has more effect on the accuracy of the MAS/TSA, and the overall response is more like what we should expect from an elongated magnetic object, axially oriented relative to the primary field [1].

2. Error analysis

To analyze the performance of the MA/TSA code we studied the accuracy of the TS assumption within the object, infinitely close to the surface. In [9], the ratio of TSA approximation to the actual derivative of the normal component of the magnetic field $H_{2,n}$ was denoted

$$\alpha_n = \frac{jkH_{2,n}}{\partial H_{2,n} / \partial n} \quad (24)$$

and provided an error criterion on the surface of the scatterer. A theoretical analysis showed error patterns in both the basic approximation and, sometimes contrastingly, in the resulting scattered field. Analytical relations produced formulas for both the level of error and the sensitivity of the numerical system to error. The analysis was carried out only for spheres and transverse infinite cylinders, in uniform primary fields, for which the analytical relations could be obtained. Here both $H_{2,n}$ and $\partial H_{2,n} / \partial n$ are obtained along the surface of a spheroidal scatterer, using the conventional MAS code, when the source of the primary field is a magnetic dipole. The source is situated on the rotational axis 45 cm from the center of the spheroid.

Fig. 6 shows the ratio of the TSA values and the numerical derivative values as a function of distance along the (interior) surface. For all three permeabilities, at very low induction numbers ($|k|a = 0.01$ and 2) the difference between $jkH_{2,n}$ and $\partial H_{2,n} / \partial n$ is very significant. They are in fact different orders of magnitude. However the comparisons



Fig. 7. UXO.

between scattered fields obtained by combined MAS/TSA and standard MAS show different error patterns, relative to the value of μ_r (Fig. 5). To some extent, one sees the same trends as in [9], despite the difference in object geometry and non-uniformity of excitation: high permeability diminishes the consequences of inaccuracy in the TSA. In order to understand this numerical behavior here, let us examine the expressions in (17). The expression in brackets can be divided into two parts: the first part is associated with the normal component of the magnetic field and with the TSA, while second part is related to the tangential components. Examination of solutions shows that the both normal and tangential components of the scattered magnetic field on the boundary of the scatterer become saturated at very low induction numbers (e.g $|k|a < 0.1$) and at correspondingly low frequencies. That is, however much μ_r is increased, the value of $H_{1,n}^{sc}$ and its magnitude relative to the other components cease to change significantly. This means that, as μ_r increases, the contribution of the first part in brackets to the whole system (18) decreases relative to the contribution from the second part. Thus the quality of our approximation of the normal derivative has reduced effect. For all values of μ_r , the TSA and actual $\partial H_{2,n} / \partial n$ values

almost coincide with each other at induction number $|k|a=10$ and 30 . Obviously at these induction numbers the combined MAS/TSA and full MAS agree very well in the far fields of Fig. 5.

The error pattern observed here differs from that in [9] in one important respect, namely here we do not see reduced error at the very lowest induction numbers when there is significant error in the middle range of induction numbers. To understand this, note that at very low induction numbers both $\partial H_{2,n} / \partial n$ and $jkH_{2,n}$ approach zero for the spheroid *uniform* primary field excitation. Therefore, while the ratio of $\partial H_{2,n} / \partial n$ and $jkH_{2,n}$ may not be correct, the latter still approximates the former adequately in that both become negligible. However in the non-uniform primary field considered here, $\partial H_{2,n} / \partial n$ does not approach zero at low induction numbers, even in the static condition. For the non-magnetic case, the internal static fields will show the same complexity of spatial variation as the primary field. The assumption of approximately 1-D gradients below the surface, on which (16) is based, will not hold. Overall, while in certain cases high μ_r values may suppress the effects of errors in the TSA at low induction numbers, in general the TSA is designed for high induction numbers. It does not take into account spatial distribution of the normal component of the magnetic field at low frequencies, and neglects its tangential gradients. See also [39] for additional illustrations of low induction number TSA error, caused by more variable geometry.

The most secure general strategy for obtaining very accurate results over entire broadband EMI frequency range is to use the full MAS and for induction numbers less than about 20 and then switch to the MAS/TSA method for higher induction numbers. Alternatively, we can use the validity of the full MAS solution in the interior to check the accuracy of TSA as we proceed upwards in frequency. When we see that (16) has become valid, we can proceed with the combined MAS/TSA for all higher frequencies.

Having established the accuracy and range of validity of the hybrid full MAS - MAS/TSA, we will use it to investigate EMI response for a real UXO, consisting of two parts: a tail with fins (length 8 cm, diameter 3.15 cm), and main part (largest diameter 8 cm, smallest diameter 3.15 cm). The total length of UXO is 26 cm Fig. 7. The primary magnetic field is generated by a GEM-3 sensor [5,41]. Two excitations were considered: 1) Axial, i.e. when the coil axis of GEM-3 is aligned with the axis of symmetry of the UXO, and 2) transverse, when the GEM-3 axis is orthogonal to its axis. For determination of the EM parameters of each section, the UXO was disassembled. For each part the EMI response was measured separately and a recently developed inverse EMI algorithm [43] was used for inferring their EM parameters. Inverted parameters are: for the main part $\sigma = 1.6 \times 10^6$ S/m, $\mu_r = 85$; for tail $\sigma = 2 \times 10^6$ S/m, $\mu_r = 130$. The numerical solution shown as a solid line in Fig. 4 was obtained by combination of conventional MAS at low induction number $|k|a < 20$, and MAS/TSA for $|k|a > 20$. The comparison between measured and simulated data for the UXO is shown in Fig. 8, with

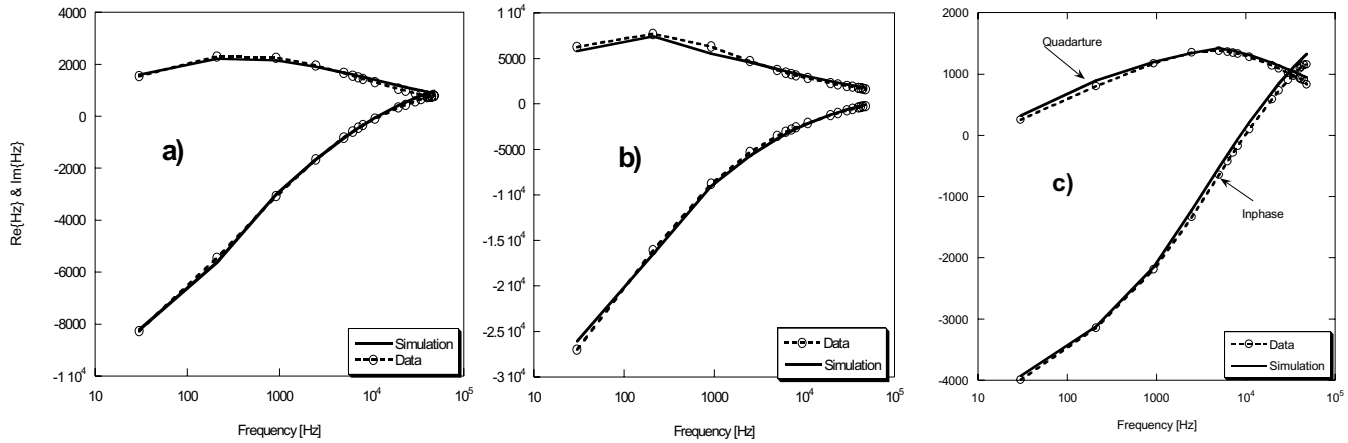


Fig. 8. Scattered magnetic fields versus frequency for real UXO oriented with (a) the nose up, (b) the tail up, and c) horizontal.

different target orientations. Again agreement is very good. These results clearly show that, depending on the target orientation relative to the sensor's point of view, the EM responses are quite different. As shown in Fig. 8 a), when the nose is close to the sensor the response behaves like a sphere, whereas when the tail is up Fig. 8 b) the scattered field spectrum suggests the object is elongated (quadrature peak shifted lower, see (5)). In the transverse case (Fig. 8 c) the response is more like that of an elongated target in transverse orientation, with quadrature peak at high frequency.

representative of most TD instruments in current use is the "Turn off" case: The initial condition is essentially the steady state solution (unvarying primary field normalized here to unity); at $t = 0^+$ the primary field is shut off and the scattered field is measured. In this case, the calculated response begins at a finite value and decays eventually to zero. For the "turn on" case, the initial condition is zero both inside and outside the object. At $t = 0^+$, the primary field is switched on and the scattered field recorded. A new version of the Geophex GEM-3 sensor will record this case as well as the "turn off." The former may be more revealing than the turn-off case,

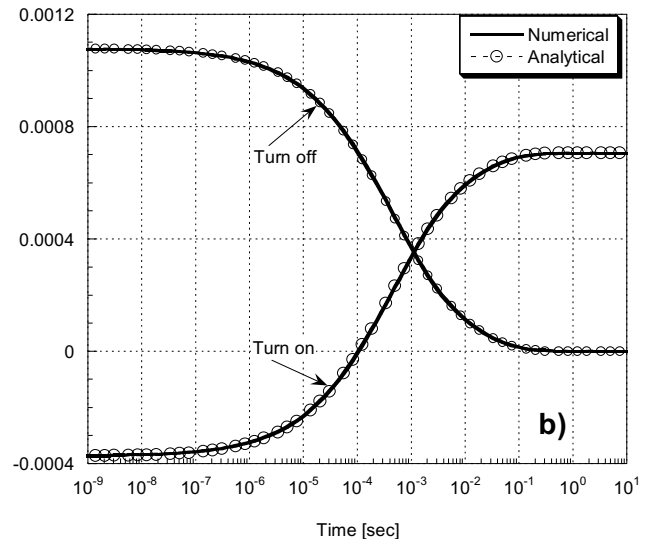
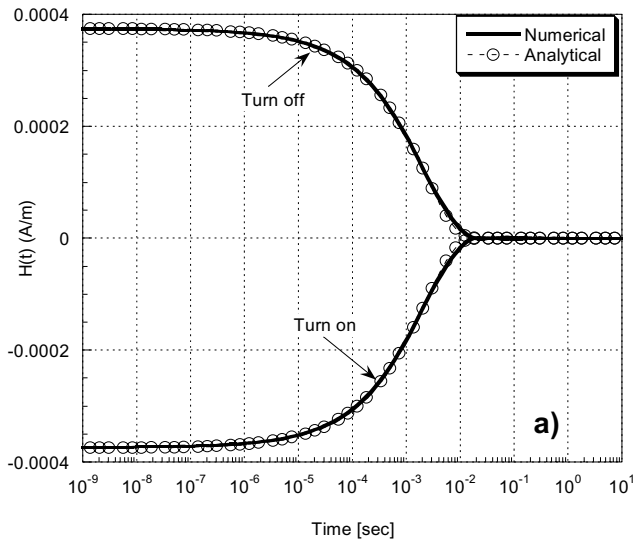


Fig. 9. Transient response for $\mu_r=1$ non-permeable a) and permeable b) $\mu_r=50$ spheres.

3. Transient response for spheroids

In this section a transient TD EMI response is analyzed for highly conducting and permeable metallic objects, beginning with spheres in both the "Turn on" and "Turn off" TD cases. For checking the accuracy of the numerical method, data are compared against available analytical results. The case

converging in late time to a steady-state value that depends on the object's permeability. The following figure shows example turn-on and turn-off results for a sphere, 5 cm in radius, with electrical conductivity $\sigma = 10^7$ S/m and relative permeabilities 1 and 50, and observation point 1 m distant. Numerical results are compared to analytical values obtained from analytical solutions by James Wait [32].

Note that the beginning value of the turn-off case and the ending value in the turn-on case are not the same. This is because the first response of the object to an imposed change in the surrounding (primary) field is to generate surface currents that oppose the change (Lenz' Law). Thus, in the turn-on case, in which a *positive* primary field value is suddenly imposed, the initial response is *negative*. (See early

$b/a=0.25$). Fig. 10 shows the scattered magnetic field versus time for turn on and turn off cases, for different permeabilities. Figs. 10a and 10b are for the prolate spheroid illuminated by axial and transverse oriented primary magnetic field, respectively. Depending on the primary magnetic field orientation and spheroid's EM parameters, the decay characteristics are different. The results show that, as

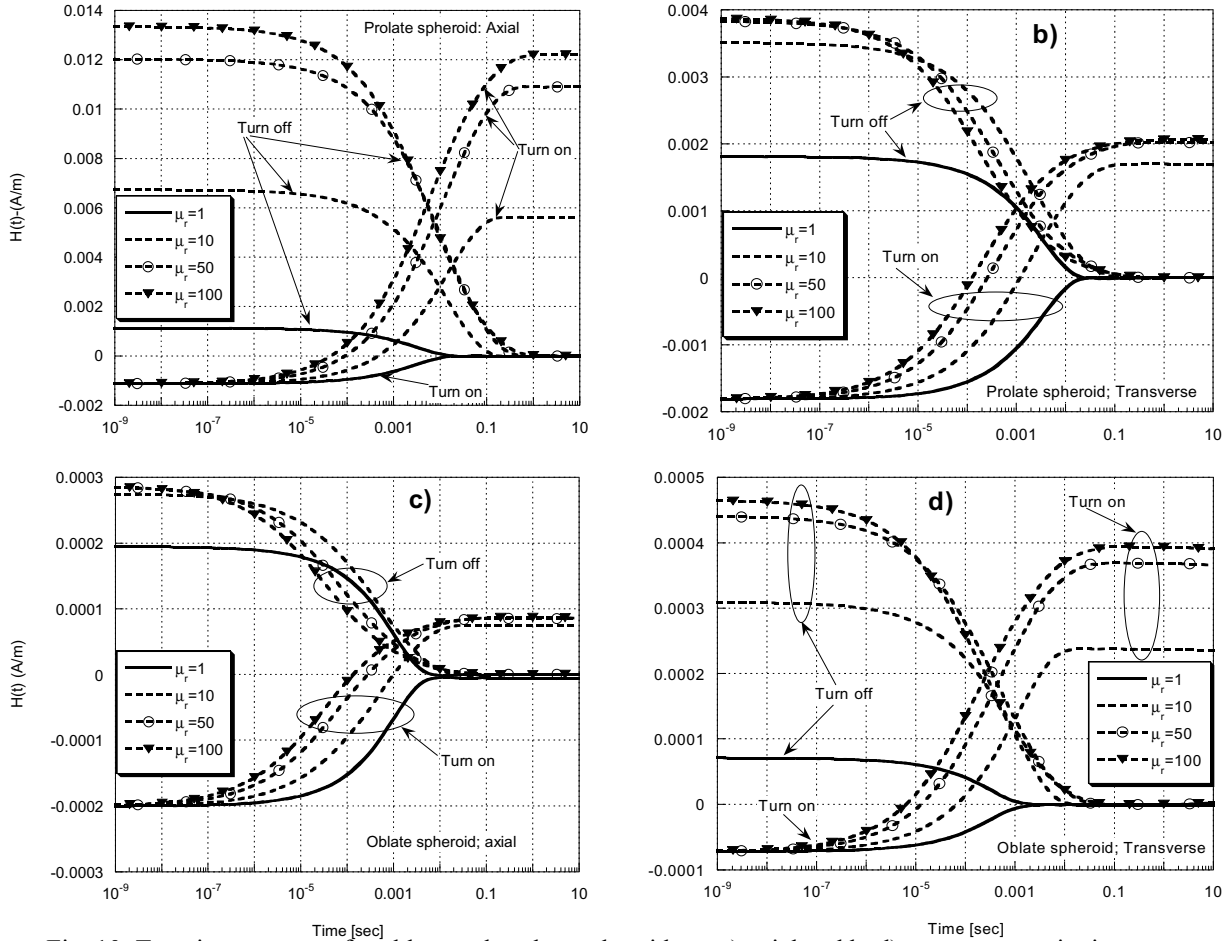


Fig. 10. Transient response for oblate and prolate spheroids, a, c) axial and b, d) transverse excitations.

time in turn-on curve in the Fig. 9). Conversely, in the turn-off case, a *negative* change in the surrounding field is imposed, so the first response of the object is *positive*. In other words, the very early time values seen at the beginning of the turn-off curve (figure above) are not the true steady state response, but are rather steady state augmented by an initial positive response. For the non-magnetic object ($\mu_r = 1$, Fig. 9 a) there is no (non-zero) static response, so the *only* early time response is the initial jump in response to the imposed field. Note that, reassuringly, the change in magnitude of the response from very early to very late time is the same in both turn-on and turn-off cases, for both magnetic (Fig. 9 b) and non-magnetic materials (Fig. 9 a).

Next the transient responses are investigated for highly conducting, permeable and non-permeable prolate (Fig. 10 a,b) and oblate spheroids (Fig. 10. c,d), illuminated by an axial and transverse primary magnetic field. Axis aspect ratios are 4 for both spheroids (prolate $b/a=4$, $a=5\text{cm}$, oblate

permeability increases, the principal transient response activity (decay curve) shifts earlier in time in both the turn on and turn off cases. Similar behavior of the transient field is observed for the oblate spheroid.

IV. Conclusion

In the paper, an innovative hybrid standard MAS and combined MAS/TSA algorithm is presented for efficiently and accurately analyzing EMI responses by highly conducting and permeable metallic targets. It has been shown that combined MAS/TSA algorithm works most reliably at high induction numbers, where skin depths are very small and more general methods are most stressed. Numerical experiments for a prolate spheroid under highly non-uniform, time varying primary magnetic field have shown that the combined MAS/TSA algorithm is inaccurate at low induction numbers for a non-permeable object. For a highly permeable object, the

MAS/TSA accuracy depends on the primary field, but only slightly, with relatively small errors in the scattered field over the entire band.

These studies suggest that for high accuracy broadband EMI simulation requiring low CPU resources it is necessary to use the standard MAS in low frequencies (induction number less than about 20), and the combined MAS/TSA algorithm at high frequencies (induction number greater than about 20). Accounting for non-uniformity effects at low frequency is particularly important for analyzing near field EMI responses for targets under highly non-uniform primary fields or for multiple, interacting objects, or for objects with very non-uniform geometries. Such cases occur frequently in subsurface unexploded ordnance discrimination problems.

To speed up calculation time it is possible to estimate the accuracy of the TSA via standard MAS, as one proceeds up through the lower frequencies. Then, when it has become valid, we can proceed with the MAS/TSA for all higher frequencies beyond the near static region.

Ultra wideband EMI frequency domain (FD) responses, obtained by the proposed hybrid MAS - MAS/TSA algorithm, are translated in time domain (TD) using a specialized inverse Fourier transform. To validate the FD to TD algorithm, the transient responses for permeable and non-permeable spheres are compared against analytical solutions for both turn on and turn off cases. Numerical TD experiments show that decay characteristics in the transient responses depend of the object geometry, primary field orientation, and EM parameters. For both flattened and elongated shapes, in both axial and transverse excitation, increasing permeability appears to shift the onset of signal decay earlier. From the point of view of discrimination, the turn-on case has the advantage that it may arrive at a non-zero steady state depending on permeability. This may be a more accessible indicator of permeability than signal characteristics near the onset of decay.

V. Acknowledgment

This work was sponsored in part by the Strategic Environmental Research and Development Program and US Army CoE ERDC BT25 and AF25 programs.

References:

1. F. Shubitidze, K. O'Neill, S. A. Haider, K. Sun, and K. D. Paulsen, "Application of the method of auxiliary sources to the wideband electromagnetic induction problem", IEEE Transactions on Geoscience and Remote Sensing, Vol: 40 Issue: 4, Pages: 928 - 942, April 2002.
2. F. Shubitidze, K. O'Neill, S. A. Haider, K. Sun, and K.D. Paulsen, "Analysis of induction responses from metal objects using the method of auxiliary sources", Proceedings of 6th international conference on Mathematical Methods in Electromagnetic Theory, Pages: 468 - 470, 2000.
3. F. Shubitidze, K. O'Neill, and K. D. Paulsen "The method of auxiliary sources for analysis low frequency EM field scattering from composite objects". 2001 IEEE Antennas and Propagation Society International Symposium, Boston MA, Pages: 522 - 525, July 8-13, 2001.
4. F. Shubitidze, K. O'Neill, S. A. Haider, and K. D. Paulsen, "The method of auxiliary sources for analysis of low frequency electromagnetic induction sensor response" URSI National Radio Science Meeting, Boulder CO, Page 289, January 8-11, 2001.
5. F. Shubitidze, K. O'Neill, K. Sun, and K. D. Paulsen, "Investigation of broadband electromagnetic induction scattering by highly conducting, permeable, arbitrarily shaped 3-D objects" IEEE Transactions on Geoscience and Remote Sensing, in press.
6. F. Shubitidze, K. O'Neill, I. Shamatava, K. Sun, and K. D. Paulsen, "Implementation of hybrid MAS and SPA algorithm for broadband electromagnetic induction problems", VII-International Workshop on Direct and Inverse Problems of Electromagnetic and Acoustic Wave Theory (DIPED - 2002) , Tbilisi, Georgia, Pages: 33 - 37, October 10-13, 2002.
7. K. Sun, K. O'Neill, S. A. Haider, and K. D. Paulsen. "Numerical modeling of electromagnetic induction scattering from target with small but non-negligible skin depths". Proceedings of International Geoscience and Remote Sensing Symposium Honolulu, Vol. 4 1411 - 1414, July 24-28, 2000.
8. K. Sun, K. O'Neill, F. Shubitidze, S. A. Haider, and K. D. Paulsen, "Simulation of electromagnetic induction scattering from targets with negligible to moderate by primary fields," IEEE Transactions on Geoscience and Remote Sensing,, Vol: 40 Issue: 4, Pages: 910 - 927, April 2002.
9. K. Sun, K. O'Neill, F. Shubitidze, I. Shamatava, and K. D. Paulsen. "Theoretical analysis of TSA formulation and its domain of validity," submitted for publication in IEEE Transactions on Geoscience and Remote Sensing.
10. A. Krawczyk and J. A. Tegopoulos: "Numerical Modeling of Eddy Currents" Oxford science publications 1993.
11. D. Webster, *Aftermath; The Remnants of War*, Pantheon, NY, 1996.
12. B. Jonson, T. G. Moore, B. J. Blejer, C.F. Lee, T. P. Opar, S. Ayasli, and C. A. Prommerman, "A Research and development strategy for unexploded ordinance sensing", Lincoln Lab. Project. Rep. Lexington, MA EMP-1, 1996.
13. C. E Baum, "Detection and Identification of Visually Obscured Targets," Taylor and Francis 1998.
14. N. Geng, K. E. Baum, L. Carin. "On the low frequency natural responses of conducting and permeable Target." IEEE Transactions on Geoscience and Remote Sensing, Vol. 37, Pages: 347 - 359, 1999.
15. L. Collins, P. Gao, J. Moulton, L. Makowsky, R. Weaver, D. Keiswetter, I. J. Won. "Detection of low metal mines using frequency domain EMI." UXO forum 1999, Alexandria, Virginia May 24, 1999.
16. K. O'Neill, F. Shubitidze, I. J. Won, and D. Keiswetter, "Use of ultra-wideband spectroscopy to enhance electromagnetic induction discrimination". URSI National Radio Science Meeting, Boulder CO, Page 293 January 8 - 11, 2001.
17. J. T. Miller, T. H. Bell, J. Soukup, D. Keiswetter, "Simple phenomenological models for wideband frequency-domain electromagnetic induction" IEEE Transactions on Geoscience and Remote Sensing, Vol: 39 Issue: 6, Pages: 1294 - 1298, June 2001.
18. K. O'Neill, S. Haider, F. Shubitidze, K. Sun, C.O. Ao, H. Braunsch, and J. A. Kong, "Ultra-wideband electromagnetic induction spectroscopy", UXO Forum April 8-11, Florida, 2001.
19. A. R. Sebak, L. Shafai, and Y. Das, "Near zone fields scattered by three dimensional highly conducting permeable objects in the field of an arbitrary loop", IEEE Transactions on Geoscience Remote Sensing, Vol. 29. Issue 1, Pages: 9 - 15, January 1991.

20. I. J. Won, D. Keiswetter, T. H. Bell, "Electromagnetic induction spectroscopy for clearing landmines" IEEE Transactions on Geoscience Remote Sensing, Vol. 39. Issue 4, Pages: 703 -709, April 2001.
21. D. Keiswetter, I. J. Won, B. Barrow, T. H. Bell, " Object identification using multi-frequency EMI data". UXO forum 2000.
22. T. H. Bell, B. Barrow, and N. Khadr, "Shape-based classification and discrimination of subsurface objects using electromagnetic induction", IEEE Transactions on Geoscience and Remote Sensing, Vol: 39 Issue: 6, Pages: 509 - 513, June 2001.
23. P. Gao, L. Collins, P. Garber, N. Geng, L. Carin "Classification of landmine like metal targets using wideband electromagnetic induction ", IEEE Transactions on Geoscience Remote Sensing, Vol. 38. Issue 3. Pages: 1352 – 1361, May 2000.
24. L. Carin, Yu Haitao; Y. Dalichaouch, A. R. Perry, P. V. Czipott, C. E. Baum "On the wideband EMI response of a rotationally symmetric permeable and conducting target" IEEE Transactions on Geoscience and Remote Sensing,, Vol: 39 Issue 6, Pages: 1206 – 1213, June 2001
25. F. Shubitidze, K. O'Neill, K. Sun, and K. D. Paulsen, "Classification of scatterer's major axis aspect ratio using broadband EMI responses" International Union of Radio Science, National Radio Science Meeting, Page 271, Boulder, Colorado, January, 9 - 12, 2002.
26. F. Shubitidze, K. O'Neill, K. Sun, and I. Shamatava "Application of broadband EMI responses to infer buried object's aspect ratio". 2002 IEEE Geoscience and remote sensing international symposium and 24-th Canadian symposium on remote sensing, Vol. 3, Pages: 1542 – 1545, Toronto, Canada, June 24 - 28, 2002.
27. K. Sun, K. O'Neill, F. Shubitidze, and K. D. Paulsen; "Treatment of broadband and multi-object electromagnetic induction scattering using high frequency approximations" 2002 IEEE Geoscience and remote sensing international symposium and 24-th Canadian symposium on remote sensing, Vol. 3, Pages: 1546 – 1549, Toronto, Canada, June 24 - 28., 2002.
28. I. Shamatava, K. O'Neill, F. Shubitidze, K. Sun, and C. Ao, "Evaluation of Approximate analytical solutions for EMI scattering from finite objects of different shapes and properties", 2002 IEEE Geoscience and remote sensing international symposium and 24-th Canadian symposium on remote sensing, Vol. 3, Pages: 1549 – 1552, Toronto, Canada, June 24-28., 2002.
29. L. M. Collins, Y. Zhang, and L. Carin "Model-Based statistical sensor fusion for unexploded ordnance detection". 2002 IEEE Geoscience and remote sensing international symposium and 24-th Canadian symposium on remote sensing, Vol. 3, Pages: 1556 –1559, Toronto, Canada, June 24-28., 2002.
30. F. Shubitidze, K. O'Neill, K. Sun and K.D Paulsen, " Analysis of UXO classification capability with the low frequency EMI sensor responses ". PIERS'2002 Progress In Electromagnetic Research Symposium, Page 44, Cambridge, MA, July 1 - 5, 2002.
31. J. R. Wait, "A conducting sphere in a time varying magnetic field". Geophysics 16, Pages: 666-672, 1951a.
32. J. R. Wait and K. P Spies, "Quasi-static transient response of a conducting and permeable sphere". Geophysics 34, Pages: 789 -792, 1969.
33. S. Ward and G. Hohmann, "Electromagnetic theory for Geophysical applications" In electromagnetic theory in Applied Geophysics. Tulsa OK: Soc. Exploration Geophysics, 1987.
34. H. Braunsch, C.O. Ao, K. O'Neill, and J. A. Kong, "Magnetoquasistatic response of conducting and permeable prolate spheroid under axial excitation". IEEE transactions on Geoscience and Remote Sensing, Vol: 39 Issue: 12 , Pages: 2689 – 2701, December 2001.
35. C.O. Ao H. Braunsch, K. O'Neill, J. A. Kong, "Quasi-magnetostatic solution for a conducting and permeable spheroid object to arbitrary excitation," Geoscience and Remote Sensing, IEEE Transactions on, Vol: 40 Issue: 4, Pages: 887 - 897, April 2002.
36. B. E. Barrowes, T. M. Grzegorzczuk, J. A. Kong, K. O'Neill. "Broadband Analytical Solution of the Electromagnetic Induction (EMI) Response by Spheroidal Objects Under Arbitrary Excitation". PIERS-03, Page: 246, Honolulu, Hawaii, October 13 - 16, 2003.
37. C. D Moss, K. O'Neill, T. M. Grzegorzczuk, and J. A. Kong, "A hybrid time domain method to calculate electromagnetic induction scattering from target with arbitrary skin depths", Proceedings of 19th Annual Review of Progress in Applied Computational Electromagnetics, Pages: 390 - 396, Monterey, CA, March 24 - 28, 2003.
38. F. Shubitidze, H. Anastassiou and D. Kaklamani, "An improved accuracy version of the method of auxiliary sources for computational electromagnetics" IEEE Transactions on Antennas and Propagations, in press.
39. F. Shubitidze, K O'Neill, K. Sun, and I. Shamatava, "Interaction between highly conducting and permeable metallic objects in the EMI frequency range," P Proceedings of 19th Annual Review of Progress in Applied Computational Electromagnetics, Pages: 625 - 631, Monterey, CA, March 24 - 28, 2003.
40. L. R. Passon and D. W. Oldenburg "Locating and Characterizing Unexploded Ordnance Using Time Domain Electromagnetic Induction ". ERDC/GSL TR-01-40 Technical report, August 2001.
41. I. J. Won, D. A Keiswetter, D.R. Hanson, E. Novikova and T. M. Hall, "GEM-3: a monostatic broadband electromagnetic induction sensor," Journal Environmental and Engineering Geophysics, Vol. 2, Issue 1, Pages: 53 - 64, 1997.
42. W. C. Chew, J. M. Jin, E. Michielssen, J. Song, 'Fast and Efficient Algorithms in Computational Electromagnetic ' Artech House, 2001.
43. F. Shubitidze, K. O'Neill, K. Sun, I. Shamatava and K. D. Paulsen. "Semi-analytical calculation of Jacobian in the electromagnetic inverse scattering problem," IEEE Antennas and Propagation Society International Symposium, Pages: 543 - 546 Columbus, OH, June 22-27, 2003.



Fridon Shubitidze received the degree of Diploma radio physicist (M.S) from the Sukhumi branch of Tbilisi State University, Republic of Georgia, in 1994 and Candidate of Sciences Ph.D degree in radio physics (applied electromagnetics) from its physics department, Tbilisi State University, Republic of Georgia, in 1997. Beginning in 1994 he was on the Research Staff of the Laboratory of Applied Electrodynamics, Tbilisi State University,

Department of Physics, Republic of Georgia. At the same time he joined department of physics and mathematics, Sukhumi branch of Tbilisi State University as a senior teacher and became Associate Professor there in 1998. From 1998 to 1999 he held a postdoctoral fellowship in National Technical University of Athens, Greece, performing research in connection with computer simulation of electrostatic discharge, electrodynamics aspects of EMC, numerical modeling of conformal antennas, electromagnetic wave scattering, field visualization and identification of objects by scattered field analysis, investigation of wave propagation through anisotropy, plasma and chiral media; and innovative numerical methods. He is currently, working as Senior Research Associate at the Thayer School of Engineering, Dartmouth College, Hanover NH. His current work interests focus on numerical modeling of electromagnetic scattering by subsurface metallic objects.



Kevin O'Neill received the B.A. magna cum laude from Cornell University, followed by M.A., M.S.E., and Ph.D. degrees from Princeton University, Department of Civil Engineering. After an NSF postdoctoral fellowship at the Thayer School of Engineering at Dartmouth College and the U.S. Army Cold Regions Research and Engineering Laboratory (CRREL), he joined CRREL as a Research Civil

Engineer. His research has focused on numerical modeling of porous media transport phenomena and of geotechnically relevant electromagnetic problems. He has been a Visiting Fellow in the Department of Agronomy at Cornell University, continues since 1989 as a Visiting Scientist at the Center for Electromagnetic Theory and Applications at MIT, and since 1984 has been on the adjunct faculty of the Thayer School. Current work centers on electromagnetic remote sensing of surfaces, layers, and especially buried objects such as unexploded ordnance.



Keli Sun received his B.S., M.S. and Ph.D. degrees in Computational and Biofluid Mechanics from the Department of Mechanics and Engineering Sciences, Peking University, Beijing, P. R. China, in 1991, 1994 and 1997 respectively. As an exchange student, he also worked in the school of Pure and Applied sciences, Tokyo University, Tokyo, Japan, from

December 1995 to December 1996, studying the mobility and mechanical properties of membrane proteins in living cells. After getting his Ph.D. degree in 1997, he worked on the faculty of

Tsinghua University, Beijing, P.R. China performing research and teaching biomechanics. He obtained a second Master of Science degree in Computational Electromagnetics in May 2001 from the Thayer School of Engineering at Dartmouth College in Hanover, NH. Dr. Sun is currently employed as a Research Associate in the Numerical Methods Laboratory in the Thayer School furthering his research in Computational Electromagnetics and its applications in remote sensing.



Irma Shamatava received the degree of Diploma radio physicist (M.S) from Sukhumi branch of Tbilisi State University, Republic of Georgia, in 1994. Since 1997, she has been on the Staff of the Computer center, Sukhumi branch of Tbilisi State University, Republic of Georgia. During the same period she joined Department of Physics

and Mathematics, as an assistant teacher. She is currently, working as researcher at the Thayer School of Engineering, Dartmouth College, Hanover NH. Her research interests focus on analytical and numerical modeling of electromagnetic scattering by subsurface metallic objects.

Keith D. Paulsen received a B.S. from Duke University and



M.S. and Ph.D. degrees from the Thayer School of Engineering, Dartmouth College, all in biomedical engineering. He was an assistant professor in electrical and computer engineering at the University of Arizona and jointly, an assistant professor in radiation oncology at the University of Arizona Health Sciences Center, and is now a

professor of engineering at the Thayer School. A recipient of numerous academic and research awards and fellowships, he has carried out sponsored research for the National Science Foundation, the National Cancer Institute, the Whitaker Foundation, and the National Institute of Health. He has served on more than 10 advisory committees for the National Cancer Institute, and has chaired or organized five symposia on hyperthermic cancer treatment. He has published over 60 journal articles, over three dozen conference presentations, abstracts, and papers, and contributed chapters on electromagnetic power deposition patterns to five books. At Thayer School he is co-founder and co-manager of the Numerical Methods Laboratory. He performs research and teaches courses in computational methods for engineering and scientific problems, with particular applications in electromagnetics, subsurface object sensing, and biomedical engineering.

A Novel Dirichlet-Neumann Random-Walk Algorithm for the Solution of Time-Harmonic Helmholtz Equation at Multiple Wavelength Length Scales: 1D and 2D Verification

K. Chatterjee, P. Matos

Electrical and Computer Engineering Department, MS/EE94

California State University, Fresno

Fresno, CA 93740-8030

Email: kchatterjee@csufresno.edu, Tel: (559) 278-6038, Fax: (559) 278-6297

Y. L. Le Coz

Department of Electrical, Computer, and Systems Engineering

Rensselaer Polytechnic Institute

Troy, NY 12180-3590

Abstract: The electrical properties of IC interconnects at multi-GHz frequencies must be described with Maxwell's equations. We have created an entirely new floating random-walk (RW) algorithm to solve the time-harmonic Maxwell-Helmholtz equations. Traditional RW algorithms for Maxwell-Helmholtz equations are constrained to length scales that are less than a quarter-wavelength. This is because of the problem of resonance in finite-domain Green's function for Helmholtz equation at multiple quarter-wavelength length scales. In this paper, we report the major discovery of extending our floating RW algorithm beyond a quarter-wavelength. The problem of Green's function resonance has been eliminated by the use of an infinite-domain Green's function. In this work, we formulate this algorithm and describe its successful application to homogeneous and heterogeneous 1D problems and homogeneous 2D problems. We believe, that with additional work, this RW algorithm will prove useful in the development of CAD tools for electromagnetic analysis of IC interconnect systems. It can be noted that the algorithm exhibits full parallelism, requiring minimal interprocessor communication. Thus, significant performance enhancement can be expected in any future parallel software or hardware implementation.

Keywords: Floating random-walk method/algorithm, Dirichlet-Neumann algorithm, Maxwell-Helmholtz equation.

1. Introduction

Fundamentally, the electrical properties of advanced multilevel IC interconnects at present multi-GHz frequencies must be described with Maxwell's equations. Traditional numerical methods[1-3] require, usually, a discretization mesh. Mesh size and resultant difficulty of solution become somewhat unmanageable in complicated 3D problem domains. The RW algorithm that we

present here does not involve the use of a mesh. In essence, the algorithm executes a Monte Carlo integration [4] of an infinite series of multi-dimensional integrals [5] by means of random walks (RWs) through the problem domain. These integrals contain both "surface" and "volume" Green's function kernels. Conventional RW algorithms for Maxwell-Helmholtz equation are constrained to sub-quarter-wavelength length scales. This is due to the mathematical difficulties associated with unwanted multiple quarter-wavelength resonances [6] in finite-domain Green's functions. In this work, the problem of finite-domain Green's function resonance has been eliminated by the use of an infinite-domain Green's function. The additional complexity of having now to propagate RWs for both the field and its derivative presents little practical difficulty. In the next section, we present the RW equations for the time-harmonic Maxwell-Helmholtz equations in 1D and 2D.

2. Random-Walk Equations

Consider the 1D time-harmonic Maxwell-Helmholtz equation with a source term on the right-hand side

$$\frac{d^2 A(x)}{dx^2} + k^2 A(x) = f(x). \quad (1)$$

The quantity A is the field variable of interest and k is a constant wave vector whose magnitude is determined by the frequency and material properties of the problem domain. Both the boundary value and derivative are assumed to be known at the two endpoints of the 1D problem domain. Now, one may wonder why we want to solve an "over-specified" problem. This criticism can be countered by observing that in IC-interconnect structures, the current is specified at certain conducting regions. These currents appear as source terms in the right hand side of the Helmholtz equation given in (1). Integrals involving these source terms will appear in our RW

formulation and the RWs will terminate at infinity, that is, at large distances from the interconnect structure, where the field vector of interest and its spatial derivatives are known to be zero from physical considerations. The non-zero contributions to the RW solution will come from integrals involving source terms. So, having established the motivation for solving the 1D problem of interest, we can write the Green's function differential equation associated with (1)

$$\frac{\partial^2 G(x|x_o)}{\partial x^2} + k^2 G(x|x_o) = \delta(x-x_o), \quad (2)$$

where $\delta(x-x_o)$ is the Dirac delta function centered at $x = x_o$. There can be any number of Green's functions satisfying equation (2), depending on the arbitrary nature of boundary conditions applied to (2). In a previous work[6], we have employed one such finite-domain Green's function that vanishes at problem-domain boundaries. For instance, over $-L \leq x \leq L$, such a Green's function has the form

$$G(x|x_o) = \frac{1}{2k \cos kL} \sin[k(|x-x_o|-L)]. \quad (3)$$

The use of a finite-domain Green's function like the one in (3) produces the most economical set of RW equations, and is traditional in RW literature. On the other hand, it is precisely this form of the finite-domain Green's function that generates unwanted multiple quarter-wavelength resonance, produced by the zeros in the denominator of (3).

In this work, we suggest the use of an infinite-domain Green's function, where both the boundary value and the boundary derivative never simultaneously vanish at domain boundaries. One such Green's function satisfying (2) is, for example,

$$G(x|x_o) = \frac{1}{2k} \sin(k|x-x_o|). \quad (4)$$

Using (4), the problem of quarter-wavelength resonance can be avoided, at the minimal expense of now propagating, by RWs, both field values and derivatives through the problem domain. We therefore call this new modification a D-N floating RW algorithm, where "D-N" signifies "Dirichlet-Neumann". To obtain the RW equations, we multiply (1) by $G(x|x_o)$ and (2) by $A(x)$ and subtract one from the other, which yields

$$A \frac{d^2 G}{dx^2} - G \frac{d^2 A}{dx^2} = A \delta(x-x_o) - f(x)G(x|x_o). \quad (5)$$

Integrating (5) from $-L$ to $+L$, yields

$$\begin{aligned} A(x_o) &= \int_{-L}^{+L} G(x|x_o) f(x) dx + \\ &G_x(L|x_o)A(L) - G_x(-L|x_o)A(-L) - \\ &G(L|x_o)A_x(L) + G(-L|x_o)A_x(-L). \end{aligned} \quad (6)$$

In the zero-centered notation, meaning $x_o = 0$, (6) can be written as

$$\begin{aligned} \bar{A} &= \int_{-L}^{+L} G(x) f(x) dx + \bar{G}_x(L)A(L) - \\ &\bar{G}_x(-L)A(-L) - \bar{G}(L)A_x(L) + \bar{G}(-L)A_x(-L), \end{aligned} \quad (7)$$

where $\bar{G}_x(L) = G_x(L|0)$, $\bar{G}(L) = G(L|0)$, and so forth. Taking a derivative of (6) with respect to x_o , and writing in zero-centered notation, gives

$$\begin{aligned} \bar{A}_{x_o} &= \int_{-L}^{+L} G_{x_o}(x) f(x) dx + \bar{G}_{xx_o}(L)A(L) - \\ &\bar{G}_{xx_o}(-L)A(-L) - \bar{G}_{x_o}(L)A_x(L) + \bar{G}_{x_o}(-L)A_x(-L). \end{aligned} \quad (8)$$

Equations (7) and (8) can be written in the vector-matrix form

$$\begin{aligned} \begin{bmatrix} \bar{A} \\ \bar{A}_{x_o} \end{bmatrix} &= \begin{bmatrix} \int_{-L}^{+L} G(x) f(x) dx \\ \int_{-L}^{+L} G_{x_o}(x) f(x) dx \end{bmatrix} \\ &+ \begin{bmatrix} \bar{G}_x(L) & -\bar{G}(L) \\ \bar{G}_{xx_o}(L) & -\bar{G}_{x_o}(L) \end{bmatrix} \begin{bmatrix} A(L) \\ A_x(L) \end{bmatrix} + \\ &\begin{bmatrix} -\bar{G}_x(-L) & \bar{G}(-L) \\ -\bar{G}_{xx_o}(-L) & \bar{G}_{x_o}(-L) \end{bmatrix} \begin{bmatrix} A(-L) \\ A_x(-L) \end{bmatrix}, \end{aligned} \quad (9)$$

where A and A_x at the center of the domain $x = x_o$, relates to the hop-interval endpoint values at $x = \pm L$. The different derivatives of the infinite-domain Green's function in (4), which shows up in the matrix-equation (9) are given by

$$\begin{aligned} \bar{G}_x(x) &= \frac{1}{2} \cos(k|x|) \operatorname{sgn}(x), \\ x \neq 0, \operatorname{sgn}(x) &= \begin{cases} -1, & x < 0, \\ 1, & x > 0, \end{cases} \end{aligned} \quad (10a)$$

$$\bar{G}_{x_o}(x) = -\frac{1}{2} \cos(k|x|) \operatorname{sgn}(x), \quad x \neq 0, \quad (10b)$$

$$\bar{G}_{xx_o}(x) = \frac{k}{2} \sin(k|x|), \quad x \neq 0. \quad (10c)$$

In the 2D case, the infinite-domain Green's function chosen is

$$G(\mathbf{r} | \mathbf{r}_o) = \frac{1}{4} Y_o(k|\mathbf{r} - \mathbf{r}_o|). \quad (11)$$

Above, Y_o represents Neumann function of zeroth order. Using the Green's function in (11), we can solve for the 2D Helmholtz equation with an arbitrary forcing function $f(r, \phi)$. Following a procedure identical to the one that led to the derivation of (7) and (8), the field variable A of interest, and its derivative at the center ($r_o = 0$) of a circular domain of radius R are given by

$$\begin{aligned} \bar{A} &= \int_0^R \int_0^{2\pi} f(r, \phi) G(r, \phi | r_o, \phi_o) r dr d\phi + \\ &\int_0^{2\pi} R G_r(R, \phi | \phi_o) A(\mathbf{r})_{r=R} d\phi - \\ &\int_0^{2\pi} R A_r(R, \phi | \phi_o) G(\mathbf{r} | \mathbf{r}_o)_{r=R} d\phi. \end{aligned} \quad (12.1)$$

$$\begin{aligned} \bar{A}_{r_o} &= \int_0^R \int_0^{2\pi} f(r, \phi) G_{r_o}(r, \phi | r_o, \phi_o) r dr d\phi + \\ &\int_0^{2\pi} R G_{rr_o}(R, \phi | \phi_o) A(\mathbf{r})_{r=R} d\phi - \\ &\int_0^{2\pi} R A_r(R, \phi | \phi_o) G_{r_o}(\mathbf{r} | \mathbf{r}_o)_{r=R} d\phi. \end{aligned} \quad (12.2)$$

Here, subscripts denote differentiation. The different derivatives of the infinite-domain Green's function given in (11) with respect to r and r_o are given by

$$G_r(R, \phi | \phi_o) = \frac{k}{4} Y_o'(kR), \quad (13.1)$$

$$G_{r_o}(R, \phi | \phi_o) = -\frac{k}{4} Y_o'(kR) \cos(\phi - \phi_o), \quad (13.2)$$

$$G_{rr_o}(R, \phi | \phi_o) = -\frac{k^2}{4} Y_o''(kR) \cos(\phi - \phi_o). \quad (13.3)$$

Thus, we have formulated the RW propagation equations for solving the Helmholtz equation in 1D and 2D. In the following section, we will present the results for test problems in 1D and 2D.

3. Benchmark Problems

We have chosen four benchmark problems. The first two problems involve the solution of Helmholtz equation in 1D. The first problem involves the solution of Helmholtz equation in a medium with real propagation constant ($k = 1.0$) with a sinusoidal ($k_f = 1.5$) forcing term. A real propagation constant corresponds to insulating medium, while a complex propagation constant corresponds to conducting medium. The analytical solution chosen is proportional to the forcing term. The rationale behind the choice of a sinusoidal forcing term is that any forcing function, piecewise continuous in the problem domain of interest can be decomposed into an infinite sum of sinusoids. The second problem involves a heterogeneous problem domain with a real propagation constant ($k = 3.0$) on the left and a complex propagation constant ($k = 3.0 + 0.4i$). An analytical solution of the form $A \sin(kx) + B \cos(kx)$ is imposed on either side of the interface, while maintaining the continuity of the solution and its derivative at the interface. The third and the fourth problem involve the solution of 2D Helmholtz equation in insulating medium. For the third problem, we have chosen a circular cross section whose radius is equal to twice the wavelength in normalized length scales with $k = 1$. The solution imposed on the problem domain is the Bessel function of zeroth order. For the fourth problem, we have chosen a Fourier mode solution in a square problem domain whose side is equal to four times the wavelength in normalized length scales with $k = 1$. The field variable of interest A is zero in the top bottom and right boundary line; along the left boundary line A is equal to $\cos(\pi y / L)$, where L represents the length of the side of the square domain with $y = 0$ coinciding with the bottom boundary line. The reason behind choosing such a solution is again that any piecewise continuous boundary condition can be decomposed into infinite number of such Fourier modes.

In order to estimate our field variable, A , of interest, we define RWs to start at the point, where we need to estimate A . The RWs propagate as "hops" of different sizes from the point of interest to the problem boundary, con-

sistent with a stochastic interpretation of (9) and (12). An accurate statistical estimate for A can be obtained by averaging over large number of such RWs.

The results for these problems are shown in Figures (1) to (5). As seen from the figures, there is very good agreement between the analytical and RW results. We also observe that our algorithm has been able to capture multiple wavelengths. In addition, it can be noted that for the heterogeneous 1D problem, the solution is purely oscillatory in dielectric, while the solution is damped in the conductor. This is consistent with the usual skin-effect type behavior expected in conducting medium. We coded the algorithm in MATLAB 5.0™, using a 400-MHz Apple PowerBook G3™ development platform. The computational details are presented in Table (1).

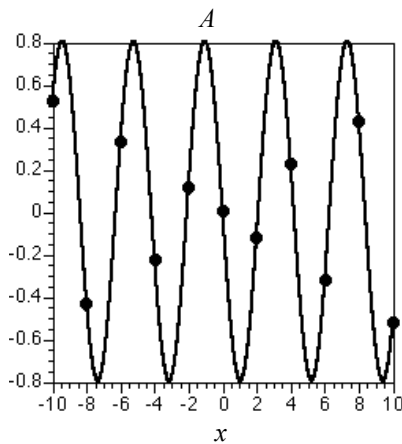


Figure 1: 1D homogeneous problem with real forcing term in insulating medium. $-10 \leq x \leq 10$ in normalized length scales and $k = 1$. A real, forcing term equal to $\sin(k_f x)$ is applied with $k_f = 1.5$. The solid line represents the exact analytical solution. The dots represent the random-walk solution points.

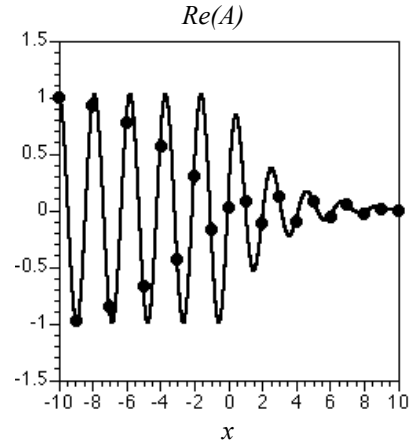


Figure 2: 1D heterogeneous problem, the real part of the solution. Heterogeneous domain with $-10 \leq x \leq 10$ in normalized length scales. For $x \leq 0$, $k = 3$, while for $x \geq 0$, $k = 3 + 0.4i$. The solid line represents the exact analytical solution. The dots represent the random-walk solution points.

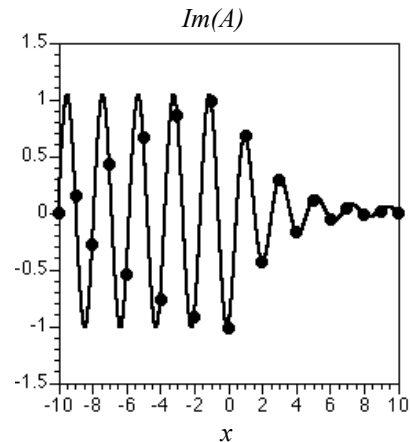


Figure 3: 1D heterogeneous problem, the imaginary part of the solution. Heterogeneous domain with $-10 \leq x \leq 10$ in normalized length scales. For $x \leq 0$, $k = 3$, while for $x \geq 0$, $k = 3 + 0.4i$. The solid line represents the exact analytical solution. The dots represent the random-walk solution points.

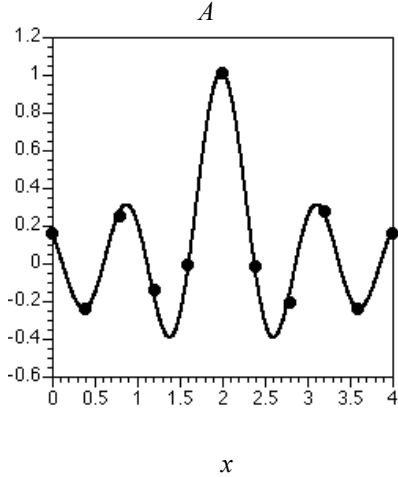


Figure 4: 2D homogeneous problem in an insulating circular cross section of diameter 4λ in normalized length scales with $k = 1$. A solution consisting of the zeroth order Bessel function is imposed. The solution is plotted along a diameter of the cross section. The solid line represents the exact analytical solution. The dots represent the random-walk solution points.

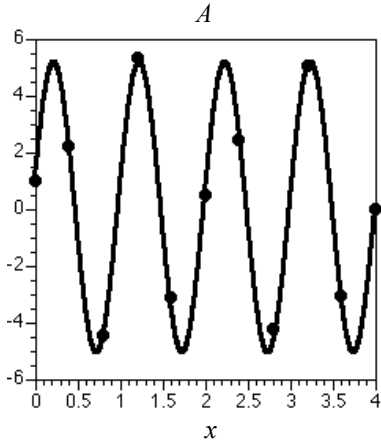


Figure 5: 2D homogeneous problem in an insulating square problem domain with a side equal to 4λ in normalized length scales and $k = 1$. A Fourier mode solution is imposed and the solution is plotted along the center-line x axis. The solid line represents the exact analytical solution. The dots represent the random-walk solution points.

Table 1: Computational details for the verification problems.

Problem Specifications	RWs per solution point	Time per solution point	Mean absolute error
1D Helmholtz equation with source term	20000	About 1 second	0.004 on a solution range (-0.8 to 0.8)
1D Helmholtz equation in heterogeneous problem domain	500	About 1 second	$(1.7+2.8i)\times 10^{-15}$ on a solution range $(-1-i)$ to $(1+i)$
2D Helmholtz equation with a zeroth order Bessel function solution	15000	About 1 minute	$0.027+0.017i$ on a solution range $(-0.4$ to $+1.0)$
2D Helmholtz equation with a Fourier mode solution	15000	About one minute	$0.106+0.143i$ on a solution range $(-5$ to $+5)$

4. Conclusions

In conclusion, we have been able to create a floating RW algorithm for Maxwell-Helmholtz equations at multiple wavelength scales. Our next goal is to extend this approach to heterogeneous problems in 2D and 3D. The absence of analytical Green's function in 2D and 3D for structures of arbitrary heterogeneity makes this an interesting problem. A possible future application of this algorithm would be the extraction of frequency-dependent inductance, resistance and capacitance. We believe that with additional development, this algorithm will lead to the development of IC CAD for high-end digital IC interconnect systems.

5. Acknowledgements

This work has been sponsored in part by the Defense Advanced Research Projects Agency (DARPA); the New York State Office of Science, Technology, and Academic Research (NYSTAR); the Semiconductor Research Corporation (SRC) Microelectronics Advanced Research Corporation (MARCO); and the SRC Custom-Funding Program (LSI Logic Corporation).

6. References

- [1] J. Jin, *The Finite Element Method in Electromagnetics*, John Wiley & Sons, New York, 1993.
- [2] K. S. Kunz and R. J. Luebbers, *The Finite Difference Time Domain Method for Electromagnetics*, CRC Press, Boca Raton, 1993.
- [3] J. J. H. Wang, *Generalized Moment Methods in Electromagnetics: Formulation and Computer Solution of Integral Equations*, John Wiley & Sons, New York, 1991.
- [4] I. M. Sobol, *A Primer for the Monte Carlo*, CRC Press, Boca Raton, 1994.
- [5] Y.L. Le Coz and R.B. Iverson, "A Stochastic Algorithm for High Speed Capacitance Extraction in Integrated Circuits", *Solid-State Electronics*, vol. 35, pp. 1005–1012, 1992.
- [6] Y. L. Le Coz, K. Chatterjee and R. B. Iverson, "A Floating Random-Walk Algorithm for Solving Maxwell's Equations in Multilevel IC-Interconnect structures: 1D Verification", *Proceedings VLSI Multilevel Interconnection Conference*, Santa Clara, CA, pp. 463-467, 1999.



Kausik Chatterjee received his Bachelor of Engineering degree in Electrical Engineering from Jadavpur University, Calcutta, India in June, 1992. Subsequently, in June, 1995, he received a Master of Technology degree in Nuclear Engineering from Indian Institute of Technology, Kanpur, India, and in May, 2002, he received his Ph.D degree in Electrical

Engineering from Rensselaer Polytechnic Institute, Troy, New York. In August 2002, he joined the faculty, full-time, at California State University, Fresno as an Assistant Professor of Electrical and Computer Engineering. His current research interests include the development of stochastic algorithms for important equations in nature, ferrohydrodynamics and a theory for high temperature superconductors. He has been awarded a Government of India Fellowship at Indian Institute of Technology, Kanpur, a University Fellowship at Ohio State University and an Intel Doctoral Fellowship. He has also received the Charles M. Close Doctoral Prize at Rensselaer Polytechnic Institute. He is a member of American Physical Society, Applied Computational Electromagnetics Society and IEEE.



Yannick Louis Le Coz was born on 26 September 1958. In May 1980, he received a BS degree in Electrical Engineering from Rensselaer Polytechnic Institute, Troy, New York. Subsequently, in May 1982 and January 1988, respectively, he received M.S. and Ph.D. degrees in Electrical Engineering from the Massachusetts Institute of

Technology, Cambridge, Massachusetts. His doctoral thesis, entitled "Semiconductor Device Simulation: A Spectral Method for Solution of the Boltzmann Transport Equation", was supervised by Prof. Alan L. McWhorter. In January 1988, he joined the faculty, full time, at Rensselaer Polytechnic Institute, as an Assistant Professor of Electrical, Computer, and Systems Engineering. He was awarded a tenured Associate Professorship in 1995. His research interests include transport in semiconductor devices, equilibrium heterojunction theory, and random-walk algorithms for the physical design of ICs. He is currently developing a novel random-walk algorithm for solving Maxwell's equations in complex, IC interconnect structures. With Dr. R.B. Iverson, he has also commercialized a random-walk IC-interconnect capacitance extractor *QuickCap*®, currently considered a "gold standard" in the chip-design industry. Dr. Le Coz has been a Digital Equipment Corporation Fellow, a Visiting Faculty at Sandia National Laboratories (Livermore, CA), a Connecticut State Scholar, and a General Motors Scholar. He has received the American Cyanamid, Perkin-Elmer, and Rensselaer Physics Awards. He is a member of Tau Beta Pi, Eta Kappa Nu, Sigma Xi, and the American Physical Society.

Paul Matos is a junior in Electrical and Computer Engineering at California State University, Fresno. His current research interests include the development of a stochastic algorithm for Maxwell's equations and building magnetically levitated trains.

A Novel Numerical Approach for the Analysis of 2D MEMS-Based Variable Capacitors Including the Effect of Arbitrary Motions

Michiko Kuroda Noriyuki Miura

kuroda@cc.teu.ac.jp

School of Engineering, Tokyo University of Technology, Hachioji, Tokyo 192-0982, Japan

Manos M. Tentzeris

School of ECE, Georgia Institute of Technology, Atlanta, GA 30332-250, USA

Abstract

A novel time-domain technique is proposed for the analysis of MEMS-based variable devices involving motion to arbitrary in-plane directions using the adaptive body fitted grid generation method with moving boundaries. MEMS technology is growing rapidly in the RF field and the accurate design of RF MEMS switches that can be used for phase shifting or reconfigurable tuners requires the computationally effective modeling of their transient and steady-state behavior including the accurate analysis of their time-dependent moving boundaries. Due to the limitations of the conventional time-domain numerical techniques, it is tedious to simulate these problems numerically. The new technique proposed in this paper is based on the time-difference time-domain method with an adaptive implementation of grid generation. Employing this transformation, it is possible to apply the grid generation technique to the analysis of geometries with time-changing boundary conditions. A variable capacitor that consists of two metal plates that can move to arbitrary in-plane directions is analyzed as a benchmark. The numerical results expressing the relationship between the velocity of the plates and the capacitance are shown and the transient effect is accurately modeled.

1. Introduction

The accurate knowledge of the electromagnetic field variation for a moving or rotating body is very important for the realization of new optical or microwave devices, such as the RF-MEMS structures used in phase-shifters, couplers or filters

[1,2]. Computational method for moving boundary problems have been presented earlier in heat and fluid flow area [3-6]. In this paper, we propose a new numerical approach for the analysis of this type of problems that alleviates the limitations of the conventional time-domain techniques in the electromagnetic field [7-12] and shows good agreement with analytical results [13]. Employing the transformation with the time factor, it is possible to apply the grid generation technique of [14] to the time-domain analysis of geometries with moving objects. With such a grid, the FD-TD method can be solved very easily on a "static" (time-invariant) rectangular mesh regardless of the shape and the motion of the physical region, something that makes it an especially good tool to analyze arbitrary shape and motion. In this paper, this simulation method is applied to the analysis of a two-dimensional MEMS variable capacitor with arbitrary in-plane motions of its interdigitated fingers.

2. General Theory of the Body-Fitted Grid Generation Method with Moving Boundaries

This technique is based on the finite-difference time-domain (FD-TD) method with an adaptive implementation of grid generation. The key feature of this method is that the time factor is added to the conventional numerical grid generation. We have improved the grid generation of [14] to the present one having a coordinate line coincident with arbitrarily shaped moving boundaries or moving bodies. Employing this transformation, it is possible to apply the grid generation technique to the analysis of geometries with time-changing boundary conditions. With such a grid, the FD-TD method can be solved very easily using

a time-invariant square grid (rectangular computational region) regardless of the shape and the motion of the physical region. Employing the transformation with the time factor, the partial differential equation in the physical region (x, y, z, t) is related to the computational region (ξ, η, ζ, τ) as follows

$$x = x(\xi, \eta, \zeta, \tau), \quad (1)$$

$$y = y(\xi, \eta, \zeta, \tau), \quad (2)$$

$$z = z(\xi, \eta, \zeta, \tau), \quad (3)$$

$$t = t(\xi, \eta, \zeta, \tau). \quad (4)$$

The inverse transformation is given by

$$\xi = \xi(x, y, z), \quad (5)$$

$$\eta = \eta(x, y, z), \quad (6)$$

$$\zeta = \zeta(x, y, z), \quad (7)$$

$$\tau = \tau(x, y, z). \quad (8)$$

According to the transformation, the first derivatives are transformed as follows,

$$\begin{bmatrix} \partial/\partial x \\ \partial/\partial y \\ \partial/\partial z \\ \partial/\partial t \end{bmatrix} = K \begin{bmatrix} \partial/\partial \xi \\ \partial/\partial \eta \\ \partial/\partial \zeta \\ \partial/\partial \tau \end{bmatrix} \quad (9)$$

The inverse transformation is given by,

$$\begin{bmatrix} \partial/\partial \xi \\ \partial/\partial \eta \\ \partial/\partial \zeta \\ \partial/\partial \tau \end{bmatrix} = L \begin{bmatrix} \partial/\partial x \\ \partial/\partial y \\ \partial/\partial z \\ \partial/\partial t \end{bmatrix} \quad (10)$$

where the matrices K and L are given by

$$K = \begin{bmatrix} \partial\xi/\partial x & \partial\eta/\partial x & \partial\zeta/\partial x & \partial\tau/\partial x \\ \partial\xi/\partial y & \partial\eta/\partial y & \partial\zeta/\partial y & \partial\tau/\partial y \\ \partial\xi/\partial z & \partial\eta/\partial z & \partial\zeta/\partial z & \partial\tau/\partial z \\ \partial\xi/\partial t & \partial\eta/\partial t & \partial\zeta/\partial t & \partial\tau/\partial t \end{bmatrix} \quad (11)$$

and

$$L = K^{-1} = \begin{bmatrix} \partial x/\partial \xi & \partial y/\partial \xi & \partial z/\partial \xi & \partial t/\partial \xi \\ \partial x/\partial \eta & \partial y/\partial \eta & \partial z/\partial \eta & \partial t/\partial \eta \\ \partial x/\partial \zeta & \partial y/\partial \zeta & \partial z/\partial \zeta & \partial t/\partial \zeta \\ \partial x/\partial \tau & \partial y/\partial \tau & \partial z/\partial \tau & \partial t/\partial \tau \end{bmatrix}. \quad (12)$$

By this transformation, there is a unique correspondence between the computational region and the physical region. The transformed region can be easily solved in the rectangular computational region by FD-TD method. The stability criterion for FD-TD algorithm is discussed in [8].

3. Two Dimensional Variable Capacitor with Arbitrary Motions

The geometry to be considered here is shown in Fig. 1. Under the combined effect of mechanical and electrical force, the two plates are assumed to move with different velocities to arbitrary in-plane directions. For the two-dimensional TM-propagation case, there are only E_x , E_y , H_z nonzero components with a time variation given by the following equations,

$$\frac{\partial H_z}{\partial t} = \frac{1}{\mu} \left(\frac{\partial E_x}{\partial y} - \frac{\partial E_y}{\partial x} \right), \quad (13)$$

$$\frac{\partial E_x}{\partial t} = \frac{1}{\varepsilon} \left(\frac{\partial H_z}{\partial y} - J_x \right), \quad (14)$$

$$\frac{\partial E_y}{\partial t} = -\frac{1}{\varepsilon} \left(\frac{\partial H_z}{\partial x} + J_y \right), \quad (15)$$

where ε , μ are the constitutive parameters of the respective media. In Fig. 1, the configurations of the physical and of the computational regions are shown. The interdigitated fingers are assumed to move to arbitrary directions in the xy -plane with velocities v and u , respectively and the direction of their motion is shown by the angles θ_v and θ_u . Using a coordinates' transformation technique, the time-changing physical region (x, y, t) can evolve to a time-invariant computational domain (ξ, η, τ) . To transform the equations, it is easy to separate the physical region in 25 subregions, where (n, m) are the indices of each subregion in x - and y -direction. The number of subregions depends on the geometry of the moving parts of the geometry.

Different subregions are characterized by different velocities in amplitude and/or direction. The transform equations between the physical and the computational regions are chosen as

$$\xi = \alpha_{n-1} \frac{x - h_{n-1}(t)}{h_n(t) - h_{n-1}(t)} + \xi_{n-1}, \quad (16)$$

$$\eta = \beta_{m-1} \frac{y - g_{m-1}(t)}{g_m(t) - g_{m-1}(t)} + \eta_{m-1}, \quad (17)$$

$$\tau = t \quad (18)$$

where $n=1, 2, 3, 4, 5$ $m=1, 2, 3, 4, 5$ and $h_0(t), h_1(t), h_2(t), h_3(t), h_4(t), h_5(t), g_0(t), g_1(t), g_2(t), g_3(t), g_4(t), g_5(t)$ are written in the following form assuming that the plate velocities remain constant for the whole time of their motion. $\alpha_{n-1}, \beta_{m-1}$ are coefficients to normalize the computational region. The coordinates x_1, x_2, x_3, x_4 , and y_1, y_2, y_3, y_4 represent the initial positions of the plates,

$$h_1(t) = x_1 + (v \cos \theta_v) t, \quad (19)$$

$$h_2(t) = x_2 + (u \cos \theta_u) t, \quad (20)$$

$$h_3(t) = x_3 + (v \cos \theta_v) t, \quad (21)$$

$$h_4(t) = x_4 + (u \cos \theta_u) t, \quad (22)$$

$$g_1(t) = y_1 + (u \sin \theta_u) t, \quad (23)$$

$$g_2(t) = y_2 + (v \sin \theta_v) t, \quad (24)$$

$$g_3(t) = y_3 + (v \sin \theta_v) t, \quad (25)$$

$$g_4(t) = y_4 + (u \sin \theta_u) t, \quad (26)$$

The functions $h_1(t), h_2(t), h_3(t), h_4(t), g_1(t), g_2(t), g_3(t), g_4(t)$, describe the movement along the x and y axis, respectively, and allow for the realization of a rectangular grid with stationary boundary conditions, where $h_0(t) = 0, h_5(t) = L_x, g_0(t) = 0, g_5(t) = L_y, 0 \leq \theta_u \leq 360^\circ, 0 \leq \theta_v \leq 360^\circ$. By choosing the angles, it is easy to apply this technique for the analysis of arbitrary motions. The partial time-derivatives in the transformed domain (ξ, η, τ) can be expressed in terms of the partial derivatives of the original domain (x, y, t) using eqs. (16)-(26). The FDTD technique can provide the time-domain solution of the rectangular (ξ, η, τ) grid. The stability criterion in this case is chosen as $c \Delta t \leq \delta / 0.707$, where $\delta = \Delta x_0 = \Delta y_0$, assuming the grid is uniformly discretized in both directions. In

general, δ is the minimum space increment (minimum cell size) for x and y directions [8].

4. Numerical Results

To validate this approach, numerical results are calculated for a two-dimensional variable capacitor with its fingers moving only to the x -direction. The grid includes 200×200 cells where $L_x = L_y = L = 5\lambda, \Delta x = \Delta y = L/200$, and $\Delta t = L/800c$. In this case, as the plates are moving only to the x -direction away from each other, the angles are $\theta_u = 0^\circ, \theta_v = 180^\circ$ and as the plates are approaching other, the angles are $\theta_u = 180^\circ, \theta_v = 0^\circ$. The initial plate separation is $L/5$ and the grid is terminated with Mur's absorbing boundary conditions. The relation between the velocity and the transient value of the capacitance between the moving fingers, assuming that they start to move away and approach each other at $t=40$ time-step and stop at $t=60$ time-step, is shown in Fig. 2. The capacitance is derived from [15] and is calculated in the area of no.43 in Fig. 2. Theoretically, the value of the capacitance is derived from $C = \epsilon_0 S/d$, where $d = \lambda, S =$

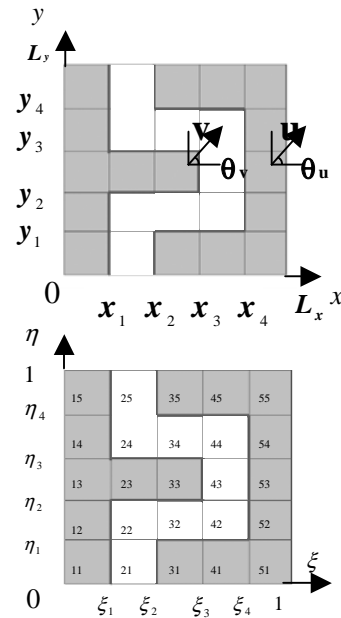


Fig. 1. Physical region (top graph) and computational (bottom graph) region.

$\lambda \times \lambda$. The stationary value ($u=v=0$) in Fig. 2, is agreed with this theoretical value. It can be observed that different velocity values lead to different values of the capacitance, since they

affect the spacing of the fingers for a specific t_0 time-step. Fig. 3 displays computational results of the time dependence of the transient capacitance for velocity values in the range of $u = v = 2 \times 10^{-3} c$ to $u = v = 8 \times 10^{-3} c$, assuming that the plates move away from each other from $t=10$ time-step to $t=60$ time-step. The horizontal axis indicates the normalized time expressed in time steps and the vertical axis indicates the value of the transient capacitance. The stationary value ($v=u=0$) is displayed for reference reasons and demonstrates a (smoother) time-variation due to the time evolution of the excitation function itself. In Fig. 4, the time dependence of the transient capacitance is demonstrated for various velocity values, assuming that the plates approach each other from $t=20$ time-step to $t=60$ time-step. Following this approach other, the angles are $\theta_u = 0^\circ, \theta_v = 180^\circ$ and as the plates are approaching other, the angles are $\theta_u = 180^\circ, \theta_v = 0^\circ$. The initial plate separation is $L/5$ and the grid is terminated with Mur's absorbing boundary conditions. The relation between the velocity and the transient value of the capacitance between the moving fingers, assuming that they start to move away and approach each other at $t=40$ time-step and stop at $t=60$ time-step, is shown in Fig. 2. The capacitance is derived from [15] and is calculated in the area of no.43 in Fig. 2. Theoretically, the value of the capacitance is derived from $C = \epsilon_0 S/d$, where $d = \lambda, S = \lambda \times 1$. The stationary value ($u=v=0$) in Fig. 2, is agreed with this theoretical value.

It can be observed that different velocity values lead to different values of the capacitance, since they affect the spacing of the fingers for a specific t_0 time-step. Fig. 3 displays computational results of the time dependence of the transient capacitance for velocity values in the range of $u = v = 2 \times 10^{-3} c$ to $u = v = 8 \times 10^{-3} c$, assuming that the plates move away from each other from $t=10$ time-step to $t=60$ time-step.

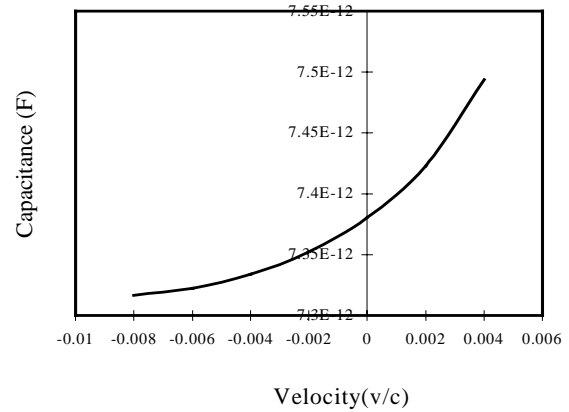


Fig. 2. Capacitance versus velocity.

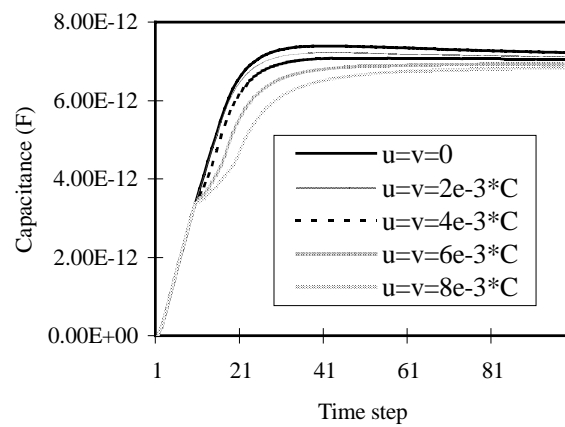


Fig. 3. Time dependence of transient capacitance for each velocity, where plates go away from $t=10$ time steps to $t=60$ time steps.

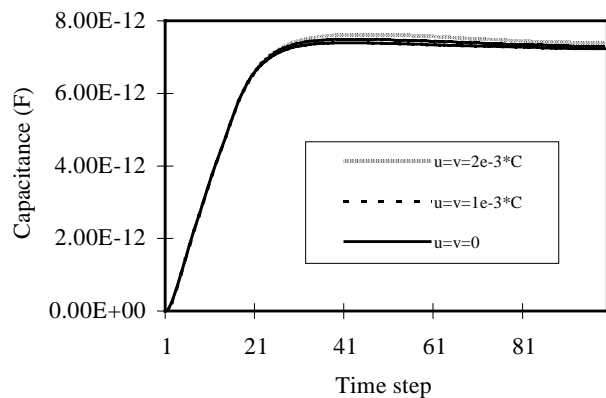


Fig. 4. Time dependence of transient capacitance for each velocity, where plates approach each other from $t=10$ time- steps to $t=60$ time-steps.

The horizontal axis indicates the normalized time expressed in time steps and the vertical axis indicates the value of the transient capacitance. The stationary value ($v=u=0$) is displayed for reference reasons and demonstrates a (smoother) time-variation due to the time evolution of the excitation function itself. In Fig. 4, the time dependence of the transient capacitance is demonstrated for various velocity values, assuming that the plates approach each other from $t=20$ time-step to $t=60$ time-step. Following this approach for the whole period of the motion of the fingers, it is easy to perform an accurate analysis of the transient response of the structure and predict the ringing parasitic effects. It is clear that the transient effect is more pronounced for the higher values of velocity.

Conclusions

A novel time-domain modeling technique that has the capability to accurately simulate the transient effect of variable capacitors with arbitrary in-plane motion of their plates has been proposed. This technique is a combination of the FDTD method and the body fitted grid generation technique. The key point of this approach is the enhancement of a space and a time transformation factor that leads to the development of a time-invariant numerical grid. The numerical results of the relation between the capacitance and the velocity of the motion are shown for a MEMS capacitor and demonstrate the proposed technique's unique computational advantages in the modeling of microwave devices with moving boundaries.

Acknowledgement

The authors wish to acknowledge the support of the Grant-in-Aid for Scientific Research ((c) No.13650435) of The Ministry of Education, Culture, Sports Science and Technology (MEXT), Japan and the NSF Career Award under #9984761, the Yamacraw Design Center of the State of Georgia and the Georgia Tech Packaging Research Center.

References

[1] A. Dec, K. Suyama, "Microwave MEMS-Based

Voltage-Controlled Oscillators," *IEEE Trans. MTT*, pp. 1943-1949, vol.48, no. 11, Nov. 2000.

- [2] N. Bushyager, B. McGarvey, M. Tentzeris, "Adaptive numerical modeling of RF Structures requiring the coupling of Maxwell's, mechanical and solid-state equations," *Proc. of the 2001 ACES*, pp. 1-6, Monterey, CA, March 2001.
- [3] Mosher Rosenfeldm, Dochan Kwak, "Time dependent solution of viscous incompressible flow in moving co-ordinates", *International Journal. for Numerical Method in Fluid*, vol.13, pp. 1311-1328, 1991.
- [4] S. Kuroda, H. Ohba, "Numerical analysis of flow around a rotation square cylinder," *JSME International Journal*, 36-4, B, pp. 592-597, 1993.
- [5] C. Xu, M. Sen, M. Gad-el-Hak, "Dynamics of a Rotatable Cylinder with Splitter Plate in Uniform Flow," *Journal of Fluids and Structures*, Vol. 7, Issue 4, pp. 401-416, May 1993.
- [6] P. J. Zwart, G. D. Raithby, "Space-time meshing for two dimensional moving boundary problems," *Proc. of the 7th International Meshing Roundtable*, Dearborn, Michigan, October 1998.
- [7] M. Kuroda, "A dielectric waveguide with moving boundary," *IEICE Trans.*, vol. E74, pp. 3952-3954, December 1991.
- [8] M. Kuroda, "Electromagnetic wave scattering from perfectly conducting moving boundary-An application of the body fitted grid generation with moving boundary," *IEICE Trans.*, vol. E77-C, No.11, pp. 1735-1739, Nov. 1994.
- [9] M. Kuroda, S. Kuroda, "FD-TD method for electromagnetic wave scattering from a moving body by using the body fitted grid generation with moving boundary", *Proc. of ICEAA99*, pp. 549-552, September 1999.
- [10] M. Kuroda, S. Kuroda, "An application of body fitted grid generation method with moving boundaries to solve the electromagnetic field in a moving boundary," *Proc. of the*

2001 ACES, pp. 519-524, Monterey CA, March 2001.

- [11] M. Kuroda, K Kawano, M. M. Tentzeris, "Body fitted grid generation method with moving boundaries and its application for analysis of MEMS devices," *Proc. of the 2002 ACES*, pp. 219-224, Monterey CA, March 2002.
- [12] M. Kuroda, N. Miura, M.M. Tentzeris, "A Novel Time-Domain Technique for the Analysis of MEMS-Based Variable Capacitors with Moving Metallic Parts," *Proc. of APMC2002*, pp. III.1208-1211, Kyoto, JAPAN, November 2002.
- [13] V. Bladel, "Relativity and Engineering," *Springer-Verlag*, Berlin, 1984.
- [14] J. F. Thompson, "Numerical grid generation", *North Holland*, Amsterdam, 1985.
- [15] A. Taflove, S. Hagness, "Computational Electrodynamics, The finite difference time domain method," Boston, Artech House, 2000.

Michiko Kuroda Professor Michiko Kuroda received the B. E. degree in Electrical Engineering from Shizuoka University, Shizuoka, Japan and the M. E. and D. E. in Electrical Engineering from Waseda University, Tokyo, Japan, She was a visiting researcher at the ElectroScience Laboratory, the Ohio State University, OH from 1986 to 1987. In 1990, she became an Associate Professor at Tokyo University of Technology. Since 1998, she has been a professor and in 2002 she became the Chair of the Department of Information Networks. She is a Correspondent of URSI (International Union of Radio Science) in Japan. Her research interests are FDTD method, grid generation method and its application for the moving boundary problems and MEMS devices.

Noriyuki Miura received the B. E. degree from Tokyo University of Technology, Tokyo, Japan in 2002. Now he is a graduate student at Tokyo University of Technology.

Manos M. Tentzeris Professor Manos M. Tentzeris received the Diploma Degree in Electrical and Computer Engineering

from the National Technical University of Athens in Greece and the M.S. and Ph.D. degrees in Electrical Engineering and Computer Science from the University of Michigan, Ann Arbor, MI and he is currently an Assistant Professor with School of ECE, Georgia Tech, Atlanta, GA. He has published more than 100 papers in refereed Journals and Conference Proceedings and 4 book chapters. Dr. Tentzeris has helped develop academic programs in Highly Integrated Packaging for RF and Wireless Applications, Microwave MEM's, SOP-integrated antennas and Adaptive Numerical Electromagnetics (FDTD, Multi Resolution Algorithms). He is the RF Alliance Leader of Georgia Tech NSF-Packaging Research Center and the leader of the Novel Integration Techniques Subthrust of the Broadband Hardware Access Thrust of the Yamacraw Research Initiative of the State of Georgia. He was the recipient of the 2003 IEEE CPMT Outstanding Young Engineer Award, the 2002 International Conference on Microwave and Millimeter-Wave Technology Best Paper Award (Beijing, CHINA), the 2002 Georgia Tech-ECE Outstanding Junior Faculty Award, the 2001 ACES Conference Best Paper Award, the 2000 NSF CAREER Award and the 1997 Best Paper Award, International Hybrid Microelectronics and Packaging Society. He was also the 1999 Technical Program Co-Chair of the 54th ARFTG Conference, Atlanta, GA and he is the Vice-Chair of the RF Technical Committee (TC16) of the IEEE CPMT Society. Dr. Tentzeris was a Visiting Professor with the Technical University of Munich, Germany for the summer of 2002. He is a Senior Member of IEEE and a member of URSI and of the Technical Chamber of Greece.

Coupling Between Highly Conducting and Permeable Metallic Objects in the EMI Frequency Range

F. Shubitidze⁽¹⁾, K. O'Neill^(1,2), I. Shamatava⁽¹⁾, and K. Sun⁽¹⁾

⁽¹⁾ Thayer School of Engineering, Dartmouth College,
Cummings Hall, HB 8000, Hanover NH, 03755, USA

e-mail: fridon.shubitidze@dartmouth.edu

Tel: 603 646 3671; Fax: 603 646 3856

⁽²⁾ USA ERDC Cold Regions Research and Engineering Laboratory,
72 Lyme Road, Hanover NH, 03755, USA

Abstract - Electromagnetic induction (EMI) sensing, from 10's of Hz up to 100's of kHz, is emerging as one of the most promising remote sensing technologies for detection and discrimination of buried metallic objects, particularly unexploded ordnance (UXO). For a single homogenous target it has been shown that the scattered EMI signal strongly depends on an object's geometry and its electromagnetic parameters. Most if not all UXO contain different kinds of metal. Additionally, UXO sites are often highly contaminated with metallic clutter. Methods are currently needed to distinguish dangerous objects, such as UXO, from innocuous clutter. Recently, analysis of broadband EMI responses from multiple objects has demonstrated significant interaction between them. The main goal of the paper is to investigate interaction phenomena between highly conducting and permeable metallic objects in the EMI frequency range. Numerical results are compared with experimental data for canonical geometries (spheres and cylinders). The results indicate when and how interaction affects the EMI responses and provides guidance for use of this understanding for future target discrimination purposes.

Keywords: UXO, Low frequency, Electromagnetic induction, Auxiliary sources, Interaction, multiple, scattering.

I. Introduction

Cleaning up buried unexploded ordnance has been identified as a very high priority environmental problem for many years. A significant fraction of all ordnance fired does not detonate and remains dangerous for a long time. In some cases, the ordnance is broken in parts upon impact with the ground, complicating discrimination and possibly contaminating ground water with explosive residues. Most if not all UXO are composite objects with distinct, relatively homogeneous sections, each consisting of different metal shown in Fig. 1, e.g., head, body, tail and fins, copper banding, etc. Further, in many highly contaminated sites, multiple UXO together with widespread clutter appear simultaneously within the field of view of the sensor. The false alarm rate produced by clutter is extremely high and typically causes the majority of remediation costs to be spent on excavating innocuous items. At present the major problem is discrimination not detection. One of most promising technologies for UXO discrimination is electromagnetic

induction (EMI) sensing, operating from 10's of Hz up to 100's of kHz. EMI sensing has some distinct advantages relative to ground penetrating radar (GPR): while still range limited, practical depth of penetration of EMI signals is typically not limited by the lossiness of conductive soils, and signal clutter due to dielectric heterogeneity is negligible. At the same time, approaches to processing and resolution improvement that are well established for GPR do not carry over to EMI surveying. Frequency domain EMI responses typically are characterized using two components: one inphase with the primary magnetic field and the other quadrature part and they depend on an object's geometry and it's EM parameters [1], [2].

The magnetic fields radiated by both the sensor and the object fall off very sharply as a function of distance, $\sim 1/R^3$. Therefore, the sensor affects different materials and sections of the target differently. The transmitted ("primary") field produces much stronger excitation of the closest portion of the target. In turn, the parts of the target radiating closest to the receiver disproportionately influence on the scattered signal. These proximity effects are particularly important for identification and discrimination of multiple and composite objects. Analytical techniques based on simple resonating magnetic and electric dipoles are insufficient [3], when sensors pass close to the target, as is often the case in UXO surveying.



Fig. 1. 120 mm HEAT round UXO consists of four sections, altogether about 80 cm long: 1) magnetic (steel), 2) non-magnetic titanium, 3) steel, and 4) aluminum.

The physics of UWB (1Hz – 300kHz) EMI phenomena is of diffusion rather than wave propagation. In general, in the EMI realm displacement currents can be neglected in both target

and surrounding media (air, ground). This means that the dielectric constant of the surrounding medium is typically unimportant for EMI identification of buried targets such as UXO and competing clutter. Soil conductivity is nine orders of magnitude lower than conductivity of a scatterer, which combine with weak electric fields produce only weak soil currents. This means that the exterior (soil) magnetic fields are irrotational, and can thus be represented efficiently using a simple scalar potential. Here we proceed in terms of such potential outside the target, while retaining a vector field formulation inside the metallic object, which an external transmitted ("primary" or excitation) magnetic field may penetrate significantly.

The main goal of the paper is to investigate interaction between highly conducting and permeable metallic sizable objects in the EMI frequency range; and further, to provide the understanding of why, when, and how the interaction affects the EMI response; and finally, to interpret data meaningfully for target classification purposes.

II. A Hybrid Full MAS and MAS-TSA Method for Multiple Targets

Assume that highly conducting and permeable multiple metallic objects $\ell = 1, 2, \dots, N_{\text{ob}}$ (where N_{ob} is the number of objects) are placed in a uniform background with the electromagnetic properties effectively of free space. The objects are illuminated by a time varying primary magnetic field and are characterized by relative permeabilities $\mu_{\ell,r}$ and conductivities σ_{ℓ} [S/m]. The time dependence expression of $e^{j\omega t}$ is suppressed subsequently. The region external to the objects is region 0, and region internal to the ℓ object is region ℓ . Let $\hat{\mathbf{n}}_{\ell}$ to be outward pointing, normal unit vector to the boundary S_{ℓ} lying between region 0 and ℓ -th region as shown in Fig. 2. The primary magnetic field penetrates inside objects to some degree, inducing currents within and producing secondary/scattered fields outside. It is very well established that, in the magneto-quasistatic regime, displacement currents $j\omega\mathbf{D}$ can be neglected in comparison with conduction currents within objects. Outside of the targets, the electric field is small. This means that Ampere's Law becomes a homogeneous equation, $\nabla \times \mathbf{H} = 0$. The magnetic field in region 0 is irrotational and can be represented as the gradient of a scalar potential. The magnetic field in region ℓ satisfies vector wave equation:

$$\nabla \times \nabla \times \mathbf{H}_{\ell} - k_{\ell}^2 \mathbf{H}_{\ell} = 0, \quad (1)$$

where $k_{\ell} = \sqrt{-j2\pi\nu\mu_0\mu_{\ell,r}\sigma_{\ell}}$ and ν is frequency [Hz].

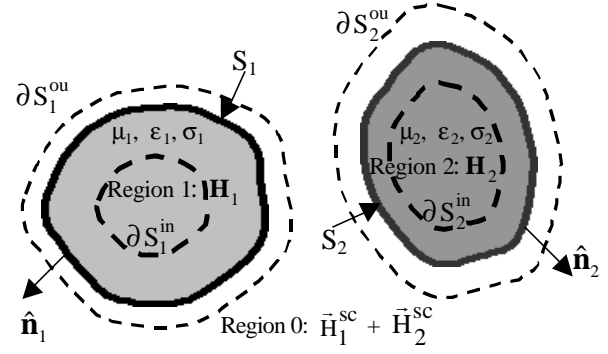


Fig. 2. MAS diagram for multiple objects.

The boundary conditions on the surfaces of the objects specify continuity of tangential components of \mathbf{H} and normal component of \mathbf{B} .

On surface S_{α} :

$$\hat{\mathbf{i}}_{1,a}(\mathbf{r}) \cdot \left[\sum_{\ell=1}^{N_{\text{ob}}} \mathbf{H}_{\ell}^{\text{sc}}(\mathbf{r}) + \mathbf{H}^{\text{pr}}(\mathbf{r}) \right] - \hat{\mathbf{i}}_{2,a}(\mathbf{r}) \cdot \left[\sum_{\ell=1}^{N_{\text{ob}}} \mathbf{d}_{\ell}^a \mathbf{H}_{\ell}(\mathbf{r}) \right] = 0. \quad (2)$$

Here the vectors $\hat{\mathbf{i}}_{i,a}(\mathbf{r})$ consist of two independent tangential and one normal vector at each point on the S_{α} surfaces, $\alpha = 1, 2, \dots, N_{\text{ob}}$. In the case of the tangential vectors, $\hat{\mathbf{i}}_{2,a}(\mathbf{r}) = \hat{\mathbf{i}}_{1,a}(\mathbf{r})$ while for the normal case $\hat{\mathbf{i}}_{2,a}(\mathbf{r}) = \mathbf{m}_{a,r} \hat{\mathbf{i}}_{1,a}(\mathbf{r})$

$$\mathbf{d}_{\ell}^a = \begin{cases} 0 & \text{if } \ell \neq a \\ 1 & \text{if } \ell = a. \end{cases} \quad (3)$$

The hybrid full MAS /MAS-TSA [4], [5] was applied for solving this problem. $\mathbf{H}_{\ell}^{\text{sc}}(\mathbf{r})$ are secondary magnetic fields and they are simulated using auxiliary magnetic charges placed on auxiliary surfaces $\partial S_{\ell}^{\text{in}}$ [1], [2]. We emphasize that these auxiliary surfaces $\partial S_{\ell}^{\text{in}}$ are enclosed by the physical surfaces S_{ℓ} and assume that they radiate in unbounded free space, with region 0 characteristics, giving rise to the secondary field, $\sum_{\ell=1}^{N_{\text{ob}}} \mathbf{H}_{\ell}^{\text{sc}}(\mathbf{r})$. Similarly, the $\mathbf{H}_{\ell}(\mathbf{r})$ is magnetic field produced by auxiliary magnetic dipoles placed on the external auxiliary surface $\partial S_{\ell}^{\text{ou}}$ and they are assumed to radiate in unbounded homogeneous space filled with ℓ -th target's material properties [1], [2]. Applying boundary conditions (2) at given point produces a linear system of

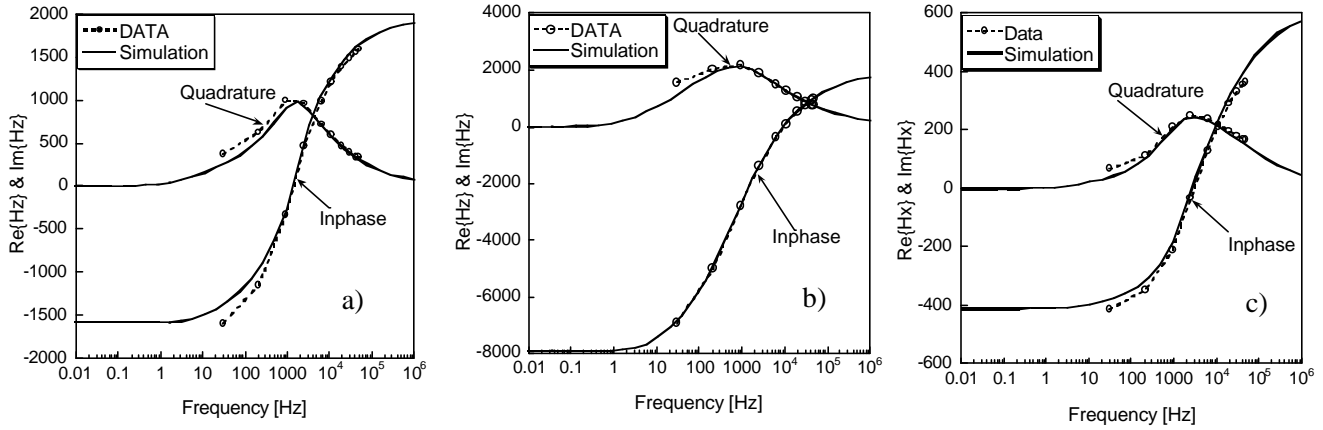


Fig. 3. Scattered magnetic fields versus frequency for two cylinders placed end to end.

equations in which the amplitudes of auxiliary sources are to be determined.

III. Results

To analyze interaction between multiple highly conducting and permeable objects, a computer code was written based on the full MAS and hybrid MAS/MAS-TSA method and several results were extracted and compared to available experimental data.

1. Two cylinders

a. Non-uniform excitation

For the validity of the hybrid full MAS/ MAS-TSA method for multiple targets, we first examine the scattered field for two cylinders illuminated by GEM-3 multi-loop antenna. Cylinders are lined up along the axis of symmetry. The primary magnetic field generated by a GEM-3 sensor was modeled as a field radiated by two concentric coils [2]. The current amplitudes on the coils were chosen such that at the

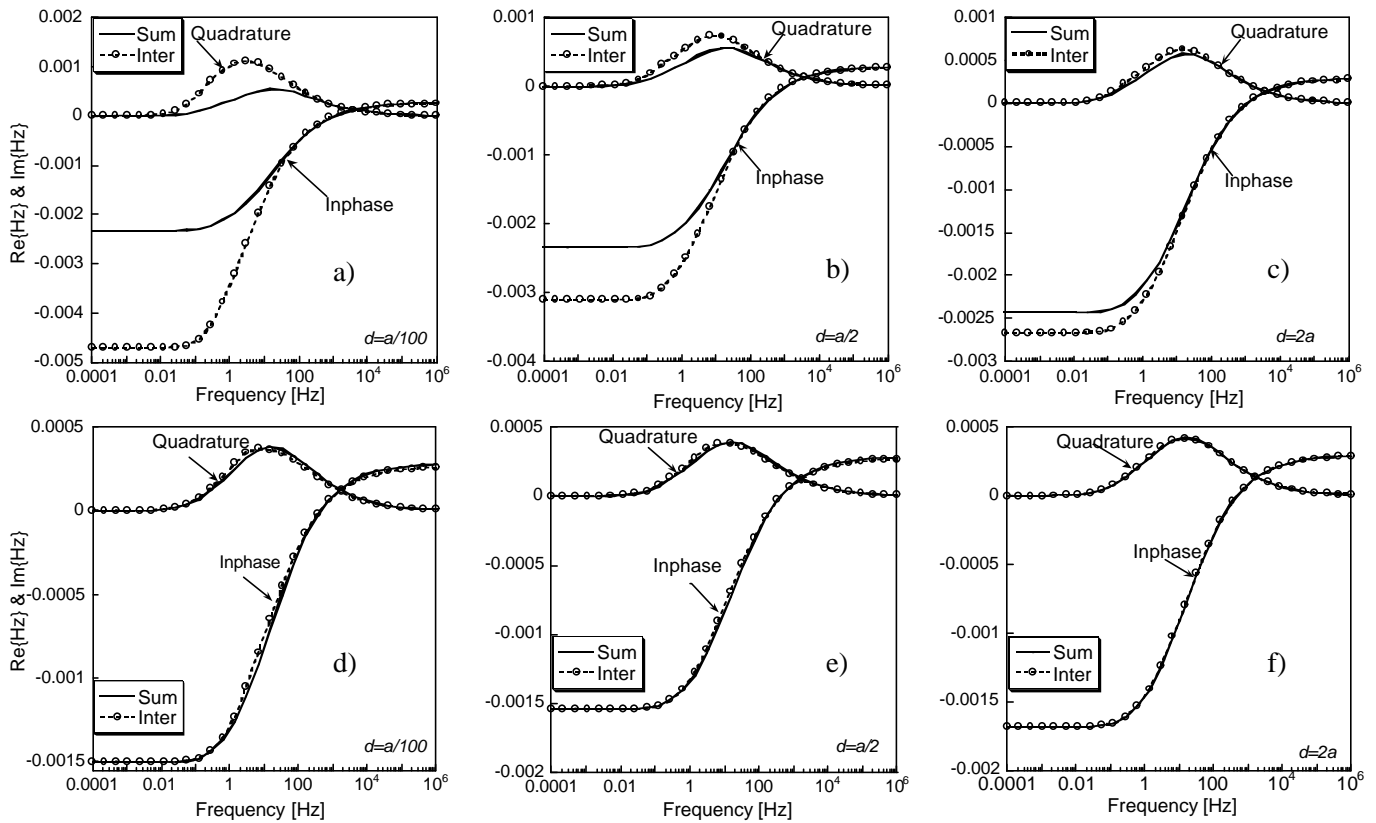


Fig. 4. Secondary magnetic fields versus frequency for two cylinders. Axial excitation: Solid lines correspond to simple summation of responses from each cylinder. Circle lines include interaction between them.

center of the coils the primary magnetic field is zero. Two excitations were considered 1) Axial, i.e. when the coil axes of GEM-3 are aligned with the axis of symmetry of the cylinders and 2) Transverse, i.e. when the GEM-3 axis is orthogonal to the cylinders' axes. In numerical tests for the transverse case, the primary field was considered to be uniform. This assumption is reasonable because the diameter of the cylinders is small relative to the targets' distance from the sensor. The cylinders parameters are: magnetic steel ($L_2 = 3$ inch, $L_2/2a_2 = 2$, $\sigma = 4 \cdot 10^6$ S/m, $\mu_{2r} = 120$) and stainless steel (non-magnetic, $L = 3$ inch, $L_1/2a_1 = 2$, $\sigma = 1.4 \cdot 10^6$ S/m, $\mu_{1r} = 1$). Fig. 3 a) shows scattered magnetic field versus frequency, when stainless steel is up (i.e. towards the sensor) and the magnetic steel cylinder is down, while the magnetic steel is up stainless steel is down in Fig. 3 b). The observation point is $z = 31$ cm from the middle point between the cylinders. In numerical calculations, the distance between cylinders was assumed to be 10 micrometers. The numerical solution is seen to be in very close agreement with measured data. A similar pattern is observed for transverse excitation in Fig. 3 c).

Note a particular advantage here from using the MAS and MAS-TSA formulations. Conventional integral equation approaches, e.g. MoM, encounter difficulties when two distinct bounding surfaces are very close to one another, as in the example above. Singularities on one surface are close enough to the other surface to disrupt simple integration routines on the latter. They cannot be separated and integrated out analytically in the same way as singularities within a

single surface can be. MAS-based methods encounter no such problems, because auxiliary surfaces containing the sources are purposely displaced from the physical surfaces.

b. Uniform excitation

Next we examine broadband EMI scattering from two geometrically identical cylinders (radius $a = 10$ cm, ratio length to the radius is $L/2a = 3$) lined up along the z -axis and excited by a spatially uniform oscillating magnetic field $\mathbf{H}^{\text{ex}} = H_0 \hat{z}$, $H_0 = 1$ (A/m). The cylinders electromagnetic parameters are: for case 1 (Fig. 3 a, b, c) in which both cylinders are the same ($\mu_{1,r} = \mu_{2,r} = 150$, $\sigma_1 = \sigma_2 = 4 \cdot 10^6$ S/m); and case 2 (Fig. 3 d, e, f) in which one cylinder is non-permeable (aluminum, $\mu_{1,r} = 1$, $\sigma_1 = 2.8 \cdot 10^7$ S/m) and one is permeable (steel, $\mu_{2,r} = 150$, $\sigma_2 = 4 \cdot 10^6$ S/m). Fig. 4 shows comparison of the secondary magnetic fields (inphase and quadrature parts) for the two cylinders with and without interaction included in the calculations. The distances between them are: $a/100$ Fig. 4 a-d; $a/2$ Fig. 4 b-e; $a/2$ and $2a$. Fig. 4 c-f. Observation point is $x=y=0$, $z=3$ m from the middle point between cylinders. These results clearly demonstrate the possibility of significant coupling between metallic objects over entire broadband EMI range. The interaction effects are much larger at low frequencies than at high frequencies. The results also show that the coupling between objects strongly

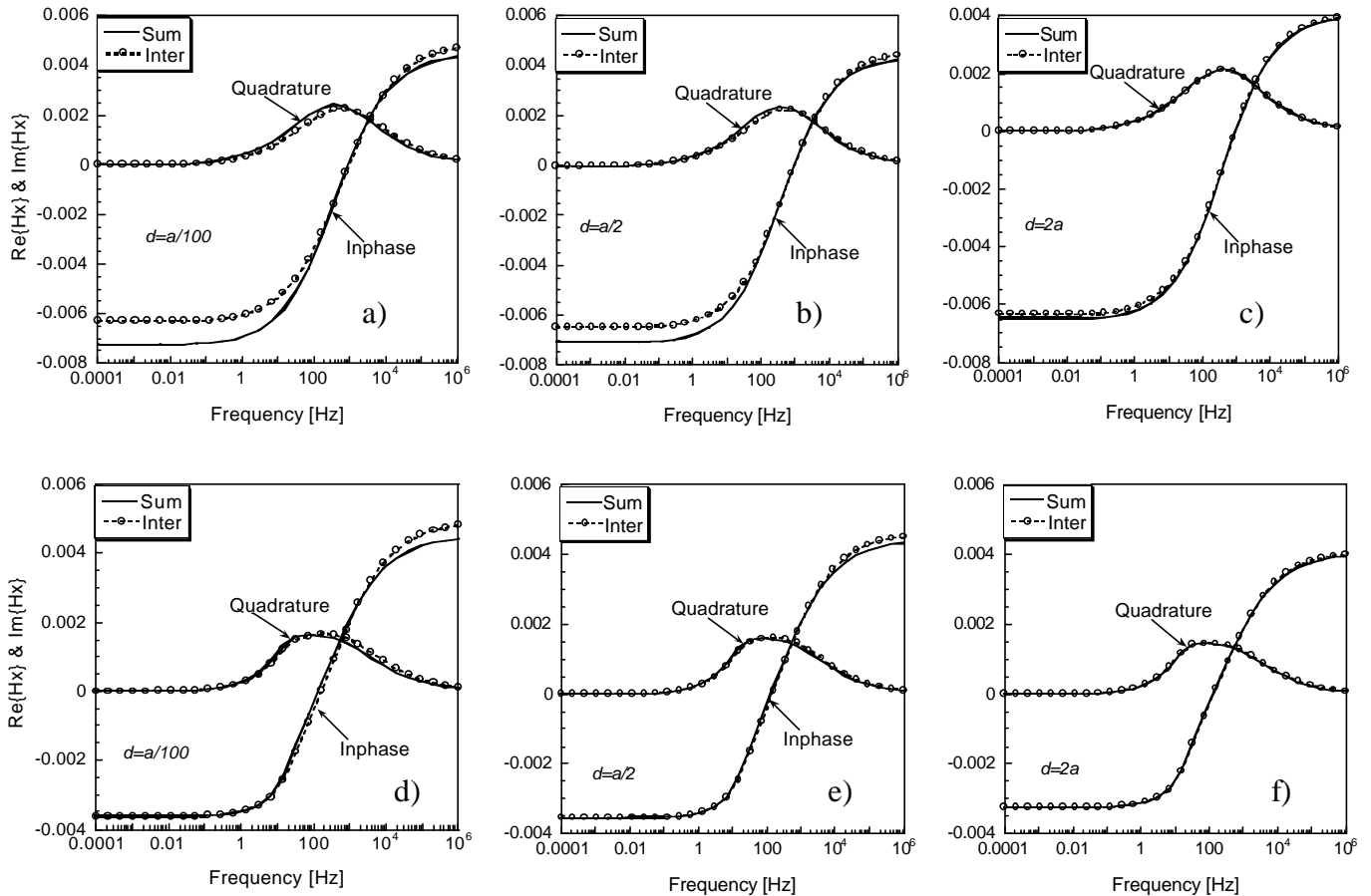


Fig. 5. Secondary magnetic fields versus frequency for two cylinders. Transverse excitation: Solid lines correspond to simple summation of responses from each cylinder. Circle lines include interaction between them.

depends on distances between objects and especially on their material properties. As distance decreases, the difference between the simple summation and full interaction increases greatly, specifically for the two permeable cylinders Fig. 4 a-c. For the two identical permeable cylinders, coupling still exists even when the distance between them is one diameter Fig. 4 c. However, the coupling between non-permeable and permeable cylinders disappears at $a/2$ distance (Fig. 4 e), and is small in any case.

The same cylinders were excited by a time varying uniform magnetic field oriented orthogonal to their axis of symmetry (transverse excitation). Fig. 5 shows the Hx component of the scattered magnetic field versus frequency at the point $y = z = 0$ and $x = 1$ m from the middle point between cylinders, for different distances between them: Fig. 5 a, d correspond to separations of $a/100$; Fig. 5 b) e) for $a/2$; and Fig. 5 for separation $2a$. Again, the results show the existence of coupling between highly conducting and permeable metallic targets in EMI frequency range. At low frequencies the interaction between permeable objects Fig. 5 a-c) is much stronger than between non-permeable and permeable objects Fig. 5 d-f). Additionally, Fig. 5 shows that in case of the

transverse excitation the coupling between cylinders is weaker than in axial excitation.

2. Two spheres under uniform primary magnetic field.

Similar tests were performed for two geometrically identical spheres (radius $a=25$ cm), lined up along the z-axis and excited by a uniform oscillating magnetic field. The spheres' electromagnetic parameters and distances between them are exactly the same as for the cylinders in section III part 1.

Fig. 6 shows EMI responses by the two spheres. In general the effect of interaction between the spheres is similar to that for the cylinders, although the degree of coupling between two permeable cylinders is much greater than between comparable spheres. However, interaction between non-permeable and permeable spheres is stronger than between the comparable cylinders. Overall, at low frequencies the amplitude of EMI responses for interacting permeable targets increases 1.3~2 times (see Fig. 3 a) and Fig. 5 a)). At highest frequencies (PEC) responses decrease, though very slightly.

The same spheres were illuminated by a primary magnetic field oriented transverse to the axis of alignment. The results

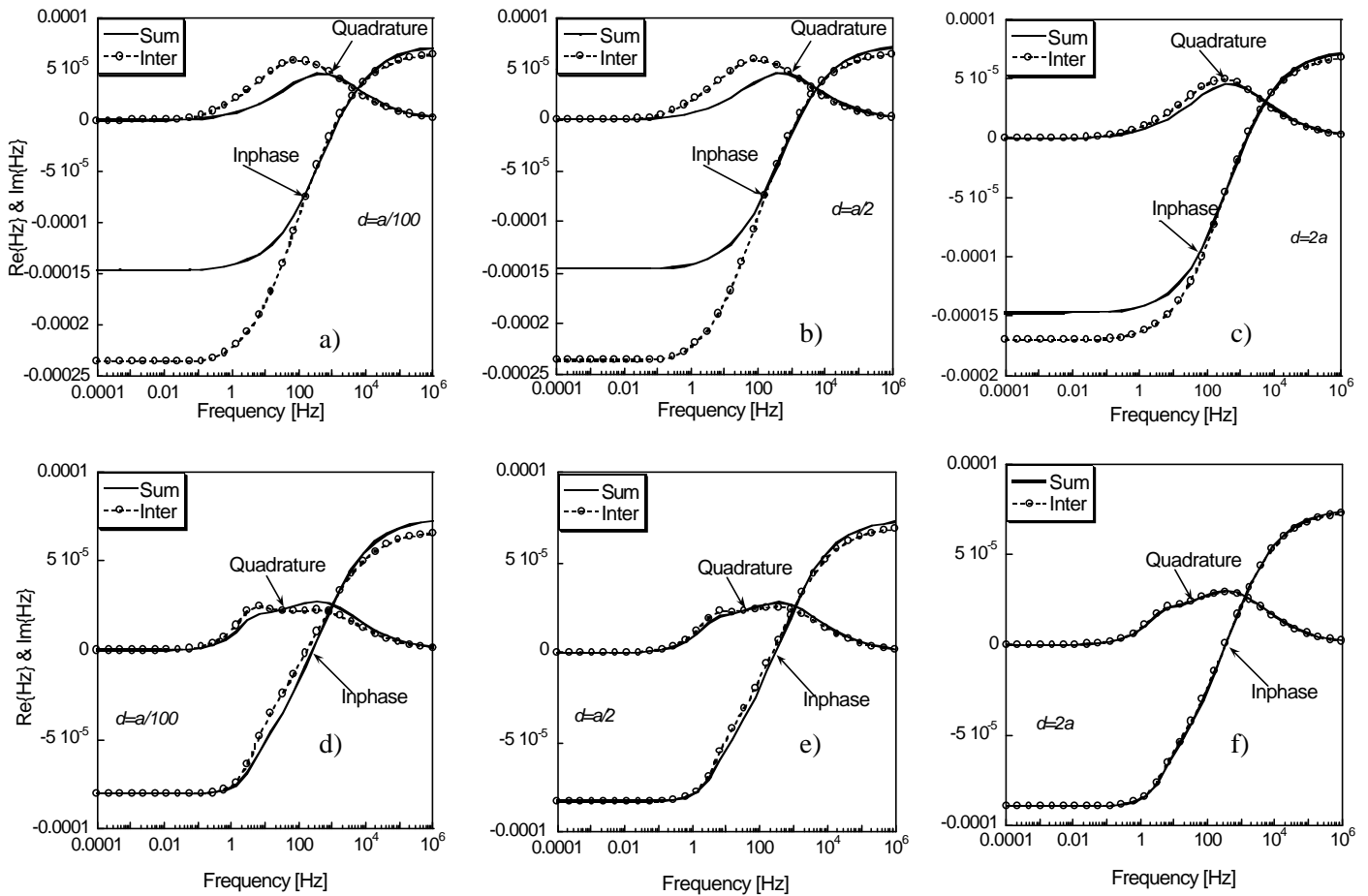


Fig. 6. Secondary magnetic fields versus frequency for two spheres aligned along the Z axis. Axial (Z) excitation: Solid lines = simple summation of responses, circle lines include all interaction between them.

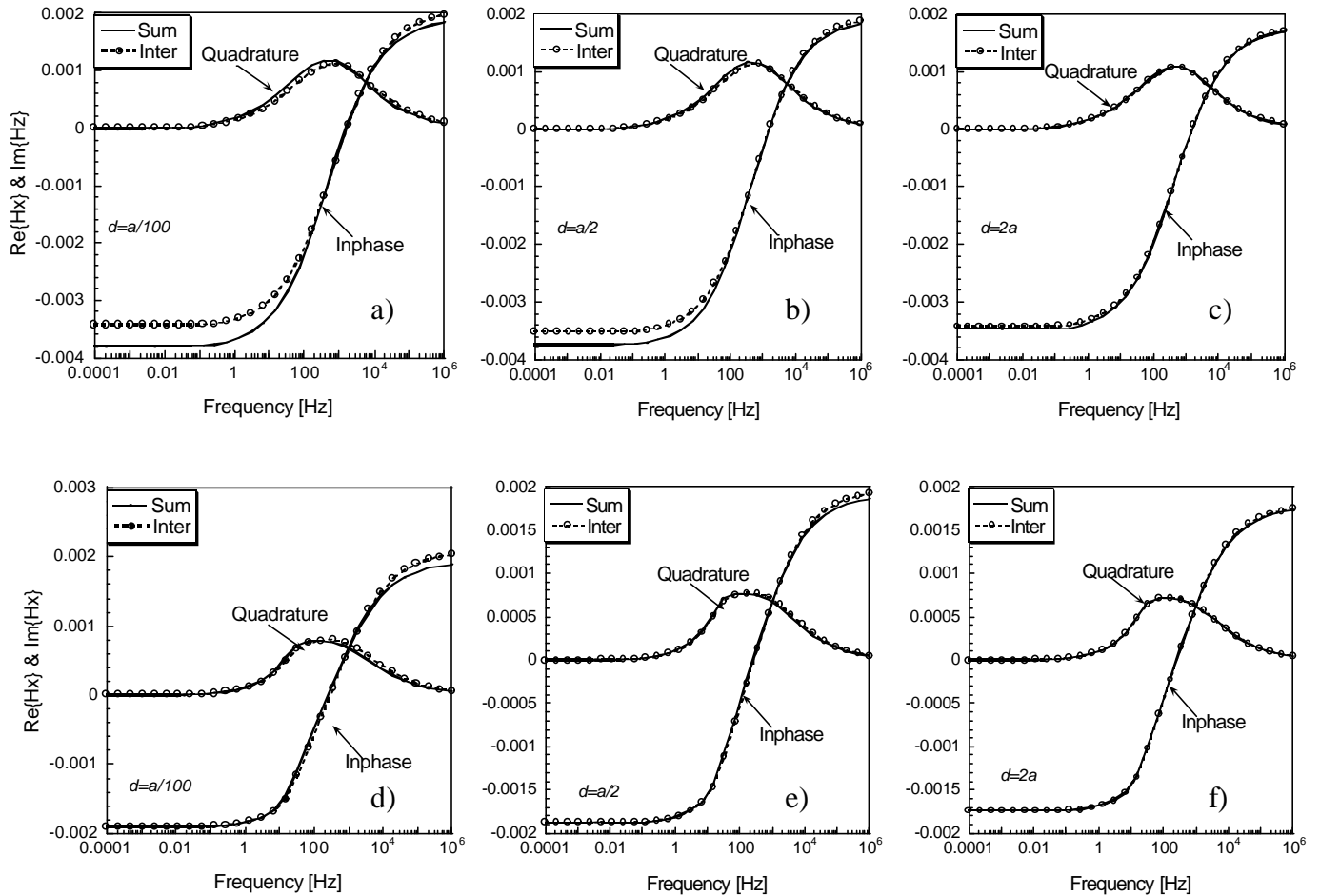


Fig. 7. Secondary magnetic fields vs frequency for two spheres, with excitation transverse to alignment axis: Solid lines = simple summation of responses, circle lines include interaction between them.

are shown on Fig. 7. In general the interaction between spheres for the cases is the same as for cylinders Fig. 5. However, the results show that at high frequencies coupling between cylinders is stronger than between spheres Fig. 5 d) Fig. 7. d).

Near field analysis

In this section we present near field analysis to provide an understanding of the interaction phenomena between metallic objects. Fig. 8 shows equal lines of the total field $\mu_{i,r} |\mathbf{H}_i|$ distributed inside and outside of the two identical objects, where the subscript i corresponds to zero for free space and 1 or 2 to the first or second targets, respectively. The EM and geometrical parameters are the same as for Fig. 3 b and Fig. 5 b cases, with spheres (a-b) and cylinders (c-d) at different frequencies, with spheres (10^{-3} Hz (\sim magnetostatic limit) and 10^5 Hz (\sim PEC limit)). The distance between objects is 5cm and they are illuminated by uniform primary magnetic field $\mathbf{H}^{pr} = \hat{z}$. Inside permeable metallic object small magnetic dipoles exist. Normally (no external magnetic fields) these

dipoles are oriented chaotically and the total field produced by them is zero. When the permeable metallic object is placed inside the low frequency 10^{-3} Hz primary magnetic field, then the primary field forces the internal dipoles to line up in one direction, so that the induced magnetic field is inphase with the primary field and amplifies that field in the external region.

For a single highly permeable sphere under uniform primary magnetic field with unit amplitude 1 (A/m) we see [6] that the amplitude of the total external magnetic field on the boundary approaches a magnitude no greater than about 3 (A/m), no matter how large μ_r is made. Numerical simulations [7] have shown that comparable external fields for the cylinder approach approximately 2~2.5. Fig. 8 shows the amplitude of the total $\mu_{i,r} |\mathbf{H}_i|$ field for permeable spheres (a) and cylinders (c). The field mostly is focused between the objects and increases dramatically from 1 to 4.2 for spheres and from 1 to 8.52 for cylinders. In other simulations we observe that, as two permeable targets approach each other at low frequency, the amplitude of the total field between them significantly increases to factors much greater than those cited above. The stronger magnetic field around each object induces stronger

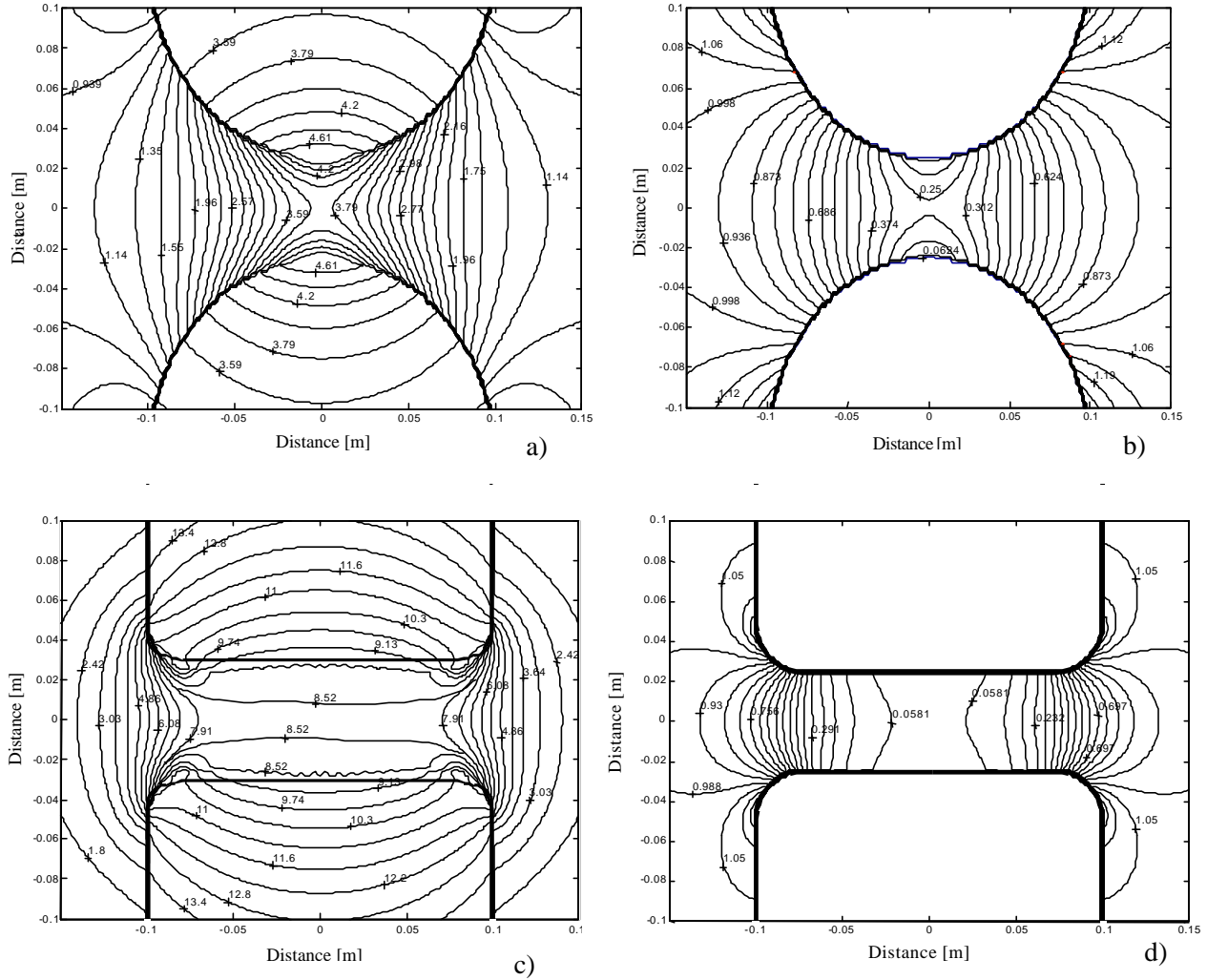


Fig. 8. Absolute value of the total $\mu_{i,r} |\mathbf{H}_i|$ field for axial excitation; left: low frequency; right: high frequency.

response within the other object, which altogether produces stronger far field. By contrast, at high frequencies the induced currents inside object become small, and are distributed only on the surface, opposing the primary magnetic field. When two objects are placed close to each other the total field between objects is suppressed. Figs. 8 b, d show the near magnetic field for the high frequency (~PEC) case. These figures show that the total magnetic fields between objects approaches zero and scattered magnetic fields from the targets are slightly smaller than summation of fields from the separate targets.

In order to understand the underlying physics of transverse excitation (Figs. 5 and 7), Fig. 9 shows contours of the total magnetic field $\mu_{i,r} |\mathbf{H}_i|$ between the same permeable cylinders and spheres as in Fig. 5 and Fig. 7. The distance between objects is 5 cm and they are excited by a uniform primary magnetic field $\mathbf{H}^{pr} = \hat{x}$, perpendicular to the line connecting their centers. In these cases the primary magnetic field is

parallel to the parts of the spheres and cylinders that are closest to one another. The results show that, at low frequency, the total magnetic fields between the objects are reduced (Fig. 9 a) and c)). This is due to the geometry of the scattered field lines. At low frequency one may think of these lines as radiating from the North pole of each object (on its side in the transverse case), in phase with the primary field, but then arcing around until they are again parallel to but opposed to the primary field in the region alongside the objects. Thus at very low frequency the tangential component of the scattered magnetic field opposes the primary magnetic field between the objects, and total external field is reduced there. According to standard EM boundary conditions, the tangential components of the total magnetic field inside and outside the object must be continuous. Along the line connecting the object centers, the primary and secondary magnetic fields are indeed tangential to the target surfaces. Thus the reduced external field corresponds to a reduced internal field and hence a

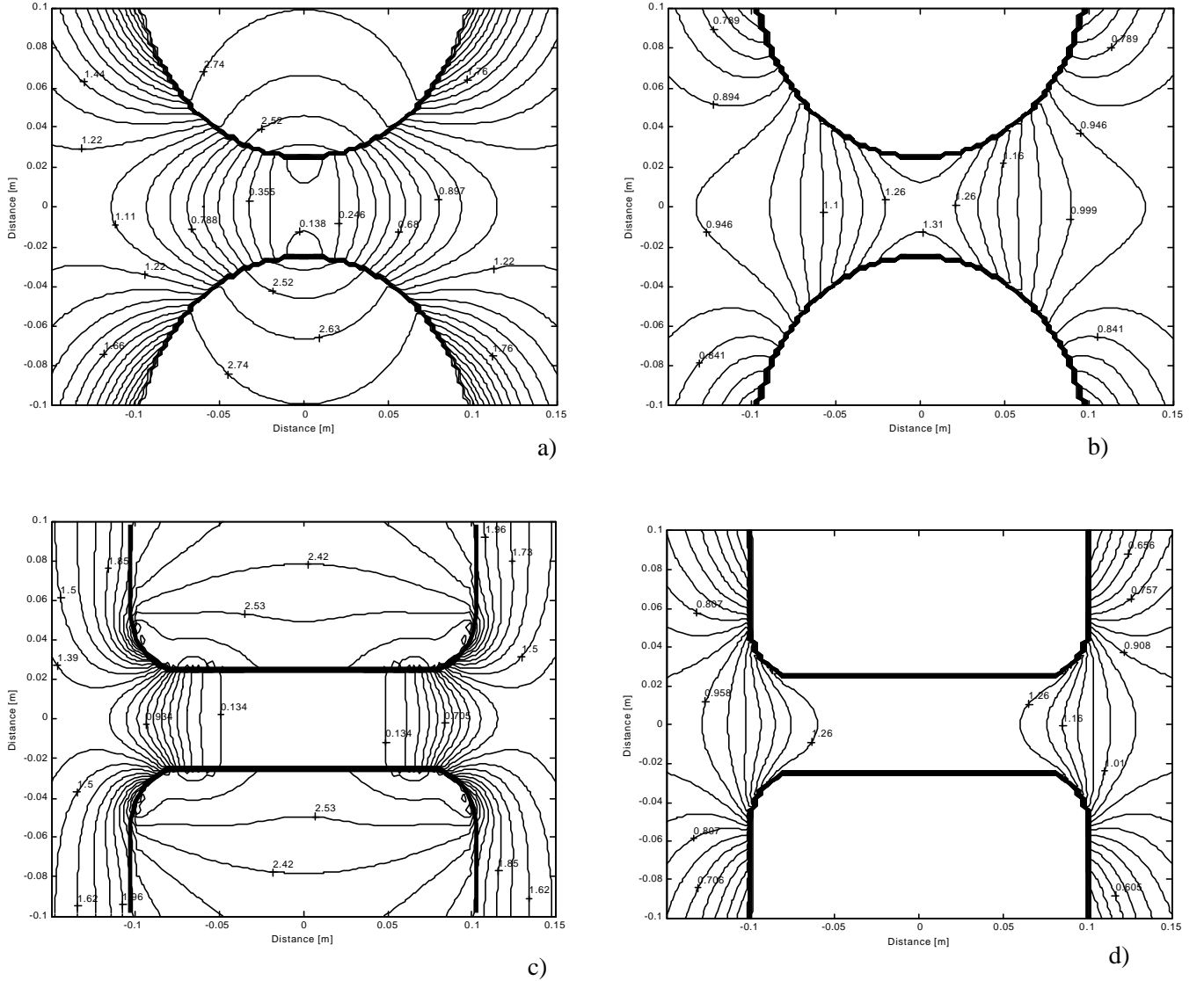


Fig. 9. Absolute value of the total $\mu_{i,r} |\mathbf{H}_i|$ field for transverse excitation; left: low frequency; right: high frequency.

smaller magnetic moment. These facts explain the observation that at low frequency the value of the scattered magnetic field for two objects with coupling Fig. 4 a-c) and Fig. 6 a-c) is smaller than simple summation would predict. At high frequency, the direction of the scattered fields is geometrically similar to those at low frequency, but with sign reversed. Thus the tangential component of the scattered magnetic field between the objects is inphase with the primary magnetic field there. Standard EM boundary conditions near the PEC limit require that the internal fields be negligible, related to the external field by a jump condition, the magnitude of which depends on the induced surface currents. The increased magnitude of the total field between the objects thus corresponds to larger surface currents than would otherwise be present, and hence a larger induced magnetic moment. This is why the results show that the secondary magnetic field from

two objects with coupling is slightly larger than predicted by simple summation at high frequency. Because the high frequency phenomenon is associated with induced surface currents, it applies equally to the permeable and non-permeable cases.

IV. Conclusion

In this paper, the hybrid MAS and MAS-TSA is applied for multiple targets, to study electromagnetic interaction problem between highly conducting and permeable metallic objects. The accuracy of the method was tested against experimental data, and numerical tests were performed for combinations of two cylinders and spheres. The numerical method has a distinct advantage relative to popular integral equation

methods because sources of induced EM activity are located on surfaces shifted away from one another.

Overall, significant effects on far field EMI response caused by coupling of multiple objects are observed, depending on the objects' electromagnetic properties, distance between them, their geometries, and orientation of the primary magnetic field. The interaction between aligned permeable metallic cylinders is much stronger than between permeable spheres. Results for target combinations with mixed (non-permeable/ permeable) EM properties show the opposite trend, with the interaction between spheres slightly stronger than between cylinders. However the interaction effects between permeable and non-permeable bodies is slight in any case. Near field analyses have shown that, under axial excitation at low frequencies, the magnetic field is intensified only between permeable targets. Its amplitude increases greatly as the two objects approach each other. Ultimately this increases the magnetic moment of the two-object combination, relative to what would be predicted by simple superposition of responses. This is not the case for permeable/non-permeable combinations at low frequency. By contrast, for transverse excitation the scattered field between permeable objects opposes the primary field at low frequencies and reinforces it at high frequencies. Thus for the transverse case the opposite coupling trend is produced at low frequency, relative to axial excitation. Because high frequency coupling effects in the transverse case are due to induced surface currents, they appear for both permeable and non-permeable combinations. These examinations of near field distributions around the interacting objects show the physical mechanisms responsible for the evidence of coupling seen in the far field, for highly conducting and permeable metallic targets in EMI frequency range.

In future work we explore these effects more comprehensively, organizing them into a suitable basis for inversion or target discrimination.

V. Acknowledgment

This work was sponsored by the Strategic Environmental Research and Development Program and US Army CoE ERDC BT25 and AF25 programs.

References:

1. F. Shubitidze, K. O'Neill, S. A. Haider, K. Sun, and K. D. Paulsen, "Application of the method of auxiliary sources to the wideband electromagnetic induction problem", IEEE Transactions on Geoscience and Remote Sensing, Vol: 40 Issue: 4, Pages: 928-942, April 2002.
2. F. Shubitidze, K. O'Neill, K. Sun, and K. D. Paulsen, "Investigation of broadband electromagnetic induction scattering by highly conducting, permeable, arbitrarily shaped 3-D objects" IEEE Transactions on Geoscience and Remote Sensing, in press.
3. N. Khadr, B. J. Barrow, T. H. Bell, and H. H. Nelson. "Target shape classification using electromagnetic induction sensor data". UXO Forum on CD, 8 pages, 1998.
4. F. Shubitidze, K. O'Neill, K. Sun, I. Shamatava, and K. D. Paulsen "A combined MAS-TSA algorithm for broadband electromagnetic induction problems. See in this issue of ACES Proceedings". The 19th Annual Review of Progress in Applied Computational Electromagnetics, Pages: 566-572, March 24-28, 2003.
5. F. Shubitidze, K. O'Neill, I. Shamatava, K. Sun, and K. D. Paulsen "A Hybrid MAS-TSA algorithm for broadband electromagnetic induction problems. See in this issue of ACES Proceedings". Applied Computational Electromagnetics Society Journal, this issue.
6. J. R. Wait, "A conducting sphere in a time varying magnetic field". Geophysics Volume 16, Pages: 666-672, 1951.
7. I. Shamatava, K. O'Neill, F. Shubitidze, K. Sun, and C. O. Ao. "Evaluation of approximate Analytical Solutions for EMI Scattering from Finite Objects of Different Shapes and Properties", IEEE International Geoscience and Remote Sensing Symposium and 24th Canadian Symposium on Remote Sensing, Pages: 1550 –1552, July 2002.



Fridon Shubitidze received the degree of Diploma radio physicist (M.S) from the Sukhumi branch of Tbilisi State University, Republic of Georgia, in 1994 and Candidate of Sciences Ph.D degree in radio physics (applied electromagnetics) from its physics department, Tbilisi State University, Republic of Georgia, in 1997. Beginning in 1994 he was on the Research Staff of the Laboratory of

Applied Electrodynamics, Tbilisi State University, Department of Physics, Republic of Georgia. At the same time he joined department of physics and mathematics, Sukhumi branch of Tbilisi State University as a senior teacher and became Associate Professor there in 1998. From 1998 to 1999 he held a postdoctoral fellowship in National Technical University of Athens, Greece, performing research in connection with computer simulation of electrostatic discharge, electrodynamic aspects of EMC, numerical modeling of conformal antennas, electromagnetic wave scattering, field visualization and identification of objects by scattered field analysis, investigation of wave propagation through anisotropy, plasma and chiral media; and innovative numerical methods. He is currently working as Senior Research Associate at the Thayer School of Engineering, Dartmouth College, Hanover NH. His current work interests focus on numerical modeling of electromagnetic scattering by subsurface metallic objects.



Kevin O'Neill received the B.A. magna cum laude from Cornell University, followed by M.A., M.S.E., and Ph.D. degrees from Princeton University, Department of Civil Engineering. After an NSF postdoctoral fellowship at the Thayer School of Engineering at Dartmouth College and the U.S. Army Cold Regions Research and Engineering Laboratory (CRREL), he joined CRREL as a Research Civil

Engineer. His research has focused on numerical modeling of porous media transport phenomena and of geotechnically relevant electromagnetic problems. He has been a Visiting Fellow in the Department of Agronomy at Cornell University, continues since 1989 as a Visiting Scientist at the Center for Electromagnetic Theory and Applications at MIT, and since 1984 has been on the adjunct faculty of the Thayer School. Current work centers on electromagnetic remote sensing of surfaces, layers, and especially buried objects such as unexploded ordnance.



Irma Shamatava received the degree of Diploma radio physicist (M.S) from Sukhumi branch of Tbilisi State University, Republic of Georgia, in 1994. Since 1997, she has been on the Staff of the Computer center, Sukhumi branch of Tbilisi State University, Republic of Georgia. During the same period she

joined Department of Physics and Mathematics, as an assistant teacher. She is currently, working as researcher at the Thayer School

of Engineering, Dartmouth College, Hanover NH. Her research interests focus on analytical and numerical modeling of electromagnetic scattering by subsurface metallic objects.



Keli Sun received his B.S., M.S. and Ph.D. degrees in Computational and Biofluid Mechanics from the Department of Mechanics and Engineering Sciences, Peking University, Beijing, P. R. China, in 1991, 1994 and 1997 respectively. As an exchange student, he also worked in the school of Pure and Applied sciences, Tokyo University, Tokyo, Japan, from December 1995 to

December 1996, studying the mobility and mechanical properties of membrane proteins in living cells. After getting his Ph.D. degree in 1997, he worked on the faculty of Tsinghua University, Beijing, P.R. China performing research and teaching biomechanics. He obtained a second Master of Science degree in Computational Electromagnetics in May 2001 from the Thayer School of Engineering at Dartmouth College in Hanover, NH. Dr. Sun is currently employed as a Research Associate in the Numerical Methods Laboratory in the Thayer School furthering his research in Computational Electromagnetics and its applications in remote sensing.

Numerical Study of Coupling between Coagulators and Electrodes of Cardiac Pacemakers under Consideration of the Human Body

Markus Schick and Friedrich M. Landstorfer
Institut fuer Hochfrequenztechnik, Universitaet Stuttgart
Pfaffenwaldring 47,
70550 Stuttgart, Germany
Email: schick@ihf.uni-stuttgart.de

Abstract

The paper presents a numerical, worst-case study of the coupling between coagulators and cardiac pacemakers under consideration of the human body. For this purpose two special body models have been implemented. With these models whose electrical properties correspond to a weighted average of those of different tissues of the human body the influence of the latter can be taken into account in the computations. Different parameters such as position of the pacemaker and its electrode, coagulation frequency, and coagulation point on the surface of the human body are considered. Based on results of previous investigations simplified approaches to account for the dielectric coating of the coagulator electrode and housing of the pacemaker can be used. The investigation shows, that for the scenario described above, strong peaks occur in the resulting graphs arising from resonance effects on the coagulator cable.

Introduction

The increasing use of electronic devices in operating theatres and intensive-care units leads to possible interactions of such devices and consequently to serious immunity problems. Particularly critical are scenarios, where extremely small patient-related electrical signals are registered. These signals can be heavily influenced by currents in the tissue of the patient or by radiation coupling originating from

other devices acting on the patient. Cardiac pacemakers are implanted medical devices controlling the rhythm of the heartbeat and giving electrical stimulation to guarantee a steady pulse. By the influence of electromagnetic fields, a malfunction of the pacemaker might happen. Devices producing such disturbances are, for example, RF surgery devices. One of them is a coagulator. Measurements inside the human body are not feasible. For dealing with these EMC-problems, simulation models have to be developed and numerical computations have to be carried out, to determine the coupling effects between coagulators and cardiac pacemakers. A near field worst-case study of these effects considering the properties of the human body is described in the following.

Human Body Models

For this analysis, appropriate model for numerical calculations representing the influence of the human body has to be generated. In order to achieve results of general validity, different scenarios need to be considered within the numerical investigations. To limit the extent of memory requirements and computation time, it is necessary to perform the investigations with simplified models. For this examination, two models have been used. The first is called Hy26 and was developed following the measures given in DIN 33 402 part 2 ([1], [2]). It is a flattened body model including shoulders and head (see Fig. 1 left) representing a male per-

son between 41 and 60 years old. It consists of canonic structures and was especially developed for the field computation program used in this study: FEKO ([3], [6]).

FEKO is a field computation programme considering objects of arbitrary shape. It is based on a full wave solution of Maxwell's equations in the frequency domain. The accurate Method of Moments (MoM) formulation is used to solve for the unknown surface currents. Asymptotic techniques, Physical Optics (PO) and Uniform Theory of Diffraction (UTD), have been hybridised with the MoM in order to solve electrically large problems. The MoM has also been extended to solve problems involving multiple homogeneous dielectric bodies, thin dielectric sheets and dielectric coated wires.

The second model was converted from a CAD model, segmented for FEKO and is called Ergoman (see Fig. 1 right). It satisfies the same conditions as Hy26. The former is more flexible regarding changes in the modeling, the second has a more humanlike shape and has less corners and edges.

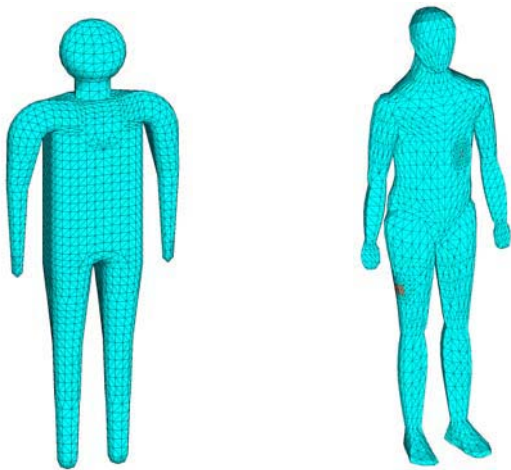


Fig. 1. Human body models Hy26 (left) an Ergoman (right).

Additionally the electrical properties of the human body have to be taken into account. As these models are homogeneous, weighted average values for the relative permittivity and the

conductivity of the tissues are used for modeling. Depending on frequency, the values for the single tissues (muscle tissue, bones, lungs, heart, stomach) are chosen according to [4] and [5] and weighted according to [7].

Coagulator

The coagulator is a RF-surgery device using high frequency currents e.g. for cutting tissues. But in contrast to a scalpel, the cut with a coagulator shows no bleeding as the egg white in the cells is coagulated by the current flowing and consequently seals the cells.

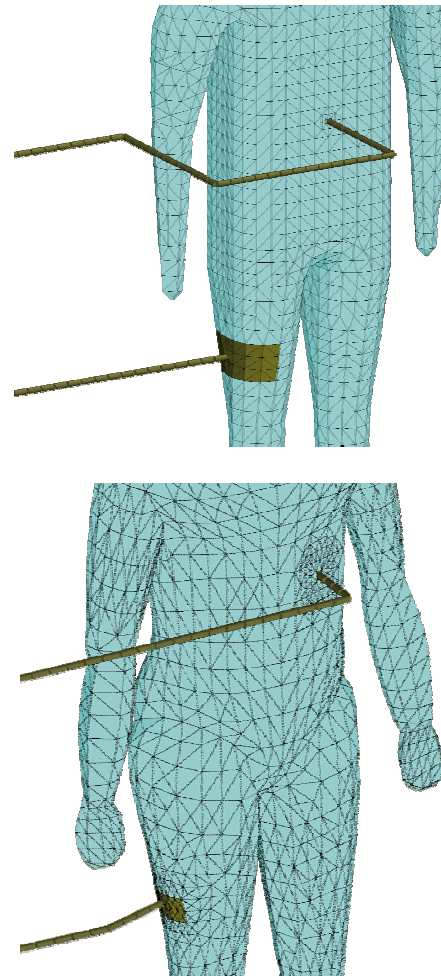


Fig. 2. Coagulation point in the chest area and position of the opposite electrode on the femoral.

The coagulator can be operated in two different modes, the monopolar and the bipolar mode. With the latter a pair of tweezers is used whose halves are identical with the two electrodes. Here the current flow is local in the human tissue. In case of the monopolar mode, a special shaped electrode is used for cutting, and a large opposite electrode is usually placed on the femoral (see Fig. 2). In this case the current flows from the coagulation point over the human body to the femoral. For investigating the worst-case input voltage at the input of the cardiac pacemaker the normally used monopolar mode is considered in this study, because of the large-scale distributed body currents created in this approach. With the bipolar mode only a very local current flow between the ends of the tweezers is to be expected, with hardly any influence on the pacemaker.

The length of the coagulator cable is chosen to 8.6 m with the voltage source placed 3.3 m after the coagulation point. The area of the neutral electrode on the body model is varied from 50 cm² to 180 cm² and is attached on the outer side of the femoral. Most of the cable routing is done in the y-z-plane on the right side of the body model.

Cardiac Pacemaker and Electrode

As a second object for consideration, a cardiac pacemaker is regarded in this study. It consists of a housing containing the electronic circuits for regulating the heard beat and an electrode leading the electrical signals to the heart. In a pre-investigation ([8]), the influence of different housings of the pacemaker was determined. In this study mentioned above a calculation method combining the Method of Moments (MoM) and the Multiple Multipole Method (MMP) was used to numerically determine the influence of electromagnetic waves on cardiac pacemakers in the frequency range from 50 MHz to 500 MHz. First a layered planar model was used. For taking body resonances into account, a 3-dimensional model of spheroidal shape was introduced. A realistic body

model for comparative measurements has been built up, and showed only small differences to the computation results. Several typical scenarios have been investigated and worst-case input voltages have been determined. For the cardiac pacemaker 2-dimensional and 3-dimensional models are taken into account as well as different geometrical shapes. Since all housings considered give nearly the same input voltage, a 2-dimensional model with a shape approximating a real pacemaker (see Fig. 3 down) is used in this study. For obtaining reliable results, it is mandatory to model the pacemaker's electrode appropriately and to take its insulation into account. The dimensions are 0.5 mm for the radius of the wire and 0.5 mm for the thickness of the insulation, which was assumed to consist of silicone, and, consequently, the conductivity and relative permittivity of the latter are used in the calculations.

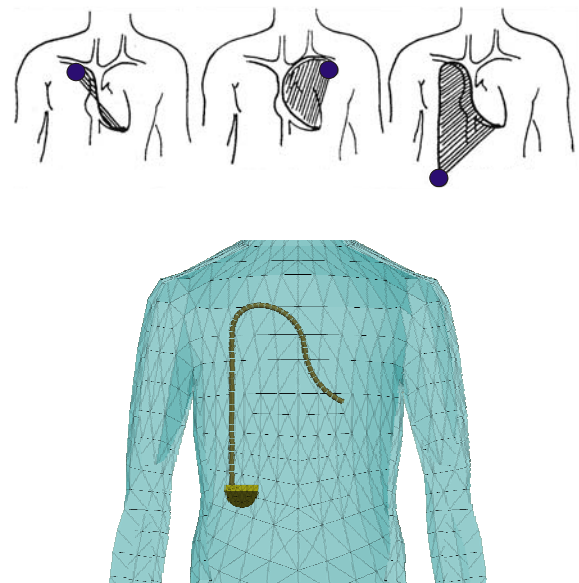


Fig. 3. Different positions for implanting a cardiac pacemaker (above) and model of the implanted cardiac pacemaker (below).

The resulting lengths of the electrodes in these three cases are 25.8 cm, for the pectoral case and 88.1 cm for the abdominal case, respec-

tively. The housing has a height of 3.5 cm and a width of 5 cm and is placed 6.5 cm inside the body model. Three different positions are usually used for implanting a cardiac pacemaker: right pectoral, left pectoral and abdominal (see Fig. 3 above). All three were taken into account in the examinations described below.

Examinations

To investigate interferences of coagulators with pacemakers, the following interference model (described in [8] and introduced in [9]) consisting of two sub-models is used. The sub-model “coupling” describes the relation between the interference source (coagulator) and auxiliary quantities such as e.g. the voltage at the electrode leading to the cardiac pacemaker. In this study this model is considered under worst-case assumptions. The sub-model “compatibility” describing the effect of the interference with the circuit of the pacemaker is not investigated here.

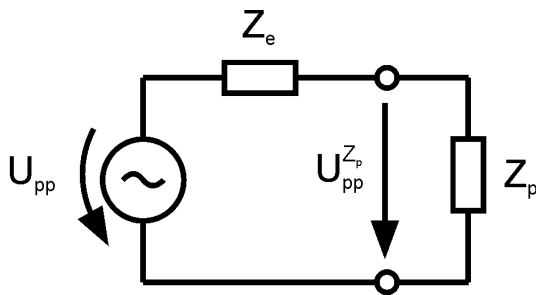


Fig. 4. Equivalent circuit diagram for the coupling model.

Figure 4 shows the equivalent circuit of the coupling model. The implanted pacemaker can be completely characterised by the complex internal impedance of the electrode Z_e and the input impedance of the pacemaker circuitry Z_p . To gain a more general validity of the coupling model, the (fictive) open circuit peak-to-peak voltage U_{pp} is determined (with $Z_p \rightarrow \infty$) in the computations.

The study deals with a typical application: coagulation in the chest area (e.g. cutting or sealing an artery). In the investigations the position of the pacemaker and the resulting lengths of the electrode, as well as frequency in the range from 100 kHz to 100 MHz, and the point of coagulation are varied. The input voltage on the electrode at the entrance of the cardiac pacemaker is calculated. To achieve values for the input voltage two computations are necessary. The first is to determine the current I_{el} in the ultimate element on the pacemaker’s electrode at the entrance of its housing when feeding the coagulator cable with a voltage source with $U_o = 1V$. The second computation is for determining the impedance Z_{el} of this very element. With these two values the voltage at the pacemaker’s entrance can then be calculated with $U_{in} = Z_{el} \cdot I_{el}$.

Results

As an example for the results obtained the voltage on the electrode at the input of the cardiac pacemaker for the model Hy26 is shown in Fig. 5 and for Ergoman in Fig. 6. In both cases the voltage for all three implantation positions are displayed. For both models the abdominal implantation leads to the highest values for the voltage at the entrance of the cardiac pacemaker. A comparison between the two models for abdominal implantation is shown in Fig. 7. Comparing the two curves it is obvious that the curves are similar for lower frequencies but differ much more for frequencies over 10 MHz, especially in the peaks that appear there. Ergoman has only one peak (62 MHz) compared to Hy26 with four peaks (26 MHz, 38 MHz, 56 MHz, 91 MHz).

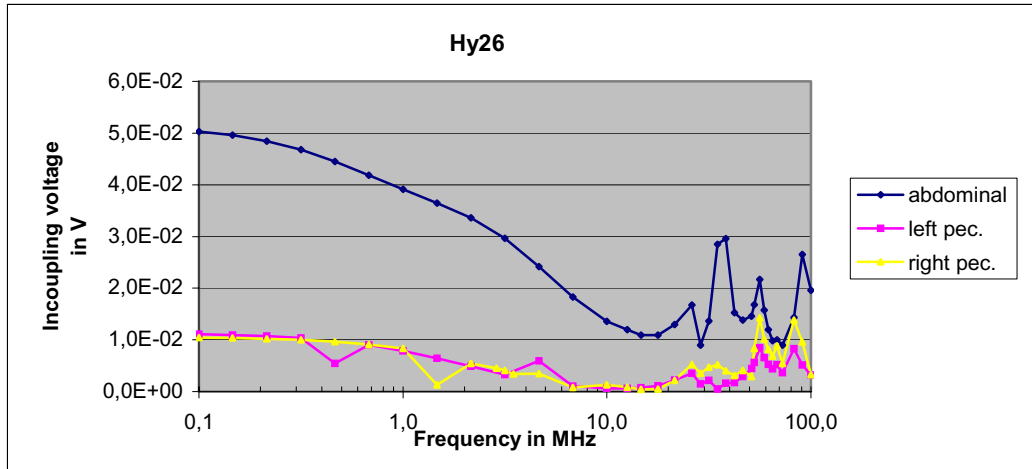


Fig. 5. Voltage on the electrode at the entrance of the pacemaker in V for the model Hy26.

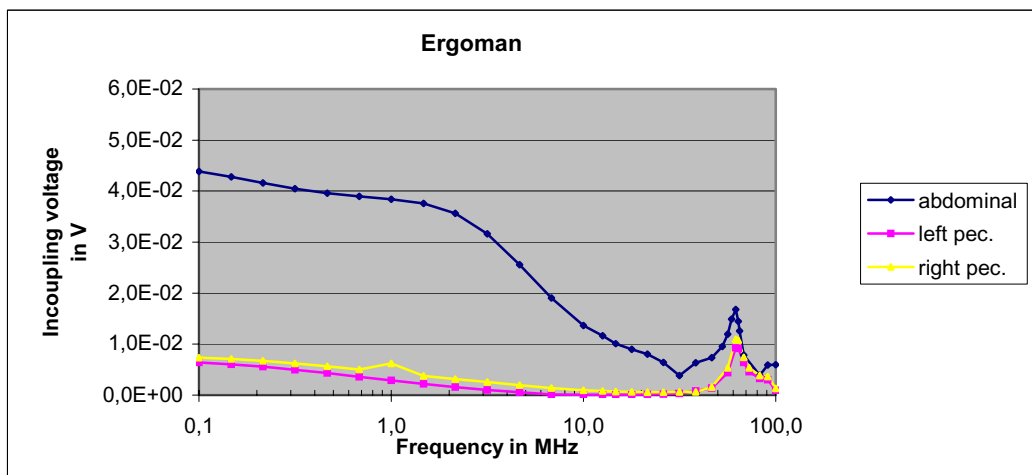


Fig. 6. Voltage on the electrode at the entrance of the pacemaker in V for the model Ergoman.

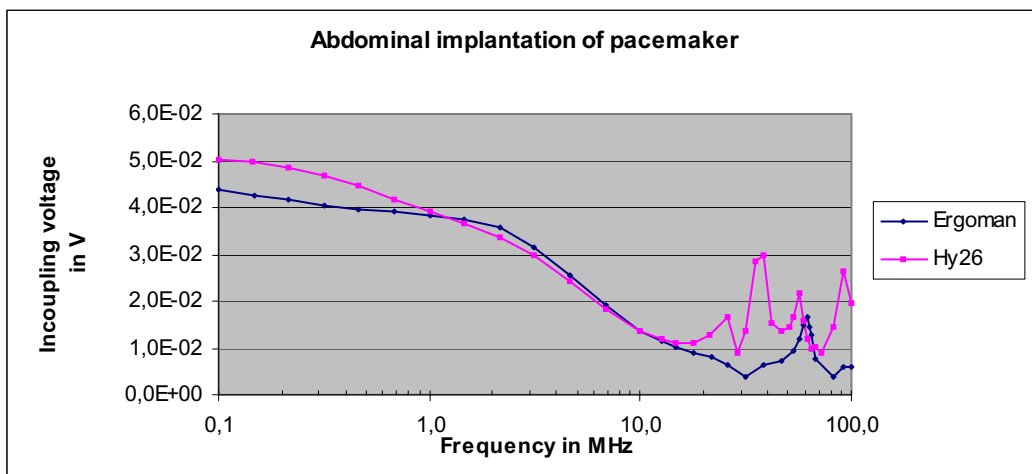


Fig. 7. Voltage on the electrode at the entrance of the pacemaker in V for abdominal implantation for both models.

One reason for these peaks is resonance effects on the coagulator cable. A relation between the resonant frequencies and the appertaining wavelengths, respectively, and the length of the cable can be determined. Variation of the cable length showed a very good agreement of the theoretical determined frequency corresponding to a wavelength resonance and the first resonance in the results for all the computed cable lengths. The size of the neutral electrodes area has almost no influence on the results. Also the variation of the coagulation point in the chest area showed no significant differences in the results.

The body model itself influences the magnitude of the voltages only but not their resonance frequencies. Resonances are taking place on the surface of the human body not inside, because of the strong attenuation of the tissue. The fact that the resulting curve of the model Hy26 has more peaks compared to that of Ergoman arises from the form of the model itself as it contains edges and corners due to adding parts of canonical structures. In contrast Ergoman has a more smoothed shape. The distances between these edges on the human body model are in the order of half a wavelength of the resonance frequencies observed in the graph.

The validation of the computational method is given in [8], where measurements were performed for comparison with the computational results and very good agreement was achieved.

Conclusions

A near field study is presented to determine the influence of a coagulator operated in monopolar mode in the presence of a cardiac pacemaker. Two human body models have been developed with corresponding electrical properties of human tissues. Different positions of pacemakers and points of coagulation are taken into account. Resonances can be found in the resulting curves and with comparing these they can be deduced from resonances on the coagulator cable.

Acknowledgement

The work for the paper was carried out within the scope of a project of the ‘Sonderforschungsbereich EMV’ of the ‘Deutsche Forschungsgemeinschaft (DFG)’. The authors would like to thank the DFG for supporting their work.

References

- [1] Deutsche Industrie Norm, *Körpermaße des Menschen; Werte*, DIN 33 402 Teil 2, S. 1–33, Okt. 1986.
- [2] Deutsche Industrie Norm, *Körpermaße des Menschen; Werte; Anwendung von Körpermaßen in der Praxis*, Beiblatt zu DIN 33 402 Teil 2, S. 1–5, Okt. 1984.
- [3] EM Software & Systems, *FEKO User's Manual, Suite 3.2.1*, March 2002, www.feko.co.za.
- [4] C. Gabriel, “Compilation of the Dielectric Properties of Body Tissues at RF and Microwave Frequencies,” Brooks Air Force Technical Report AL/OE-TR-1996-0037, Jun. 1996.
- [5] Italian National Research Council, Dielectric Properties of Body Tissues in the frequency range 10 Hz – 100 GHz, Electromagnetic Wave Research Institute, Florence Italy, Available at <http://safeemf.iroe.fi.cnr.it/tissprop/>.
- [6] U. Jakobus, “Erweiterte Momentenmethode zur Behandlung kompliziert aufgebauter und elektrischer großer elektromagnetischer Streuprobleme,” Dissertation, Nr. 171 in Fortschrittsberichte, Reihe 21, Düsseldorf: VDI Verlag, 1995.
- [7] J. G. Koritke and H. Sick, *Atlas of Sectional Human Anatomy*, Baltimore: Urban & Schwarzenberg, 1988.

- [8] F. Landstorfer et al., *Development of a model describing the coupling between electrodes of cardiac pacemakers and transmitting antennas in their close vicinity in the frequency range from 50 MHz to 500 MHz*, Study for the Forschungsgemeinschaft Funk e. V., Institut für Hochfrequenztechnik, Universität Stuttgart 1999.
- [9] M. Schick, "Numerical Study of Coupling between Coagulators and Electrodes of Cardiac Pacemakers," *Proceedings of the 31st European Microwave Conference EuMC 2001*, vol. 3, pp. 231–234, London, Sep. 2001.



Markus Schick was born in Düsseldorf, Germany in 1973. He received the Dipl.-Ing. degree in electrical engineering from the Universität Stuttgart, Germany, in 1998.

He is now a staff member of the Institut für Hochfrequenztechnik of the Universität Stuttgart, Germany. His main interest is in solving electromagnetic problems with the Method of Moments and hybrid methods, accelerating computations over large frequency ranges as well as dealing with electromagnetic compatibility problems especially in medical areas.



Friedrich M. Landstorfer (SM'79–F'95) was born in Munich, Germany, in 1940. He received the Dipl.-Ing. and the Dr. Ing. degrees in electrical engineering from the Technical University of Munich, Germany, in 1964 and 1967, respectively. In

1971, he became a Lecturer and in 1976 he became a Professor at the Technical University of Munich, Germany. In 1986 he moved to Stuttgart to become Professor and head of the RF-institute at the University of Stuttgart, Germany. His research interests include antennas, microwaves, electromagnetic theory, wave propagation in connection with mobile communication, navigation, and electromagnetic compatibility.

Dr. Landstorfer received the award of the NTG (Nachrichtentechnische Gesellschaft im VDE, now ITG) for the optimization of wire antennas in 1977 and was Chairman of the 21st European Microwave Conference in Stuttgart, Germany, in 1991. For eight years he headed the antenna group of the NTG/ITG and has been a member of URSI. He was awarded Honorary Professor of Jiaotong University in Chengdu, China, in 1993.

Correlation between the geometrical characteristics and dielectric polarizability of polyhedra

Ari Sihvola, Pasi Ylä-Oijala, Seppo Järvenpää, Juha Avelin

Electromagnetics Laboratory, Helsinki University of Technology
P.O. Box 3000, FIN-02015 HUT, Finland

Abstract

This article analyzes polarizability characteristics of the five regular polyhedra (tetrahedron, cube, octahedron, dodecahedron, and icosahedron) and sphere. In particular, the variation of the polarizabilities (polarizability is the amplitude of the static dipole moment caused by an incident electric field of unit amplitude) is correlated with various geometrical parameters of these Platonic solids: specific surface, number of edges, vertices, and faces, and the volumes of inscribed and circumscribed spheres. It is found that the polarizabilities of perfect electric conductor (PEC) and perfect electric insulator (PEI) objects are most strongly correlated with two different parameters: the radius ratio of circum- and inscribed spheres (PEC case) and the normalized radius of the inscribed sphere (PEI case).

a PEC (perfect electric conductor, $\epsilon_r = \infty$) and PEI (perfect electric insulator, $\epsilon_r = 0$) inclusions:

$$\alpha_{n,s,PEC} = 3, \quad \alpha_{n,s,PEI} = -3/2. \quad (4)$$

In this paper, we will focus on the polarizabilities of inclusions with certain special basic shapes: in addition to the sphere also the five Platonic polyhedra (tetrahedron, hexahedron (cube), octahedron, dodecahedron, and icosahedron) are under consideration. As reported in [3], we have conducted an extensive study of the static polarizabilities of these shapes, and numerical values for these polarizabilities are now available to an accuracy of the order of 10^{-5} . Based on the calculations of [3], the estimates in Table 1 have been found for the normalized polarizabilities of Platonic polyhedra of the PEC and PEI type. The calculations were made by solving the surface integral equation for the potential function with Method of Moments and third-order basis functions.

1 Introduction

When a dielectric inclusion is put into a homogeneous and static electric field, there will be a perturbation in the behavior of the field function in the vicinity of the inclusion. The strongest component of this “scattered” field is that due to a (static) electric dipole moment \mathbf{p} . This dipole field is proportional to the incident uniform field \mathbf{E} . The proportionality coefficient is called polarizability α :

$$\mathbf{p} = \alpha \mathbf{E}_e. \quad (1)$$

For example, for a dielectric sphere with volume V and permittivity ϵ , the polarizability is [1, 2]

$$\alpha_s = 3V\epsilon_0 \frac{\epsilon - \epsilon_0}{\epsilon + 2\epsilon_0} \quad (2)$$

where ϵ_0 is the free-space permittivity (the permittivity of the environment in which the inclusion is embedded). Let us define the normalized dimensionless polarizability by

$$\alpha_n = \frac{\alpha}{\epsilon_0 V} \quad (3)$$

whence it is $\alpha_{n,s} = 3(\epsilon_r - 1)/(\epsilon_r + 2)$ for a sphere with relative permittivity ϵ_r . The two extreme cases are

The numerical values of Table 1 tell that the polarizability amplitude values for the PEC and PEI cases are correlated: a “sharper” object, like the tetrahedron, has stronger polarizabilities (in both cases) than smoother ones, and the smoothest shape is obviously the sphere.¹ However, the amplitudes of these polarizabilities vary slightly differently in the two cases as can be seen in Figure 1, where they are plotted on the same PEC/PEI graph.

The aim in the present paper is to try to find correlation of the polarizability values with various geometrical characteristics of the polyhedra. The normalized polarizabilities for the limiting cases of PEC and PEI are correlated against several parameters which intuitively could be anticipated to have effect on the creation of the dipole moment. The geometrical parameters that are treated are the number of faces, edges, and vertices of the polyhedron, the solid angle subtended by the faces when looked inside from a vertex, the specific surface of the inclusion, as also various parameters connected with the spheres inscribed and circumscribed on the polyhedron. All these parameters vary from one polyhedron to another, and they can be thought as certain measures

¹In fact, sphere is an extremum shape which has the minimum polarizability, given the permittivity and volume of the inclusion. Any deviation from this form will increase, averaged over all directions, the dipole field [4].

of “non-sphericity” or “unsmoothness.” However, each of the parameters measure this abstract sharpness property in a different way. It is therefore very interesting to see which of the geometrical characteristic figures varies most similarly with the polarizabilities.

Although the connection between the polarizabilities of regular polyhedra and their basic geometrical characteristics is interesting from the general mathematical nature, the electric polarizabilities are very important also from the practical point of view in modeling of materials. In practically all models for the effective permittivity of inhomogeneous media, polarizability is the mostly determining parameter. For dilute mixtures, the effective permittivity is linearly dependent on it and for higher loadings of the inclusion phase, the effect of the polarizability becomes nonlinear and more pronounced.

The objects of the present study, polyhedra, are very natural forms. On microscopic scale, solid-state matter takes its shape in basic regular crystal forms which makes good reason and need for the results of polarizabilities of polyhedra. And even if on a larger scale matter may be disordered, polycrystal or even amorphous and isotropic, the microscopic objects retain the basic structure. Then also the polarizabilities of the basic forms are essential when modelling the macroscopic response of such matter.

Furthermore, the results for electric polarizabilities are readily available for magnetic modeling of materials. This is thanks to the duality between the electric and magnetic problems; hence the exact analogy between permittivity and permeability on one hand and the electric and magnetic polarizabilities on the other.

2 Calculation of the polarizabilities with the method of moments

Let us suppose that a dielectric inclusion is put into a uniform z -directed incident field $\mathbf{E}_e = E_e \mathbf{u}_z$. The corresponding electrostatic field problem can be formulated as an integral equation for the unknown surface potential function ϕ [5]:

$$\begin{aligned} \phi_e(\mathbf{r}) = & \frac{\tau + 1}{2} \phi(\mathbf{r}) + \\ & \frac{\tau - 1}{4\pi} \int_S \phi(\mathbf{r}') \frac{\partial}{\partial n'} \left(\frac{1}{|\mathbf{r} - \mathbf{r}'|} \right) dS', \\ & \mathbf{r} \text{ on } S. \end{aligned} \quad (5)$$

Here S is the surface of the inclusion, $\phi_e = -E_e z$ is the incident potential, $\tau = \epsilon_i/\epsilon_e$ is the ratio of the permit-

tivities of the inclusion and exterior, respectively, and \mathbf{n}' is the outward normal vector to the surface at point \mathbf{r}' .

Once the potential is known on the surface, the dipole moment \mathbf{p} can be calculated by

$$\mathbf{p} = -(\tau - 1)\epsilon_e \int_S \phi(\mathbf{r}) \mathbf{n}(\mathbf{r}) dS \quad (6)$$

and the polarizability α is obtained from (1).

The potential function that is needed in the estimation of the polarizability can be calculated by solving integral equation (5) with the method of moments (MoM) [6]. Let us suppose that the surface S is divided into planar triangular elements. Then the unknown potential ϕ is expressed as a linear combination of continuous high order polynomial basis functions $u_n^{(q)}$ defined on these elements [3]

$$\phi = \sum_{n=1}^N c_n u_n^{(q)}. \quad (7)$$

Here $q = 1, 2, \dots$, is the order of a basis function. Using Galerkin's method equation (5) is next multiplied by testing functions $u_m^{(q)}$, $m = 1, \dots, N$, and integrated over S . The resulting set of equations can be written as the following matrix equation

$$A c = b, \quad (8)$$

where $c = [c_1, \dots, c_N]^T$ is the unknown coefficient vector of ϕ .

Equation (5) is a Fredholm integral equation of the second kind with a weakly singular kernel. However, for non-smooth surfaces, like a tetrahedron or a cube, the order of the singularity of the kernel increases at the edges and corners. To improve the efficiency of the numerical algorithm, the integrals with singularities are evaluated in closed form. This method is based on the singularity extraction technique, originally introduced by Wilton et. al. [7] and Graglia [8] for linear basis functions, and more recently, generalized for high order polynomial basis functions in [9]. After the singular term is integrated analytically, the outer integral with respect to \mathbf{r} and the other terms are regular and can be evaluated by standard numerical methods, for example with Gaussian quadrature. The singularity extraction technique clearly improves the accuracy of the calculation of the near interaction terms of the system matrix, and thus, leads to a more stable algorithm than pure numerical integration. The method also improves the accuracy of the near-singular terms, not only the singular ones.

Other factors that effect to the accuracy of the solution are e.g. mesh density and type of the basis functions. Since the potential ϕ varies strongly near the corners of S [10], an appropriate refinement of the mesh, which takes into account the behavior of the potential at the edges and corners, usually increases the accuracy. A couple of mesh refinements were tested in [3] and it was found that a mesh with a square root refinement towards the edges gives the best results. Also higher order basis function representations improve the numerical accuracy. Both second and third order basis functions were tested in [3], and the third order ones gave better results.

As is already pointed out, equation (5) is a Fredholm integral equation of the second kind. When iterative solvers are applied to solve such equations, usually accurate results are obtained within a few iterations. This seems to be the case when the matrix equation (8) is solved iteratively with the restarted version of the GMRES method [11] and τ is small. However, for high $\tau > 100$, the convergence dramatically slows down and in some cases the method does not converge at all. The reason is that equation (5) does not have a unique solution if the inclusion is PEC, i.e., if $\tau = \infty$. This non-uniqueness problem can be avoided, for example, by adding a constant value $1/N$ to each element of the matrix A [12]. Numerical experiments have demonstrated that by this simple modification the convergence can be essentially improved for inclusions with high τ values.

3 Polarizabilities and characteristic figures

Let us next list and define several geometrical parameters that could be interpreted as an abstract distance from sphericalness. For all five polyhedra and the sphere, these are correlated against each other in the figures to follow. Since there are five polyhedra, there are six points in the figures.

Table 2 gives various fundamental geometrical characteristics of the regular polyhedra. These are the number of faces, edges, and vertices. One further measure is the ‘‘sharpness’’ of the vertex, defined by the solid angle which is bounded by the faces when one looks into the polyhedron.² Note that on the table, sphere is also taken to be a special case of a Platonic polyhedron, having an infinite number of faces, edges, and vertices. Also, for

²There are different ways to calculate the vertex solid angle. Perhaps the most elegant is the following (Girard’s theorem): given the dihedral angles between the faces, the solid angle is the excess angle of the sum of the dihedral angles over the corresponding planar polygon angle-sum. This property is used in Table 2.

the sphere, the solid angle seen from the vertex (that is, on any point on the surface of the sphere) is obviously half of the total solid angle, $4\pi/2 = 2\pi$.

Table 3 collects some other, more indirect, geometrical parameters of the polyhedra. The edge length a of each of the polyhedra is normalized such that the volume is unity. The parameters are

- the specific surface of the polyhedron, defined as the area of the surface of the object when its volume is unity (e.g., for a cube, edge length $a = 1$ gives unit volume, meaning that the surface is $6a^2 = 6$),
- the ratio of the radii of the circumscribed sphere R_{circ} and the inscribed sphere r_{in} ,
- the normalized equivalent radii of the circumscribed and inscribed spheres, g_{circ} and g_{in} . These two equivalent radii are defined with the volumes of the circum- and inscribed spheres with

$$g_{\text{circ}} = \left(\frac{V_{\text{circ}}}{V} \right)^{1/3}, \quad g_{\text{in}} = \left(\frac{V}{V_{\text{in}}} \right)^{1/3} \quad (9)$$

where V is the volume of the given polyhedron. Note that both are defined to be larger than unity.

It is tempting to predict that the polarizabilities of the various polyhedra follow the pattern of these characteristic parameters that measure how ‘‘nonspherical’’ or ‘‘sharp-formed’’ the polyhedra are. Let us try to make a graphical and quantitative estimation of this correlation.

In Figures 2–5, the geometrical parameters are plotted against the PEC and PEI polarizabilities of the objects.

A numerical measure for the correlation between two sets of parameter variables is the correlation coefficient ρ , defined by the following [13]:

$$\rho = \frac{\frac{1}{6} \sum_{i=1}^6 (x_i - m_x)(y_i - m_y)}{\sqrt{\frac{1}{6} \sum_{i=1}^6 (x_i - m_x)^2 \cdot \frac{1}{6} \sum_{i=1}^6 (y_i - m_y)^2}} \quad (10)$$

where the six cases (five polyhedra and the sphere) are all included in the summation. The two variables, x and

y (with arithmetic means m_x and m_y) represent any pair of the polarizabilities and the characteristic geometrical parameters listed above.

The correlation coefficients between the parameters are collected in Tables 4 and 5.

4 Conclusions

The trivial hypothesis that both polarizabilities (PEC and PEI) correlate with the geometrical “sharpness” parameters of the polyhedra is obviously confirmed by the constellation of points in Figures 2–5 and even more by the correlation numbers.³ But certainly also more non-trivial conclusions can be drawn from the above results.

Firstly, it is conspicuous that the PEC and PEI polarizabilities behave differently (although the correlation coefficient between them is numerically quite high, 0.9901, as shown in Figure 1). The difference reflects the fact that there are various mechanisms that are causing the dipole moment creation, and therefore also the geometry and its parameters stand in different relation to the polarizabilities in the two cases.

It seems that the polarizability of the PEI sphere correlates more strongly with some of the geometrical parameters than the polarizability of the PEC sphere (in average, the correlation coefficients are higher for the PEI plots). We can observe that the strongest correlation exists between the normalized inradius g_{in} and the PEI polarizability of the objects ($\rho = 0.9977$), and also the PEI polarizability correlates quite well with the specific surface of the object ($\rho = 0.9957$). On the other hand, the best correlation of PEC polarizability is with the circumscribed–inscribed sphere radius ratio ($\rho = 0.9953$), the other good correlation being with the inverse of the solid angle seen from the vertex of the object ($\rho = 0.9937$).

It may be difficult to find hard physics from statistical numbers. However, some qualitative, yet significant, observations can be made. First, it is perhaps not totally foolish to connect the solid angle of the vertex of a polyhedron with the polarizability of a perfectly conducting object. In terms of a dielectric polarizability, the contrast between the object and the environment is extreme in such case. On a sharp vertex, charge is concentrated.⁴

³To be sure, not all geometrical parameters fall in the same order as the polarizabilities. The increasing behavior of the six points is not strictly monotonous in some of the plots. The sharpness of the vertices is one example: icosahedron has sharper corners (smaller solid angle) than dodecahedron, even it is more “spherical” in most other respects; the same goes for octahedron and hexahedron (the solid angle of the vertex of the octahedron is smaller than in a cube).

⁴The field components and the charge density vary as $r^{\nu-1}$ with r being the distance from a conical conducting corner. For sharp corners, ν is close to zero [1, Section 3.4], and the dependence is quite singular.

Hence the polarizability increases in the PEC case as the vertex solid angle decreases. On the other hand, in the PEI case the situation is the opposite: the external side of the polyhedron is “more conducting” and again the contrast is infinite. But the convex form of the polyhedra does not allow any sharp corners into the object. In the PEI case, then the properties of the inscribed sphere, rather than the sharpness of the vertices, are more essential parameters with respect to the polarizability.

Acknowledgments. A.S. acknowledges discussions with Dr. Matthys Botha and Dipl.-Eng. Markus Schick during the ACES Conference (Monterey, March 2003).

References

- [1] J.D. Jackson, *Classical Electrodynamics*, Third Edition, John Wiley, New York, 1999.
- [2] A. Sihvola, *Electromagnetic Mixing Formulas and Applications*, IEE Publishing, Electromagnetic Wave Series 47, London, 1999.
- [3] A. Sihvola, P. Ylä-Oijala, S. Järvenpää, J. Avelin: Polarizabilities of Platonic solids. To appear in *IEEE Transactions on Antennas and Propagation*, 2004.
- [4] M. Schiffer and G. Szegő: Virtual mass and polarization, *Transactions of the American Mathematical Society*, Vol. 67, pp. 130-205, 1949.
- [5] J. Van Bladel: *Electromagnetic Fields*, New York, Hemisphere Publishing Corporation, 1985. Revised edition.
- [6] R. F. Harrington: *Field Computation by Moment Methods*, Macmillan, New York, 1968.
- [7] D. R. Wilton, S. M. Rao, A. W. Glisson, D. H. Schaubert, O. M. Al-Bundak and C. M. Butler: Potential integrals for uniform and linear source distributions on polygonal and polyhedral domains. *IEEE Transactions on Antennas and Propagation*, Vol. 32, pp. 276-281, March 1984.
- [8] R. D. Graglia, On the numerical integration of the linear shape functions times the 3-D Green’s function or its gradient on a plane triangle: *IEEE Transactions on Antennas and Propagation*, Vol. 41, pp. 1448-1455, October 1993.

- [9] S. Järvenpää, M. Taskinen and P. Ylä-Oijala, Singularity extraction technique for integral equation methods with higher order basis functions on plane triangles and tetrahedra: *International Journal for Numerical Methods in Engineering*, Vol. 58, pp. 1149-1165, 2003.
- [10] J. Avelin, R. Sharma, I. Hänninen, and A. H. Sihvola: Polarizability analysis of cubical and square-shaped dielectric scatterers: *IEEE Transactions on Antennas and Propagation*, Vol. 49, No. 3, pp. 451-457, March 2001.
- [11] Y. Saad and M. H. Schultz: GMRES: a generalized minimal residual algorithm for solving non-symmetric linear systems, *SIAM Journal of Scientific and Statistical Computing*, Vol. 7, pp. 856-869, 1986.
- [12] M. S. Hämäläinen and J. Sarvas: Realistic conductivity geometry model of the human head for interpretation of neuromagnetic data, *IEEE Transactions on Biomedical Engineering*, Vol. 36, No. 2, February 1989.
- [13] L. Råde and B. Westergren: *Mathematics Handbook for science and engineering*, Studentlitteratur, Lund, 1995.

Bio-sketches

Ari Sihvola is professor of electromagnetics at Helsinki University of Technology (HUT), Espoo, Finland. He

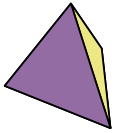
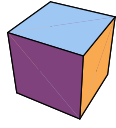
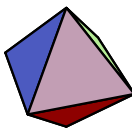
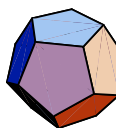

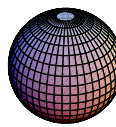
received the degree of Doctor of Technology from HUT in 1987, and has been a visiting scientist and professor at the Massachusetts Institute of Technology (1985–1986), the Pennsylvania State University (1990-1991), Lund University (1996), and the Swiss Federal Institute of Technology, Lausanne (2000–2001). Ari Sihvola is vice-chairman of the Finnish National Committee of URSI (the International Union of Radio Science).

Pasi Ylä-Oijala received the M.Sc. degree in 1992 and the Ph.D. degree in 1999, both in applied mathematics in the University of Helsinki, Finland. Since October 2002 he has been working as a researcher in Electromagnetics Laboratory, Helsinki University of Technology, Finland. His field of interest includes numerical techniques in computational electromagnetics based on the integral equation methods.

Seppo Järvenpää was born in 1965 received the M.Sc. degree in 1992 and the Ph.D degree in 2001, both in applied mathematics in the University of Helsinki, Finland. Currently he is working as a researcher in the Electromagnetics Laboratory at Helsinki University of Technology. His field of interest include numerical techniques in computational electromagnetics based on finite element and integral equation methods.

Juha Avelin received the degree of Diploma Engineer in 1999, in Electrical Engineering, from Helsinki University of Technology. He is now working as researcher in the Electromagnetics laboratory of HUT. His current research interests are homogenization of mixtures and canonical problems in electromagnetics.

Table 1: Limiting values ($\epsilon_r \rightarrow \infty$, PEC; and $\epsilon_r \rightarrow 0$, PEI) for the normalized polarizabilities $\alpha_n = \alpha/(\epsilon_e V)$ of regular polyhedra. Best numerical results according to [3]. The accuracy is such that the last number in the results for polyhedra should be correct to ± 1 , except for tetrahedron in which case it is ± 5 .

	<i>polyhedron</i>	$\alpha_n(\epsilon_r = \infty)$, PEC	$\alpha_n(\epsilon_r = 0)$, PEI
	tetrahedron	5.0285	-1.8063
	hexahedron	3.6442	-1.6383
	octahedron	3.5507	-1.5871
	dodecahedron	3.1779	-1.5422
	icosahedron	3.1304	-1.5236
	sphere	3	-3/2

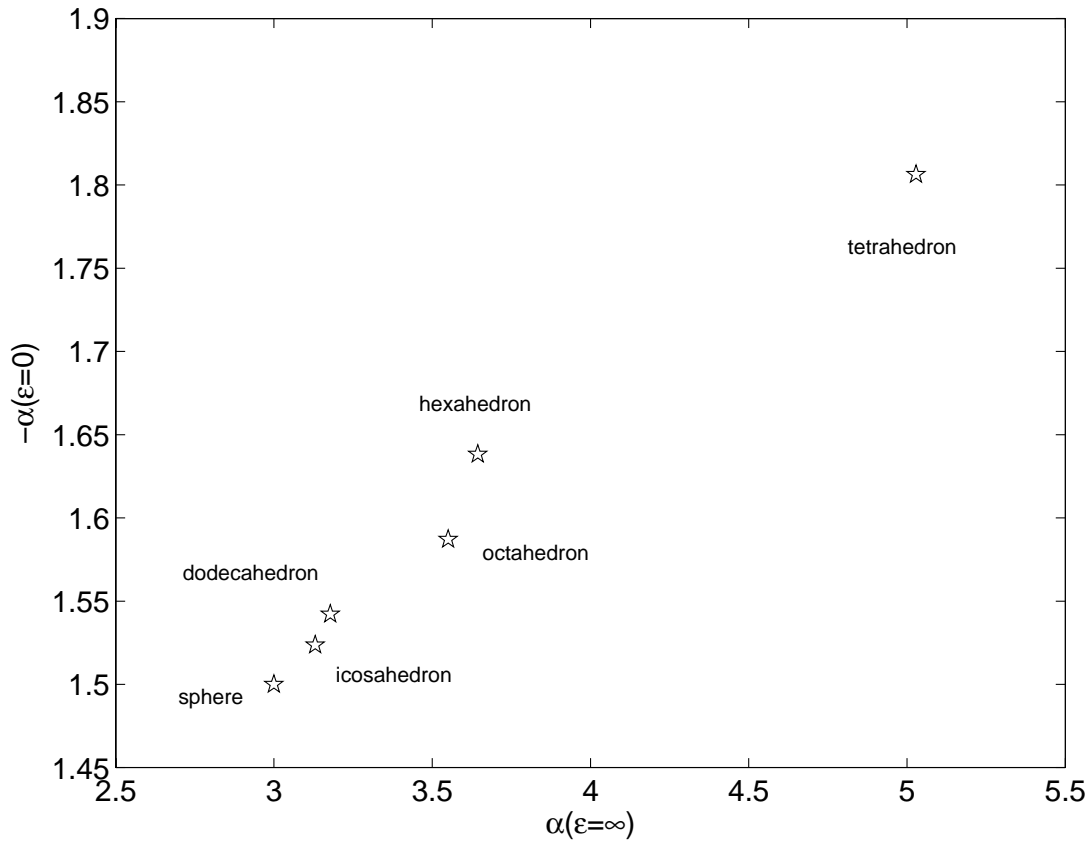


Figure 1: The polarizabilities of PEC and PEI inclusions against each other. The correlation coefficient of these two variables is 0.9901, meaning that the polarizabilities behave slightly differently for different polyhedra.

Table 2: Geometrical characteristics of polyhedra, with the corresponding parameters for a sphere.

<i>polyhedron</i>	faces	edges	vertices	solid angle seen from the vertex
tetrahedron	4	6	4	$3 \arccos(1/3) - \pi \approx 0.55129$
hexahedron	6	12	8	$3\pi/2 - \pi \approx 1.5708$
octahedron	8	12	6	$4 \arccos(-1/3) - 2\pi \approx 1.3593$
dodecahedron	12	30	20	$3 \arccos(-1/\sqrt{5}) - \pi \approx 2.9617$
icosahedron	20	30	12	$5 \arccos(-\sqrt{5}/3) - 3\pi \approx 2.6345$
sphere	∞	∞	∞	$2\pi \approx 6.2832$

Table 3: Additional geometric characteristics of polyhedra and the sphere. Note that the parameter a is the edge length (for the polyhedra) and radius (for the sphere) chosen with the requirement that the volume of the object be unity.

<i>polyhedron</i>	$a(V = 1)$	specific surface	$R_{\text{circ}}/r_{\text{in}}$	g_{circ}	g_{in}
tetrahedron	2.039	7.20562	3	1.9359	1.5497
hexahedron	1	6.000	1.7321	1.3960	1.2407
octahedron	1.2849	5.71911	1.7321	1.4646	1.1826
dodecahedron	0.50722	5.31161	1.2584	1.1457	1.0984
icosahedron	0.771025	5.14835	1.2584	1.1821	1.0646
sphere	0.62035	4.83598	1	1	1

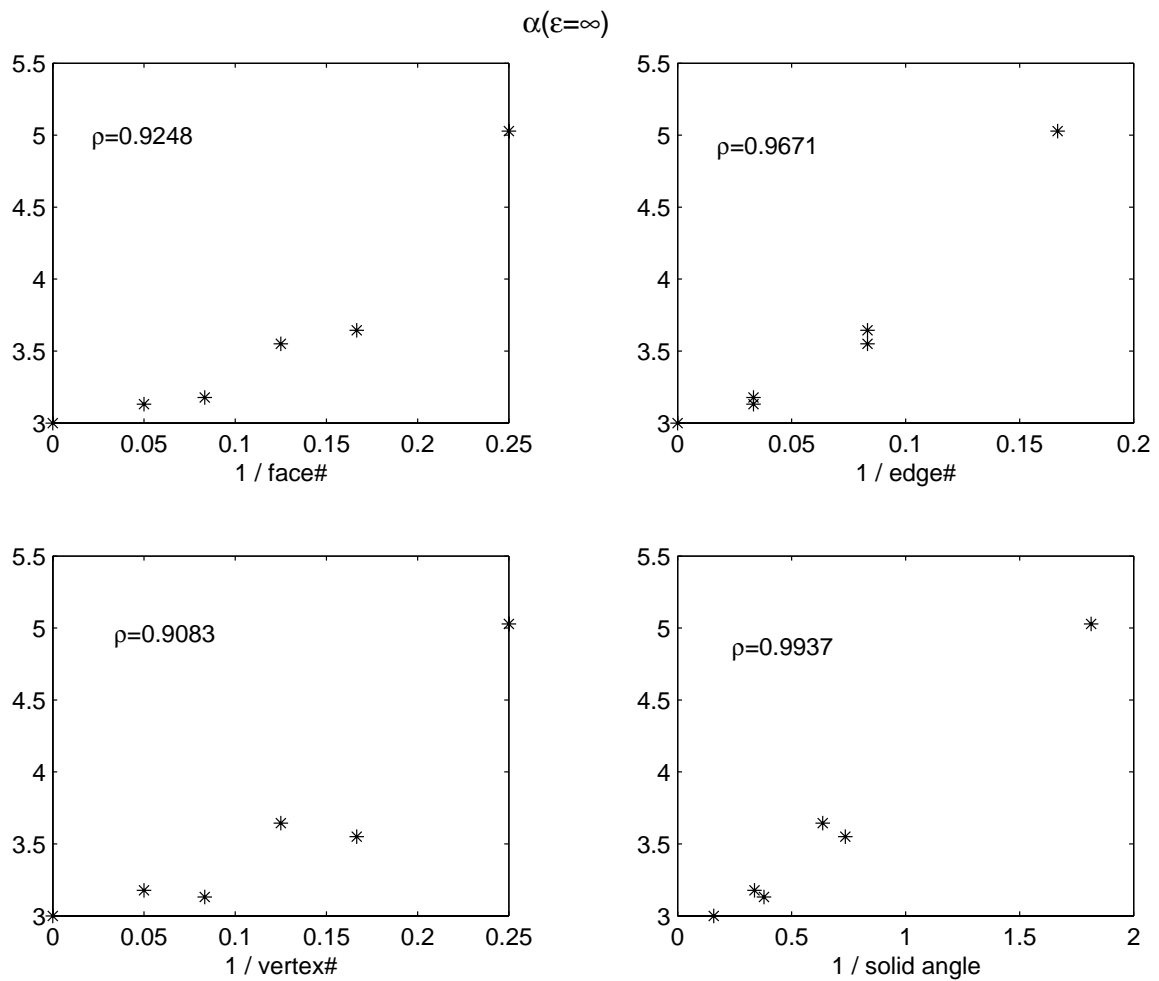


Figure 2: The polarizability of PEC inclusions and the geometrical parameters of Table 2.

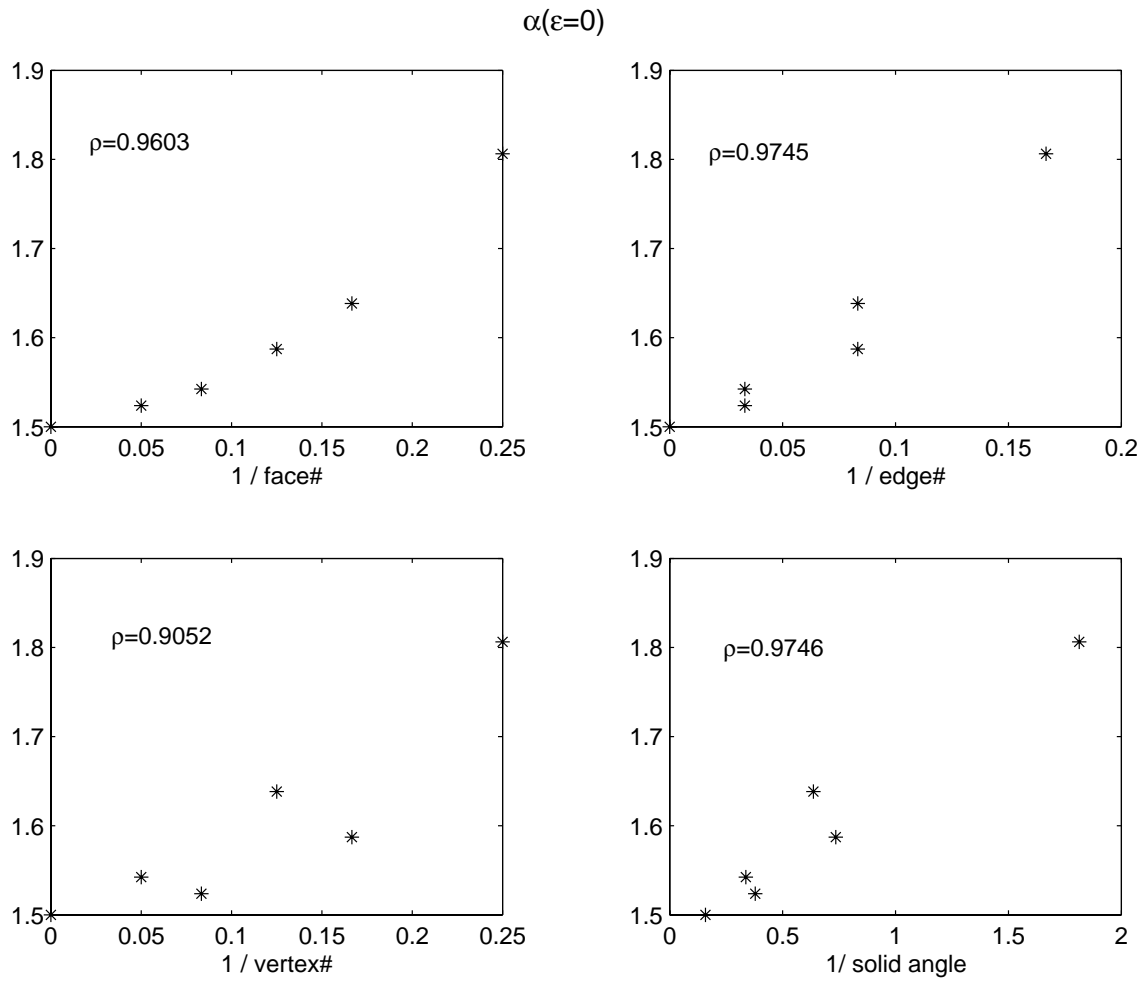


Figure 3: The polarizability of PEI inclusions and the geometrical parameters of Table 2.

Table 4: The correlation coefficients between the PEC and PEI polarizabilities with the geometrical parameters in Table 2.

	$\alpha(\epsilon = \infty)$	$-\alpha(\epsilon = 0)$	$1/\text{face\#}$	$1/\text{edge\#}$	$1/\text{vertex\#}$	$1/\text{solid angle}$
$\alpha(\epsilon = \infty)$	1.0000	0.9901	0.9248	0.9671	0.9083	0.9937
$-\alpha(\epsilon = 0)$	0.9901	1.0000	0.9603	0.9745	0.9052	0.9746
$1/\text{face\#}$	0.9248	0.9603	1.0000	0.9756	0.9278	0.9150
$1/\text{edge\#}$	0.9671	0.9745	0.9756	1.0000	0.9756	0.9724
$1/\text{vertex\#}$	0.9083	0.9052	0.9278	0.9756	1.0000	0.9359
$1/\text{solid angle}$	0.9937	0.9746	0.9150	0.9724	0.9359	1.0000

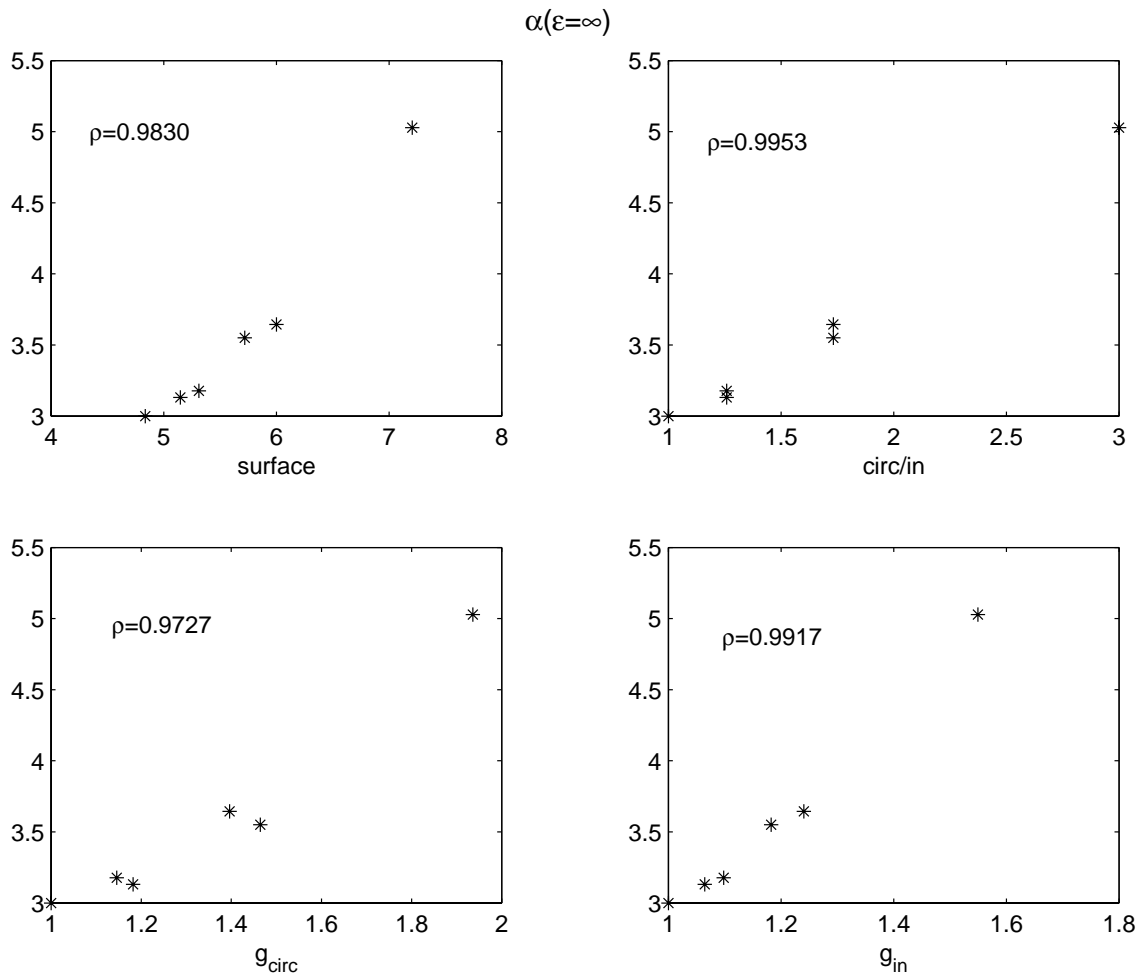


Figure 4: The polarizability of PEC inclusions and the geometrical parameters of Table 3.

Table 5: The correlation coefficients between the PEC and PEI polarizabilities with the geometrical parameters in Table 3.

	$\alpha(\epsilon = \infty)$	$-\alpha(\epsilon = 0)$	surface	$R_{\text{circ}}/r_{\text{in}}$	g_{circ}	g_{in}
$\alpha(\epsilon = \infty)$	1.0000	0.9901	0.9830	0.9953	0.9727	0.9917
$-\alpha(\epsilon = 0)$	0.9901	1.0000	0.9957	0.9878	0.9677	0.9977
surface	0.9830	0.9957	1.0000	0.9892	0.9802	0.9982
$R_{\text{circ}}/r_{\text{in}}$	0.9953	0.9878	0.9892	1.0000	0.9904	0.9938
g_{circ}	0.9727	0.9677	0.9802	0.9904	1.0000	0.9789
g_{in}	0.9917	0.9977	0.9982	0.9938	0.9789	1.0000

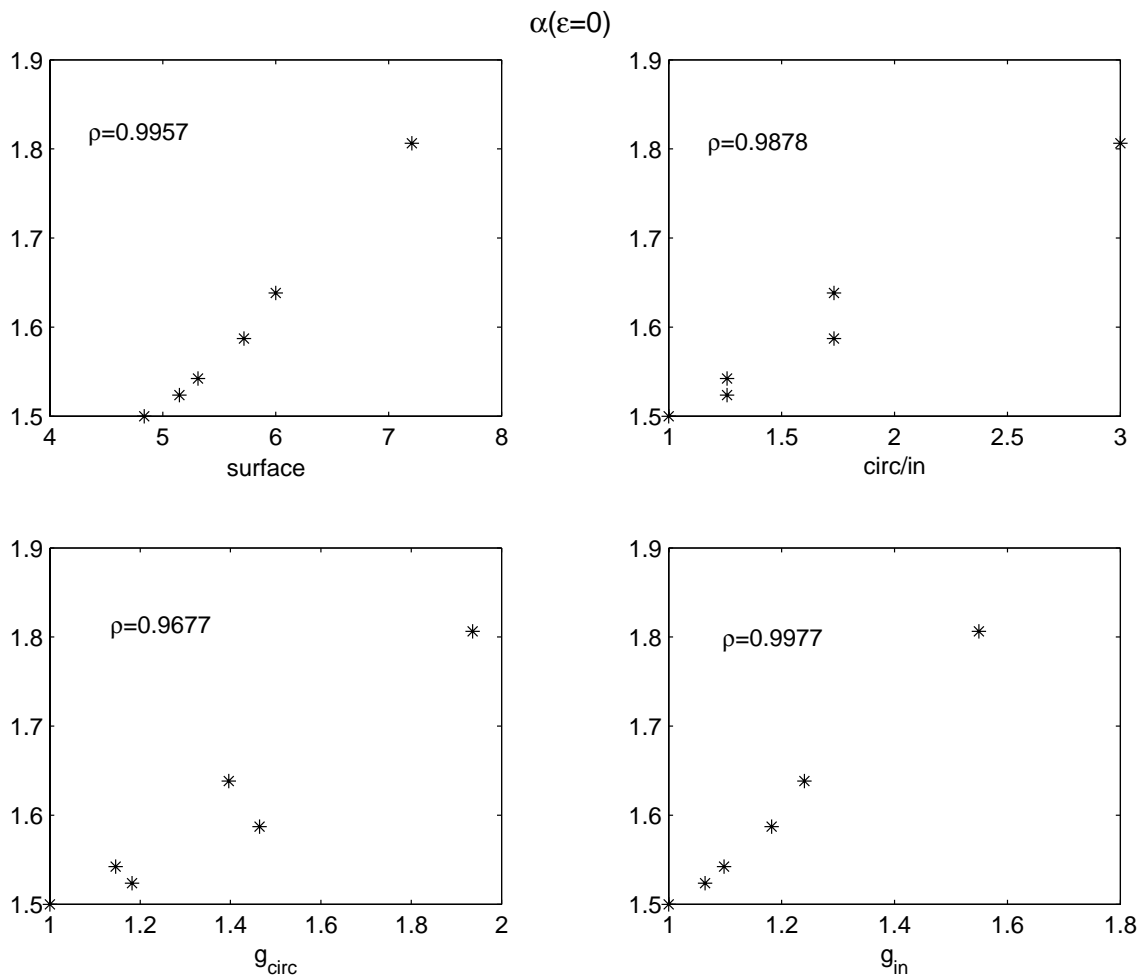


Figure 5: The polarizability of PEI inclusions and the geometrical parameters of Table 3.

2004 INSTITUTIONAL MEMBERS

AUSTRALIAN DEFENCE LIBRARY
Northcott Drive
Campbell, A.C.T. 2600 AUSTRALIA

EM SOFTWARE & SYSTEMS
PO Box 1354
Stellenbosch, S. AFRICA 7599

IIT RESEARCH INSTITUTE
185 Admiral Cochrane Drive
Annapolis, MD 21401-7396

BAE SOWERBY RESEARCH CTR.
FPC 267 Po Box 5
Filton, Bristol, BS134 7QW
UNITED KINGDOM

ENGINEERING INFORMATION, INC
PO Box 543
Amsterdam, Netherlands 1000 Am

IND CANTABRIA
PO Box 830470
Birmingham, AL 35283

BAE SYSTEMS
W423A, Warton Aerodrome
Preston, PR41AY
UNITED KINGDOM

ERA TECHNOLOGY, LTD
Cleeve Rd
Leatherhead, Surrey, UK OX5 1JE

INSTITUTE FOR SCIENTIFIC INFO.
Publication Processing Dept.
3501 Market St.
Philadelphia, PA 19104-3302

BAE SYSTEMS, ADV. TECH. CTR
W. Hanningfield Rd, Tech Centre Lib.
Gt. Baddow, Chelms., CM2 8HN UK

ETSE TELECOMUNICACION
Biblioteca, Campus Lagoas
Vigo, 36200 SPAIN

INSYS LTD.
Reddings Wood, Ampthill
Bedford, MK45 2HD UK

BEIJING BOOK COMPANY, INC
701 E Lindon Ave.
Linden, NJ 07036-2495

FANFIELD LTD
Braxted Park
Witham, Essex, CM8 3XB UK

IPS RADIO & SPACE SVC/LIBRARY
PO Box 5606
W. Chatswood, 2057 AUSTRALIA

BIBLIO. FACOLTA' INGEGNERIA
Lib: Dott. Gaetana Bocc. Fiandra
Via G Duranti
Perugia, ITALY 89-06125

FLORIDA INTERNATIONAL U.
10555 W. Flagler St.
ECE Dept., EAS-3983
Miami, FL 33174

LIBRARY of CONGRESS
Reg. Of Copyrights
Attn: 40T Deposits
Washington DC, 20559

CULHAM EM
Bldg F5, Culham
Abingdon, Oxford, OX14 3ED UK

GEORGIA TECH LIBRARY
225 North Avenue, NW
Atlanta, GA 30332-0001

LINDA HALL LIBRARY
5109 Cherry Street
Kansas City, MO 64110-2498

DARTMOUTH COLL-FELDBERG LIB
6193 Murdough Center
Hanover, NH 03755-3560

HANGANG UNIVERSITY / IS LIB.
17 Haengdang-Dong, Seongdong KU
Seoul, S KOREA 133-791

MAAS
16 Peachfield Road
Great Malvern, Worc.
WR 14 4AP UNITED KINGDOM

DEFENCE RESEARCH ESTAB. LIB.
3701 Carling Avenue
Ottawa, ON, K1A 0Z4 CANADA

HELSINKI UNIV. OF TECHNOLOGY
Otakaari 5-A
PO Box 3000
Espoo, FINLAND 02015 HUT

MISSISSIPPI STATE UNIV LIBRARY
PO Box 9570
Mississippi State, MS 39762

DTIC-OCP/IBRARY
8725 John J. Kingman Rd. Ste 0944
Ft. Belvoir, VA 22060-6218

HEWLETT PACKARD
14012 NE 47TH Avenue
Vancouver, WA 98686

MIT LINCOLN LABORATORY
Periodicals Library
244 Wood Street
Lexington, MA 02420

EDINBURGH DSTO
PO Box 830673
Birmingham, AL 35283-0673

HRL LABS, RESEARCH LIBRARY
3011 Malibu Canyon
Malibu, CA 90265

NA KANSAI KINOKUNNA CO.
Attn: M. MIYOSHI
PO Box 36 (NDLA KANSAI)
Hongo, Tokyo, JAPAN 113-8688

ELEC. COMM. LAB LIBRARY
Hikarinooka Yokosuka Shi
Kanagawa-Ken
239-0847 MZ JAPAN

IEE INSPEC
Acquisitions Section
Michael Faraday House
6 Hills Way
Stevenage, Herts UK SG1 2AY

NATIONAL INSTITUTE OF AIST
AIST Tsukuba Central 2-1-1-1
Umezono
Tsukuba-Shi, Ibariki
305-8568 JAPAN

NATL RADIOLOGICAL PROT. BD.
Chilton, Didcot, OXON,
OX11 0RG UK

RENTON TECH LIBRARY/BOEING
PO BOX 3707
SEATTLE, WA 98124-2207

UNIV OF CENTRAL FLORIDA LIB.
PO Box 162666
Orlando, FL 32816-2440

NAVAL POSTGRADUATE SCHOOL
Attn: J. Rozdal
411 Dyer Rd./ Rm 111
Monterey, CA 93943-5101

SOUTHWEST RESEARCH INST.
6220 Culebra Road
San Antonio, TX 78238

UNIV OF COLORADO LIBRARY
Campus Box 184
Boulder, CO 80309-0184

NAVAL RESEARCH LABORATORY
C. Office, 4555 Overlook Avenue, SW
Washington, DC 20375

SWETS BLACKWELL
440 Creamery Way, Suite A
Exton, PA 19341

UNIVERSITY OF MISSISSIPPI
John Davis Williams Library
PO Box 1848
University, MS 38677-1848

OVIEDO LIBRARY
LRC 04440
PO Box 830679
Birmingham, AL 35283

TAMKANG UNIVERSITY
PO Box 380470
Birmingham, AL 35283

UNIV OF MISSOURI-ROLLA LIB.
1870 Miner Circle
Rolla, MO 65409-0001

PENN STATE UNIVERSITY
126 Paterno Library
University Park, PA 16802-1808

TECHNISCHE UNIV. DELFT
Mekelweg 4, Delft, Holland, 2628 CD
NETHERLANDS

USAE ENG. RES. & DEV. CENTER
Attn: Library/Journals
72 Lyme Road
Hanover, NH 03755-1290

PHILIPS RESEARCH LAB LIBRARY
Cross Oak Lane, Salfords
Redhill, RH1 5HA SURREY UK

TIB & UNIV. BIB. HANNOVER
DE/5100/G1/0001
Welfengarten 1B
Hannover, GERMANY 30167

RUBENS VALERIO
2129 Flatbush Ave., #4000
Brooklyn, NY 11234-4336

QUEEN MARY & WESTFIELD
COLLEGE
Mile End Rd.
London E1 4NS UK

TOKYO KOKA UNIV
1404-1 Katakura-Cho
Hachioji, Tokyo, JAPAN 192-0914

VECTOR FIELDS, LTD
24 Bankside
Kidlington, Oxford OX51JE

ACES COPYRIGHT FORM

This form is intended for original, previously unpublished manuscripts submitted to ACES periodicals and conference publications. The signed form, appropriately completed, MUST ACCOMPANY any paper in order to be published by ACES. PLEASE READ REVERSE SIDE OF THIS FORM FOR FURTHER DETAILS.

TITLE OF PAPER:

RETURN FORM TO:

Dr. Atef Z. Elsherbeni
University of Mississippi
Dept. of Electrical Engineering
Anderson Hall Box 13
University, MS 38677 USA

AUTHORS(S)

PUBLICATION TITLE/DATE:

PART A - COPYRIGHT TRANSFER FORM

(NOTE: Company or other forms may not be substituted for this form. U.S. Government employees whose work is not subject to copyright may so certify by signing Part B below. Authors whose work is subject to Crown Copyright may sign Part C overleaf).

The undersigned, desiring to publish the above paper in a publication of ACES, hereby transfer their copyrights in the above paper to The Applied Computational Electromagnetics Society (ACES). The undersigned hereby represents and warrants that the paper is original and that he/she is the author of the paper or otherwise has the power and authority to make and execute this assignment.

Returned Rights: In return for these rights, ACES hereby grants to the above authors, and the employers for whom the work was performed, royalty-free permission to:

1. Retain all proprietary rights other than copyright, such as patent rights.
2. Reuse all or portions of the above paper in other works.

3. Reproduce, or have reproduced, the above paper for the author's personal use or for internal company use provided that (a) the source and ACES copyright are indicated, (b) the copies are not used in a way that implies ACES endorsement of a product or service of an employer, and (c) the copies per se are not offered for sale.

4. Make limited distribution of all or portions of the above paper prior to publication.

5. In the case of work performed under U.S. Government contract, ACES grants the U.S. Government royalty-free permission to reproduce all or portions of the above paper, and to authorize others to do so, for U.S. Government purposes only.

ACES Obligations: In exercising its rights under copyright, ACES will make all reasonable efforts to act in the interests of the authors and employers as well as in its own interest. In particular, ACES REQUIRES that:

1. The consent of the first-named author be sought as a condition in granting re-publication permission to others.
2. The consent of the undersigned employer be obtained as a condition in granting permission to others to reuse all or portions of the paper for promotion or marketing purposes.

In the event the above paper is not accepted and published by ACES or is withdrawn by the author(s) before acceptance by ACES, this agreement becomes null and void.

AUTHORIZED SIGNATURE

TITLE (IF NOT AUTHOR)

EMPLOYER FOR WHOM WORK WAS PERFORMED

DATE FORM SIGNED

Part B - U.S. GOVERNMENT EMPLOYEE CERTIFICATION

(NOTE: if your work was performed under Government contract but you are not a Government employee, sign transfer form above and see item 5 under Returned Rights).

This certifies that all authors of the above paper are employees of the U.S. Government and performed this work as part of their employment and that the paper is therefor not subject to U.S. copyright protection.

AUTHORIZED SIGNATURE

TITLE (IF NOT AUTHOR)

NAME OF GOVERNMENT ORGANIZATION

DATE FORM SIGNED

PART C - CROWN COPYRIGHT

(NOTE: ACES recognizes and will honor Crown Copyright as it does U.S. Copyright. It is understood that, in asserting Crown Copyright, ACES in no way diminishes its rights as publisher. Sign only if ALL authors are subject to Crown Copyright).

This certifies that all authors of the above Paper are subject to Crown Copyright. (Appropriate documentation and instructions regarding form of Crown Copyright notice may be attached).

AUTHORIZED SIGNATURE

TITLE OF SIGNEE

NAME OF GOVERNMENT BRANCH

DATE FORM SIGNED

Information to Authors

ACES POLICY

ACES distributes its technical publications throughout the world, and it may be necessary to translate and abstract its publications, and articles contained therein, for inclusion in various compendiums and similar publications, etc. When an article is submitted for publication by ACES, acceptance of the article implies that ACES has the rights to do all of the things it normally does with such an article.

In connection with its publishing activities, it is the policy of ACES to own the copyrights in its technical publications, and to the contributions contained therein, in order to protect the interests of ACES, its authors and their employers, and at the same time to facilitate the appropriate re-use of this material by others.

The new United States copyright law requires that the transfer of copyrights in each contribution from the author to ACES be confirmed in writing. It is therefore necessary that you execute either Part A-Copyright Transfer Form or Part B-U.S. Government Employee Certification or Part C-Crown Copyright on this sheet and return it to the Managing Editor (or person who supplied this sheet) as promptly as possible.

CLEARANCE OF PAPERS

ACES must of necessity assume that materials presented at its meetings or submitted to its publications is properly available for general dissemination to the audiences these activities are organized to serve. It is the responsibility of the authors, not ACES, to determine whether disclosure of their material requires the prior consent of other parties and if so, to obtain it. Furthermore, ACES must assume that, if an author uses within his/her article previously published and/or copyrighted material that permission has been obtained for such use and that any required credit lines, copyright notices, etc. are duly noted.

AUTHOR/COMPANY RIGHTS

If you are employed and you prepared your paper as a part of your job, the rights to your paper initially rest with your employer. In that case, when you sign the copyright form, we assume you are authorized to do so by your employer and that your employer has consented to all of the terms and conditions of this form. If not, it should be signed by someone so authorized.

NOTE RE RETURNED RIGHTS: Just as ACES now requires a signed copyright transfer form in order to do "business as usual", it is the intent of this form to return rights to the author and employer so that they too may do "business as usual". If further clarification is required, please contact: The Managing Editor, R. W. Adler, Naval Postgraduate School, Code EC/AB, Monterey, CA, 93943, USA (408)656-2352.

Please note that, although authors are permitted to re-use all or portions of their ACES copyrighted material in other works, this does not include granting third party requests for reprinting, republishing, or other types of re-use.

JOINT AUTHORSHIP

For jointly authored papers, only one signature is required, but we assume all authors have been advised and have consented to the terms of this form.

U.S. GOVERNMENT EMPLOYEES

Authors who are U.S. Government employees are not required to sign the Copyright Transfer Form (Part A), but any co-authors outside the Government are.

Part B of the form is to be used instead of Part A only if all authors are U.S. Government employees and prepared the paper as part of their job.

NOTE RE GOVERNMENT CONTRACT WORK: Authors whose work was performed under a U.S. Government contract but who are not Government employees are required so sign Part A-Copyright Transfer Form. However, item 5 of the form returns reproduction rights to the U. S. Government when required, even though ACES copyright policy is in effect with respect to the reuse of material by the general public.

January 2002

INFORMATION FOR AUTHORS

PUBLICATION CRITERIA

Each paper is required to manifest some relation to applied computational electromagnetics. **Papers may address general issues in applied computational electromagnetics, or they may focus on specific applications, techniques, codes, or computational issues.** While the following list is not exhaustive, each paper will generally relate to at least one of these areas:

1. **Code validation.** This is done using internal checks or experimental, analytical or other computational data. Measured data of potential utility to code validation efforts will also be considered for publication.
2. **Code performance analysis.** This usually involves identification of numerical accuracy or other limitations, solution convergence, numerical and physical modeling error, and parameter tradeoffs. However, it is also permissible to address issues such as ease-of-use, set-up time, run time, special outputs, or other special features.
3. **Computational studies of basic physics.** This involves using a code, algorithm, or computational technique to simulate reality in such a way that better, or new physical insight or understanding, is achieved.
4. **New computational techniques,** or new applications for existing computational techniques or codes.
5. **“Tricks of the trade”** in selecting and applying codes and techniques.
6. **New codes, algorithms, code enhancement, and code fixes.** This category is self-explanatory, but includes significant changes to existing codes, such as applicability extensions, algorithm optimization, problem correction, limitation removal, or other performance improvement. **Note: Code (or algorithm) capability descriptions are not acceptable, unless they contain sufficient technical material to justify consideration.**
7. **Code input/output issues.** This normally involves innovations in input (such as input geometry standardization, automatic mesh generation, or computer-aided design) or in output (whether it be tabular, graphical, statistical, Fourier-transformed, or otherwise signal-processed). Material dealing with input/output database management, output interpretation, or other input/output issues will also be considered for publication.
8. **Computer hardware issues.** This is the category for analysis of hardware capabilities and limitations of various types of electromagnetics computational requirements. Vector and parallel computational techniques and implementation are of particular interest.

Applications of interest include, but are not limited to, antennas (and their electromagnetic environments), networks, static fields, radar cross section, shielding, radiation hazards, biological effects, electromagnetic pulse (EMP), electromagnetic interference (EMI), electromagnetic compatibility (EMC), power transmission, charge transport, dielectric, magnetic and nonlinear materials, microwave components, MEMS technology, MMIC technology, remote sensing and geometrical and physical optics, radar and communications systems, fiber optics, plasmas, particle accelerators, generators and motors, electromagnetic wave propagation, non-destructive evaluation, eddy currents, and inverse scattering.

Techniques of interest include frequency-domain and time-domain techniques, integral equation and differential equation techniques, diffraction theories, physical optics, moment methods, finite differences and finite element techniques, modal expansions, perturbation methods, and hybrid methods. This list is not exhaustive.

A unique feature of the Journal is the publication of unsuccessful efforts in applied computational electromagnetics. Publication of such material provides a means to discuss problem areas in electromagnetic modeling. Material representing an unsuccessful application or negative results in computational electromagnetics will be considered for publication only if a reasonable expectation of success (and a reasonable effort) are reflected. Moreover, such material must represent a problem area of potential interest to the ACES membership.

Where possible and appropriate, authors are required to provide statements of quantitative accuracy for measured and/or computed data. This issue is discussed in “Accuracy & Publication: Requiring, quantitative accuracy statements to accompany data,” by E. K. Miller, *ACES Newsletter*, Vol. 9, No. 3, pp. 23-29, 1994, ISBN 1056-9170.

EDITORIAL REVIEW

In order to ensure an appropriate level of quality control, papers are peer reviewed. They are reviewed both for technical correctness and for adherence to the listed guidelines regarding information content.

JOURNAL CAMERA-READY SUBMISSION DATES

March issue	deadline 8 January
July issue	deadline 20 May
November issue	deadline 20 September

Uploading an acceptable camera-ready article after the deadlines will result in a delay in publishing this article.

STYLE FOR CAMERA-READY COPY

The ACES Journal is flexible, within reason, in regard to style. However, certain requirements are in effect:

1. The paper title should NOT be placed on a separate page. The title, author(s), abstract, and (space permitting) beginning of the paper itself should all be on the first page. The title, author(s), and author affiliations should be centered (center-justified) on the first page.
2. An abstract is REQUIRED. The abstract should be a brief summary of the work described in the paper. It should state the computer codes, computational techniques, and applications discussed in the paper (as applicable) and should otherwise be usable by technical abstracting and indexing services.
3. Either British English or American English spellings may be used, provided that each word is spelled consistently throughout the paper.
4. Any commonly-accepted format for referencing is permitted, provided that internal consistency of format is maintained. As a guideline for authors who have no other preference, we recommend that references be given by author(s) name and year in the body of the paper (with alphabetical listing of all references at the end of the paper). Titles of Journals, monographs, and similar publications should be in italic font or should be underlined. Titles of papers or articles should be in quotation marks.
5. Internal consistency shall also be maintained for other elements of style, such as equation numbering. As a guideline for authors who have no other preference, we suggest that equation numbers be placed in parentheses at the right column margin.
6. The intent and meaning of all text must be clear. For authors who are NOT masters of the English language, the ACES Editorial Staff will provide assistance with grammar (subject to clarity of intent and meaning).
7. Unused space should be minimized. Sections and subsections should not normally begin on a new page.

PAPER FORMAT

The preferred format for initial submission and camera-ready manuscripts is 12 point Times Roman font, single line spacing and double column format, similar to that used here, with top, bottom, left, and right 1 inch margins. Manuscripts should be prepared on standard 8.5x11 inch paper.

Only camera-ready electronic files are accepted for publication. The term **“camera-ready”** means that the material is neat, legible, and reproducible. Full details can be found on ACES site, Journal section.

ACES reserves the right to edit any uploaded material, however, this is not generally done. It is the author(s)

responsibility to provide acceptable camera-ready pdf files. Incompatible or incomplete pdf files will not be processed, and authors will be requested to re-upload a revised acceptable version.

SUBMITTAL PROCEDURE

All submissions should be uploaded to ACES server through ACES web site (<http://aces.ee.olemiss.edu>) by using the upload button, journal section. Only pdf files are accepted for submission. The file size should not be larger than 5MB, otherwise permission from the Editor-in-Chief should be obtained first. The Editor-in-Chief will acknowledge the electronic submission after the upload process is successfully completed.

COPYRIGHTS AND RELEASES

Each primary author must sign a copyright form and obtain a release from his/her organization vesting the copyright with ACES. Copyright forms are available at ACES, web site (<http://aces.ee.olemiss.edu>). To shorten the review process time, the executed copyright form should be forwarded to the Editor-in-Chief immediately after the completion of the upload (electronic submission) process. Both the author and his/her organization are allowed to use the copyrighted material freely for their own private purposes.

Permission is granted to quote short passages and reproduce figures and tables from and ACES Journal issue provided the source is cited. Copies of ACES Journal articles may be made in accordance with usage permitted by Sections 107 or 108 of the U.S. Copyright Law. This consent does not extend to other kinds of copying, such as for general distribution, for advertising or promotional purposes, for creating new collective works, or for resale. The reproduction of multiple copies and the use of articles or extracts for commercial purposes require the consent of the author and specific permission from ACES. Institutional members are allowed to copy any ACES Journal issue for their internal distribution only.

PUBLICATION CHARGES

ACES members are allowed 12 printed pages per paper without charge; non-members are allowed 8 printed pages per paper without charge. Mandatory page charges of \$75 a page apply to all pages in excess of 12 for members or 8 for non-members. Voluntary page charges are requested for the free (12 or 8) pages, but are NOT mandatory or required for publication. A priority courtesy guideline, which favors members, applies to paper backlogs. Authors are entitled to 15 free reprints of their articles and must request these from the Managing Editor. Additional reprints are available to authors, and reprints available to non-authors, for a nominal fee.

ACES Journal is abstracted in INSPEC, in Engineering Index, DTIC, Science Citation Index Expanded, the Research Alert, and to Current Contents/Engineering, Computing & Technology.